



**Faculteit Wetenschappen**

Departement Chemie

**Computer Modeling of Low-pressure  
Fluorocarbon-based Discharges for Etching Purposes**

**Computer Simulaties van Lage Druk Gasontladingen  
in CF<sub>4</sub> Mengsels voor Plasma-ets Toepassingen**

Proefschrift voorgelegd tot het behalen van de graad  
van doctor in de Wetenschappen aan de Universiteit Antwerpen,  
te verdedigen door

**Violeta GEORGIEVA**

**Promotor: Prof. Dr. Annemie Bogaerts**

**Co-Promotor: Prof. Dr. Renaat Gijbels**

**Antwerpen**

**2005**



## ***Acknowledgments***

This work would not have been possible without the help and support of countless people.

I am deeply indebted to my advisors Prof. Renaat Gijbels and Prof. Annemie Bogaerts. I would like to thank them for their constant encouragement and support, as well as for giving me considerable latitude in accomplishing this task. They were always available for discussions even in matters not directly connected with this study.

My research group has changed a lot over the years. I am grateful to Dr. Min Yan for introducing me to the particle-in-cell idea and providing me with the basic PIC code. Special thanks to Dr. Andrey Okhrimovskyy, Ivan Kolev and Neyda Baguer for several thoughtful discussions which contributed greatly to my understanding of plasma behavior. I am especially grateful to Erik Neyts for translating the summary of the present thesis in Dutch and for his kind assistance always I have asked for. I would like to thank them and my other colleagues for the pleasant moments spent with them over the years of my research.

I am especially thankful to Prof. Kenichi Nanbu and Dr. Kazuki Denpoh for supplying me their ion-CF<sub>4</sub> reaction data and details of their ion-molecule collision model for endothermic reactions.

Thanks are due to Dr. Wim Goedheer and Dr. Adam Cenian for several interesting and valuable discussions over the energy distribution and cross-section data interpretation.

I am thankful to Wim Schoenmaker and Herbert Struyf from the research center IMEC, Leuven, for supplying us with the experimental conditions and dual-frequency reactor geometry.

Since this study is entirely computer-oriented, I would also like to thank Koen De Cauwsemaecker and Luc Van't dack for their technical support of the workstations and their prompt response to every problem arisen in the computer surroundings.

As an international student I am especially grateful to the coordinator for the international students Martine Depauw for her significant assistance and

understanding over the years. I would also like to thank the coordinator of the doctoral study program Eric Mathieu for his excellent management. I benefit a lot from this program addressed to all PhD students in the UA in order to deepen and broaden their knowledge and skills, both within and outside the scope of their research domain. It increased my written and oral skills as a researcher, and prepared me for a career both within and outside the university.

Many thanks are due to the secretaries of the Chemistry Department Nelly Suijkerbuijk, Tania Beyers and Ingrid Swenters for their help about any academic administration matter.

I would like to thank my parents for their love and constant encouragement at all times. I especially thank my husband for his endless love, support and understanding, and our little daughter who has brought in our family so much joy and exciting moments.

This research was supported by the Flemish Fund for Scientific research (FWO) and the Federal Services for Scientific, Cultural and Technical Affairs of the Prime Minister's Office through IUAP – V.

Antwerp, October 2005

## **Contents**

<b>Acknowledgements</b>	<b>iii</b>
<b>Contents</b>	<b>v</b>
<b>List of symbols</b>	<b>ix</b>
<b>List of abbreviations</b>	<b>xiii</b>
<b>Physical constants</b>	<b>xv</b>
<b>1 Introduction</b>	<b>1</b>
1.1 Motivation.....	1
1.2 Introduction to low-pressure discharges.....	2
1.3 Plasma etching.....	5
1.4 The RF cc etching reactor and the etch process.....	8
1.5 Dual-frequency etching reactor.....	11
1.6 Numerical modeling of RF discharges.....	13
1.7 Experimental and computational study of CF <sub>4</sub> discharges and its mixtures..	14
1.8 Present work.....	15
<b>2 The PIC/MCC method and its numerical application</b>	<b>17</b>
2.1 Introduction.....	17
2.2 A PIC model.....	18
2.2.1 A 1d electrostatic case in rectangular coordinates.....	19
2.2.2 Bounded plasma particle simulation.....	22
2.3 A MCC model.....	25
2.3.1 Null-collision method.....	25
2.3.2 The PIC/MCC computational cycle.....	29
2.4 Charged particles followed in the simulation.....	29
2.5 Electron-neutral collisions .....	30
2.5.1 Cross-section data.....	30
2.5.2 Calculation of the post-collision velocities.....	33

2.6 Ion-neutral collisions.....	40
2.6.1 Cross-section data.....	40
2.6.2 Calculation of the post-collision velocities.....	42
2.6.3 Ion-molecule collision model for endothermic reactions.....	43
2.6.4 Theoretical $\text{CF}_3^{+/-} + \text{CF}_4$ and $\text{F}^- + \text{CF}_4$ cross-sections .....	47
2.7 Positive-negative ion recombination.....	49
2.8 Electron-positive ion recombination.....	52
2.9 Stability and accuracy of the PIC/MCC model.....	54
2.10 Methods for speeding up the calculations.....	56
2.10.1 Subcycling (different electron and ion time-steps).....	56
2.10.2 Different particle weights.....	57
2.10.3 Improved initial densities.....	57
2.11 Approximations in the discharge model.....	57
<b>3 Study of Ar/CF<sub>4</sub> discharges: effect of gas composition</b>	<b>61</b>
3.1 Introduction.....	61
3.2 Input data.....	62
3.3 Results and discussion.....	63
3.3.1 Pure Ar discharge.....	63
3.3.2 Pure CF <sub>4</sub> discharge.....	65
3.3.3 Ar/CF <sub>4</sub> mixtures.....	69
3.4 Summary.....	75
<b>4 Study of Ar/CF<sub>4</sub>/N<sub>2</sub> discharges in single- and dual-frequency etching reactors</b>	<b>77</b>
4.1 Introduction.....	77
4.2 Input data.....	78
4.3 Results and discussion.....	79
4.3.1 Potential and electric field distributions .....	80
4.3.2 Electron density distribution.....	81
4.3.3 Ion density distribution.....	82
4.3.4 Electron energy distribution.....	85
4.3.5 Ion energy distribution.....	86
4.4 Summary.....	89
<b>5 Ion energy distributions in single- and dual-frequency etching reactors</b>	<b>91</b>
5.1 Introduction.....	91

5.2 Analytical model of the IEDF in a dual-frequency reactor.....	93
5.3 Input data.....	96
5.4 Results and discussion.....	97
5.4.1 Effect of pressure.....	97
5.4.2 Effect of the applied voltage amplitude.....	99
5.4.3 Effect of the applied frequency regime.....	100
5.5 Summary.....	105
<b>6 Influence of the external process parameters on the plasma characteristics in dual-frequency reactors</b>	<b>107</b>
6.1 Introduction.....	107
6.2 Input data.....	108
6.3 Results and discussion.....	109
6.3.1 From HF to VHF, keeping the HF voltage amplitude constant and varying the LF voltage amplitude.....	109
6.3.2 From HF to VHF, varying the HF voltage amplitude and keeping the LF voltage amplitude constant.....	114
6.3.3 Independence of the plasma density, ion current density and electron energy from the LF voltage source at (60+2) MHz.....	118
6.3.4 Dependence of the sheath potential and width, and the ion energy on the HF and LF voltage sources.....	122
6.3.5 Dependence of the plasma characteristics on the LF voltage source in the (27+2) and (27+1) MHz regimes.....	126
6.4 Calculated power.....	130
6.5 Comparison with experiment.....	133
6.6 Summary.....	134
<b>7 Plasma behavior in asymmetric dual-frequency reactors</b>	<b>135</b>
7.1 Introduction.....	135
7.2 1d spherical model.....	136
7.3 Input data.....	137
7.4 Results and discussion.....	137
7.4.1 Influence of the electrode area ratio on the plasma characteristics....	139
7.4.2 Influence of the power source parameters on the plasma characteristics.....	145
7.5 Summary.....	151

<b>8 Negative ion behavior in single- and dual-frequency reactors</b>	<b>153</b>
8.1 Introduction.....	153
8.2 Input data.....	154
8.3 Results and discussion.....	155
8.3.1 Single-frequency reactors.....	155
8.3.1 Dual-frequency reactors.....	160
7.5 Summary.....	169
<b>9 Conclusions</b>	<b>171</b>
9.1 Summary.....	171
9.2 Future opportunities.....	173
<b>Samenvatting</b>	<b>175</b>
<b>Appendix A:</b> Solving of the potential equations in spherical coordinates	<b>179</b>
<b>Appendix B:</b> $\text{CF}_x^{+/-} + \text{CF}_4$ and $\text{F}^- + \text{CF}_4$ reactive collision data	<b>181</b>
<b>Appendix C:</b> List of publications, contributions to international conferences and invited talks	<b>185</b>
<b>Bibliography</b>	<b>189</b>

## ***List of Symbols***

$a_0$	Bohr radius (m)
$A$	electrode area (m <sup>2</sup> )
$b$	impact parameter (m)
$\mathbf{B}$	magnetic field (T)
$C$	capacitance (F/m)
$d$	distance between electrodes (m)
$e$	elementary charge (C)
$E$	magnitude of the electric field $\mathbf{E}$ (V/m); particle energy (eV)
$E_{th}$	threshold energy (eV)
$f$	frequency (Hz or s <sup>-1</sup> )
$f_e$	electron energy probability function
$F_e$	electron energy distribution function
$F_i$	ion energy distribution function
$\mathbf{F}$	force (N)
$g$	magnitude of the relative velocity $\mathbf{g}$ (m/s)
$j_i$	ion current density at the electrodes (A/m <sup>2</sup> )
$k_r$	ion-ion recombination rate constant (m <sup>3</sup> /s)
$k_{re-i}$	electron-ion recombination rate constant (m <sup>3</sup> /s)
$m$	mass; electron mass (kg)
$M$	mass; ion or neutral mass (kg)
$n_e$	electron density (m <sup>-3</sup> )
$n_g$	neutral gas density (m <sup>-3</sup> )
$n_+$	positive ion density (m <sup>-3</sup> )
$n_-$	negative ion density (m <sup>-3</sup> )
$N$	number superparticles

$p$	pressure (Pa) or (mTorr)
$P$	probability; power (W)
$q$	electric charge (C)
$Q$	electric charge of a capacitor (C)
$r$	radial position (m); error
$R$	random number, uniformly distributed in $[0,1]$ ; electrode radius (m)
$\mathbf{R}$	unit random vector
$s$	sheath thickness (m)
$S$	weighting function; area (m <sup>2</sup> )
$t$	time (s)
$T_e$	electron temperature (eV)
$T_g$	gas temperature (eV)
$T_i$	ion temperature (eV)
$v$	magnitude of the electron velocity $\mathbf{v}$ (m/s)
$V$	magnitude of the neutral or ion velocity $\mathbf{V}$ (m/s); volume (m <sup>3</sup> )
$V_c$	volume of a grid cell (m <sup>3</sup> )
$V_{HF}$	high frequency voltage amplitude (V)
$V_{LF}$	low frequency voltage amplitude (V)
$V_p$	plasma potential (V)
$V_s$	sheath voltage (V)
$W$	particle weight
$x$	rectangular coordinate (m)
$y$	rectangular coordinate (m)
$z$	rectangular coordinate (m)
$z_{pi}$	position of the $i$ th particle (m)
$Z_j$	grid point
$\alpha$	$n_- / n_e$ electronegativity
$\alpha_p$	atomic or molecular polarizability (m <sup>3</sup> )
$\beta$	dimensionless impact parameter
$\chi$	deflection angle (rad) in center-of-mass reference frame
$\gamma$	secondary electron emission coefficient
$\Gamma$	particle flux (1/m <sup>2</sup> s <sup>2</sup> )
$\Delta$	denotes the change of a quantity

$\Delta t$	time-step (s)
$\Delta z$	grid spacing (m)
$\varepsilon$	dimensionless energy; relative energy ( $= \mu g^2 / 2$ ) (eV)
$\varepsilon_0$	vacuum permittivity (F/m)
$\Phi$	electric potential (V)
$\lambda_{De}$	electron Debye length (m)
$\mu$	reduced mass (kg)
$\nu$	collision frequency ( $s^{-1}$ )
$\pi$	3.1416
$\rho$	volume charge density ( $C/m^3$ )
$\sigma$	surface charge density ( $C/m^2$ ); differential cross-section ( $m^2/sr$ )
$\sigma_T$	total/integral cross-section ( $m^2$ )
$\varphi$	angle (rad), spherical azimuthal angle
$\theta$	angle (rad), spherical polar angle
$\tau_{ion}$	ion transit time (s)
$\tau_{HF}$	high frequency period (s)
$\tau_{LF}$	low frequency period (s)
$\tau_{RF}$	radio frequency period (s)
$\omega_{HF}$	high frequency (rad/s)
$\omega_{LF}$	low frequency (rad/s)
$\omega_{pe}$	electron plasma frequency (rad/s)
$\omega_{pi}$	ion plasma frequency (rad/s)
$\Omega$	solid angle (sr)
$A$	scalar
$\mathbf{A}$	vector
$\bar{A}$	average
$\langle A \rangle$	average



## ***List of Abbreviations***

cc	capacitively-coupled
EED(F)	Electron energy distribution (function)
EEPF	Electron energy probability function
GE	Grounded electrode
HF	High frequency
IED(F)	Ion energy distribution (function)
LF	Low frequency
MC	Monte Carlo
MCC	Monte Carlo collision
PE	Powered electrode
PIC	Particle-in-cell
RF	Radio frequency

## ***Subscript Abbreviations***

CM	center-of-mass
CT	charge transfer
coll	collision
conv	convection
e	electron
ej	ejected
el	elastic
g	gas
i	ion
inc	incident
m	momentum
max	maximum
min	minimum
p	particle; polarizability
r	recombination

T	total
th	threshold
$\perp$	perpendicular

## ***Physical Constants***

Bohr radius	$a_0 = 5.2918 \times 10^{-11} \text{ m}$
Boltzmann constant	$k = 1.3807 \times 10^{-23} \text{ J/K}$
Elementary charge	$e = 1.6022 \times 10^{-19} \text{ C}$
Electron mass	$m = 9.1095 \times 10^{-31} \text{ kg}$
Vacuum permittivity	$\varepsilon_0 = 8.8542 \times 10^{-12} \text{ F/m}$

## **Conversion factors**

Energy associated with 1 eV	$1.6022 \times 10^{-19} \text{ J}$
Temperature associated with 1 eV	11605 K
Pressure of 1 Torr	133.32 Pa

## **Ion and neutral masses used in the model**

$$M_{Ar^+} \approx M_{Ar} = 6.63 \times 10^{-26} \text{ kg}$$

$$M_{N_2^+} \approx M_{N_2} = 4.65 \times 10^{-26} \text{ kg}$$

$$M_{CF_4} = 1.46 \times 10^{-25} \text{ kg}$$

$$M_{CF_3^{+/-}} = 1.15 \times 10^{-25} \text{ kg}$$

$$M_{F^-} = 3.15 \times 10^{-26} \text{ kg}$$



## **Chapter 1**

### **INTRODUCTION**

#### **1.1 Motivation**

Glow discharges find an increasing application in the microelectronics industry to modify the surface properties of materials, in particular for the deposition of thin films and for plasma etching of metals and semiconductors [1, 2]. Radio-frequency (RF) plasma etching is well recognized for its anisotropy, which is a key process parameter in integrated circuit manufacturing, and the study of this plasma processing is therefore of great interest. In order to achieve high-resolution plasma processing it is important to understand the discharge physics and chemistry. The electron and ion densities and the electron temperature determine the production of the neutral radicals, responsible for chemical etching. The kinetics of the ions incident on the wafer is crucial in determining the etch rates and anisotropy in the ion reactive etching. Experiments reveal certain aspects of the process but many of the details remain obscure. Modeling can help to understand basic physical and chemical mechanisms but it is often limited to idealized systems, which are hardly ever used in practice. However, there is a constant improvement and development of the models and the advance in the computer technologies allows more and more complex and realistic systems to be simulated. In the past decade computer simulations have become a powerful tool to study the plasmas. Combined with experimental measurements they advance plasma science and engineering.

This work develops a computer model of a discharge in a complex gas-mixture sustained in an industrial etching reactor with as few restrictions and approximations as possible. The numerical model, *particle-in-cell/Monte Carlo collision (PIC/MCC) method* is chosen because the field and the energy distributions of the charged species are obtained self-consistently from first principles. The electron energy distribution (EED) determines the production of the ions and radicals, i.e. the reactive species concentration. The energy distribution of the ions incident on the wafer (IED) and their fluxes determine the anisotropy and etch rates.

The investigated feed-gas mixtures of carbon tetrafluoride,  $\text{CF}_4$ , with Ar and  $\text{N}_2$ , are used in plasma etching of silicon. Comparison is made with experimental results available in the literature.

The following *objectives* have guided the present study. The *first objective* is the development of the existing one-dimensional (1d) PIC/MCC model for an Ar discharge to a PIC/MCC model for Ar/ $\text{CF}_4$  and pure  $\text{CF}_4$  discharges in a single-frequency capacitively coupled (cc) reactor, and a comparison of the electropositive and electronegative plasma behavior, as well as investigation of the effect of the gas composition. The simulation results of electronegativity, i.e. the ratio of the negative ion to electron densities, are compared with experimental data.

Feed-gas mixtures are usually complex because of the conflicting requirements on the etch rate, selectivity to mask, and anisotropy. Ar/ $\text{CF}_4$ / $\text{N}_2$  is a typical feedstock gas used in plasma etching and the *second objective* is to add  $\text{N}_2$  to the developed model and study the Ar/ $\text{CF}_4$ / $\text{N}_2$  discharges. In addition, a dual-frequency reactor is considered because of the recent increasing interest to this setup. A comparison with the single-frequency reactor is made and the advantages of the two-frequency scheme are demonstrated.

The ion bombardment energy is a key parameter in the etching process and this determines the *third objective*, which is a detailed computer study of the ion energy distribution function (IEDF) in the two reactor types and development of an analytical model describing the IEDF in the dual-frequency reactor.

The *fourth objective* is to investigate the influence of the external process parameters on the plasma characteristics and to define the parameters at which the independent control of the ion flux and energy is possible, since this is the main advantage of the two frequency scheme.

Finally, the reactors are generally asymmetric in reality, i.e. the area of the powered electrode is typically smaller than the area of the grounded electrode and the developed 1d model is therefore transformed to a spherical coordinate system in order to describe an asymmetric dual-frequency reactor, which is the *fifth objective*.

The rest of this chapter is devoted to the theoretical background of plasmas and RF cc discharges, numerical modeling and experimental study of glow discharges used in etching reactors.

## 1.2 Introduction to low-pressure discharges

A *plasma* is a partially or completely ionized gas containing electrons, ions and neutrals, and on average is electrically neutral. It is generally characterized by the number density [particles/ $\text{m}^3$ ] and average kinetic energy or temperature in eV of the charged species. In the electropositive plasmas the electron density,  $n_e$ , and positive ion density,  $n_+$ , are considered equal because of the quasi-neutrality, and

they are often known as plasma density  $n$ . In the electronegative plasmas, which are investigated in this study, the positive ion density is equal to the sum of the negative ion and electron densities, i.e.  $n_+ = n_e + n_- = n_e(1 + \alpha)$ , where  $n_-$  is the negative ion density and  $\alpha = n_- / n_e$  is the electronegativity. The average electron and ion temperatures,  $T_e$  and  $T_i$ , respectively, can vary significantly. Different kinds of plasmas, classified by their electron temperature and charged particle density, are presented in Fig. 1.1 [1].

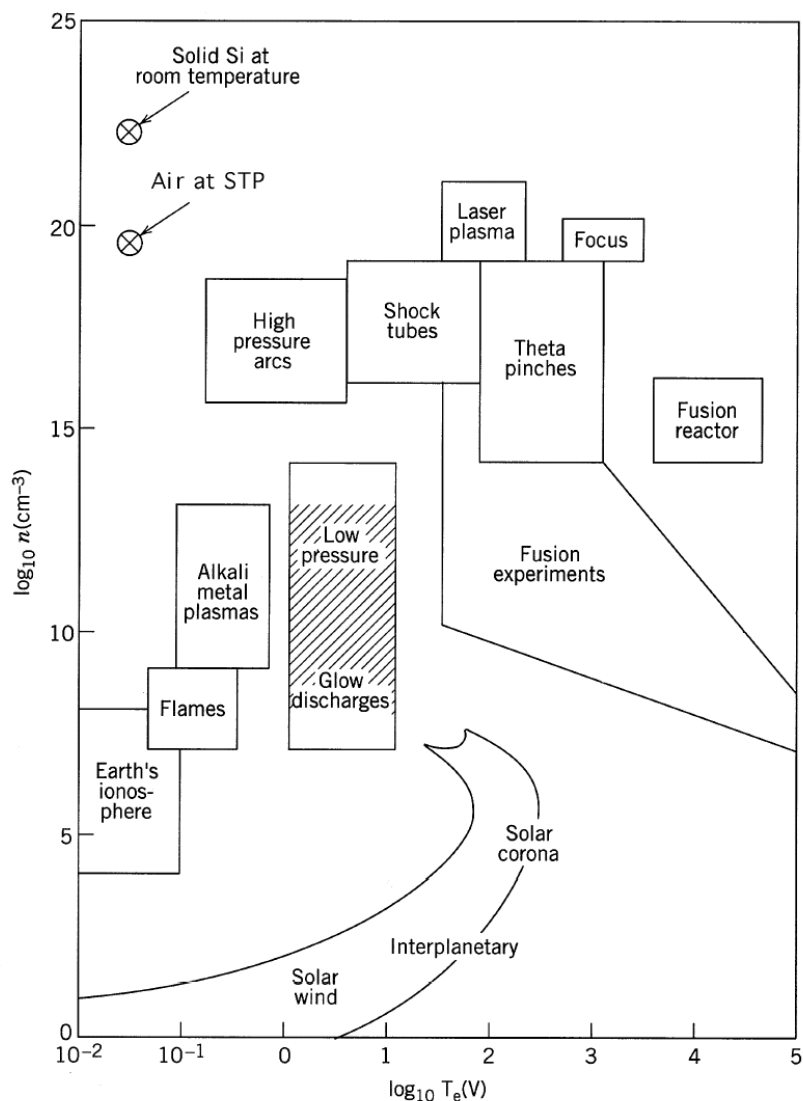


FIGURE 1.1. Space and laboratory plasmas, classified by their electron temperature  $T_e$  (in eV) and charged particle density (in  $\text{cm}^{-3}$ ) on a logarithmic scale. Reproduced from Ref. 1.

*Low-pressure glow discharges* are the subject of this study because they are used in material processing. The operating pressure is between 1 and 1000 mTorr. The charged particles are almost never in thermal equilibrium because these discharges are electrically driven and the applied power preferentially heats the much lighter electrons in comparison with the heavy ions. Thus the electrons, heated by the electric field, attain energies as high as 10 eV while the heavy ions remain close to the neutral gas temperature  $T_g$ . These discharges are characterized by typical number density  $n = 10^{14} - 10^{19} \text{ m}^{-3}$  [1].

The plasma itself as well as the plasma-substrate system is not in thermal equilibrium, which determines the importance of low-pressure plasmas for removing materials from surfaces. Figure 1.2 presents the densities and temperatures for various species in a typical cc RF low-pressure discharge, e.g. a  $\text{CF}_4$  discharge, used in plasma etching. As it is seen from the figure, the feedstock gas, etchant radicals and etch products, and plasma ions have roughly the same temperature, which does not exceed few times the room temperature (0.026 eV). However, the ions bombarding the substrate can reach 100–1000 eV, much exceeding the electron temperature, which is in the range of 1–10 eV.

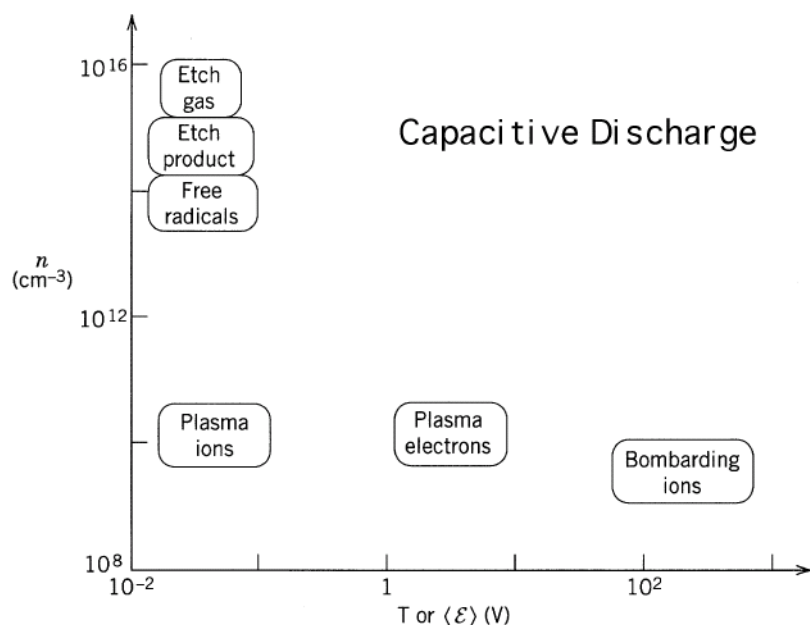


FIGURE 1.2. Densities and temperatures (or energies) for various species in low-pressure capacitive discharges, used in plasma etching. Reproduced from Ref. 1.

### 1.3 Plasma etching

Plasma etching relies on the chemical combination of the solid surface to be etched with an active gaseous species produced in the discharge. The conventional wet etching leads to an isotropic profile as shown in Fig. 1.3 (a), which is produced by the same etch rate in all directions. This undercutting was acceptable many years ago when the space between trenches was tens of micrometers. At present sub-micrometer feature spacing a directional, anisotropic, etching is required, which is possible only by plasma processing [Fig. 1.3(b)]. Plasma etching can be chemically selective, i.e. removing one type of material while leaving other materials unaffected. For example, etching of silicon using a  $\text{CF}_4/\text{Ar}$  discharge is considered.  $\text{CF}_4$  and Ar do not react with the silicon. The etchant F atoms, however, react with the silicon substrate and the product is the volatile  $\text{SiF}_4$  (see also Fig. 1.7), which is pumped away. This process etches the silicon isotropically. For an anisotropic etch there must be highly energetic ions, i.e.  $\text{Ar}^+$  and  $\text{CF}_3^+$ , bombarding the substrate. The directional etch removes material at the bottom of a trench while leaving the same material on the sidewall unaffected [Fig. 1.3(b)]. The bombarding ions increase the reaction rate at the surface or expose the surface to the etchant by removing the passivating films that cover the surface (see below).

The following basic low-pressure plasma processes are used for removing material from surfaces: sputtering, pure chemical etching, ion energy-driven etching and ion inhibitor etching [1]. The processes are schematically illustrated in Fig. 1.4.

*Sputtering* [Fig. 1.4(a)] is the ejection of atoms from the surface because of energetic ion bombardment. The discharge supplies ions with energies above few 100 eV. Sputtering is an unselective process and it depends on the surface binding energy and the masses of the ions and sputtered atoms.

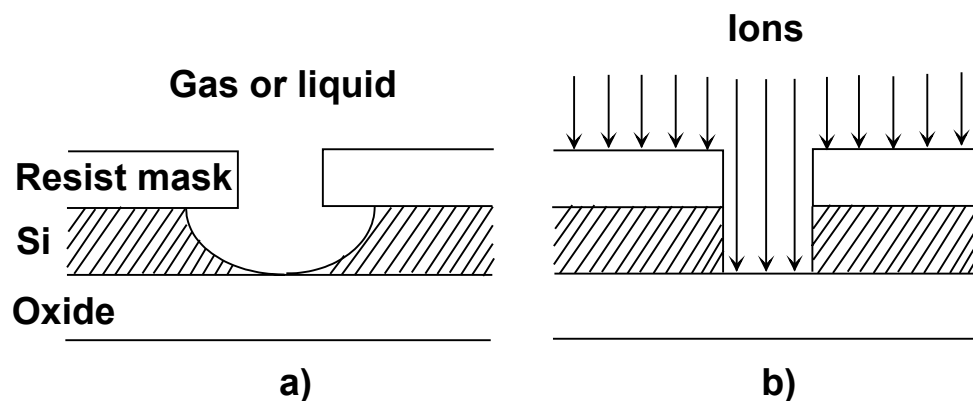


FIGURE 1.3. Example of isotropic etch (a) and anisotropic (directional) etch (b).

These characteristics do not vary significantly for different materials; hence the sputtering rates are roughly the same. In addition, the rates are generally low because the yield is typically one atom per incident ion [1]. The ion fluxes at the substrate are often small compared to the commercially required significant rates for removing materials. Sputtering is, however, an anisotropic process, because the incident ions have a highly directional angular distribution at the surface. Therefore, it is important for removing low fraction involatile components during film etching, using other processes.

*Pure chemical etching* [Fig. 1.4(b)] is the second etch process. The discharge supplies etchant atoms or molecules that chemically react with the surface to form a volatile product. This process can be highly chemically selective, however, it is isotropic, because the etchants arrive at the surface with nearly uniform angular distribution. The etch rates can be quite high because the etchant flux in the discharges can be high compared to the ion flux (see Fig. 1.2 for the densities of the various species in the discharge).

*Ion-enhanced energy-driven etching* [Fig. 1.4(c)] is the third etch process, in which both etchant atoms and energetic ions are supplied to the surface. The rates in this case can be much larger than the rates of either sputtering or pure chemical etching. For example, in the etching of silicon with a high incident F atom flux, a single  $\text{Ar}^+$  ion with an energy of  $10^3$  eV can cause the removal of as many as 25 Si atoms from the surface in the form of the gaseous  $\text{SiF}_4$  (see below) [1]. Experiments suggest that the etching is chemical in nature but with a reaction rate determined by the energetic incident ions. The *anisotropy* is defined as the ratio of the vertical to the horizontal etch rate. However, the ion-energy driven etching may have poor selectivity in comparison with the pure chemical etching. The *selectivity* is defined as the ratio of the etch rate of the silicon, which is considered in this example, to the etch rate of the resist mask. The trade-off between anisotropy and selectivity is important in designing the etch processes as it is shown in Ref. 1. The detailed mechanism for the etch product formation and the rate of formation are not well understood yet.

*Ion-enhanced inhibitor etching* [Fig. 1.4(d)] is the fourth etch process, in which an inhibitor species is used. The discharge supplies etchants, energetic ions and inhibitor precursor molecules. These molecules deposit on the substrate to form a protective layer or polymer film. The etchant is chosen in such a way that it produces high chemical etch rates in the absence of either the energetic ions or the inhibitor. The bombarding ions prevent forming of the inhibitor layer or clear it if it is formed, and expose the surface to the etchant. The inhibitor protects the surface from the etchant where the ion flux does not fall. An example for this process is the anisotropic etching of aluminum trenches or holes using  $\text{CCl}_4/\text{Cl}_2$  or  $\text{CHCl}_3/\text{Cl}_2$

discharges [1]. Both Cl and Cl<sub>2</sub> rapidly etch aluminum and the process is isotropic. The addition of C results in formation of a protective chlorocarbon film on the surface. Ion bombardment clears the film from the trench bottom, exposing this surface to the etchants. The same film on the sidewalls protects them from etching. The ion inhibitor etching has the same other features as the ion energy-driven etching, i.e. it may be poorly selective and volatile etch products must be formed. However, contamination of the substrate and final removal of the inhibitor layer must also be considered in this etch process.

Often etching of a substrate involves a parallel or serial combination of the processes, described above. For example, consider the etching of a silicon film that must stop at the oxide layer (see Fig. 1.3). The first step might be a fast, highly anisotropic ion energy-driven etching. Pure chemical etching at the sidewalls at the same time determines the anisotropy. When 90% of the silicon film has been removed, the next step is a slow highly selective, but isotropic etch in order to remove the rest of the silicon layer with minimum etching of the underlying oxide. The small undercut produced in this case might be acceptable if the remaining silicon layer is thin enough.

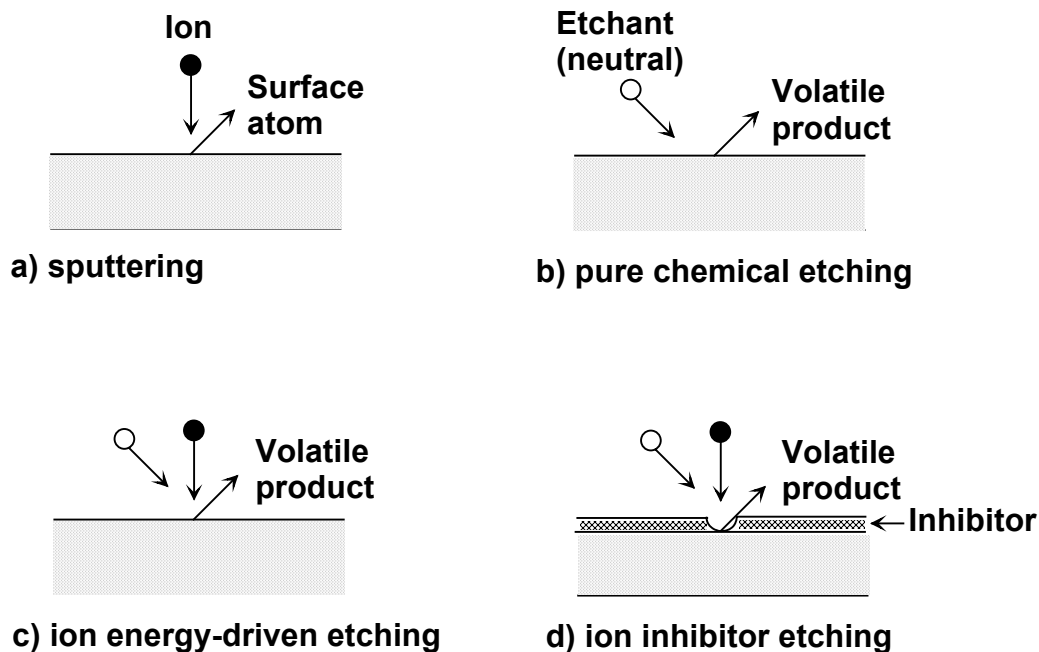


FIGURE 1.4. Illustration of the basic plasma etching processes: sputtering (a), pure chemical etching (b), ion-enhanced energy-driven etching (c), and ion-enhanced inhibitor etching.

Plasma etching is one of the several major steps (e.g. oxidation, chemical and physical vapor deposition, ion implantation and lithography for deposition and modifying materials and etching for removal materials) in an integrated circuit fabrication. Manufacture of microchips involves repeating the above types of processing steps several times, until a complete device, such as a transistor is fabricated. Currently, a state-of-the-art silicon microchip contains more than hundreds million transistors, within an area of about 1 cm<sup>2</sup>! As it is stated in the Intel Silicon Innovation brochure published in 2005, “because of shrinking process geometries, today’s Intel® Itanium® 2 processor packs 410 million transistors onto a piece of silicon wafer not much larger than your fingernail” (to be found at [http://www.intel.com/pressroom/kits/events/moores\\_law\\_40th/index.htm](http://www.intel.com/pressroom/kits/events/moores_law_40th/index.htm)). The individual transistors are so small that one will need an electron microscope to see them. Hundreds of steps may be needed to fabricate a chip, which may have multiple layers. Shrinking linewidths to the nanometer scale requires a precise control of each of the processing steps, including plasma etching. Therefore, it is important to understand plasma behavior as is focused on in the present work.

#### 1.4 The RF cc etching reactor and the etch process

Advances in miniaturization of ultra-large scale integrated circuits have driven the optimization of the technology. At present optimum processing in etching of Si and SiO<sub>2</sub> may be achieved by a cc plasma in a narrow gap reactive ion etcher operating in RF, typically 13.56 MHz. A typical RF cc etching reactor is shown in Fig. 1.5. It is a cylindrical vacuum chamber containing two planar electrodes. Usually the upper electrodes and the walls are grounded, the bottom electrode, where the wafer is placed, is driven by a single- or dual-frequency RF power source. The discharges are generally *asymmetric*, i.e. the area of the powered electrode (PE) is smaller than the area of the grounded electrode (GE). The smaller electrode develops a dc self-bias voltage. The distance between the electrodes is in the order of a few cm; the diameter of the electrodes is in the order of a few 10 cm. The supplying power can be in the order of 1 – 2000 W.

The potential distribution at different times of the RF cycle, as well as the plasma potential  $V_p$  and PE potential  $V_{PE}$  as a function of time in the single-frequency cc reactor are shown in Figs. 1.6 (a) and (b), respectively. The dc bias voltage  $V_{dc}$  is also presented.

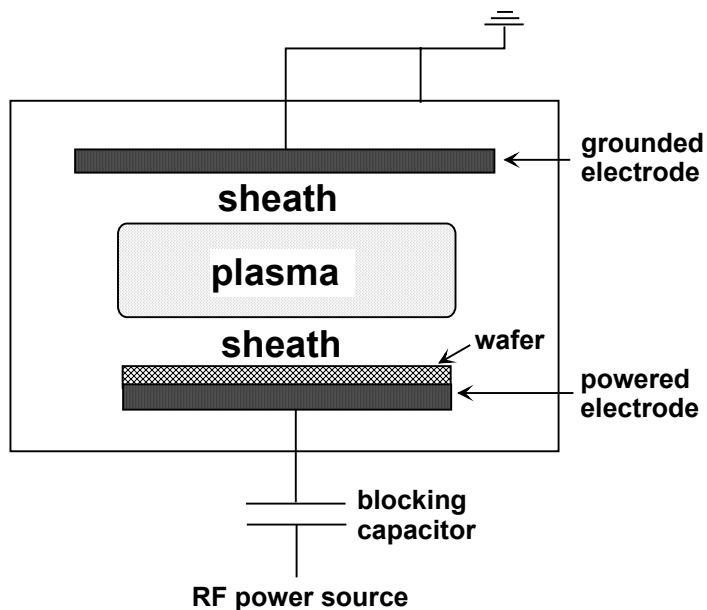


FIGURE 1.5. Schematic diagram of the RF cc etching reactor.

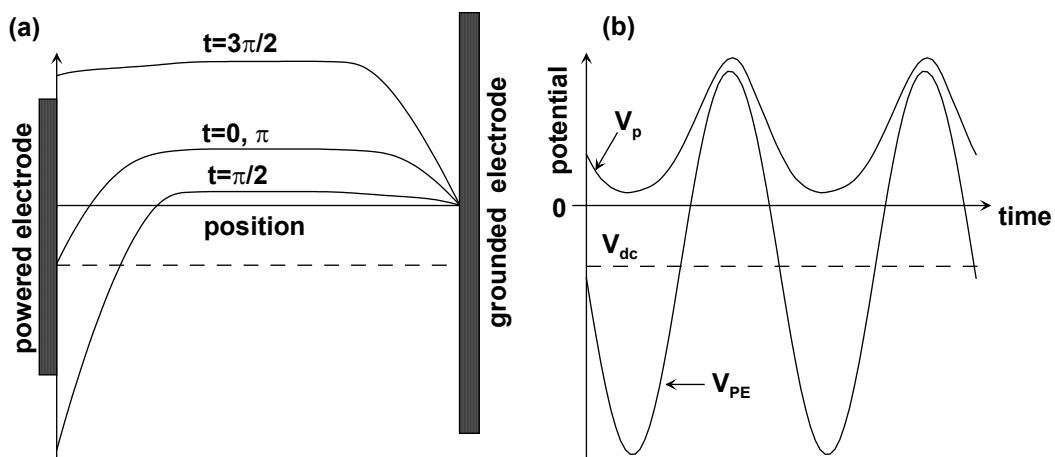


FIGURE 1.6. Calculated potential distribution at different times in the RF cycle (a) and plasma potential  $V_p$  and powered electrode potential  $V_{PE}$  as a function of time (b) in the single-frequency cc reactor. The dashed lines show the dc bias voltage  $V_{dc}$  developed at the powered electrode.

The processes that occur in the etching reactor in the case of  $\text{CF}_4$  as etching gas are presented in Fig. 1.7. The energetic electrons collide with the neutral molecules of the background gas and produce reactive species (radicals, ions and excited molecules). The dissociation reactions, which have high activation energies, proceed at room temperature. The rates of recombination and ion-neutral reactions involving the neutral radicals are unaffected by the presence of the energetic electrons. This non-equilibrium situation raises the concentration of the radicals by several orders of magnitude. Typical radical concentration can reach  $10^{20} \text{ m}^{-3}$ , while the charged particle concentrations are in the order of  $10^{16} \text{ m}^{-3}$  (see Fig. 1.2). The etchant species diffuse to the wafer surface where they etch the material through the formation of volatile reaction products (see Fig. 1.7). If polymerizing species are formed, they tend to deposit on the surface forming passivation layers.

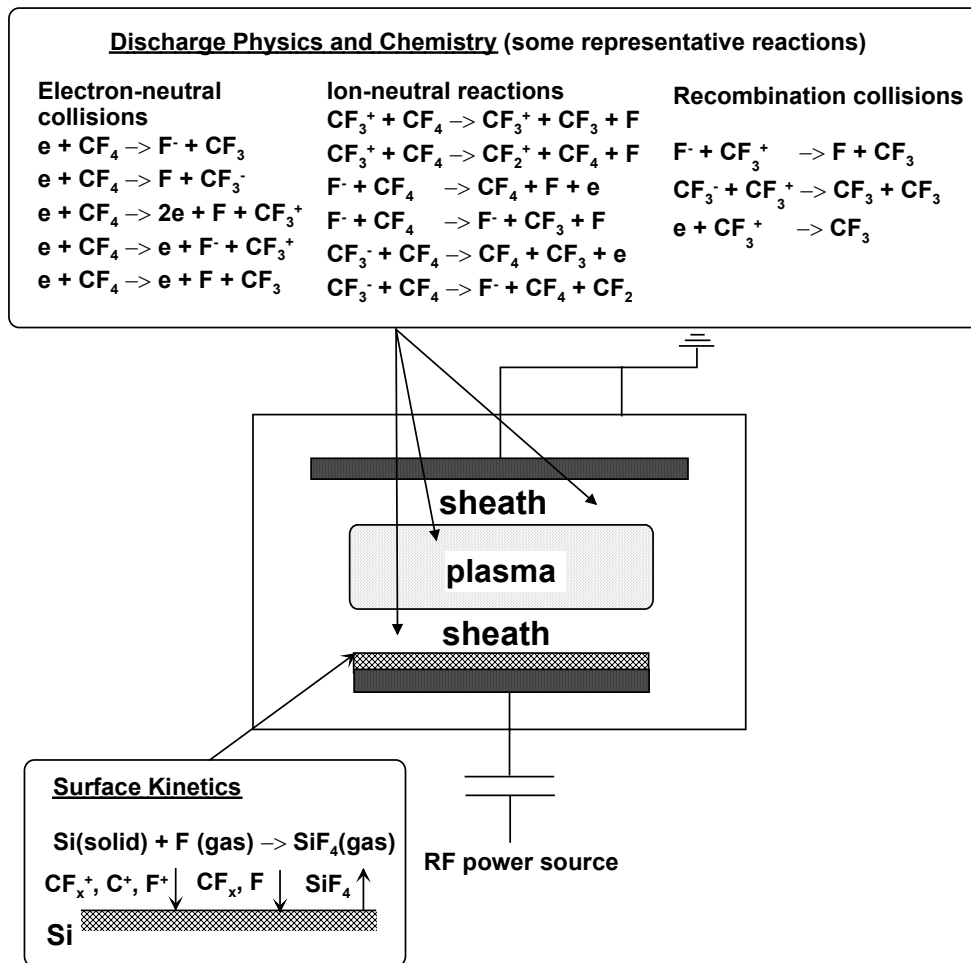


FIGURE 1.7. Schematic picture of some important processes in the etching reactor.

The inequality in the diffusion coefficients for electrons and ions forces the plasma to bias itself positive with respect to the wafer and the chamber walls in order to maintain the quasi-neutrality (see Fig. 1.6). In the absence of the electric field the electron flux to a surface far exceeds the positive ion flux and therefore the surface becomes negatively charged, i.e. repelling the electrons and attracting positive ions. Thin positive ion sheaths form near both electrodes. The electric fields within the sheaths established at steady state point from plasma to the electrodes. Consequently, the electrostatic force acting on the electrons is directed into the plasma and it returns the electrons traveling to the walls back to the plasma, while the ions enter the sheaths and are accelerated to the walls. After a few RF cycles the time-averaged electron and ion fluxes become equal. In the electronegative discharges negative ions are also present and they are confined in the plasma at standard operating conditions. However, under some conditions like in dual-frequency reactors, they can also reach the surface and play a role in the etching process. This characteristic of the electronegative discharges is treated in Chapter 8. The positive ions gain an energy approaching the plasma potential in the symmetric reactor and even exceeding it by the dc self bias voltage formed in the asymmetric reactor. The bombarding ions not only enhance the etch rates but may also sputter off the passivation layers exposed to the ion flux. Most of the ions arrive perpendicular to the surface, which results in directional etch profiles.

It is clear that the etching process is quite complex and it depends on the external parameters such as the RF source, gas pressure, gas composition and flow rate, reactor volume and electrode gap, electrode area, and electrode material and temperature. These parameters control the plasma and its characteristics. The principal discharge characteristics of interest are the concentrations, fluxes and energies of the charged particles, and the radical concentrations, as a function of position and time. The scaling evolution of semiconductor devices needs more and more accurate transfer pattern with minimum damage on the substrate, which can be achieved only by the precise control of the internal discharge parameters. This explains the huge number of investigations of the RF cc discharges by experiment [e.g. Refs. 3 - 19], theory [e.g. Refs. 20 - 27] or computer modeling (e.g. Refs 28 - 69).

### **1.5 Dual-frequency cc etching reactor**

Dual-frequency reactors were introduced in the early 90s [14,15] but recently there has been an increasing interest and study of these systems [17-19, 27, 34, 60-68]. The two-frequency scheme allows independent control of the ion flux and ion-bombarding energy, which is important for surface etching applications, and this cannot be achieved by conventional single-frequency cc reactors. In addition, it

provides a significantly wider ion-bombarding energy range in comparison with the single-frequency configuration.

In the dual-frequency reactor the discharge is sustained by a two-frequency power scheme, i.e. in case of a voltage-driven discharge the applied voltage is the sum of the high frequency (HF) and low frequency (LF) voltages,

$$V = V_{HF} \sin(\omega_{HF}t) + V_{LF} \sin(\omega_{LF}t) \quad (1.1)$$

where  $V_{HF}$  and  $V_{LF}$  are the HF and LF voltage amplitudes, and  $\omega_{HF}$  and  $\omega_{LF}$  are the applied HF and LF. Typical operating parameters are the following: pressure is in the range of 30–300 mTorr, HF is in the range of 27–160 MHz, LF is in the range of 2–13.56 MHz, absorbed HF and LF powers 500–3000 W [68]. Typical feedstock gases for etching of silicon are gas mixtures of  $\text{CF}_4$  or  $\text{C}_4\text{F}_8$  with non-reactive gases like Ar and  $\text{N}_2$ .

In the single-frequency reactors the ions respond to the electric field averaged over the RF cycle and their densities do not depend on the phase in the RF cycle, while the electrons respond to the instantaneous electric field. In the dual-frequency reactor the ions can partially respond to the instantaneous electric field because the ion transit time becomes comparable to the LF period. The potential distribution and the time evolution of the plasma and PE potentials are quite different from the potential distribution in single-frequency reactor [see Figs. 1.8 (a) and (b)].

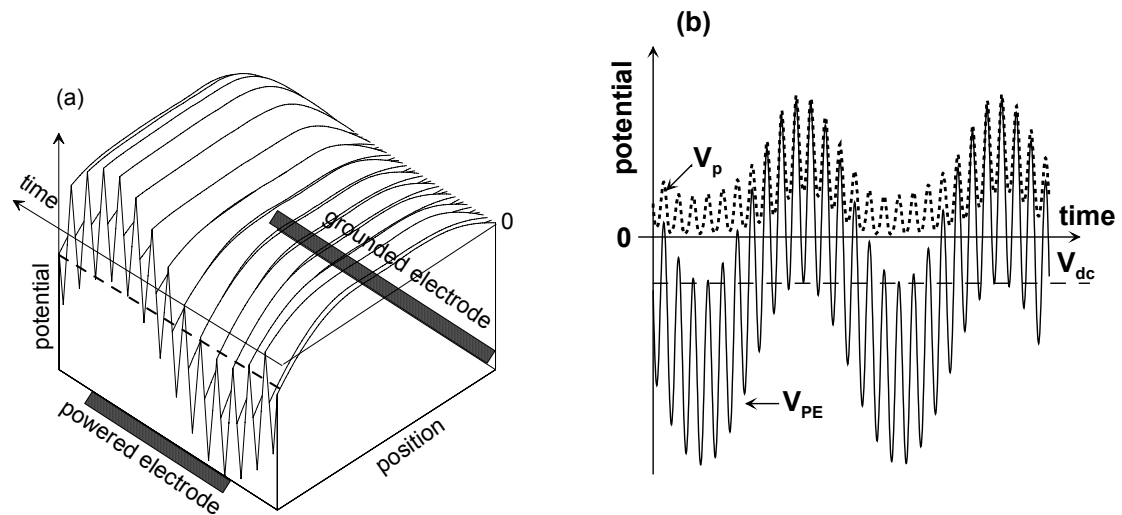


FIGURE 1.8. Calculated potential distribution at different times in the RF cycle (a) and plasma potential  $V_p$  and powered electrode potential  $V_{PE}$  as a function of time (b) in the dual-frequency cc reactor. The dashed lines show the dc bias voltage developed at the powered electrode.

## 1.6 Numerical modeling of RF discharges

In order to improve the etching process it is important to understand the discharge physics and chemistry. Computer simulations have proved to be a powerful tool to study the plasmas. Numerical modeling of RF discharges uses different approaches to simulate the discharge behavior.

*Global* or analytical models use analytical scaling laws describing the dependence of plasma characteristics on external parameters like pressure and RF power. These models assume some approximations based on the specific discharge conditions and solve particle and energy balance equations [28-30]. They are fast and consequently are suitable for a quick prediction of the basic discharge behavior.

*Fluid* models describe the particle transport by solving the continuity, momentum and energy balance equations [31-37]. These equations are generally coupled with Poisson's equation to obtain a self-consistent electric field distribution. The models are comparatively fast but they assume that the velocity distribution functions are almost in equilibrium with the electric field, which is not true especially in the sheaths. These assumptions restrict the application of the fluid model to plasmas, where the mean free path for electron or ion collisions is small compared to the electrode gap, which typically is true for pressures above 300 mTorr. The etching reactors operate at pressures below 300 mTorr, which makes the fluid model not very suitable for studying these reactors. In addition, it does not resolve EED and IED, which are key parameters to improve the etch process. The advantage of the fluid model is that it resolves the density of all species, including the charged particles and radicals, which is essential in the simulation of the complex gas mixtures.

*Hybrid* models have been introduced as a method to speed up computations while retaining important nonequilibrium aspects of the EED [e.g. Ref. 38-43]. In these models the conventional fluid equations resolve the charged particle densities and a kinetic description of the electron transport describes the nonequilibrium aspects of the EED. Therefore, the hybrid models can be applied for pressures, below the limit of the fluid models.

*Monte Carlo* simulations account for the nonequilibrium behavior of the plasma species. A large number of particles are followed and their trajectories are calculated by Newton's laws. The collisions are determined by random numbers and cross-section data. However, the models are not self-consistent and they require a certain time-dependent electric field distribution as an input, which is calculated for example from a sheath model [44, 45].

Finally, the *PIC/MCC* models describe the discharge kinetically [46 – 67]. We have chosen this approach because the EED and IED are fully resolved as a function of space and time. The basic idea of the PIC model is that thousands of computer-

simulated particles (super-particles) represent many more ( $10^{14} - 10^{17} \text{ m}^{-3}$ ) real particles in the reactor. The particles interact with the electromagnetic field calculated on a numerical grid. The method uses first principles, i.e. the classical mechanics for the equations of motion, and Maxwell's equations for the electromagnetic fields, generated by the particle densities. The interactions between the charged particles and neutrals are added by the MCC method, including null-collision method, equal time step between collisions, and uniform distribution of the neutral gas. The PIC/MCC is not suitable for calculating the radical densities because their distribution is not uniform. The main disadvantage of the model is that it requires a long computational time to reach convergence in case of high plasma densities or electronegative discharges. In the latter case the negative charges are confined in the bulk plasma and the main loss mechanism, i.e. ion-ion recombination, has a relatively low reaction frequency. In case of high plasma densities, the Debye length becomes small, and hence more "super-particles" have to be followed on a finer grid. There are many physical and numerical methods to speed up the PIC calculations such as longer ion time steps, different weights for electrons and ions, implicit mover and improved initial density profiles [69]. The PIC/MCC method, developed in this work, is presented in detail in Chapter 2.

## **1.7 Experimental and computational study of CF<sub>4</sub> discharges and its mixtures**

Ar discharges are often used as an example for describing the fundamental principles of plasma behavior. Due to its relative simplicity the cc RF Ar discharges have been studied extensively both experimentally [3 – 10] and by computer modeling [34, 38 – 41, 44, 45, 50 – 56, 63 – 67]. However, plasma chemical issues are as much important in the further optimization of etching processes as plasma processing units. Feed-gas mixes are usually complex because of the conflicting requirements on the etch rate, selectivity to mask, and anisotropy. CF<sub>4</sub> is a basic component in gas mixtures for plasma etching of silicon and silicon dioxide and, therefore, is the most well-studied etch system (e.g., Refs. 1, 11-15, 35-37, 57, 58). CF<sub>4</sub> is generally mixed with non-reactive gases like Ar and N<sub>2</sub>, or non-reactive Ar and oxidant O<sub>2</sub>. Nitrogen is added in order to control the radical temperature [70]. While the investigation of pure CF<sub>4</sub> discharges gives the pattern for describing plasma etching, the study of discharges in complex gas mixtures of CF<sub>4</sub>, such as Ar/CF<sub>4</sub>, Ar/CF<sub>4</sub>/O<sub>2</sub> and Ar/CF<sub>4</sub>/N<sub>2</sub>, which are often used for etching, provides insight into the process (e.g. Ref. 16-19, 42, 43, 59-62).

CF<sub>4</sub> is an electronegative gas and its radicals play an important role in the etching process. The electron and ion densities and the electron temperature determine the production of the neutral radicals. It was shown experimentally and

by modeling that the negative ion density in the bulk plasma exceeds the electron density by one order of magnitude. The abundance of negative ions is one of the main features of discharges in electronegative gases and this profoundly influences the sheath dynamics (i.e., one observes electric field reversal, double layer structure and local maxima of electron density in the sheath region). In a mixture with the electropositive Ar, the discharge can exhibit strong electronegative behavior depending on the operating condition and  $\text{CF}_4$  concentration.

Some example reactions in the pure  $\text{CF}_4$  discharge are shown in Fig. 1.7. In contrast with the Ar discharge, even the pure  $\text{CF}_4$  discharge is already a complex system and a lot of reactions, i.e. production and loss of particles have to be taken into account. The  $\text{CF}_4$  discharge contains several positive ions  $\text{CF}_3^+$ ,  $\text{CF}_2^+$ ,  $\text{CF}^+$ ,  $\text{C}^+$ , and  $\text{F}^+$ , negative ions  $\text{F}^-$  and  $\text{CF}_3^-$ , and radicals  $\text{CF}_3$ ,  $\text{CF}_2$ ,  $\text{CF}$ ,  $\text{C}$ , and  $\text{F}$ . At low pressures, which are used in the etching reactors the main positive ion is  $\text{CF}_3^+$  with density hundreds to thousands times higher than the density of the other positive ions, and consequently the presence of the other ions can be neglected in a model. In the single-frequency reactor the  $\text{F}^-$  ion is the main negative ion. However, in the dual-frequency reactor at some operating conditions the  $\text{CF}_3^-$  becomes the main negative charge. Therefore, both negative ions are important for sustaining the discharge.

As it is discussed above, pure  $\text{CF}_4$  discharges are investigated extensively in experimental [e.g. Ref. 1, 11-15] or numerical simulation [e.g. Ref. 1, 35-37, 57, 58] works. However, gas mixtures of  $\text{CF}_4$  are used for etching purposes. Moreover, the concentration of the  $\text{CF}_4$  typically does not exceed 10%, so that discharges of such gas mixtures behave differently from pure  $\text{CF}_4$  discharges. There are some experimental [16-19] and few computational [42, 43] papers describing different plasma characteristics in Ar/ $\text{CF}_4$  and Ar/ $\text{CF}_4/\text{O}_2$  discharges sustained in conventional cc single-frequency reactors. A systematic study of a complex fluorocarbon-based gas mixture in a dual-frequency reactor, which has become an industry standard in recent years, however, cannot be found in the open literature. In order to fill in this gap, the present simulation model has been developed and numerical investigation of Ar/ $\text{CF}_4$  and Ar/ $\text{CF}_4/\text{N}_2$  discharges in single- and dual-frequency reactors has been systematically carried out.

## 1.8 Present work

The present work investigates pure Ar, pure  $\text{CF}_4$ , Ar/ $\text{CF}_4$  at different concentration of  $\text{CF}_4$ , and Ar/ $\text{CF}_4/\text{N}_2$  discharges in single- and dual-frequency cc reactors by a PIC/MCC method. The developed model is focused on the plasma characteristics such as charged particle density and energy distributions, electric field and potential distributions, currents and fluxes, and reaction rates, which are

calculated and presented as a function of time and space. Comparison is made with experimental results available in the literature. Dependence of the plasma characteristics on the external parameters such as pressure, applied voltages and frequencies, and gas composition is investigated and presented. This study covers a wide range of external parameters so that they can be adjusted to obtain desirable plasma characteristics and therefore this work can be useful in improving the etching process.

*Chapter 2* describes the outline of the model and the input data such as cross-sections and reaction rates for the collisions. The choice of the charged particles followed in the model, and the collisions between them and with neutrals are presented and discussed. The validation of the model is also examined.

*Chapter 3* presents the simulation results for pure Ar, pure CF<sub>4</sub>, and Ar/CF<sub>4</sub> at different concentration of CF<sub>4</sub>. The transition from an electropositive to an electronegative discharge is illustrated. The calculated electronegativities at different CF<sub>4</sub> concentration and pressure are compared with experimental data.

*Chapter 4* examines systematically the Ar/CF<sub>4</sub>/N<sub>2</sub> discharges in single- and dual-frequency cc reactors. The influence of the applied second, i.e. low, frequency on the plasma behavior is discussed.

*Chapter 5* presents a detailed study of the IED in single- and dual-frequency cc reactors. The influence of pressure, applied voltages and frequencies on the ion bombarding energy is shown. The simulation results in the dual-frequency reactor are compared with the results from the developed analytical model. The influence of the different types of ion-neutral collisions is discussed.

*Chapter 6* investigates the influence of the external process parameters on the plasma characteristics in the dual-frequency reactor. Special attention is paid to the conditions when the independent control of the ion flux and energy is possible. Comparison with experimental results for the electron density in the plasma center and the ion current density at the electrodes is presented.

*Chapter 7* examines the Ar/CF<sub>4</sub>/N<sub>2</sub> discharge in asymmetric single- and dual-frequency reactors. The simulation results of the influence of the electrode area ratio and power source parameters are presented and discussed.

*Chapter 8* presents a study on the behavior of negative ions in single- and dual-frequency reactors. Trajectories and energies of randomly sampled negative ions are shown in both reactors. The F<sup>-</sup> ion flux at the electrodes in dual-frequency reactors is discussed because it is important in reducing the local charging and establishing of charge-free plasma processes for etching.

Finally, in *Chapter 9* a summary of the work is given. The principal contribution of this work and recommendations for further research are presented.

## **Chapter 2**

# **THE PIC/MCC METHOD AND ITS NUMERICAL APPLICATION**

## **2.1 Introduction**

The widespread use of low-pressure RF discharges for material processing has stimulated numerous papers on numerical simulation of these discharges. The low pressure means that the collision frequencies between charged particles and neutrals are insufficient to reach equilibrium in the velocity distributions of these species. In some cases such as in electronegative discharges the electron velocity distribution considerably deviates from the Maxwellian distribution. Therefore, the continuum or fluid approach fails to describe such discharges in an accurate way. The alternative approach, i.e. the kinetic approach, is required to analyze physical or chemical processes in low-pressure plasma reactors [46 - 48]. It can be shown that many-particle modeling is equivalent to solving the Boltzmann equation [71]. Particle modeling resolves also the energy distributions of ions incident on the etched wafer, and this characteristic is indispensable for the prediction of the etch rate and anisotropy. With the availability of faster and cheaper workstations and personal computers, this approach, which is based on first principles with a minimum of assumptions and approximations, is becoming more and more attractive.

The plasma physics is concerned mainly with the simulation of the charged particles. Thus the PIC method has been developed based on theory of charge assignment and force interpolation. The details of the PIC method can be found in Refs. 46 – 48. The Monte Carlo treatment of collisions is coupled with PIC [47, 53, 71] and results in a PIC/MCC method, which is used in the present study. The neutral background gas is assumed to have uniform distribution in time and space. Simulation of both charged and neutral species is necessary to examine the discharge structure and behavior. In order to make the simulation less computationally expensive neutral species like radicals, the distribution of which

cannot be assumed uniform, are not followed. This approximation is reasonable for the considered operating conditions in this study and it is discussed further in the chapter. We will mention only that a particle simulation method of neutrals, so called direct simulation Monte Carlo (DSMC) method, is also available and it has been developed for the purposes of aerodynamics [72, 73].

The rest of the chapter presents the one-dimensional (1d) coordinate space and three-dimensional velocity space (3v) PIC/MCC method, the input data for collisions, methods for calculation of the post-collision velocities, a discussion on the stability and accuracy of the PIC/MCC model, methods to speed up the calculations, and a discussion on the approximations made in the present numerical model.

## 2.2 A PIC model

A PIC model consists of charged particles moving around due to the forces they generate and the applied fields. The method remains close to the use of first principles, i.e. the use of classical mechanics for the equations of motion  $\mathbf{F} = m\mathbf{a} = q(\mathbf{E} + \mathbf{v} \times \mathbf{B})$  and Maxwell's equations for the  $(\mathbf{E}, \mathbf{B})$  fields generated by the particle densities  $(\rho, \mathbf{J})$ . The particle simulation can be done with a small number of particles, which is many orders of magnitude lower than in a real plasma. Each computer particle or so-called super-particle represents for example  $10^6 - 10^9$  real particles. The simulation must run with a sufficient number of superparticles in order to minimize the discrete particle noise, i.e. number of superparticles/number of grid cells must be much greater than 1. The fields are calculated from Maxwell's equations from the position of all the particles and their velocities. The forces on the particles are found from the electric and magnetic fields in the Newton-Lorentz equations of motion.

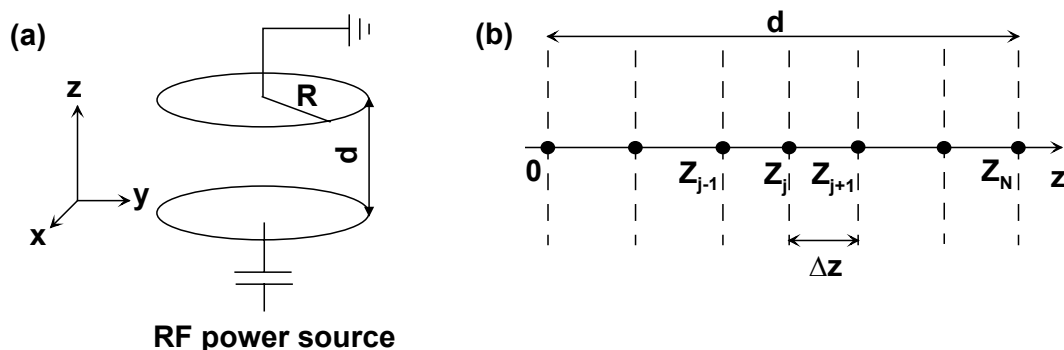


FIGURE 2.1. The coordinate system used in the model (a), and the spatial grid along the  $z$ -axis (b). The PE is positioned at the point 0 and the GE is positioned at the point  $Z_N$ .

### 2.2.1 A 1d electrostatic case in Cartesian coordinates

For our 1d purpose we consider the particle displacement to be along the  $z$ -axis. Let us remind that in the simulation we consider the three components of the velocity  $v_x, v_y$  and  $v_z$ . The Cartesian coordinate system and the 1d spatial grid are presented in Figs. 2.1 (a) and (b), respectively. Throughout this work, except in Chapter 7, a symmetric reactor is considered, i.e. the electrodes with radius  $R$  have equal area, and are placed at a distance  $d$  from each other.

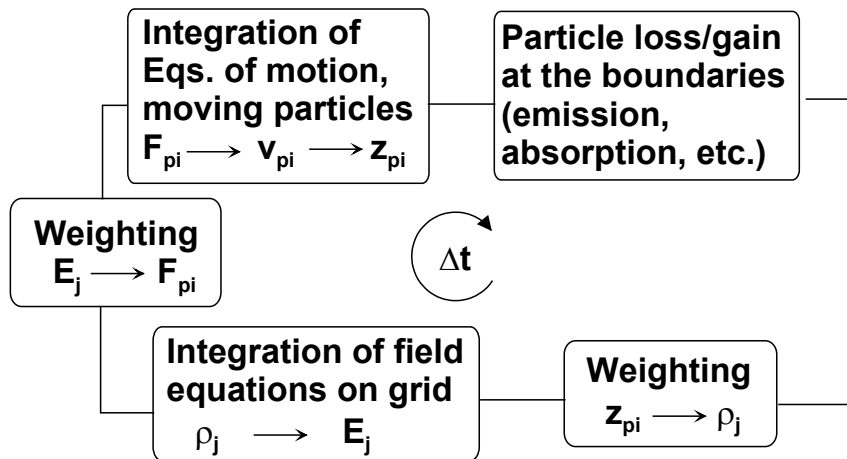


FIGURE 2.2. The PIC computational cycle, one time-step.

In general, the computational cycle consists of the following procedures (see also Fig. 2.2):

(1) The charge density  $\rho_j$  in every grid point  $j$  is obtained by a weighting of the particles to the spatial grid, which procedure is called charge assignment. Therefore, the charge density is calculated on the discrete grid points  $Z_j$  from the continuous particle position  $z_{pi}$ . The *weighting function*  $S(Z_j - z_{pi})$  can be zero-order (the nearest-grid-point), first-order or higher-order. We have chosen (see Sec. 2.9) the *first-order weighting* presented in Fig. 2.3. This weighting puts the part of the charged particle or cloud, which is in the  $j$ th cell at  $Z_j$ , i.e. fraction (i), and the part which is in the  $(j+1)$ th cell at  $Z_{j+1}$ , i.e. fraction (ii) in Fig. (2.3). The charged particles are considered to be finite-size rigid clouds, which may pass freely through each other. This model is called *cloud-in-cell* or CIC [46].

If the particle or cloud has a uniform density, a width equal to the grid spacing  $\Delta z$ , and charge  $q_{pi}$  the part assigned to grid point  $j$  is

$$q_j = q_{pi} \left[ \frac{\Delta z - (z_{pi} - Z_j)}{\Delta z} \right] = q_{pi} \frac{Z_{j+1} - z_{pi}}{\Delta z}, \quad (2.1)$$

and the part assigned to grid point  $(j+1)$  is

$$q_{j+1} = q_{pi} \left[ \frac{\Delta z - (Z_{j+1} - z_{pi})}{\Delta z} \right] = q_{pi} \frac{z_{pi} - Z_j}{\Delta z}. \quad (2.2)$$

Therefore, the *grid charge density*  $\rho_j$  is obtained from charges  $q_{pi}$  located at positions  $z_{pi}$

$$\rho_j = \sum_{pi} q_{pi} S(Z_j - z_{pi}) \quad (2.3)$$

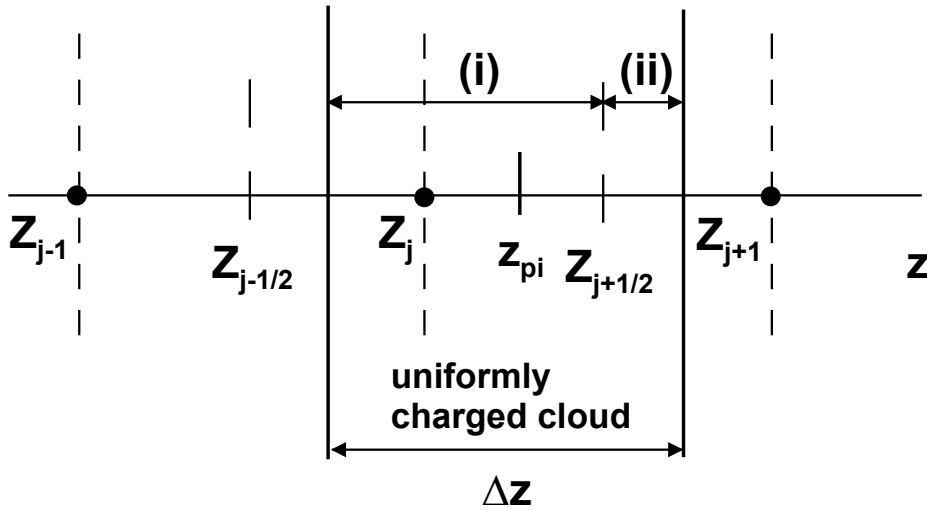


FIGURE 2.3. First-order particle weighting, or cloud-in-cell model CIC. The finite-size charged particle, or cloud, is one cell wide, with center at  $z_{pi}$ . Reproduced from Ref. 46.

(2) The charge densities are used to solve the electric field  $\mathbf{E}$  on the grid. For *electrostatic simulations*, i.e.  $\nabla \times \mathbf{E} = -\partial \mathbf{B} / \partial t \approx 0$  so that  $\mathbf{E} = -\nabla \Phi$ , *Poisson's equation* is solved. In 1d it is given by

$$\frac{\partial^2 \Phi}{\partial z^2} = -\frac{\rho}{\epsilon_0}. \quad (2.4)$$

This equation is solved by finite-difference equations to calculate the potential  $\Phi$  in every grid point. The electric field is calculated from

$$E_z = -\frac{\partial\Phi}{\partial z} . \quad (2.5)$$

(3)  $\mathbf{E}$  is weighted back to each particle position by the same weighting function  $S(Z_j - z_{pi})$ . In our electrostatic 1d case, the electric field is interpolated from the grid points

$$E(z_{pi}) = \left[ \frac{Z_{j+1} - z_{pi}}{\Delta z} \right] E_j + \left[ \frac{z_{pi} - Z_j}{\Delta z} \right] E_{j+1} . \quad (2.6)$$

Consequently, the force  $\mathbf{F}$  on the particle is  $\mathbf{F} = q\mathbf{E}$  or in 1d case is calculated from

$$F_{pi} = q_{pi} \sum_j E_j S(Z_j - z_{pi}) . \quad (2.7)$$

(4) The *equations of motion* are used to advance the particles to new positions and velocities. Thus for each particle the following first-order differential equations are solved

$$m \frac{d\mathbf{v}}{dt} = \mathbf{F} \quad (2.8)$$

$$\frac{d\mathbf{x}}{dt} = \mathbf{v} \quad (2.9)$$

These equations are replaced by the finite-difference equations

$$m \frac{(v_z^{t+\Delta t/2} - v_z^{t-\Delta t/2})}{\Delta t} = F^t \quad (2.10)$$

$$\frac{z^{t+\Delta t} - z^t}{\Delta t} = v^{t+\Delta t/2} . \quad (2.11)$$

The *explicit leap-frog* finite difference scheme is used because  $\mathbf{v}$  and  $\mathbf{x}$  are not known at the same time. A schematic of the leap-frog integration method is presented in Fig. 2.4.

Care should be taken that the initial condition for particle velocities given at time  $t=0$  must be changed, i.e. the velocity  $\mathbf{v}(0)$  must be pushed back to  $\mathbf{v}(-\Delta t/2)$  using the force calculated at  $t=0$  (see Fig. 2.4).

(5) The boundaries are checked and the particles out of the reactor region are removed, while particles injected at the boundaries (e.g. secondary emitted electrons) are added to the simulation.

At time  $t=0$  initial particle positions and velocities pushed to  $-\Delta t/2$  are given and the charge density is calculated. The above described steps from (1) to (5) are repeated every time-step until convergence is reached.

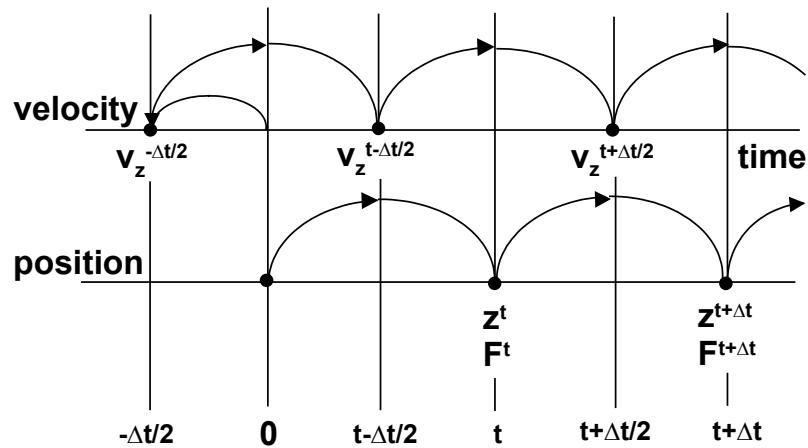


FIGURE 2.4. A schematic of the leap-frog integration method showing time-centering of force while advancing  $v_z$  and of  $v_z$  while advancing  $z$ .

### 2.2.2 Bounded plasma particle simulation

In order to model not only the bulk plasma but also the sheaths in the RF discharges we have to handle the charges at the boundaries and couple the external circuit. Figure 2.5 presents a 1d bounded plasma system with a general voltage-driven series RLC circuit. In our case we consider only a capacitor with a capacitance  $C$  (see Fig. 1.4). The current in the external circuit interacts with the plasma current via the electrode surface charge. The potential within the plasma region is modified by the distribution and motion of space charge, the electrode surface charge, and the current in the external circuit. Therefore, a simultaneous solution for the potential and circuit equations is needed. The method is well presented by Verboncoeur *et al.* [74].

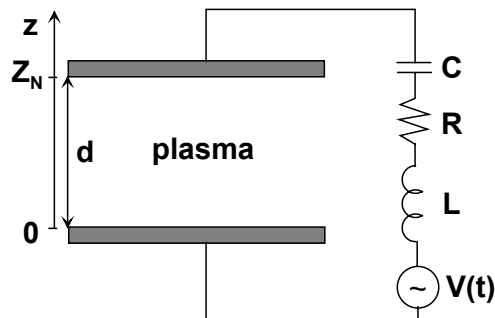


FIGURE 2.5. A 1d bounded plasma model with an external circuit source.

The boundary conditions for the potential equation are given by Gauss' law applied to the system, i.e.

$$\oint_S \mathbf{E} \cdot d\mathbf{S} = \int_V \frac{\rho}{\epsilon_0} dV + \frac{A_0 \sigma_0 + A_N \sigma_N}{\epsilon_0} = 0, \quad (2.12)$$

where the surface  $\mathbf{S}$  encloses the plasma and electrodes.  $A_0$  and  $A_N$  are the surface areas of the bottom and top electrodes, respectively,  $\sigma_0$  and  $\sigma_N$  are the surface charges on the respective electrode.

Applying Gauss' law to each grid point and using the definition of potential, the potential equation in Cartesian coordinates is [74]

$$\frac{\Phi_{j-1} - 2\Phi_j + \Phi_{j+1}}{(\Delta z)^2} = -\frac{\rho_j}{\epsilon_0}, \quad (2.13)$$

where  $j=1,2,\dots,N-1$  and  $N$  is the number of the cells in the grid. The boundary conditions for the 1d system can be written

$$\Phi_N = 0 \quad (2.14)$$

and

$$E_0 = \frac{\sigma_0}{\epsilon_0}. \quad (2.15)$$

Equation (2.14) fixes a reference potential for the system without implying a grounded electrode. Equation (2.15) can be written at one-half grid cell from the boundary, in conjunction with the central difference applied to the definition of potential,

$$E_{1/2} = \frac{\Phi_0 - \Phi_1}{\Delta z} = \frac{1}{\epsilon_0} \left( \sigma_0 + \rho_0 \frac{\Delta z}{2} \right). \quad (2.16)$$

Equations (2.13) and the boundary conditions are written in a general matrix form evaluated at time  $t$  [74]

$$\begin{pmatrix} b_0 & c_0 & 0 & \cdot & \cdot & \cdot & \cdot \\ a_1 & b_1 & c_1 & 0 & \cdot & \cdot & \cdot \\ 0 & a_2 & b_2 & c_2 & 0 & \cdot & \cdot \\ \cdot & \cdot & \cdot & \cdot & \cdot & \cdot & \cdot \\ \cdot & \cdot & \cdot & \cdot & \cdot & \cdot & \cdot \\ \cdot & \cdot & \cdot & 0 & a_{N-2} & b_{N-2} & c_{N-2} \\ \cdot & \cdot & \cdot & \cdot & 0 & a_{N-1} & b_{N-1} \end{pmatrix}^t \times \begin{pmatrix} \Phi_0 \\ \Phi_1 \\ \Phi_2 \\ \cdot \\ \cdot \\ \Phi_{N-2} \\ \Phi_{N-1} \end{pmatrix}^t = -\frac{\Delta z^2}{\epsilon_0} \begin{pmatrix} d_0 \\ d_1 \\ d_2 \\ \cdot \\ \cdot \\ d_{N-2} \\ d_{N-1} \end{pmatrix}^t. \quad (2.17)$$

The matrix elements in the Cartesian coordinates are

$$\begin{aligned} a_j &= 1, & j &= 1, 2, \dots, N-1; \\ b_0 &= -1, \quad b_j &= -2, & j &= 1, 2, \dots, N-1; \end{aligned} \quad (2.18)$$

$$c_j = 1, \quad j = 0, 1, \dots, N-2;$$

$$d_0 = \frac{\sigma_0^t}{\Delta z} + \frac{\rho_0^t}{2}, \quad d_j = \rho_j^t, \quad j = 1, 2, \dots, N-1.$$

The external circuit is coupled to Eqs. (2.17) and (2.18) through conservation of charge at each wall,

$$A\Delta\sigma = Q_{conv} + \Delta Q \quad (2.19)$$

where  $Q_{conv}$  and  $\Delta Q$  is the charge deposited by the convection (particle) and external circuit current, respectively, over some interval in time. Eq. (2.19) is applied at the bottom electrode. The surface charge on the top electrode is determined readily from Eq. (2.12) when the bottom surface charge is known. The charge conservation equation at the bottom electrode becomes

$$\sigma_0^t = \sigma_0^{t-\Delta t} + \frac{Q_{conv}^t + Q^t - Q^{t-\Delta t}}{A_0}, \quad (2.20)$$

where  $Q$  is the charge on one plate of the external capacitor. The charge on the capacitor is not known at  $t$ . It is obtained using Kirchoff's voltage law. A detailed description for a general series RLC circuit is given in Ref. 74. Here we present the result for a capacitor

$$Q^t = \frac{V(t) + \Phi_N^t - \Phi_0^t}{\alpha_0}, \quad (2.21)$$

where  $\alpha_0 = 1/C$ . Combining the potential equation results (2.17) and (2.18), the circuit equation result (2.21), and the boundary condition (2.20) we obtain the self-consistent field solution matrix for the voltage-driven discharge. The matrix is represented by Eqs. (2.17) and (2.18) replacing the elements  $b_0$  and  $d_0$  in Cartesian coordinates by

$$b_0 = -1 - \frac{\Delta z}{\alpha_0 \epsilon_0 A_0},$$

$$d_0 = \frac{\rho_0^t}{2} + \frac{\sigma_0^{t-\Delta t}}{\Delta z} + \frac{1}{A_0 \Delta z} \left( Q_{conv}^t - Q^{t-\Delta t} + \frac{V(t)}{\alpha_0} \right). \quad (2.22)$$

The system of linear equations presented by Eq. (2.17) is a tridiagonal system, i.e. it has nonzero elements only on the diagonal plus or minus one column. It is solved numerically by the *tridag* routine (see Ref. 75, p.42 for details).

In order to simulate an asymmetric discharge in one dimension a spherical model is applied [21]. The 1d spherical model, and the potential equations and matrix elements in spherical coordinates, are presented in the Appendix A.

## 2.3 A MCC model

### 2.3.1 Null-collision method

The PIC method is a collisionless model. Even at low pressure the collisions between charged particles and neutrals play an important role for sustaining the discharge. Collisions can be included by coupling the PIC method with a Monte Carlo (MC) method. The PIC simulation moves all particles simultaneously using the same time-step. On the other hand, conventional MC methods calculate the time between collisions for each particle by a random number, which is not compatible with the PIC method. A MC method with only few particles colliding per field time-step, called MCC model, was developed by a group from the University of California, at Berkeley [47, 53]. The MCC package considers a constant time-step and includes the null-collision method [76], explained below. The collision is modeled with three velocity components.

Let the  $i$  th charged particle be known by its total kinetic energy  $E_i = mv_i^2/2$  and its velocity, with magnitude  $g = |\mathbf{v}_i - \mathbf{V}_t|$ , relative to some target particles with local density  $n_t(\mathbf{x}_i)$  at the position of the  $i$  th particle. If the collision cross section is  $\sigma(E_i)$ , the collision frequency  $\nu_{coll}$  is

$$\nu_{coll} = n_t(\mathbf{x}_i)\sigma(E_i)g. \quad (2.23)$$

In electron-neutral collisions an assumption that the neutrals are stationary in comparison with the incident electrons is made, so that the velocity  $g$  relative to the neutral particles is equal to the electron velocity  $v_i$ . The same cannot be assumed for ion-neutral collisions. In the bulk plasma the ions and neutrals typically have similar velocities. Therefore, each ion selected to undergo a collision must be transferred first to a reference frame in which the neutral is at rest, that is, the velocity of the neutral is subtracted from the velocity of the ion. After a collision happens the ion must be transferred back to the laboratory system by adding the pre-collision neutral velocity to the ion post-collision velocity.

If  $N$  different types of collisions can happen, then the total cross section  $\sigma_T(E_i)$  is the sum of the cross sections for every  $j$  th type  $\sigma_j(E_i)$ ,  $1 \leq j \leq N$ ,

$$\sigma_T(E_i) = \sigma_1(E_i) + \dots + \sigma_N(E_i) \quad (2.24)$$

The collision probability  $P_i$  for the  $i$  th particle is calculated based on the distance traveled in each time-step  $v_i\Delta t$  to be [53]

$$P_i = 1 - \exp(-v_i\Delta t\sigma_T(E_i)n_t(\mathbf{x}_i)) \quad (2.25)$$

A collision takes place if a random number  $R$  uniformly distributed in the interval  $[0,1]$  is less than the probability  $P_i$ . If a collision occurs then another random number is selected to determine the type of collision.

The time-step  $\Delta t$  determines how often to check for collisions. Since the MCC model allows only one collision per time-step this can produce an error  $r$ , which is defined as the number of the missed collisions in  $\Delta t$  for a given particle. For example, the energy of the scattered electron remains roughly the same and consequently, the probability for  $n$  collisions in  $\Delta t$  is roughly  $P_i^n$ . The generated error is

$$r \approx \sum_{k=2}^{\infty} P_i^k = \frac{P_i^2}{1-P_i}. \quad (2.26)$$

An error of  $r < 0.01$  requires  $P_i < 0.095$ , i.e. from (2.25) the time-step should be set so that  $v_i \Delta t \sigma_t(E_i) n_t(\mathbf{x}_i)$  would be less than or equal to 0.1.

The scheme presented above is compatible with the PIC model because the position and velocity of particles are advanced each time-step. However, it is computationally very expensive to calculate the probability  $P_i$  for all particles each time-step. For that reason, a constant collision frequency  $\nu_{\max}$  is defined by [53]

$$\nu_{\max} = \max_{\mathbf{x}} (n_t(\mathbf{x})) \max_E \left( \sigma_T(E) \left( \frac{2E}{m_p} \right)^{1/2} \right), \quad (2.27)$$

where  $m_p$  is the charged particle mass. This frequency is obtained once at the beginning of the calculation. Eq. (2.27) means that another collisional process, i.e. null-collision, is introduced so that when its collision frequency is added to the total collision frequency  $n_t(\mathbf{x}) \sigma_T(E) v$ , it gives a constant value over all  $\mathbf{x}$  and  $E$ . This collisional process is called null-collision since no real interaction takes place.

Typically, the neutral gas is distributed uniformly with a constant density  $n_t$ . In this case it is necessary to obtain only the maximum over the energy, which is graphically shown in Fig. 2.6. However, in case of ion-ion or electron-ion recombination the density of the target particles, i.e. ions, is a function of position and time. In this case it is necessary to obtain the maximum over  $\mathbf{x}$  at each time-step.

The probability determined by the null-collision method  $P_{null}$  for each time-step is obtained to be

$$P_{null} = 1 - \exp(-\nu_{\max} \Delta t). \quad (2.28)$$

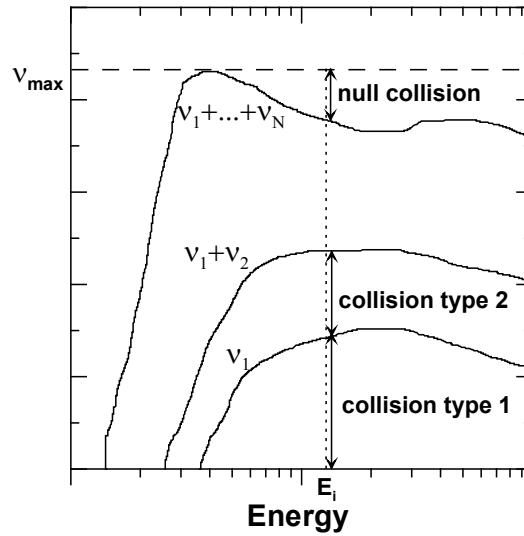


FIGURE 2.6. Graphical presentation of the addition of the null-collision process, which results in a constant collision frequency over all energies when the target density is uniformly distributed. Reproduced from Ref. 53.

If  $N_{part}$  is the total number of particles of a certain species then the maximum number of particles which experience collisions  $N_{coll}$  is given by

$$N_{coll} = N_{part} P_{null} = N_{part} (1 - \exp(-v_{max} \Delta t)). \quad (2.29)$$

The colliding particles are chosen randomly. Each particle is checked for the type of collision by a random number  $R$  between zero and one in the following manner:

$$\begin{aligned}
 R \leq \frac{v_1(E_i)}{v_{max}} & \quad \text{Collision type 1} \\
 \frac{v_1(E_i)}{v_{max}} \leq R \leq \frac{v_1(E_i) + v_2(E_i)}{v_{max}} & \quad \text{Collision type 2} \\
 \dots & \\
 \frac{\sum_{j=1}^N v_j(E_i)}{v_{max}} \leq R & \quad \text{Null-collision.}
 \end{aligned} \quad (2.30)$$

Typically  $N_{coll} \ll N_{part}$  which brings the advantage of the null-collision method over the standard method. The standard method requires  $N_{part}$  evaluations of  $P_i$ , whereas the null-collision method requires only  $N_{part} P_{null}$  evaluations of  $P_i$ .

Typically  $P_{null}$  is in the order of  $10^{-2}$ , which means that the computational saving can be quite significant.

Once a collision occurs the scattering angle and energy of the particle after collision are determined based on the model assumed for that type of collision. That brings us to the question what kind of collisions should be taken into account. Let us consider, for example, an Ar discharge, which consist of electrons,  $\text{Ar}^+$  ions and ground state atoms Ar. Collisions between charged particles and neutrals ( $e\text{-Ar}$ ,  $\text{Ar}^+\text{-Ar}$ ), and collisions between neutrals ( $\text{Ar-Ar}$ ) are subject to a short-range force. Collisions between charged particles ( $e\text{-e}$ ,  $e\text{-Ar}^+$ ,  $\text{Ar}^+\text{-Ar}^+$ ) are subject to a long-range force and result in Coulomb collisions. The collision algorithms for the short-range and long-range force collisions are different. In Coulomb collisions, small-angle scattering is dominant in the transfer of momentum and energy, whereas in the short-range force collisions large-angle scattering is much more important. The collisions that are taken into account depend on what plasma is considered. Let  $n_e$ ,  $n_+$ , and  $n_A$  be the number densities of  $e$ ,  $\text{Ar}^+$ , and Ar, respectively. The collision rate between species  $i$  and  $j$  is proportional to  $n_i n_j$  times the collision cross-section, where the indexes  $i$  and  $j$  denote  $e$ ,  $+$  or  $A$ . If some  $n_i n_j$  is much smaller than all other density products, we can disregard the  $i-j$  collisions. For example, in a cc RF plasma with  $n_e = n_+ = 10^{16} \text{ m}^{-3}$  and  $n_A = 2 \times 10^{21} \text{ m}^{-3}$  the ratio of  $n_i n_j$  to  $n_A^2$  is  $5 \times 10^{-6}$  for  $e\text{-Ar}$ ,  $\text{Ar}^+\text{-Ar}$ , and  $2.5 \times 10^{-11}$  for Coulomb collisions. This suggests that the gas flow of Ar is calculated considering only  $\text{Ar-Ar}$  collisions. The plasma discharge in the Ar flow is calculated considering charged particle-neutral collisions since the Coulomb collisions can be disregarded in this case. In an inductively coupled plasma (ICP) with  $n_e = n_+ = 10^{18} \text{ m}^{-3}$  and  $n_A = 2 \times 10^{20} \text{ m}^{-3}$  the ratio of  $n_i n_j$  to  $n_A^2$  is 0.005 for  $e\text{-Ar}$ ,  $\text{Ar}^+\text{-Ar}$ , and  $2.5 \times 10^{-5}$  for Coulomb collisions. In this case, the ratio  $n_+ n_A$  to  $n_A^2$  is much larger than in the cc plasma and therefore, coupling of the gas flow with the plasma is stronger. The Coulomb collisions should then also be taken into consideration. Hence, Coulomb collisions are important in high-density plasma. However, positive-negative charge neutralizing collisions, i.e. electron-ion and positive-negative ion recombination, should also be considered if a cc RF discharge of electronegative gas, such as  $\text{CF}_4$ , is simulated. Indeed, since the negative ions are confined in the bulk plasma, the charge neutralization is the dominant mechanism for the loss of negative ions.

### 2.3.2 The PIC/MCC computational cycle

The computational cycle of the PIC method coupled with the MCC method in one time-step is presented in Fig. 2.7. Starting with the charge assignment, the first 5 procedures describe the PIC model, and they are presented in the Sec. 2.2.1. The MCC procedure is called after the point where the boundaries are checked. In the MCC procedure all collisions that can happen in one time-step are considered and the post-collision velocities  $\mathbf{v}'$  are calculated so that the particles, which participated in collisions leave the MCC part with the new velocities. It is taken into account that some particles disappear after collisions, such as detachment or recombination processes, and other particles appear in ionization or attachment processes. When all the particle positions and velocities are known, the simulation continues with the charge assignment in the next time-step.

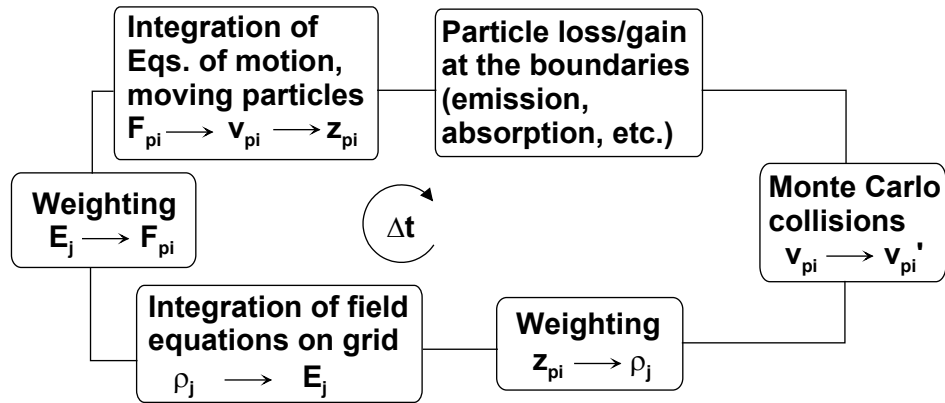


FIGURE 2.7. The PIC/MCC computational cycle, one time-step.

## 2.4 Charged particles followed in the simulation

The charged particles considered in the present study are: *electrons, Ar<sup>+</sup>, CF<sub>3</sub><sup>+</sup>, N<sub>2</sub><sup>+</sup>, F<sup>+</sup> and CF<sub>3</sub><sup>+</sup>*. This list can vary depending on the simulated gas mixture, i.e. pure Ar, pure CF<sub>4</sub>, Ar/CF<sub>4</sub>, or Ar/CF<sub>4</sub>/N<sub>2</sub>. In order to simulate the collisions between the particles a complete set of cross-sections is needed. The cross-section data are not always available and therefore the presented null-collision method in section 2.3.1 is not always applicable. To calculate the collision probability for collisions when the cross-sections are unknown other techniques are adopted such as the *ion-molecule collision model for endothermic reactions* [57, 77] and *Monte Carlo*

*collision simulation of positive-negative ion recombination for a given rate constant* [78]. These techniques are presented in detail below in the sections describing the ion-molecule collisions and charge neutralization.

First, the cross-section data for collisions between electrons and neutrals and methods to determine the post-collision velocity of the electron are presented. Subsequently, the ion-neutral collision data and calculating the post-collision velocity of the particles is considered. Finally, the particle simulation of ion-ion and electron-ion recombination is described.

## **2.5 Electron-neutral collisions**

### **2.5.1 Cross-section data**

We assume that the neutral gas (Ar, CF<sub>4</sub> and N<sub>2</sub>) is uniformly distributed and its velocity distribution is Maxwellian at room temperature ( $T_g = 0.026$  eV or 300 K). Hence the neutrals are much less energetic and we can assume that they do not move in comparison with the highly energetic electrons (on average  $T_e > 2$  eV). The fundamental quantity that characterizes a collision is its cross section  $\sigma(g)$ , where  $g$  is the magnitude of the relative velocity of the particles before collision. All electron-neutral (Ar, CF<sub>4</sub> and N<sub>2</sub>) collisions considered in the model, with the corresponding threshold energies and references for the cross-section data are presented in Table 2.1.

The electron-Ar, electron-CF<sub>4</sub>, and electron-N<sub>2</sub> cross-sections are plotted as a function of the electron energy in Figs. 2.8, 2.9, and 2.10, respectively. The method of calculating the post-collision velocities depends on the type of collisions. The main processes are elastic scattering in which primarily the electron momentum is changed, and inelastic collisions such as excitation, ionization, attachment, or dissociation.

TABLE 2.1 All electron-neutral (Ar, CF<sub>4</sub> and N<sub>2</sub>) collisions considered in the model, with the corresponding threshold energies and references for the cross-section data.

Type of collision	Reaction	Threshold (eV)	Ref.
<b>Ar</b>			
(1) Elastic scattering	$e + \text{Ar} \rightarrow e + \text{Ar}$		[79]
(2) Total electronic excitation	$e + \text{Ar} \rightarrow e + \text{Ar}^*$	11.5	[79]
(3) Ionization	$e + \text{Ar} \rightarrow 2e + \text{Ar}^+$	15.8	[79]
<b>CF<sub>4</sub></b>			
(4) Momentum transfer	$e + \text{CF}_4 \rightarrow e + \text{CF}_4$		[80]
(5) Vibrational excitation	$e + \text{CF}_4 \rightarrow e + \text{CF}_4(\nu_1)$	0.108	[80]
(6) Vibrational excitation	$e + \text{CF}_4 \rightarrow e + \text{CF}_4(\nu_3)$	0.168	[80]
(7) Vibrational excitation	$e + \text{CF}_4 \rightarrow e + \text{CF}_4(\nu_4)$	0.077	[80]
(8) Electronic excitation	$e + \text{CF}_4 \rightarrow e + \text{CF}_4^*$	7.54	[80]
(9) Electron attachment	$e + \text{CF}_4 \rightarrow \text{F}^- + \text{CF}_3$	5	[81]
(10) Electron attachment	$e + \text{CF}_4 \rightarrow \text{F} + \text{CF}_3^-$	5	[81]
(11) Dissociation	$e + \text{CF}_4 \rightarrow e + \text{F}^- + \text{CF}_3^+$	12	[81]
(12) Dissociative ionization	$e + \text{CF}_4 \rightarrow 2e + \text{F} + \text{CF}_3^+$	16	[80]
(13) Neutral dissociation	$e + \text{CF}_4 \rightarrow e + \text{F} + \text{CF}_3$	12	[80]
(14) Neutral dissociation	$e + \text{CF}_4 \rightarrow e + 2\text{F} + \text{CF}_2$	17	[80]
(15) Neutral dissociation	$e + \text{CF}_4 \rightarrow e + 3\text{F} + \text{CF}$	18	[80]
<b>N<sub>2</sub></b>			
(16) Momentum transfer	$e + \text{N}_2 \rightarrow e + \text{N}_2$		[82]
(17) Excitation	$e + \text{N}_2 \rightarrow e + \text{N}_2^*(\text{Y})^a$	...	[82]
(18) Ionization	$e + \text{N}_2 \rightarrow 2e + \text{N}_2^+(\text{Y})^b$	15.6	[82]
(19) Ionization	$e + \text{N}_2 \rightarrow 2e + \text{N}_2^+(\text{B } ^2\Sigma)$	18.8	[82]

<sup>a</sup> N<sub>2</sub><sup>\*</sup>(Y) = N<sub>2</sub> (  $\nu = 0-8$ , A <sup>3</sup>Σ, B <sup>3</sup>Π, W <sup>3</sup>Δ, B' <sup>3</sup>Σ, a' <sup>1</sup>Σ, a <sup>1</sup>Π, w <sup>1</sup>Δ, C <sup>3</sup>Π, E <sup>3</sup>Σ, a'' <sup>1</sup>Σ, and “sum of singlets”, including dissociation). The threshold energy is different for every kind of excitation, with values from 0.020 eV to 13 eV. See Ref. 82 for details.

<sup>b</sup> N<sub>2</sub><sup>+</sup>(Y) = N<sub>2</sub><sup>+</sup> ( X <sup>2</sup>Σ and A <sup>2</sup>Π ).

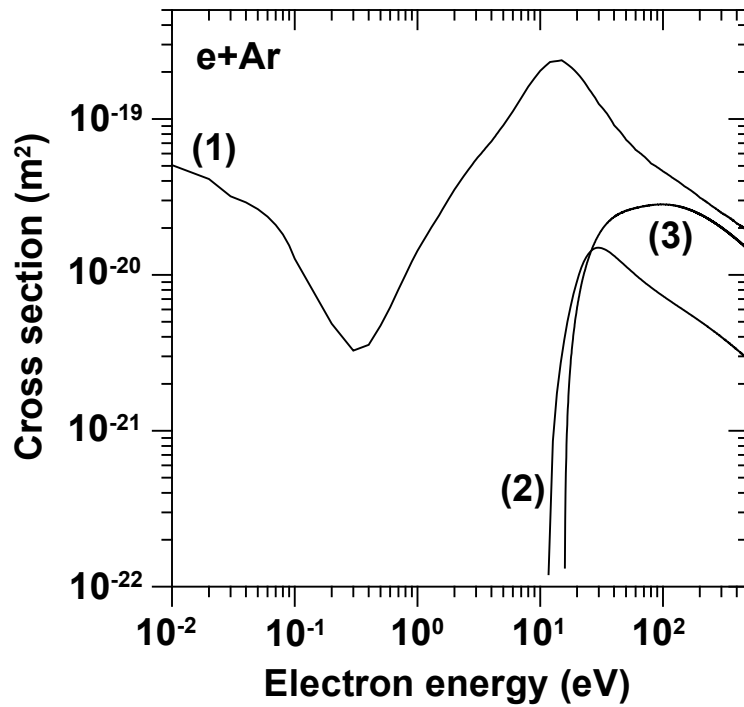


FIGURE 2.8. Electron-Ar elastic (1), total excitation (2) and ionization (3) cross-sections. The numbers correspond to the list of collisions presented in Table 2.1.

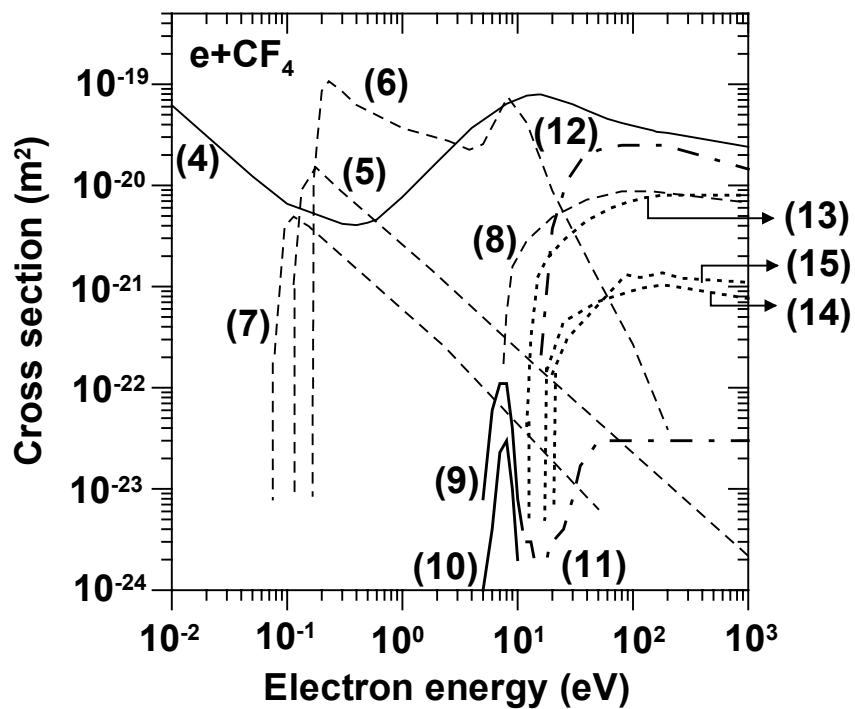


FIGURE 2.9. Electron-CF<sub>4</sub> elastic momentum transfer (4), vibrational excitation (5), (6) and (7), electronic excitation (8), F<sup>-</sup> attachment (9), CF<sub>3</sub><sup>-</sup> attachment (10), dissociation (11), dissociative ionization (12), and neutral dissociation (13), (14), and (15) cross-sections. The numbers correspond to the list of collisions presented in Table 2.1.

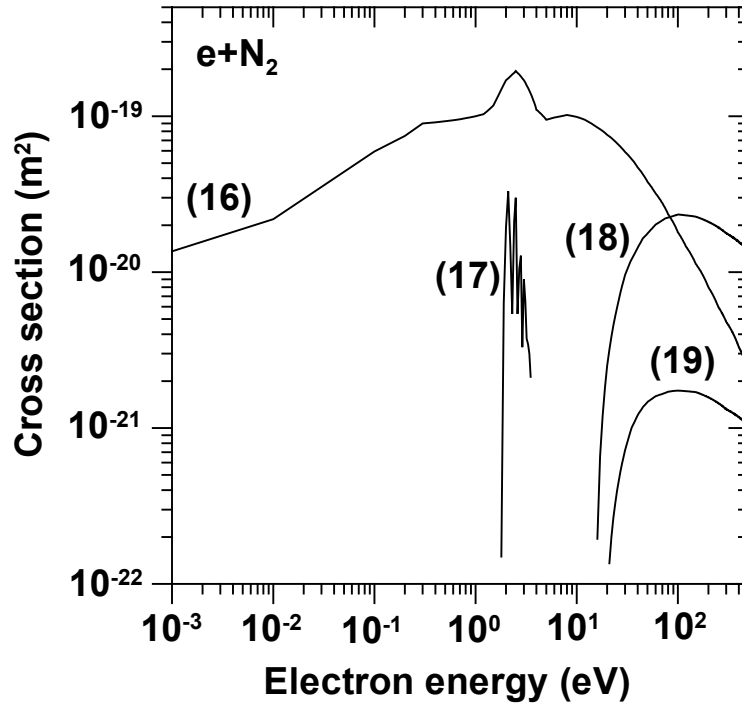


FIGURE 2.10. Electron-N<sub>2</sub> elastic momentum transfer (16), vibrational excitation  $v=2$  as an example (17) (for the full set of excitation cross-sections, used in the present study see Ref. 82), ionization N<sub>2</sub><sup>+</sup> (X <sup>2</sup>Σ and A <sup>2</sup>Π states) (18), and ionization N<sub>2</sub><sup>+</sup> (B <sup>2</sup>Σ) (19) cross-sections. The numbers correspond to the list of collisions presented in Table 2.1.

### 2.5.2 Calculation of the post-collision velocities

In a more general case, let us consider an elastic collision between two spherically symmetric particles. The pre-collision velocities of the particles with masses  $m$  and  $M$ , are  $\mathbf{v}$  and  $\mathbf{V}$ , respectively, so that the relative velocity between them is  $\mathbf{g} = \mathbf{v} - \mathbf{V}$ . Without loss of generality, we can transform to a coordinate system in which one of the particle is stationary before the collision, i.e.  $\mathbf{V} = 0$  and  $\mathbf{v} = \mathbf{g}$ . The post-collision particle velocities and relative velocity are  $\mathbf{v}'$ ,  $\mathbf{V}'$ , and  $\mathbf{g}' = \mathbf{v}' - \mathbf{V}'$ , respectively. Since the total momentum of the two colliding particles is unchanged during the collision it is convenient to perform the calculation in a coordinate system moving with a constant velocity  $\mathbf{V}_{CM}$  of the center of mass (see Fig. 2.11, which shows the particle trajectories in the center-of-mass reference frame)

$$\mathbf{V}_{CM} = \frac{m\mathbf{v} + M\mathbf{V}}{m + M}. \quad (2.31)$$

Therefore, the pre-collision velocities in the center-of-mass reference frame are

$$\tilde{\mathbf{v}} = \mathbf{v} - \mathbf{V}_{CM} = \frac{M}{m + M} \mathbf{g} = \frac{\mu}{m} \mathbf{g}, \quad (2.32)$$

$$\tilde{\mathbf{V}} = \mathbf{V} - \mathbf{V}_{CM} = -\frac{m}{m + M} \mathbf{g} = -\frac{\mu}{M} \mathbf{g}, \quad (2.33)$$

where  $\mu$  denotes the reduced mass, i.e.

$$\mu = \frac{mM}{m + M}. \quad (2.34)$$

Consequently, in the center-of-mass reference frame the initial momenta of the two particles are equal and opposite, that is

$$m\tilde{\mathbf{v}} = \mu\mathbf{g}, \quad (2.35)$$

$$M\tilde{\mathbf{V}} = -\mu\mathbf{g}. \quad (2.36)$$

Furthermore, the force acting upon each of the particles is equal in magnitude and opposite in direction. As a result the final momenta are also equal and opposite. The particle velocities therefore remain parallel but deflected at angle  $\chi$ , as in Fig. 2.11,

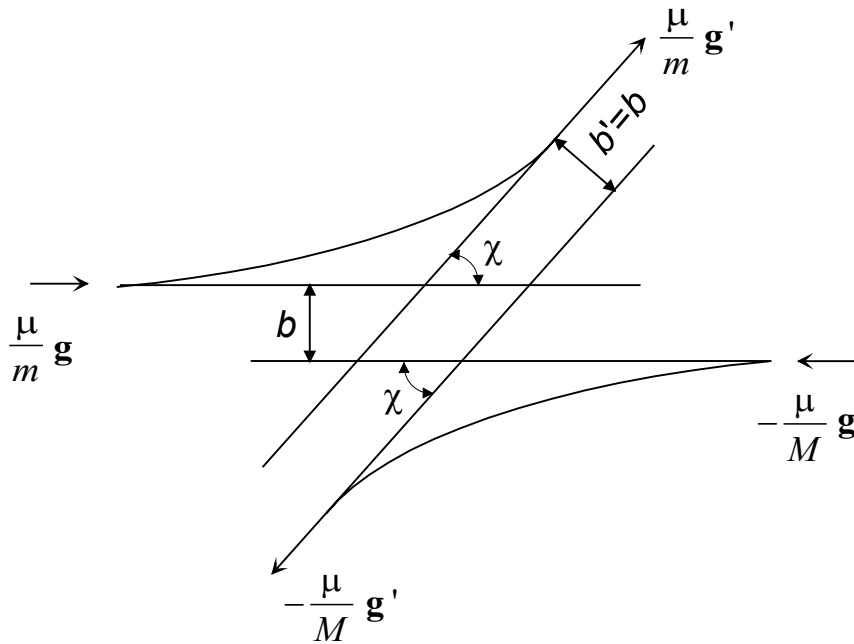


FIGURE 2.11. Particle trajectories in the center-of-mass reference frame. Symbol  $b$  denotes the impact parameter and  $\chi$  is the deflection angle.

The determination of the post-collision velocities reduces to the calculation of the change in direction of the relative velocity, i.e. the *deflection angle of the relative velocity*  $\chi$ . Once the deflection angle is known, which is explained below, the post-collision velocities can be calculated from [71, 83]

$$\mathbf{v}' = \mathbf{v} - \frac{M}{m+M} [\mathbf{g}(1 - \cos \chi) + \mathbf{h} \sin \chi] \quad (2.37)$$

$$\mathbf{V}' = \mathbf{V} + \frac{m}{m+M} [\mathbf{g}(1 - \cos \chi) + \mathbf{h} \sin \chi]. \quad (2.38)$$

The Cartesian components of  $\mathbf{h}$  are

$$\begin{aligned} h_x &= g_{\perp} \cos \varphi \\ h_y &= -\frac{g_x g_y \cos \varphi + g g_z \sin \varphi}{g_{\perp}} \\ h_z &= -\frac{g_x g_z \cos \varphi - g g_y \sin \varphi}{g_{\perp}}, \end{aligned} \quad (2.39)$$

where  $g = \sqrt{g_x^2 + g_y^2 + g_z^2}$  and  $g_{\perp} = \sqrt{g_x^2 + g_y^2}$ . The detailed discussion of Eqs. (2.37) - (2.39) can be found in Ref. 83, p.348.

The plane in which the trajectories lie in the center-of-mass-reference frame is called the collision plane (see Fig. 2.11). The angle between the collision plane and some reference plane is the angle  $\varphi$ . The orientation of the reference frame is arbitrary and therefore, the probability density function of the angle  $\varphi$  is  $(2\pi)^{-1}$ . As a result, the angle  $\varphi$  is randomly sampled

$$\varphi = 2\pi R, \quad (2.40)$$

where  $R$  is a random number uniformly distributed in the interval  $[0,1]$ . Apart from the post-collision velocities of the two particles, the angle  $\varphi$  is one of the *two impact parameters* that completely specify the binary collision. The other impact parameter is the distance of closest approach  $b$  of the undisturbed trajectories in the center-of-mass reference frame (see Figs. 2.11 and 2.12). Figure 2.12 illustrates the two impact parameters. The flux conservation requires that all particles entering through the differential annulus  $2\pi b db$  leave through a differential solid angle  $2\pi \sin \chi d\chi$ , i.e. [1]

$$\Gamma 2\pi b db = -\Gamma \sigma(g, \chi) 2\pi \sin \chi d\chi. \quad (2.41)$$

The minus sign means that an increase in  $b$  leads to a decrease in  $\chi$ . The proportionality constant  $\sigma(g, \chi)$  has the dimension of area per steradian and is called differential cross-section. From Eq. (2.41) it is obtained

$$\sigma(g, \chi) = \frac{b}{\sin \chi} \left| \frac{db}{d\chi} \right|. \quad (2.42)$$

The absolute value of  $db/d\chi$  is used since it is negative. This expression is determined from the scattering force.

The total collision cross-section  $\sigma_T$  is defined by [1]

$$\sigma_T = \int_0^{4\pi} \sigma(g, \chi) d\Omega = 2\pi \int_0^\pi \sigma(g, \chi) \sin \chi d\chi. \quad (2.43)$$

The deflection angle  $\chi$  is related to the two-particle interaction potential and the relative velocity by means of the differential cross-section  $\sigma(g, \chi)$ . The probability that  $\mathbf{v}'$  is in the solid angle  $d\Omega = \sin \chi d\chi d\phi$  is [71]

$$P(g, \chi) = \frac{\sigma(g, \chi)}{\sigma_T} \sin \chi d\chi d\phi. \quad (2.44)$$

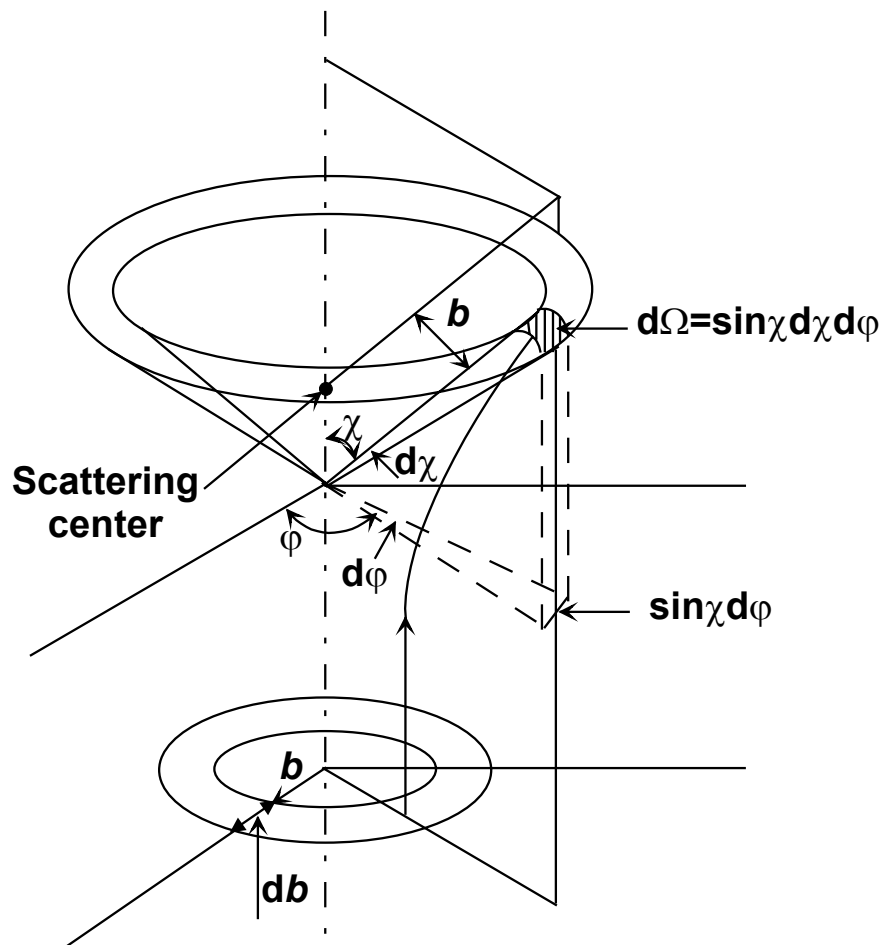


FIGURE 2.12. Illustration of the impact parameters  $b$  and  $\phi$ .

Consequently, the deflection angle can be randomly sampled by [71]

$$\frac{2\pi}{\sigma_T} \int_0^\chi \sigma(g, \chi') \sin \chi' d\chi' = R. \quad (2.45)$$

The calculation of the differential cross-section depends on the interacting force and potential. For example, in the *electron-Ar collisions* the interaction potential can be approximated by the screened Coulomb potential (see Ref. 84 for details) for all collisional events (i.e. elastic, excitation and ionization collisions). The normalized differential cross-section in this case is given by [84]

$$\sigma(\varepsilon, \chi) = \frac{1}{4\pi} \frac{1 + 8\varepsilon}{(1 + 4\varepsilon - 4\varepsilon \cos \chi)^2}, \quad (2.46)$$

where  $\varepsilon = E/E_0$  is the dimensionless energy,  $E$  is the relative energy of the electron, and  $E_0$  is the atomic unit of energy ( $E_0 = 27.21$  eV). To find the deflection angle a random number  $R$  is compared with the probability of scattering and the result is [84]

$$\cos \chi = 1 - \frac{2R}{1 + 8\varepsilon(1 - R)}. \quad (2.47)$$

Now the deflection angle is known and the post-collisional velocities for an *elastic collision* are calculated from Eqs. (2.37) to (2.39) considering a random sample of the angle  $\varphi$  as in Eq. (2.40). The more general equations (2.37) to (2.39) can be somewhat simplified for electron-neutral collisions by use of  $M + m \approx M$  and  $\mathbf{g} \approx \mathbf{v}$ .

Next, let us consider *excitation* in an e-Ar collision. The conservation equations for momentum and energy are [71]

$$m\mathbf{v}' + M\mathbf{V}' = m\mathbf{v} + M\mathbf{V} \quad (2.48)$$

$$\frac{1}{2} \mu (\mathbf{v}' - \mathbf{V}')^2 + E_{th} = \frac{1}{2} \mu (\mathbf{v} - \mathbf{V})^2, \quad (2.49)$$

where  $E_{th}$  is the threshold energy of the inelastic collision, i.e. the excitation in this case. Taking into consideration that  $M + m \approx M$  and  $\mathbf{g} \approx \mathbf{v}$  we obtain

$$v' = \sqrt{v^2 - \frac{2E_{th}}{m}}. \quad (2.50)$$

Nambu proposed to define the velocity  $\tilde{\mathbf{v}}$  with magnitude  $v'$  and direction  $\mathbf{v}/v$  by [71]

$$\tilde{\mathbf{v}} = \mathbf{v} \sqrt{1 - \frac{E_{th}}{E}}, \quad (2.51)$$

where  $E = mv^2/2$  is the electron energy before collision. The excitation process is treated as if it were an elastic collision with pre-collision velocities  $\tilde{\mathbf{v}}$  and  $\mathbf{V}$ . The post-collision velocities are given by Eqs. (2.37) - (2.39) in which all  $\mathbf{v}$ 's are replaced by  $\tilde{\mathbf{v}}$ . The validity of this treatment is discussed in Ref. 71.

Finally, let us consider electron- $A$  ionization, where  $A$  denotes the neutral particle with a mass, which can be assumed equal to that of the ion  $M$ . The process is represented as [71]

$$e_1(\mathbf{v}) + A(\mathbf{V}) \rightarrow e_1(\mathbf{v}') + e_2(\mathbf{v}'') + A^+(\mathbf{V}'), \quad (2.52)$$

where  $A^+$  denotes an ion,  $e_1$  is the incident electron,  $e_2$  is the ejected electron, and the symbols in the parentheses denote the velocities. The energy balance equation is

$$\frac{mv^2}{2} + \frac{MV^2}{2} = \frac{mv'^2}{2} + \frac{mv_{ej}'^2}{2} + \frac{MV'^2}{2} + E_{th}, \quad (2.53)$$

where  $E_{th}$  is the threshold energy of the ionization. Because of the large ion-to-electron mass ratio, we can assume that the momentum of the incident electron is much lower than the momentum of the neutral particle, i.e. the incident electron removes an electron from the neutral, and the neutral becomes an ion, continuing on its trajectory undisturbed. On one hand, this assumption means that the created ion takes the velocity and direction of the neutral particle before collision, i.e.  $\mathbf{V}' = \mathbf{V}$ . On the other hand, the energy balance can be rewritten

$$\frac{mv^2}{2} - E_{th} = \frac{mv'^2}{2} + \frac{mv_{ej}'^2}{2}. \quad (2.54)$$

The left-hand side is known as the excess energy  $\Delta E$  after ionization and we need to find an algorithm how to divide it into the scattered and ejected electrons. In general, when there is no published work on the division of the excess energy, it is divided randomly into two [71]

$$E_{scat} = \frac{mv'^2}{2} = R\Delta E \quad (2.55)$$

$$E_{ej} = \frac{mv_{ej}'^2}{2} = (1-R)\Delta E. \quad (2.56)$$

For the electron-Ar ionization, however, we use the expression for sampling the  $E_{ej}$  by a random number  $R$ , presented in Ref. 71

$$E_{ej} = \alpha_o + a \tan \left[ R \left( \tan^{-1} \frac{\alpha_1}{a} + \tan^{-1} \frac{\alpha_0}{a} \right) - \tan^{-1} \frac{\alpha_0}{a} \right] \quad (2.57)$$

$$\alpha_0 = 2 - \frac{100}{E_{inc} + 10}$$

$$\alpha_1 = \frac{E_{inc} - E_{th}}{2} - \alpha_0$$

$$a = 10.3,$$

where  $E_{inc} = mv^2/2$  is the energy of the incident electron. The units of  $\alpha_0$  and  $\alpha_1$  are electronvolts. Once the excess energy is divided,  $v'$  is calculated from Eq. (2.54)

$$v' = \sqrt{v^2 - \frac{2(E_{th} + E_{ej})}{m}}. \quad (2.58)$$

Similar to the excitation collision (see above) we define the velocity  $\tilde{\mathbf{v}}$  with magnitude  $v'$  and direction  $\mathbf{v}/v$  by [71]

$$\tilde{\mathbf{v}} = \mathbf{v} \sqrt{1 - \frac{E_{th} + E_{ej}}{E_{inc}}}. \quad (2.59)$$

The post-collision velocity of the scattered electron  $\mathbf{v}'$  is obtained by Eq. (2.37) in which  $\mathbf{v}$  is replaced by  $\tilde{\mathbf{v}}$ . The pre-collision velocity for the ejected electron, which does not exist in reality, is assumed [71]

$$\tilde{\mathbf{v}}_{ej} = \frac{\mathbf{v}}{v} \sqrt{\frac{2E_{ej}}{m}} \quad (2.60)$$

and the post-collision velocity is obtained again from Eq. (2.37) by replacing  $\mathbf{v}$  with  $\tilde{\mathbf{v}}_{ej}$  and  $\mathbf{v}'$  with  $\mathbf{v}'_{ej}$  [71].

For many types of collisions no data on differential cross-sections are available in the literature. If there are no data, the differential cross-section is assumed not to depend to the deflection angle  $\chi$ . The total cross-section calculated from Eq. (2.43) gives  $\sigma_T = 4\pi\sigma(g)$ . Therefore, the probability defined by (2.44) becomes  $\sin\chi d\chi d\varphi/4\pi$ . This means that the post-collision velocities take random direction. The scattering with this property is called isotropic. Since there are no sufficient data for the differential cross-sections of *electron-CF<sub>4</sub>* and *electron-N<sub>2</sub>* collisions we assume that the scattering is isotropic. The approximation of the interaction potential with the screened Coulomb potential made for collisions with atomic Ar is not valid for molecular gases [84]. In case of isotropic scattering the deflection angle, which is in the interval  $[0, \pi]$ , is randomly sampled by

$$\cos\chi = 1 - 2R. \quad (2.61)$$

The angle  $\varphi$  is randomly sampled from (2.40) and the post-collision velocities for electron-CF<sub>4</sub> and electron-N<sub>2</sub> elastic collisions can be found from Eqs. (2.37) - (2.39). Similar to electron-Ar elastic collisions, these equations can be somewhat simplified by use of  $M + m \approx M$  and  $\mathbf{g} \approx \mathbf{v}$ .

Electron-CF<sub>4</sub> and electron-N<sub>2</sub> inelastic collisions are treated similar to electron-Ar inelastic collisions, taking into account the isotropic scattering after collision. In case of ionization, the excess energy is divided by a random number using Eqs. (2.55) and (2.56) between the scattered and ejected electron. In case of attachment the incident electron is removed from the calculation and the created negative ion takes the velocity and direction of the neutral particle before the collision.

## 2.6 Ion-neutral collisions

### 2.6.1 Cross-section data

The ion-neutral collisions that are taken into account in the present study are the following:

(a) *Collisions of Ar<sup>+</sup> with neutrals*

Ar<sup>+</sup>-Ar elastic isotropic scattering and scattering in backward direction (to simulate charge transfer), Ar<sup>+</sup>-N<sub>2</sub> charge transfer, and Ar<sup>+</sup>-CF<sub>4</sub> elastic collisions are considered. The cross-section data for Ar<sup>+</sup>-Ar collisions [85] and Ar<sup>+</sup>-N<sub>2</sub> collisions [86] are presented in Fig. 2.13. The Ar<sup>+</sup>-CF<sub>4</sub> elastic cross-section is approximated to the Langevin cross-section for polarization scattering. Since the cross-section data are available for all these collisions, the Ar<sup>+</sup>-neutral collisions are treated by the null-collision method.

(b) *Collisions of N<sub>2</sub><sup>+</sup> with neutrals*

N<sub>2</sub><sup>+</sup>-N<sub>2</sub> and N<sub>2</sub><sup>+</sup>-Ar elastic and charge transfer collisions are considered. Figure 2.14 shows the N<sub>2</sub><sup>+</sup> - N<sub>2</sub> elastic isotropic scattering and charge transfer cross sections as a function of the laboratory ion energy in eV [85], and N<sub>2</sub><sup>+</sup> - Ar charge transfer [86] and elastic isotropic scattering cross sections as a function of the relative energy in eV. The cross section for N<sub>2</sub><sup>+</sup> - N<sub>2</sub> elastic isotropic scattering  $Q_i$  is approximated up to 50 eV to the Langevin cross section for polarization scattering and for energies higher than 50 eV to  $(Q_m - 2Q_{CT})$  like it has been done for the Ar<sup>+</sup> - Ar elastic isotropic cross section in Ref. 85.  $Q_m$  and  $Q_{CT}$  are the momentum and charge transfer cross sections, respectively. The data for N<sub>2</sub><sup>+</sup> - Ar elastic isotropic scattering cross section are estimated from the data available for the Ar<sup>+</sup> - Ar collisions taking into account that  $Q_i \sim 1/\sqrt{\mu}$ , where  $\mu$  is the reduced mass. Since the cross-section data are available for all these collisions, the N<sub>2</sub><sup>+</sup>-neutral collisions are treated by the null-collision method.

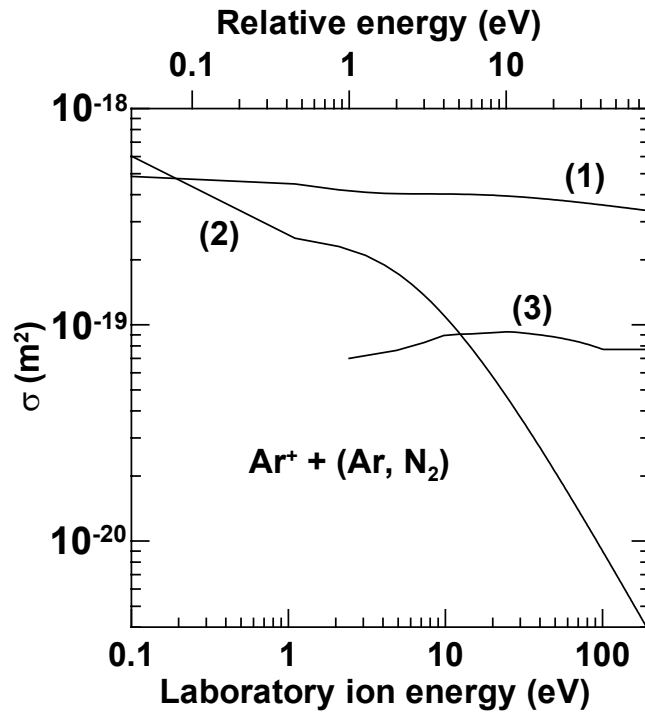


FIGURE 2.13  $\text{Ar}^+ + \text{Ar}$  charge transfer (1) and  $\text{Ar}^+ + \text{Ar}$  elastic isotropic scattering (2) cross sections as a function of the laboratory ion energy in eV [84], and  $\text{Ar}^+ + \text{N}_2$  charge transfer (3) cross section as a function of the relative energy in eV [85].

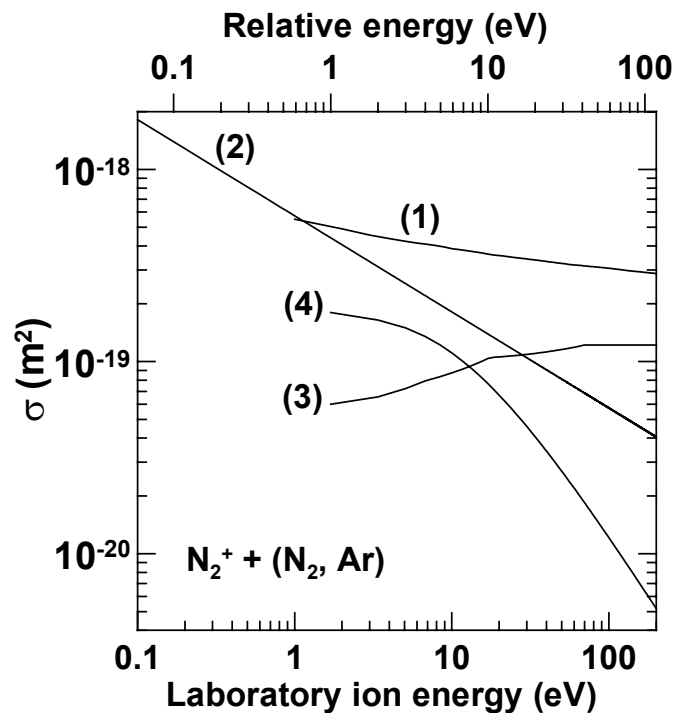


FIGURE 2.14.  $\text{N}_2^+ + \text{N}_2$  charge transfer (1) and  $\text{N}_2^+ + \text{N}_2$  elastic isotropic scattering (2), cross sections as a function of the laboratory ion energy in eV [84], and  $\text{N}_2^+ + \text{Ar}$  charge transfer (3) [85] and elastic isotropic scattering (4) cross sections as a function of the relative energy in eV.

(c) Collisions of  $CF_3^+$ ,  $CF_3^-$  and  $F^-$  with neutrals

$CF_3^{+/-}$  -  $CF_4$  and  $F^-$  -  $CF_4$  elastic and reactive collisions are simulated using the ion-molecule collision model for endothermic reactions [57, 77]. The total cross-section of the ion-molecule collisions is derived from the Langevin-Hasse model. The method calculates the probability for a given reaction by applying the Rice-Rampsperger-Kassel (RRK) theory. All the reactive collisions with corresponding threshold energies are presented in the Appendix B. The calculated cross-sections from this method are shown below in the section discussing  $CF_3^{+/-}$  -  $CF_4$  and  $F^-$  -  $CF_4$  collisions.  $CF_3^{+/-}$  - Ar and  $F^-$  - Ar elastic collision cross-sections are approximated to the Langevin cross-section for polarization scattering.

The  $Ar^+$  -  $N_2$  elastic collisions are not considered in the present simulations since the density of  $N_2$  is low compared to that of Ar or  $CF_4$  and consequently, the probability for collision is small. Similarly,  $N_2^+$  -  $CF_4$  and  $CF_3^{+/-}$  -  $N_2$  and  $F^-$  -  $N_2$  collisions are neglected in the model.

**2.6.2 Calculation of the post-collision velocities**

Let us consider an elastic collision  $A^+ - B$  without charge exchange

$$A^+(\mathbf{v}_A) + B(\mathbf{v}_B) \rightarrow A^+(\mathbf{v}_A') + B(\mathbf{v}_B') \quad (2.62)$$

and with charge exchange

$$A^+(\mathbf{v}_A) + B(\mathbf{v}_B) \rightarrow A(\mathbf{v}_A') + B^+(\mathbf{v}_B'). \quad (2.63)$$

If the collision  $A^+ - B$  is treated by the hard-sphere model, the scattering is isotropic. The post-collision velocities for elastic collisions presented by (2.62) are [71]

$$\mathbf{v}_A' = \frac{1}{m_A + m_B} (m_A \mathbf{v}_A + m_B \mathbf{v}_B + m_B |\mathbf{v}_A - \mathbf{v}_B| \mathbf{R}) \quad (2.64)$$

$$\mathbf{v}_B' = \frac{1}{m_A + m_B} (m_A \mathbf{v}_A + m_B \mathbf{v}_B - m_A |\mathbf{v}_A - \mathbf{v}_B| \mathbf{R}), \quad (2.65)$$

where  $m_A$  and  $m_B$  are the mass of the ion and neutral, respectively, and  $\mathbf{R}$  is a unit vector with a random direction. The components of  $\mathbf{R}$  are calculated from

$$R_x = \sin \theta \cos \varphi, \quad R_y = \sin \theta \sin \varphi, \quad R_z = \cos \theta, \quad (2.66)$$

where  $\theta$  and  $\varphi$  are randomly sampled taking into account that  $\theta$  is in the interval  $[0, \pi]$ , and  $\varphi$  is in the interval  $[0, 2\pi]$ .

If we consider the same model for the charge exchange collision presented by (2.63) when  $m_A = m_B$ , i.e. resonant charge exchange, the ion velocity is given by

$$\frac{1}{2}(\mathbf{v}_A + \mathbf{v}_B \pm |\mathbf{v}_A - \mathbf{v}_B| \mathbf{R}), \quad (2.67)$$

where plus is for elastic collision (2.62) and minus is for charge exchange (2.63). Because the unit vector is randomly sampled, the ion velocity is essentially the same in both processes. However, in dc or RF discharges an ion, which gained a kinetic energy in the sheath, is changed to an ion with thermal energy after charge exchange collision. This effect cannot be taken into consideration if the hard-sphere model is used as it is described.

Therefore, the identity switch model [71] is used in order to treat the charge exchange. In this model, the charge of an ion is transferred to a molecule without the velocity of either being changed. As a result,  $\mathbf{v}_A' = \mathbf{v}_A$  and  $\mathbf{v}_B' = \mathbf{v}_B$ , and the ion velocity relative to the neutral is changed from  $\mathbf{v}_A - \mathbf{v}_B$  to  $-(\mathbf{v}_A - \mathbf{v}_B)$ , that is, the deflection angle is  $\pi$ . Consequently, the charge exchange can be simulated as an elastic collision with backward scattering.

Finally, let us remind that in the bulk plasma ions and neutrals typically have similar velocities and the assumption in the null-collision method that the neutral is stationary, as it is made for electron-neutral collisions, is not applicable. For that reason, before collision occurs the ion is transformed to a reference frame in which the neutral is at rest, i.e. the velocity of the neutral (randomly sampled from a Maxwellian distribution) is subtracted from the velocity of the ion. After collision occurs the ion must be transferred back to the laboratory system by adding the chosen neutral velocity to the ion post-collision velocity.

### **2.6.3 Ion-molecule collision model for endothermic reactions: $\text{CF}_3^+$ , $\text{CF}_3^-$ or $\text{F}^-$ with $\text{CF}_4$**

The MCC is a probabilistic approach. In order to treat the collisions between particles it is necessary to calculate the collision probability and therefore, collision frequency. That requires having a full set of cross-section data. However, many gases are not well studied and the corresponding cross-section data are far from sufficient. Hence, the present model uses several techniques to define the collision probabilities even when the collision cross-sections are unknown. One of these techniques is the ion-molecule collision model for endothermic reactions [57, 77], which is used to simulate the  $\text{CF}_3^+$ ,  $\text{CF}_3^-$  or  $\text{F}^-$  elastic and reactive collisions with  $\text{CF}_4$ . The  $\text{CF}_3^+$ ,  $\text{CF}_3^-$  and  $\text{F}^-$  reactive collisions with  $\text{CF}_4$  with corresponding threshold energies, considered in the present study, are given in the Appendix B.

The total cross-section  $\sigma_T$  of the ion-molecule collisions is derived from the Langevin-Hasse model and in the case of singly charged ions it is given by [57]

$$\sigma_T = \left( \frac{\pi \alpha_p e^2}{\epsilon_0 \mu} \right)^{1/2} \beta_\infty^2 g^{-1}, \quad (2.68)$$

where  $\mu = m_i m_n / (m_i + m_n)$  is the reduced mass,  $e$  is the electron charge,  $\epsilon_0$  is the dielectric constant of vacuum,  $\alpha_p$  is the polarizability of the molecule,  $g = |\mathbf{V}_i - \mathbf{V}_n|$  is the relative velocity,  $\mathbf{V}_i$  and  $\mathbf{V}_n$  are the pre-collision velocities of the ion and neutral particle respectively, and  $\beta_\infty$  is the value of the dimensionless impact parameter  $\beta$ , for which the deflection angle is negligibly small. The value of  $\beta_\infty$  is set to 3 for  $\text{CF}_4$  [77]. For  $\text{CF}_4$  the polarizability  $\alpha_p$  is equal to  $19.0a_0^3$ , where  $a_0$  is the Bohr radius [1].

Hence the ion-molecule collision probability,  $P_c = n_g \sigma_T \Delta t$ , for the time-step  $\Delta t$ , at a neutral gas density  $n_g$ , equals

$$P_c = \left( \frac{\pi \alpha_p e^2}{\epsilon_0 \mu} \right)^{1/2} \beta_\infty^2 n_g \Delta t. \quad (2.69)$$

For every colliding ion, the value of the dimensionless impact parameter  $\beta$  is determined by a random number  $R$  from  $\beta = \beta_\infty \sqrt{R}$ . The critical value of  $\beta$  for reactive collisions is equal to one, i.e. for  $\beta \leq 1$  a reactive collision occurs and isotropic scattering is assumed [57, 77]. It should be mentioned that a reactive collision is specified as an elastic collision with isotropic scattering whenever the colliding pair of an ion and a molecule are unchanged after the collision. For simplicity, this is called an “elastic reactive” collision further in the text. For  $\beta > 1$ , on the other hand, the collision is assumed to be elastic with anisotropic scattering. The method of calculating the post-collision velocities for any value of  $\beta$  is presented below.

In a reactive collision, the colliding ion and molecule, called reactants, form a complex, which separates to products via the  $i$ th reaction path. As mentioned above, when the products are the same as the colliding particles, the collision is specified as “elastic reactive”. The reaction rate of the  $i$ th reaction and the rate of the “elastic reactive” collision, are determined by applying the Rice-Rampsperger-Kassel (RRK) theory [57, 77]. Hence the probability  $P_{r-i}$  of generating products from the complex via the  $i$ th reaction path is given by [57, 77]

$$P_{r-i} = \frac{(\epsilon - \Delta E_i)^{s-1}}{\epsilon^{s-1} + \sum_{i=1}^I (\epsilon - \Delta E_i)^{s-1}}, \quad (2.70)$$

where  $\varepsilon = \mu g^2 / 2$  is the relative kinetic energy of the reactants,  $\Delta E_i$  is the thermodynamic threshold energy of the  $i$ th reaction,  $s$  is the number of vibrational modes of the complex,  $I$  is the number of reaction paths satisfying  $\varepsilon > \Delta E_i$ . The number of vibrational modes is described as  $s = (3N - 6) / 2$ , where  $N$  is the number of atoms forming the complex [57, 77].

Similarly, the probability of “elastic reactive” collision  $P_{el}$  is expressed by

$$P_{el} = \frac{\varepsilon^{s-1}}{\varepsilon^{s-1} + \sum_{i=1}^I (\varepsilon - \Delta E_i)^{s-1}}. \quad (2.71)$$

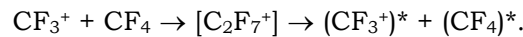
According to the probabilities  $P_{r-i}$  and  $P_{el}$  a reaction path is randomly sampled from 1 to  $(I + 1)$ , where  $(I + 1)$  denotes the “elastic reactive” collision. If the relative kinetic energy  $\varepsilon$  is less than the lowest threshold energies  $\Delta E_i$  and the sampled impact parameter  $\beta \leq 1$ , then elastic isotropic scattering is assumed.

Let us present the calculation of the post-collision velocities of the products. If *elastic isotropic scattering* occurs, i.e.  $\beta \leq 1$ , the post-collision velocities of the ion and neutral are found from Eqs. (2.64) and (2.65), replacing the indexes  $A$  and  $B$  with  $i$  and  $n$ , respectively.

In case of a *reactive collision* the velocities of the products are calculated based on the energy and momentum conservation equations, which is illustrated by the following example [77]. The reaction with threshold energy  $\Delta E$



is divided into 3 stages. First, a complex  $\text{C}_2\text{F}_7^+$  ion is formed and second, the excited ion and neutral are formed



If the post-collision velocities of the excited ion and molecule are  $\mathbf{V}_i'$  and  $\mathbf{V}_n'$ , respectively, the energy and momentum conservation are

$$\frac{1}{2} \mu g^2 = \frac{1}{2} \mu g'^2 + \Delta E, \quad (2.72)$$

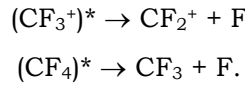
$$m_i \mathbf{V}_i + m_n \mathbf{V}_n = m_i \mathbf{V}_i' + m_n \mathbf{V}_n', \quad (2.73)$$

where  $g' = |\mathbf{V}_i' - \mathbf{V}_n'|$  is the relative velocity after collision and it is found from Eq. (2.72) to be

$$g' = \sqrt{g^2 - \frac{2\Delta E}{\mu}} \quad (2.74)$$

Isotropic scattering is assumed, i.e.  $\mathbf{g}' = g' \mathbf{R}$ , where  $\mathbf{R}$  is the unit vector with random direction [see above Eq. (2.66)].

In the third step, dissociation of the excited ion and molecule follows



Assuming that all internal energy of the excited ion and molecule is used for dissociation, and applying again the energy and momentum conservation equations, the velocities of  $\text{CF}_2^+$  and F are equal to that of the excited ion  $\mathbf{V}_i'$ , and the velocities of  $\text{CF}_3$  and F are equal to that of the excited neutral  $\mathbf{V}_n'$  [77].

Finally, if the sampled impact parameter is  $\beta > 1$ , then an *elastic collision with anisotropic scattering* is considered. The deflection angle  $\chi$  of the relative velocity  $\mathbf{g}$  is a function of the impact parameter  $\beta (= \beta_\infty \sqrt{R})$ . It is [71, 77]

$$\chi(\beta) = \pi - \frac{2^{3/2} \beta}{\xi_1} K(\zeta), \quad (2.75)$$

where  $\zeta = \xi_0 / \xi_1$ ,  $\xi_0 = [\beta^2 - (\beta^4 - 1)^{1/2}]^{1/2}$ ,  $\xi_1 = [\beta^2 + (\beta^4 - 1)^{1/2}]^{1/2}$ , and  $K(\zeta)$  is the complete elliptic integral of the first kind

$$K(\zeta) = \int_0^{\pi/2} \frac{d\theta}{(1 - \zeta^2 \sin^2 \theta)^{1/2}}. \quad (2.76)$$

The integral is solved numerically by a standard function (Ref. 75, p.260).

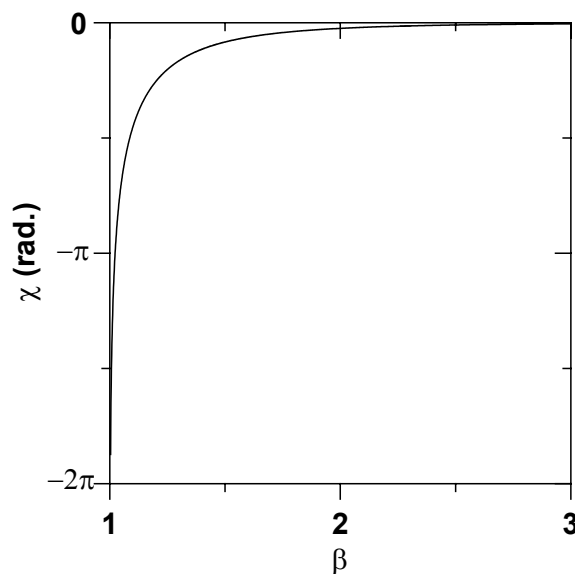


FIGURE 2.15. The deflection angle  $\chi$  as a function of the impact parameter  $\beta$ .

The calculated angle  $\chi$  is negative for  $\beta > 1$ . Since the deflection angle is negative, a polar angle  $\chi'$  is defined so that  $\chi' = |\chi|$  for  $-\pi < \chi < 0$ ,  $\chi' = 2\pi - |\chi|$  for  $-2\pi < \chi < -\pi$ , and so on. In this case  $\cos \chi' = \cos \chi$  and  $\sin \chi' = |\sin \chi|$ . The dependence of the angle  $\chi$  from the impact parameter  $\beta$  is presented in Fig. 2.15, Figure 2.15 also illustrates the choice of the cut-off parameter  $\beta_\infty = 3$ , the value of  $\beta$  for which the deflection angle is negligibly small.

The post-collision velocities can be found from Eqs. (2.37) - (2.39), replacing  $m$  and  $M$  with  $m_i$  and  $m_n$ ;  $\mathbf{v}$  and  $\mathbf{V}$  with  $\mathbf{V}_i$  and  $\mathbf{V}_n$ ;  $\mathbf{v}'$  and  $\mathbf{V}'$  with  $\mathbf{V}_i'$  and  $\mathbf{V}_n'$ ; and  $\sin \chi$  with  $|\sin \chi|$ . The angle  $\varphi$  is randomly sampled from Eq. (2.40).

For the elastic collisions of the  $\text{CF}_3^+$ ,  $\text{CF}_3^-$  or  $\text{F}^-$  with Ar the cross-section is approximated to the Langevin cross-section for polarization scattering, which is given by [1]

$$\sigma_L = \left( \frac{\pi \alpha_p e^2}{\epsilon_0 \mu} \right)^{1/2} g^{-1}, \quad (2.77)$$

where the polarizability  $\alpha_p$  is equal to  $11.08a_0^3$  for an Ar atom. The scattering is assumed isotropic and hence, the post-collision velocities are calculated from Eqs. (2.64) – (2.66).

#### 2.6.4 Theoretical $\text{CF}_3^{+/-} + \text{CF}_4$ and $\text{F}^- + \text{CF}_4$ cross-sections

Because of the importance of ion-neutral collisions for the calculation of the ion energy distribution function (IEDF), we present the cross-sections for the  $\text{CF}_3^+$ ,  $\text{CF}_3^-$  or  $\text{F}^-$  elastic and reactive collisions with  $\text{CF}_4$  and Ar, calculated from the probabilities given by Eqs. (2.70) and (2.71), and with Ar elastic collisions, calculated by Eq. (2.77).

Since only  $\text{CF}_3^+$ ,  $\text{F}^-$ , and  $\text{CF}_3^-$  ions (i.e. not the other positive  $\text{CF}_x$  ions and radicals) are followed in the model we do not present the cross section of every reaction, given in the Appendix B, separately. Figure 2.16 shows  $\text{CF}_3^+ + \text{CF}_4$  (1) and  $\text{CF}_3^+ + \text{Ar}$  (2) elastic isotropic scattering; sum of all reactive  $\text{CF}_3^+ + \text{CF}_4$  collisions, presented in Table B.1 (3), the sum of reactive collisions in case of dissociation of the initial ion, i.e. loss of the ion (4), and the sum of the reactive collisions after which one of the products is the initial ion (5). In the last case (5) there is no production of the ion, only its energy is reduced more or less significantly (see above). However, this kind of collision cannot be considered as symmetric charge transfer since the post-collision velocity of the ion is not close to the thermal velocity of the neutrals.

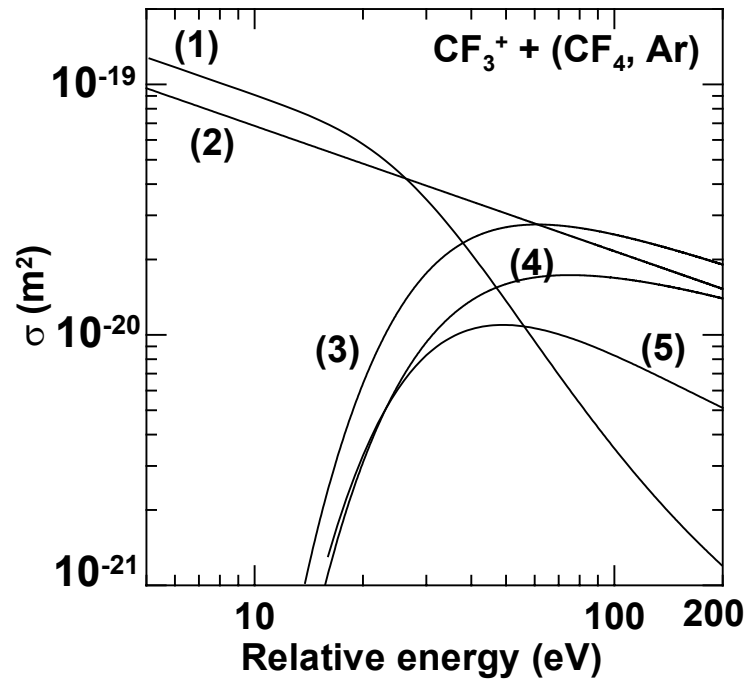


FIGURE 2.16.  $\text{CF}_3^+ + (\text{CF}_4, \text{Ar})$  cross-sections.  $\text{CF}_3^+ + \text{CF}_4$  (1) and  $\text{CF}_3^+ + \text{Ar}$  (2) elastic isotropic scattering; sum of all reactive  $\text{CF}_3^+ + \text{CF}_4$  collisions (3); sum of reactive  $\text{CF}_3^+ + \text{CF}_4$  with a loss of  $\text{CF}_3^+$  ion (4); and sum of reactive  $\text{CF}_3^+ + \text{CF}_4$  collisions after which the  $\text{CF}_3^+$  ion is one of the products (5).

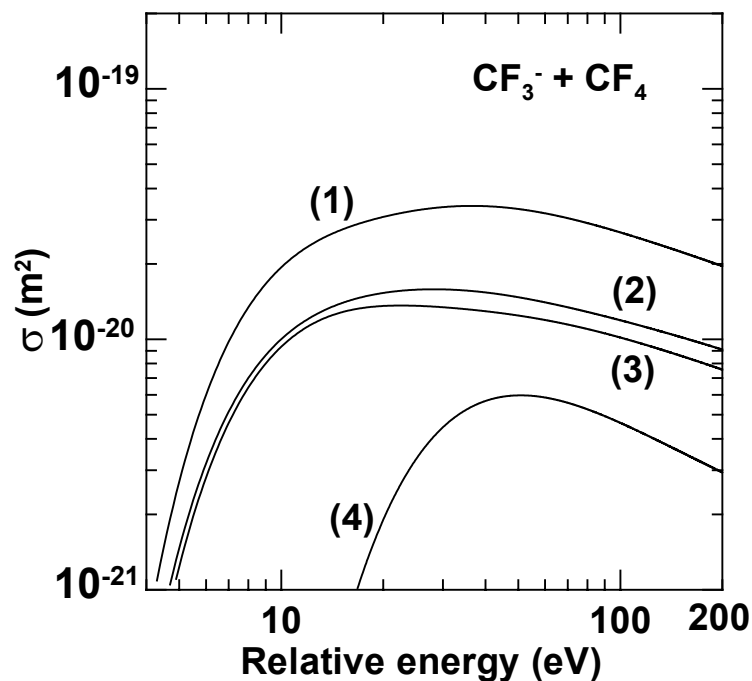


FIGURE 2.17.  $\text{CF}_3^- + \text{CF}_4$  cross-sections. Sum of all reactive  $\text{CF}_3^- + \text{CF}_4$  collisions (1); sum of electron detachment (2); sum of reactive  $\text{CF}_3^- + \text{CF}_4$  collisions after which the  $\text{F}^-$  ion is one of the products (3); and sum of reactive  $\text{CF}_3^- + \text{CF}_4$  collisions after which the  $\text{CF}_3^-$  ion is one of the products (4).

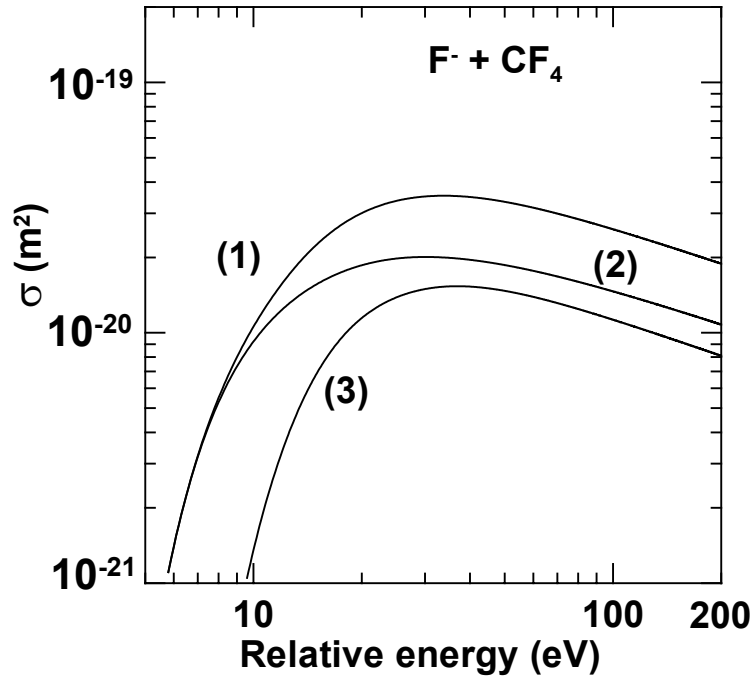


FIGURE 2.18.  $F^- + CF_4$  cross-sections; Sum of all reactive  $F^- + CF_4$  collisions (1); sum of electron detachment (2); and sum of reactive  $F^- + CF_4$  collisions after which the  $F^-$  ion is one of the products (3).

Similarly, Fig. 2.17 shows cross sections of the sum of all reactive  $CF_3^- + CF_4$  collisions, presented in Table B.2 (1), the sum of electron detachment collisions (2), the sum of reactive collisions after which  $F^-$  or  $CF_3^-$  is one of the products (3) or (4), respectively. Finally, Fig. 2.18 presents cross sections of the sum of all reactive  $F^- + CF_4$  collisions, presented in Table B.3 (1), the sum of electron detachment collisions (2), and the sum of reactive collisions after which  $F^-$  is one of the products (3).

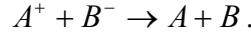
Only the  $CF_3^+ - CF_4$  and Ar elastic cross sections are shown [Fig. 2.16 curves (1) and (2)] because the  $F^- - CF_4$  and Ar, and the  $CF_3^- - CF_4$  and Ar elastic cross-sections have similar values.

## 2.7 Positive-negative ion recombination

As discussed in section 2.3.1 the collision rates for Coulomb collisions in cc RF discharges are low enough to disregard these collisions. However, in cc RF discharges of electronegative gases the negative ions are confined in the bulk and the positive-negative ion recombination is the dominant mechanism for the loss of negative ions. Therefore, it is necessary to consider these types of collisions. Hence, we need the corresponding cross-sections. Often the rate constant is known instead

of the cross-section. A method to determine the recombination cross-section from a given rate constant was proposed by Nanbu and Denpoh [78].

Let us consider the reaction between positive  $A^+$  and negative  $B^-$  ions



In general, the reaction rate constant  $k_r(T)$  is assumed to be a function of temperature  $T$  [78]

$$k_r(T) = k_0(T_0/T)^n, \quad (2.78)$$

where  $n \geq 0$ . The rate constant is defined by [1]

$$k_r(T) = \overline{g\sigma(g)} = \int_0^\infty g\sigma(g) \left( \frac{\mu}{2\pi kT} \right)^{3/2} \exp\left(-\frac{\mu g^2}{2kT}\right) 4\pi g^2 dg, \quad (2.79)$$

where  $g(=|\mathbf{v}_A - \mathbf{v}_B|)$  is the relative velocity,  $\sigma(g)$  the recombination cross-section,  $\mu$  the reduced mass and  $k$  the Boltzmann constant. Eq. (2.79) is solved and there are two solutions for  $\sigma(g)$  [78]

$$\sigma(g) = k_0 g^{-1}, \quad (n = 0) \quad (2.80)$$

$$\sigma(g) = k_0 \sqrt{\frac{\pi k T_0}{2\mu}} g^{-2}, \quad \left(n = \frac{1}{2}\right). \quad (2.81)$$

In the first case given by Eq. (2.80) the rate constant is independent of  $T$ . This case is assumed for the positive-negative ion recombination considered in the model (see the rate constants presented below).

Let the numbers of the simulated positive  $A^+$  and negative ions  $B^-$  in a cell with volume  $V_c$  be  $N_A$  and  $N_B$ , respectively, and the weights (representing the number of real particles in one superparticle) are  $W_A$  and  $W_B$ . The number density  $n_A$  of  $A^+$  is given by  $W_A N_A / V_c$ . Similarly, the number density  $n_B$  of  $B^-$  is given by  $W_B N_B / V_c$ . The probability that the  $i$ th sample of  $A^+$  (sample ( $A_i$ )) recombines with some  $B^-$  in a time  $\Delta t_r$  is given by

$$P_{Ai} = n_B \Delta t_r \overline{g\sigma(g)} = \frac{n_B}{N_B} \Delta t_r \sum_{j=1}^{N_B} g_{ij} \sigma(g_{ij}) = \sum_{j=1}^{N_B} P_{ij}, \quad (2.82)$$

where  $P_{ij}$  is the probability that sample ( $A_i$ ) recombines with sample ( $B_j$ ), expressed by

$$P_{ij} = \frac{n_B}{N_B} g_{ij} \sigma(g_{ij}) \Delta t_r, \quad (2.83)$$

and  $g_{ij} = |\mathbf{v}_{Ai} - \mathbf{v}_{Bj}|$ . The average  $\overline{g\sigma(g)}$  is taken over all samples  $B^-$  in the cell.

The number of recombination collisions of type  $A^+$  is

$$N_{rA} = \sum_{i=1}^{N_A} P_{Ai} = \sum_{i=1}^{N_A} \sum_{j=1}^{N_B} P_{ij}. \quad (2.84)$$

If the rate constant is independent of  $T$  then we apply the expression (2.80) for the cross-section, hence the probability  $P_{ij}$  is constant

$$P_{ij} = \frac{n_B}{N_B} k_0 \Delta t_r. \quad (2.85)$$

Combining (2.84) and (2.85) the number of superparticles of type  $A^+$ ,  $N_{rA}$ , which can recombine in a time  $\Delta t_r$  in a cell, is obtained

$$N_{rA} = N_A n_B k_0 \Delta t_r = W_B \frac{N_A N_B}{V_c} k_0 \Delta t_r. \quad (2.86)$$

Similarly the number of superparticles of type  $B^-$ ,  $N_{rB}$ , is

$$N_{rB} = W_A \frac{N_A N_B}{V_c} k_0 \Delta t_r. \quad (2.87)$$

The superparticle numbers  $N_{rA}$  and  $N_{rB}$  are different but the numbers of real particles of  $A^+$  and  $B^-$  that can recombine are equal, i.e.  $N_{rA} W_A = N_{rB} W_B$ .

Since the probability  $P_{ij}$  is independent of  $g$  every pair is equally probable to recombine. Therefore,  $N_{rA}$  and  $N_{rB}$  particles are picked up randomly in a cell and are recombined.

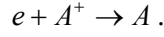
The positive-negative ion recombination collisions and the corresponding rate constants, considered in the simulation are presented in Table 2.2. The rate constant does not depend on the ion temperature and consequently, we use the above described simulation model. The evaluation of (2.81), i.e.  $k_r \sim (T)^{1/2}$ , is presented in the next section for electron-positive ion recombination.

TABLE 2.2 Positive-negative ion recombination reactions considered in the model and corresponding rate constants and reference numbers.

Reaction	Rate constant ( $\text{m}^3 \text{s}^{-1}$ )	Reference
$\text{F}^- + \text{Ar}^+ \rightarrow \text{F} + \text{Ar}$	$10^{-13}$	[87]
$\text{F}^- + \text{CF}_3^+ \rightarrow \text{F} + \text{CF}_3$	$10^{-13}$	[87]
$\text{CF}_3^- + \text{Ar}^+ \rightarrow \text{CF}_3 + \text{Ar}$	$10^{-13}$	[87]
$\text{CF}_3^- + \text{CF}_3^+ \rightarrow \text{CF}_3 + \text{CF}_3$	$10^{-13}$	[87]

## 2.8 Electron-positive ion recombination

Similar to the positive-negative ion recombination, the probability for the electron-positive ion recombination is simulated from a given rate constant [58, 78]. Let us consider the reaction between an electron with mass  $m$  and an ion with mass  $M_i$



The electron temperature  $T_e$  is much higher than the ion temperature  $T_i$ . The dependence of the electron - ion recombination rate constant on the electron or both electron and ion temperatures makes the model more complicated. The electron-ion recombination collisions, considered in the model, with the corresponding rate constants  $k_{re-i}$  and reference numbers are presented in Table 2.3.

Let us express the electron - ion rate constant as  $k_{re-i} = a / (T_e)^{1/2}$  where  $a$  is equal to  $3.95 \times 10^{-15} / T_i$  and  $7.72 \times 10^{-14}$  for electron -  $\text{CF}_3^+$  and electron -  $\text{N}_2^+$  recombination, respectively. The rate constant is also given by  $\overline{g\sigma(g)}$ , where the relative velocity  $g(=|\mathbf{v} - \mathbf{V}_i|)$  can be replaced by the electron velocity  $\mathbf{v}$  ( $v \gg V_i$ ). The probability that an electron with temperature  $T_e$  recombines with an ion in a time-step  $\Delta t_r$  is [58]

$$P_{re-i} = n_i \Delta t_r \overline{g\sigma(g)} = n_i \Delta t_r k_{re-i} = \frac{W_i N_i}{V_c} \frac{a}{\sqrt{T_e}} \Delta t_r, \quad (2.88)$$

where  $n_i = W_i N_i / V_c$  is the ion number density in a cell with a volume  $V_c$ ;  $N_i$  is the number of superparticles of type  $A^+$  and  $W_i$  is the weight.

TABLE 2.3 Electron-positive ion recombination reactions considered in the model and corresponding rate constants and reference numbers.  $T_e$  and  $T_i$  are in eV.

Reaction	Rate constant ( $\text{m}^3 \text{s}^{-1}$ )	Reference
$e + \text{CF}_3^+ \rightarrow \text{CF}_3$	$\frac{3.95 \times 10^{-15}}{T_i} \frac{1}{\sqrt{T_e}}$	[58]
$e + \text{N}_2^+ \rightarrow 2\text{N}(^4\text{S})$	$7.72 \times 10^{-14} \frac{1}{\sqrt{T_e}}$	[88]

The recombination rate constant shows that the electrons with lower temperature, that is, slower velocity, are more likely to recombine with ions. Let us express the electron velocity from the concept for the particle temperature

$$T_e = \frac{m}{3e} v^2, \quad (2.89)$$

where  $e$  is the elementary charge. Hence, the probability becomes

$$P_{re-i} = \frac{W_i N_i}{V_c} \frac{a}{\sqrt{m/3e}} \frac{\Delta t_r}{v}. \quad (2.90)$$

Evaluation of a double summation as in Eq. (2.84) is computationally intensive. The idea of the null-collision method is used to solve this problem [58, 78]. Since the probability is inversely proportional to the electron velocity, a practical lower minimum is chosen,  $v_{\min}$ , for which the probability is at maximum and becomes

$$(P_{re-i})_{\max} = \frac{W_i N_i}{V_c} \frac{a}{\sqrt{m/3e}} \frac{\Delta t_r}{v_{\min}}. \quad (2.91)$$

The minimum velocity is chosen to be 1/5th of the mean electron velocity in each cell so that the probability that a randomly sampled electron has a velocity less than  $v_{\min}$  is only 1.1 % in equilibrium [58]. If the number of the simulated electrons in a cell is  $N_e$ , the maximum number of the simulated electrons  $(N_{re})_{\max}$  that can recombine is calculated from

$$(N_{re})_{\max} = N_e (P_{re-i})_{\max} = W_i \frac{N_e N_i}{V_c} \frac{a}{\sqrt{m_e/3e}} \frac{\Delta t_r}{v_{\min}}. \quad (2.92)$$

Since the real numbers of recombined electrons and ions have to be equal, that is  $N_{re} W_e = N_{ri} W_i$  the maximum number of the simulated ions that can recombine is given by

$$(N_{ri})_{\max} = W_e \frac{N_e N_i}{V_c} \frac{a}{\sqrt{m_e/3e}} \frac{\Delta t_r}{v_{\min}}. \quad (2.93)$$

The number  $(N_{re})_{\max}$  is the sum of the real collisions and that of null-collisions. Therefore, the rate of the recombination would be overestimated if  $(N_{re})_{\max}$  is used instead of  $N_{re}$ . The probability that a real electron-ion pair will recombine is  $P_{ij} / P_{\max} = v_{\min} / v$ . Now the simulation procedure consists of:

- (1) Choose  $(N_{re})_{\max}$  electrons and  $(N_{ri})_{\max}$  ions randomly.
- (2) For every electron with a velocity  $v$  call a random number  $R$ . If  $R < v_{\min} / v$  is true, recombination occurs. If  $R \geq v_{\min} / v$  recombination does not happen, i.e. null-collision.

For the electron –  $\text{CF}_3^+$  recombination model the ion temperature is determined as the mean energy in each cell, i.e.,

$$T_i = \frac{M_i}{3} \langle V_i^2 \rangle. \quad (2.94)$$

In the simulation the recombination time step  $\Delta t_r$  is taken to be  $10^5$  times longer than the field (or electron) time step; the probability for recombination is, indeed, low because of the much lower electron and ion densities (in the order of  $10^{16} \text{ m}^{-3}$ ) in comparison with the neutral gas density (in the order of  $10^{21} \text{ m}^{-3}$ ).

## 2.9 Stability and accuracy of the PIC/MCC model

The PIC model simulates a limited number of particles. In order to minimize the discrete particle noise, the ratio of the number of super-particles/number of grid cells must be much greater than 1. Next, the choice of the weighting function can also reduce the noise. The *first-order weighting* has been chosen for the present simulation because it is an improvement in using finite-size particles in comparison with the zero-order weighting and at the same time it is computationally less expensive in comparison with the higher-order weighting [46].

Further, the PIC code uses the standard *explicit leap-frog finite difference scheme* to advance the particles (see section 2.2.1). The stability and accuracy of this numerical scheme is tested by applying it to the simple harmonic oscillator described by the second-order differential equation [46]

$$\frac{d^2 x}{dt^2} = -\omega_0^2 x. \quad (2.95)$$

This equation has physical solutions

$$x(t, t_0) = A(t_0) \cos \omega_0 t + B(t_0) \sin \omega_0 t. \quad (2.96)$$

If the leap-frog scheme is applied and the exact acceleration is substituted into the finite-difference scheme, one obtains

$$\frac{x^{t+\Delta t} - 2x^t + x^{t-\Delta t}}{\Delta t^2} = -\omega_0^2 x^t. \quad (2.97)$$

This equation is readily solved by assuming a solution of the form

$$x^t = A \exp(-i\omega t), \quad (2.98)$$

where  $\omega$  is unknown. Now substituting this and the corresponding expressions for  $x^{t-\Delta t}$  and  $x^{t+\Delta t}$ , it is found

$$\sin\left(\omega \frac{\Delta t}{2}\right) = \pm \omega_0 \frac{\Delta t}{2}. \quad (2.99)$$

For  $\omega_0 \Delta t / 2 \ll 1$ ,  $\omega \approx \omega_0$ , as desired. If  $\omega_0 \Delta t > 2$ , the real solution for  $\omega$  becomes complex with growing and decaying roots, which indicates numerical instabilities

[46]. The accuracy for the leap-frog mover is also obtained from (2.99). For  $\omega_0 \Delta t \ll 1$ ,

$$\frac{\omega}{\omega_0} = 1 + O(\omega_0 \Delta t)^2 \quad (2.100)$$

showing a quadratic phase error term. Typically the accuracy criterion is [46]

$$\omega_0 \Delta t \leq 0.2. \quad (2.101)$$

In a typical RF discharge fast plasma phenomena may not be significant. Consequently, the highest frequency, which is needed to resolve, is the driving RF  $\omega_{RF}$  plus a few harmonics, and the shortest length is the sheath width  $s$ . However, if an explicit mover is used, the accuracy criteria require resolving of the electron plasma density  $\omega_{pe}$  and the electron Debye length  $\lambda_{De}$ , which are given by [1]

$$\omega_{pe} = \left( \frac{e^2 n_e}{\epsilon_0 m} \right)^{1/2} \quad (2.102)$$

$$\lambda_{De} = \left( \frac{\epsilon_0 T_e}{en_e} \right)^{1/2}. \quad (2.103)$$

Thus the criteria for the time-step and grid spacing  $\Delta z$ , which have to be satisfied, are [46, 69]:

$$\omega_{pe} \Delta t \leq 0.2 \quad (2.104)$$

$$\Delta z \leq \lambda_{De}. \quad (2.105)$$

An additional condition, which must always be satisfied, is the Courant condition [69]

$$\frac{v_s \Delta t_s}{\Delta z} < 1, \quad (2.106)$$

where  $v_s$  is the characteristic velocity of a particle of species  $s$  and  $\Delta t_s$  is the time-step of this particle. The different time-steps for electrons and ions are discussed in the next section. The criterion (2.106) ensures that most particles will not travel more than one cell per time-step and will sample the electric fields properly.

The MCC part also implies a restriction on the time-step, which is discussed in section 2.3.1. Let us remind only that the MCC allows only one collision per particle per time-step, hence, the time-step must be chosen in such a way that the probability of having a particle collide more than once per time step is low. The generated error is expressed by Eq. (2.26) and an example about the limitation of the time-step is shown there.

The accuracy of the Poisson solver is discussed in Ref. 46, p. 72. There is a great store of information and practice on solving equations such as the Poisson

equation. We only mention here that the error is  $\sim (\Delta z)^2$ , as desired, when the finite difference scheme uses 3 points [see Eq. (2.13)].

Finally, generally in simulation methods it is needed to keep track of quantities like field or potential, kinetic, and total energies. The electrostatic field energy is calculated at time  $t$ . However, if the kinetic energy is simply calculated as a sum over  $mv^2/2$  of all particles, it will be obtained at time  $t + \Delta t/2$ . It is better to average the kinetic energy between the old and new times  $(t - \Delta t/2, t + \Delta t/2)$ . One can choose among [46]

$$\frac{1}{2}(v_{new}^2 + v_{old}^2) \quad (2.107)$$

$$\left(\frac{v_{new} + v_{old}}{2}\right)^{1/2} \quad (2.108)$$

$$v_{new}v_{old} \quad (2.109)$$

The last form is quickest to calculate. All the forms have the same value through order  $\Delta t$  and differ only in  $(\Delta t)^2$ , which is the order of accuracy of the leap-frog integrator producing  $v_{new}$  and  $v_{old}$ . Consequently, a better interpolation of kinetic energy would imply an accuracy that is not reached with the numerical scheme.

## 2.10 Methods for speeding up the calculation

Physical and numerical methods of speeding up particle simulations applied to RF discharges are well described and discussed in Ref. 69. Only the methods applied to the present investigation are discussed below.

### 2.10.1 Subcycling (different electron and ion time-steps)

The accuracy criteria discussed in the previous section imply short time-steps for the electrons. For example, in the present simulations the time-step varies from  $10^{-11}$  to  $7.4 \times 10^{-11}$  s depending on the electron plasma density and electron temperature. The far heavier ions move hardly at one electron time-step. Hence the ions might be moved less frequently, that is  $\Delta t_i = k\Delta t_e$ , where  $k$  may be 10 to 100 depending on the ion mass. This is called subcycling [69]. In electropositive discharges the number of ions and electrons are about the same. However, in electronegative discharges the number of ions can far exceed the number of electrons so that subcycling can significantly reduce the simulation time. In the present study the ion time-step is set 25 to 50 times longer than the electron time-step. In addition the recombination time-step is  $10^5$  times longer than the electron

time-step because of the much lower electron and ion densities in comparison with the neutral gas density.

### **2.10.2 Different weights**

As already mentioned, in electronegative discharges the number of electrons is quite different from the number of ions. The presence of the negative ions completely changes the plasma characteristics. For example, the electronegativity  $\alpha = n_- / n_e$  can reach values of  $10^2$ . Suppose that the same weight is used for electrons and ions. It is necessary to consider at least  $10^3$  electrons in a grid with 100 cells in order to satisfy the condition that the number of electrons per Debye length  $\lambda_{De}$  is much greater than 1. This means that  $10^5$  ions of every type have to be followed. Processing the particles is the most time-consuming part of the simulation. One way to reduce the number of computer particles is to weight the ion superparticles more heavily than the electron superparticles. In the present simulations the weights of the electron and different ions is chosen in such a way that the numbers of super-particles of every species are similar. For example, an electron super-particle represents  $10^7$  real particles, an  $\text{Ar}^+$  super-particle corresponds to  $10^9$  real particles, a  $\text{N}_2^+$  super-particle stands for  $10^8$  real particles, etc. depending on their number density. If there were no collisions the variable weighting procedure would be fairly straightforward. Since there are interactions between superparticles representing a different number of real particles one should take care for the particle balance.

### **2.10.3 Improved initial densities**

The PIC/MCC simulation usually starts with spatially uniform particle density profiles. The density distributions then evolve to their equilibrium states. This suggests that the time to reach equilibrium could be shortened by starting with non-uniform initial density profiles that are close to their final equilibrium values. In the present study initial density distributions calculated from previous runs are used. Experimental data are also taken into account in order to estimate the initial densities.

## **2.11 Approximations in the discharge model**

In the developed model some approximations are made depending on the operating conditions that are considered.

First, the model does not consider  $\text{CF}_2^+$ ,  $\text{CF}^+$ ,  $\text{C}^+$  and  $\text{F}^+$  ions. Increasing the types of species followed in the model makes the simulation computationally very expensive. In addition, in case of modeling of electronegative discharges the system

reaches convergence in a long computational time and the run time is much longer than the run time for electropositive discharges. Simulation results in a pure cc RF  $\text{CF}_4$  discharge [57] show that the dominant positive ions are  $\text{CF}_3^+$ , with a density exceeding those of  $\text{CF}_2^+$ ,  $\text{CF}^+$ ,  $\text{C}^+$  and  $\text{F}^+$  by 2 to 3 orders of magnitude, and  $N_{\text{CF}_3^+} \cong N_{\text{F}^-} + N_{\text{CF}_3^-} + N_e$ , where  $N$  denotes the number densities of the corresponding species in the bulk plasma. Simulation of a pure  $\text{CF}_4$  discharge following also the  $\text{CF}_2^+$  ion, which is considered to be second in importance after  $\text{CF}_3^+$  ion [57], is carried out in the present study and the results show that the ratio  $n_{\text{CF}_3^+} / n_{\text{CF}_2^+}$  is more than 40 (see Chapter 3). Moreover, the concentration of  $\text{CF}_4$  does not exceed 10% for etching purposes in practice, which suggests that the effect of all  $\text{CF}_x$  positive ions, except for  $\text{CF}_3^+$ , on the plasma parameters will be negligible in such mixtures. For that reason  $\text{CF}_3^+$  is the only type of positive ions of  $\text{CF}_4$  followed in the model. It should be mentioned, however, that in a  $\text{CF}_4$  ICP both measured and calculated data show that the number densities of  $\text{CF}_3^+$ ,  $\text{CF}_2^+$ ,  $\text{CF}^+$ , and  $\text{F}^+$  are comparable at low pressure and high power in the ICP [89, 90]. Since only capacitively coupled plasmas are considered in the present study, the approximation described above is reasonable.

Second, the collisions of electrons with neutrals, different from the background gas neutrals, like  $\text{CF}_x$  radicals ( $\text{CF}_3$ ,  $\text{CF}_2$ ,  $\text{CF}$ , and  $\text{F}$ ), excited states of  $\text{N}_2$ , and atomic nitrogen can significantly influence the ion and electron densities, and electron temperature, depending on the power, pressure, flow rate, etc. The present model does not take into account these collisions and the approximation is reasonable based on the following considerations. The computational and experimental results in a pure  $\text{CF}_4$  discharge show that the densities of the radicals at low pressure are much lower in comparison with the  $\text{CF}_4$  density, with values in the order of  $10^{18} \text{ m}^{-3}$  [13, 35, and 37] compared to  $10^{21} \text{ m}^{-3}$  for  $\text{CF}_4$ . An experimental investigation of DC magnetron  $\text{Ar}/\text{N}_2$  discharges at a pressure of 25 mTorr demonstrates that atomic nitrogen equals between 0.13 and 0.24% of the molecular nitrogen depending on the fractional  $\text{N}_2$  concentration [91]. Consequently, in the gas mixtures investigated in the present work, and at low pressure (20-200 mTorr) and low applied RF power the collision frequency of the electrons with the other neutrals is expected to be much smaller than the concentration and the collision frequency of the electrons with the background gas neutrals. In addition, in comparison with the PIC/MC method, a fluid or hybrid model is more suitable to follow the radicals and excited states, since the PIC/MC method assumes that the background gas neutrals are uniformly distributed in the discharge, which is not applicable to the other neutral species (e.g. see the space distributions of  $\text{CF}$  and  $\text{CF}_2$  presented in Ref. 13). On the other hand, the PIC/MCC model is more suitable to present the discharge

dynamics and detailed behavior of the electron and ion energies, as is focused on in the present work.



## **Chapter 3**

# **STUDY OF AR/CF<sub>4</sub> DISCHARGES: EFFECT OF GAS COMPOSITION**

### **3.1 Introduction**

Carbon tetrafluoride, CF<sub>4</sub>, and its mixtures are widely used in plasma etching of silicon and silicon dioxide [1]. In order to achieve high-resolution plasma processing it is important to understand the discharge physics and chemistry. In recent years a number of papers appeared dealing with high-density inductively coupled CF<sub>4</sub> and Ar/CF<sub>4</sub> discharges; especially diagnostic measurements and modeling [89, 90, 92-95]. Maeshige *et al.* [43] describe the design of a pulsed two-frequency capacitively coupled (cc) plasma in CF<sub>4</sub>/Ar for sustaining a high-density plasma and discuss its ability to generate charge-free processes for producing high-aspect-ratio holes or trench etching. However, simulations and experimental data for conventional cc RF discharges in Ar/CF<sub>4</sub> mixtures in the open literature are very scarce [16, 87]. Rauf and Kushner [87] investigated numerically the argon metastable densities in Ar/CF<sub>4</sub> discharges. Kaga *et al.* [16] present measurements of the charged particle densities and electron energy distribution function (EEDF) and their dependences on the CF<sub>4</sub> content.

CF<sub>4</sub> is an electronegative gas and its radicals play an important role in the etching process. The electron and ion densities and the electron temperature determine the production of the neutral radicals. Both experimental measurements [11, 12] and computational results [35-37, 57,58] of charged particle densities in pure cc RF CF<sub>4</sub> plasmas have been reported in the literature. There is a good qualitative agreement among them considering the different operating conditions. It was shown that the negative ion density in the bulk plasma exceeds the electron density by one order of magnitude. The abundance of negative ions is one of the main features of discharges in electronegative gases and this profoundly influences

the sheath dynamics (i.e., one observes electric field reversal, double layer structure and local maxima of electron density in the sheath region) [1, 35-37, 57].

Ar is a typical electropositive atomic gas and it is often used as an example for describing the fundamental principles of particle and energy balances in discharges [1]. Due to its relative simplicity the RF Ar discharge has been studied extensively both experimentally (e.g. Refs. 3-10) and by computer modeling (e.g. Refs. 34, 38-41, 50-56). Discharges in electropositive gases behave differently from those in electronegative gases. The contrast in the density profiles, the electric field properties, and the electron energy distribution has been the subject of several investigations [36, 56].

The purpose of the present chapter is a systematic study of the plasma parameters in a conventional cc RF Ar/CF<sub>4</sub> discharge by means of a 1d3v PIC/MCC model. This chapter deals with the influence of the gas composition on the discharge properties at more or less standard operating conditions. Comparison of the calculated ratio of negative ion to electron densities with the experimental data is also made.

In Sec. 3.2 the input data are given, in Sec 3.3 the results of the simulation, such as the electric field, the densities, the particle energies, and collision rates are presented and discussed. A summary is given in Sec. 3.4.

### 3.2 Input data

The numerical model used in this investigation is described in detail in Chapter 2. The charged species taken into account in the model are: electrons, Ar<sup>+</sup>, CF<sub>3</sub><sup>+</sup>, F<sup>-</sup>, and CF<sub>3</sub><sup>-</sup>. The collisions treated by the MCC model include electron - neutral (Ar and CF<sub>4</sub>) collisions, various kinds of collisions of Ar<sup>+</sup>, CF<sub>3</sub><sup>+</sup>, F<sup>-</sup>, or CF<sub>3</sub><sup>-</sup> with neutrals, and positive - negative ion recombination.

A schematic diagram of the RF reactor is shown in Fig. 2.1 (a). It is a cylindrical vacuum chamber containing two planar electrodes separated by a distance  $d = 2.5$  cm and driven by an RF power source. The other electrode is grounded. The amplitude and the frequency of the applied voltage to one of the electrodes are  $V = 200$  V and  $f = 13.56$  MHz, respectively.

The calculations are performed in one dimension for Ar/CF<sub>4</sub> mixtures at molar ratios of 0.1/0.9, 0.5/0.5 and 0.9/0.1, and for pure Ar and pure CF<sub>4</sub> discharges. The gas pressure is fixed at 200 mTorr. In Figures 3.1 - 3.6 the axis at  $z = 0$  corresponds to the RF powered electrode and the one at  $z = 2.5$  cm represents the grounded electrode. The gas temperature is set to 300 K. The simulation grid is uniform and it consists of 100 cells. The electron time step is  $3.7 \times 10^{-11}$  s for an Ar discharge simulation and  $7.4 \times 10^{-11}$  s for all other simulations. To speed up the

calculation, the ion time step is set to be 25 times longer than the electron time step. The choice of the grid spacing and the time steps is defined by the accuracy criteria for PIC/MC codes with explicit mover (see Sec. 2.9).

Secondary electron emission is not included here because the RF discharge is assumed to be in the  $\alpha$ -regime at the conditions under study [38, 50]. The initial densities of the charged species in the model are based on experimental and simulation data [12, 57]; the initial velocities are calculated from the Maxwellian distribution at an average electron temperature of 2 eV and an average ion temperature of 0.043 eV (500 K).

Typical results of this model are electron and ion densities, fluxes and energy distributions, collision rates and electric field and potential distributions.

### 3.3 Results and discussion

#### 3.3.1 Pure Ar discharge

Figure 3.1 presents the simulation results of the electric field distribution at four phases (a), the charged particle density distributions (b), the average electron and Ar<sup>+</sup> ion energies (c), and the time-averaged ionization rate (d) in a pure Ar discharge. In the bulk plasma the potential is nearly constant and therefore the electric field is weak. Strong electric fields are found in the sheath regions, where the voltage drops are concentrated. The only charged particles are Ar<sup>+</sup> ions and electrons [Fig. 3.1(b)]. As expected, the ion density profile is constant throughout the RF cycle, since the ions cannot follow the rapidly fluctuating electric field, whereas the electron density profile varies largely in the sheaths. At  $\omega t = \pi/2$  the electron density in the left sheath is approximately equal to the Ar<sup>+</sup> density and has a more or less constant value. However, the electron density in the right sheath decreases rapidly to zero towards the grounded electrode at this time in the RF cycle. As the cycle advances, the electrons move to the right sheath and the density profile at  $\omega t = 3\pi/2$  is a mirror image of that at phase  $\pi/2$ . At phases 0 and  $\pi$  the electron density decreases to zero towards both electrodes but less rapidly than at phases  $3\pi/2$  and  $\pi/2$ , respectively. The electron density profile at  $\omega t = \pi$  is not shown in the picture because it is very similar to the profile at  $\omega t = 0$ . The movement of the electrons causes the modulation of the sheath width.

The average electron energy is around 3 eV in the bulk plasma [see Fig. 3.1(c)] and it reaches its maximum of 4 eV in the sheath. To investigate the role of secondary electron emission on the discharge properties simulations were carried out with a secondary electron emission coefficient of 0.03. The results are not presented here since they confirm that the discharge is indeed in  $\alpha$ -regime.

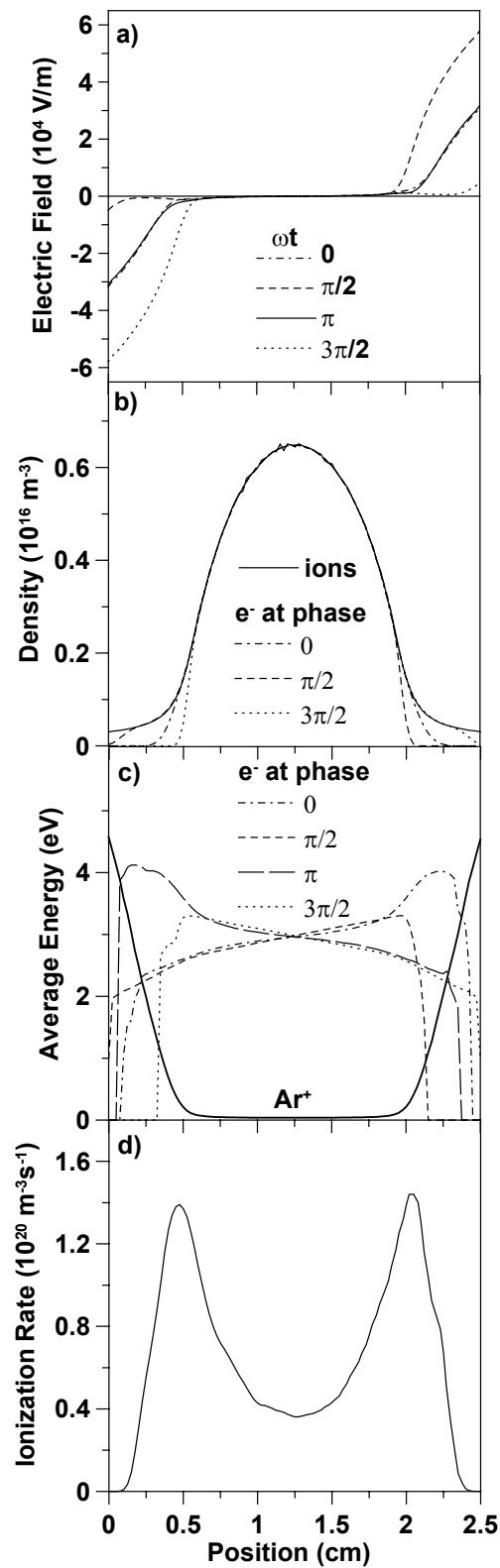


FIGURE 3.1 Electric field distribution at four phases (a), electron and  $Ar^+$  ion density distributions (b), average electron and  $Ar^+$  ion energies (c), and time-averaged ionization rate (d) in a pure Ar discharge at  $p = 200$  mTorr and  $\gamma = 0$ .

In this regime the effect of secondary electron emission on most plasma parameters is rather small except for the average electron energy in the sheath where high electron energy peaks are observed, in agreement with previous investigations of an Ar discharge (cf. Ref. 36). The Ar<sup>+</sup> ion energy is around 0.04 eV in the bulk plasma. The argon ions are accelerated towards the electrodes in the sheath and therefore the ions have their average maximum energy close to the electrodes, which is about 4.5 eV in this simulation.

The time-averaged ionization rate has maxima at the bulk-sheath interface [Fig. 3.1(d)]. The simulation results for the ionization rate at different phases of the RF cycle, which are not presented here, show that the right peak appears at phase 0 and the left one at phase  $\pi$ , i.e. the maxima of the ionization collisions do not coincide with the non-zero values of the electron density in the sheaths (see above). The ionization peaks appear because of the energy gained by the electrons during their acceleration away from the electrodes into the discharge [cf. the maximum values of the electron energy at phase 0 and  $\pi$  in Fig. 3.1(c)].

All the characteristic features of the Ar discharge discussed here are in agreement with those available in the literature (e.g. see Refs. 1, 38-41).

### 3.3.2 Pure CF<sub>4</sub> discharge

The electric field distribution at four phases (a), the charged particle density distributions (b), the average electron and ion energies (c) and the time-averaged reaction rates (d) in a pure CF<sub>4</sub> discharge are shown in Fig. 3.2. The structure of the discharge is typically electronegative and is characterized by the presence of negative ions (F<sup>-</sup> and CF<sub>3</sub><sup>-</sup>), which are the dominant negative charged species. Indeed, the electron density in the bulk is about 50 times less than the density of the major negative ion F<sup>-</sup> [see Fig. 3.2(b)]. Unlike in the Ar discharge the electric field in the bulk plasma is substantial (order of 1000 V/m) [Fig. 3.2(a) and Fig. 3.3] since the potential is not constant. Another difference with the electropositive discharge is the appearance of the double layer structure (i.e. the local maxima or minima of the electric field) near the bulk-sheath interface, which is related to the density distribution. Moreover, a field reversal is observed at the right bulk-sheath interface at phase 0 and at the left bulk-sheath interface at phase  $\pi$ , respectively (see Fig. 3.3). The ion density profiles [Fig. 3.2(b)] are constant in time throughout the RF cycle, like in the Ar discharge. Since the diffusive flux of the negative ions is very low and the electric field is always directed outwards, the negative ions are confined in the bulk plasma and are almost absent in the sheath. In the sheath mainly positive ions and electrons are found. The electrons move toward one of the electrodes depending on the phase of the applied voltage.

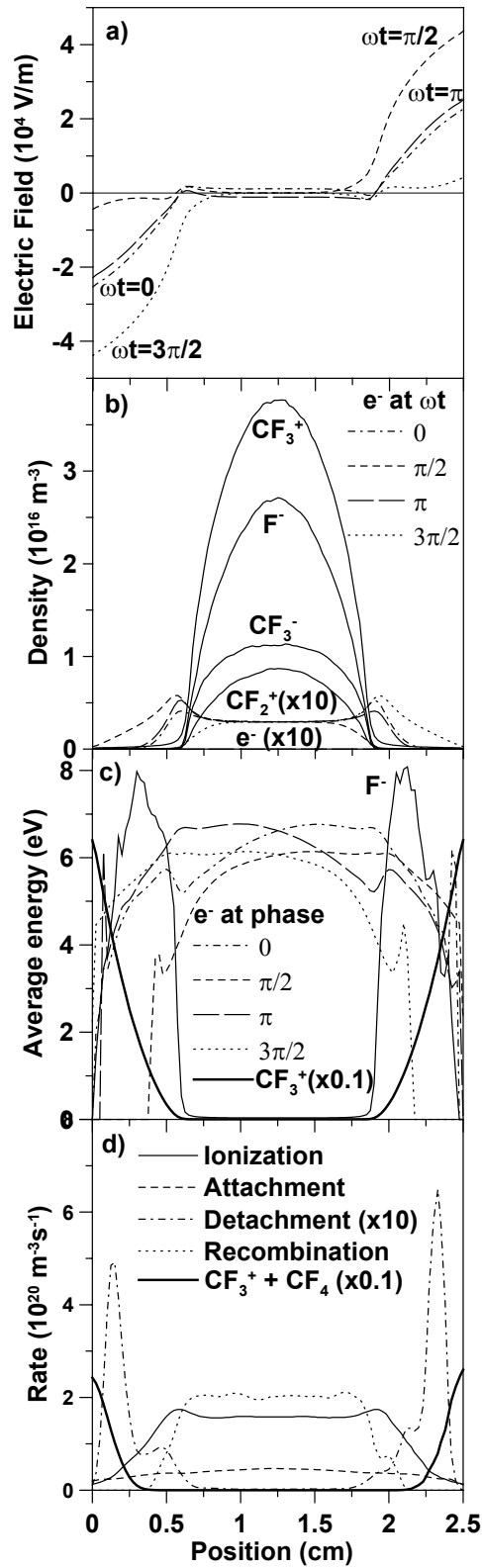


FIGURE 3.2. Electric field distribution at four phases (a), charged particle density distributions (b), average electron and ion energies (c) and the time-averaged reaction rates (d) in a pure CF<sub>4</sub> discharge at  $p = 200$  mTorr and  $\gamma = 0$ .

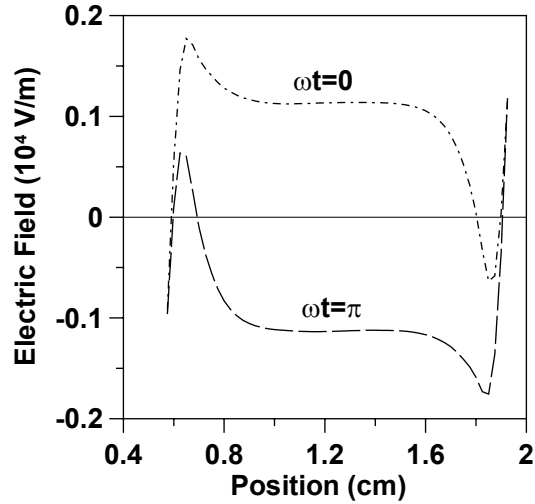


FIGURE 3.3. Electric field distribution at phases 0 and  $\pi$  in the bulk plasma in a pure CF<sub>4</sub> discharge at  $p = 200$  mTorr and  $\gamma = 0$ .

Their movement affects the local fields, which are developed by the differences of positive and negative ion concentration near the electrodes, and they cause the electrons to pile up in the bulk-sheath region. Hence, peaks in the electron density appear at the bulk-sheath interface, which cannot be observed in electropositive discharges.

Because of the non-zero bulk electric field the average electron energy in the bulk plasma is higher than in a pure Ar discharge and its value is around 6 eV [Fig. 3.2(c)]. Like in the Ar discharge high electron energy peaks are not observed in the sheath since the secondary electron emission coefficient is set to 0. All ions have constant average energy around 0.04 eV in the bulk plasma, i.e., the ion temperature is close to the gas temperature, because of the frequent collisions with the neutral molecules [1]. The positive CF<sub>3</sub><sup>+</sup> ions gain energy in the sheath like the argon ions and their energy at the electrodes has a maximum value of around 65 eV [Fig. 3.2(c)]. As described above, few negative ions exist in the sheath. Negative ions are produced by electron attachment; the attachment rate is shown in Fig. 3.2(d). They are accelerated toward the bulk plasma and gain energy in the sheath. Their average energy reaches a maximum of 8 eV [see Fig. 3.2(c)]. More details about the movement of the negative ions in the sheath and the energy they gain are presented in Chapter 8. The average energy of the CF<sub>3</sub><sup>-</sup> ions is not given because its profile and value are similar to that of the F<sup>-</sup> ions.

Time-averaged rates for ionization, electron attachment, electron detachment, positive-negative ion recombination and CF<sub>3</sub><sup>+</sup> - CF<sub>4</sub> reactive collisions

are shown in Fig. 3.2 (d). The electron attachment, electron detachment and ion-ion recombination are represented as the sum of all corresponding reaction collisions. Ionization and electron attachment occur anywhere in the discharge space [Fig. 3.2 (d)]. The electron attachment rate is lower than the ionization rate because of the smaller cross-section. The electron detachment occurs in the sheath where the negative ion energy is high enough (see the threshold energies for the detachment processes in Tables B.2 and B.3 in the Appendix B). Similarly, the CF<sub>3</sub><sup>+</sup> - CF<sub>4</sub> reaction rate, which is again taken as the sum of all reactions, shows that the reactive collisions take place in the sheath. The positive-negative ion recombination is observed only in the bulk plasma and is the major loss process of negative ions.

The simulation results for the electric field, the particle densities and energies, and collision rates are in reasonable agreement with the simulation results of Denpoh and Nanbu [57] except for the ion density profiles in the bulk plasma, which are parabolic in the present calculation. Concave ion density profiles are observed in other simulations of a CF<sub>4</sub> discharge [35, 37] as well as in other electronegative discharges [37] when ionization exceeds ion-ion recombination in the plasma-sheath interface. A possible explanation for the present results is that this simulation does not follow all CF<sub>x</sub> positive ions because of their much lower density compared to the CF<sub>3</sub><sup>+</sup> density. This simplification is done because the aim of the present model is actually to study the discharge properties in Ar/CF<sub>4</sub> mixtures. Moreover, the concentration of CF<sub>4</sub> does not exceed 10% for etching purposes in practice, which suggests that the effect of all positive CF<sub>x</sub> ions, except for CF<sub>3</sub><sup>+</sup>, on the plasma parameters will be negligible in such mixtures (see the results below).

Simulations of the CF<sub>4</sub> discharge at the same operating condition and considering also CF<sub>2</sub><sup>+</sup> ions together with electrons, CF<sub>3</sub><sup>+</sup>, F<sup>-</sup> and CF<sub>3</sub><sup>-</sup> were carried out in order to calculate the CF<sub>2</sub><sup>+</sup> density and compare it with the density of the major positive CF<sub>3</sub><sup>+</sup> ion. The ionization process with the corresponding cross-section data taken from Ref. 80 is included



The threshold energy is 21 eV and it is higher than the threshold energy of 16 eV of the ionization process of CF<sub>3</sub><sup>+</sup>, presented in Table 2.1 in Chapter 2



In addition, the cross-section of (3.1) is 1 order of magnitude lower than the cross-section of (3.2). Both cross-sections are presented in Fig B.1 in the Appendix B. This explains the much lower density of CF<sub>2</sub><sup>+</sup> ( $9 \times 10^{14} \text{ m}^{-3}$ ) in comparison with that of CF<sub>3</sub><sup>+</sup> ( $3.8 \times 10^{16} \text{ m}^{-3}$ ) calculated in the simulation [see Fig. 3.2 (b)]. The CF<sub>2</sub><sup>+</sup> - CF<sub>4</sub> collisions are considered by means of the ion-molecule collision model for

endothermic reactions. The reactive collisions and the corresponding threshold energies are presented in Table B.4 in the Appendix B.

### 3.3.3 Ar/CF<sub>4</sub> mixtures

Figures 3.4, 3.5 and 3.6 show the structure of the discharge in an Ar/CF<sub>4</sub> mixture for a ratio of 0.9/0.1, 0.5/0.5 and 0.1/0.9, respectively. The electric field (a) and electron density (b) at four times in the RF cycle, the time-averaged ion densities (c), and the average electron (at four phases), Ar<sup>+</sup> and F<sup>-</sup> ion energies (d) are presented for each of the three gas compositions. The profile of the F<sup>-</sup> energy is not symmetric in this and next figures because of bad statistics. The negative ions are confined in the bulk plasma as discussed above. Few negative ions created in electron attachment collisions are present in the sheaths. The average energy of the CF<sub>3</sub><sup>+</sup> ions is not presented since it has a similar profile and similar values as in a pure CF<sub>4</sub> discharge [see Fig. 3.2(c)]. The average energy of the CF<sub>3</sub><sup>-</sup> ions is not given either, because its profile and value are similar to that of the F<sup>-</sup> ions. Based on the results for pure Ar and CF<sub>4</sub> discharges, described above, a comparative analysis of the discharge structure in a mixture of Ar and CF<sub>4</sub> is carried out here.

At high concentration of Ar (90%) the structure of the discharge is similar to that of an electropositive discharge (Fig. 3.4). The electric field distribution resembles the one of a pure Ar discharge [cf. Fig. 3.1(a) and Fig. 3.4(a)]. The major positive ions are Ar<sup>+</sup> ions; the density of CF<sub>3</sub><sup>+</sup> in the center of the bulk plasma is about two orders of magnitude lower than that of Ar<sup>+</sup> [Fig. 3.4(c)]. A similar ion composition was measured in an Ar/CF<sub>4</sub> ICP [92 and 93], although quantitative comparison is difficult to be made because of the differences in the operating conditions of capacitively and inductively coupled discharges.

Some features of electronegative discharges begin to appear in Fig. 3.4. The dominant negative carriers are not the electrons, but the negative ions (F<sup>-</sup> and to a lesser extent CF<sub>3</sub><sup>-</sup>). In the bulk center the F<sup>-</sup> ion density has a value of  $1.4 \times 10^{16} \text{ m}^{-3}$ , whereas the electron density is only  $2.1 \times 10^{15} \text{ m}^{-3}$  [cf. Fig. 3.4(b) and Fig. 3.4(c)]. The rapid decrease in the electron density with the addition of even small amount of CF<sub>4</sub> was observed also in an Ar/CF<sub>4</sub> ICP [92]. The electron density profile is quite flat in the bulk plasma and it resembles the one of a pure CF<sub>4</sub> discharge, but the peaks at the bulk-sheath interface are not yet formed. Experimental results at CF<sub>4</sub> concentrations up to 10% also revealed a flat electron density profile in the bulk plasma [16].

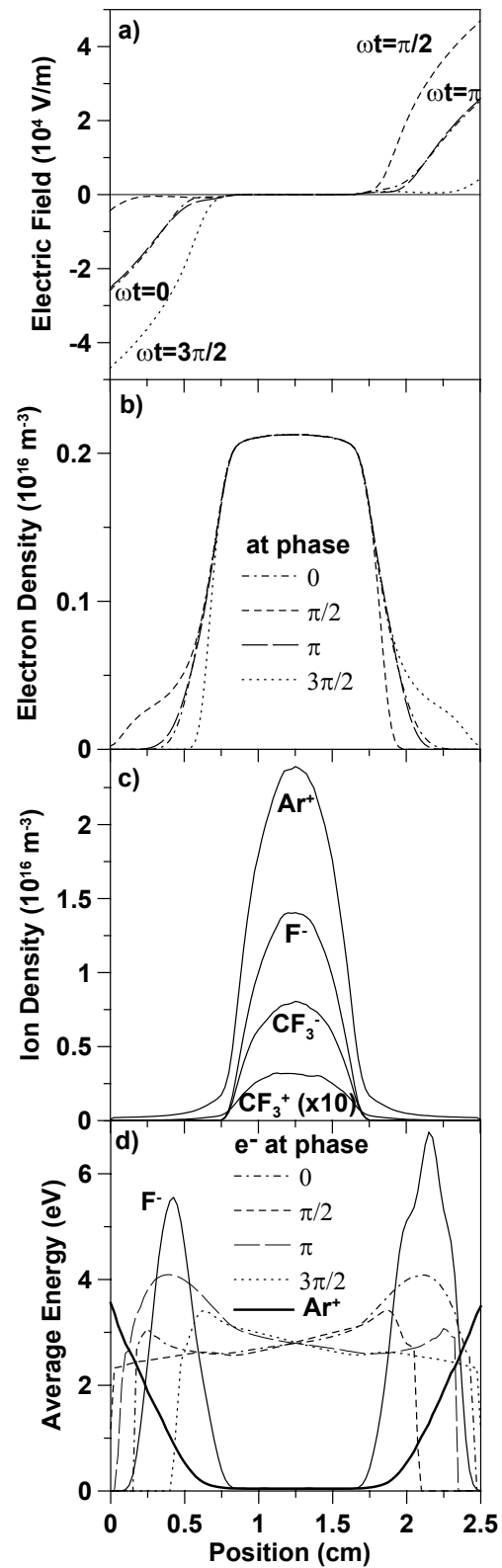


FIGURE 3.4 Electric field (a) and electron density (b) at four times in the RF cycle, ion densities (c), and average electron, Ar<sup>+</sup> and F<sup>-</sup> ion energies (d) in an Ar/CF<sub>4</sub> 0.9/0.1 discharge at  $p = 200$  mTorr and  $\gamma = 0$ .

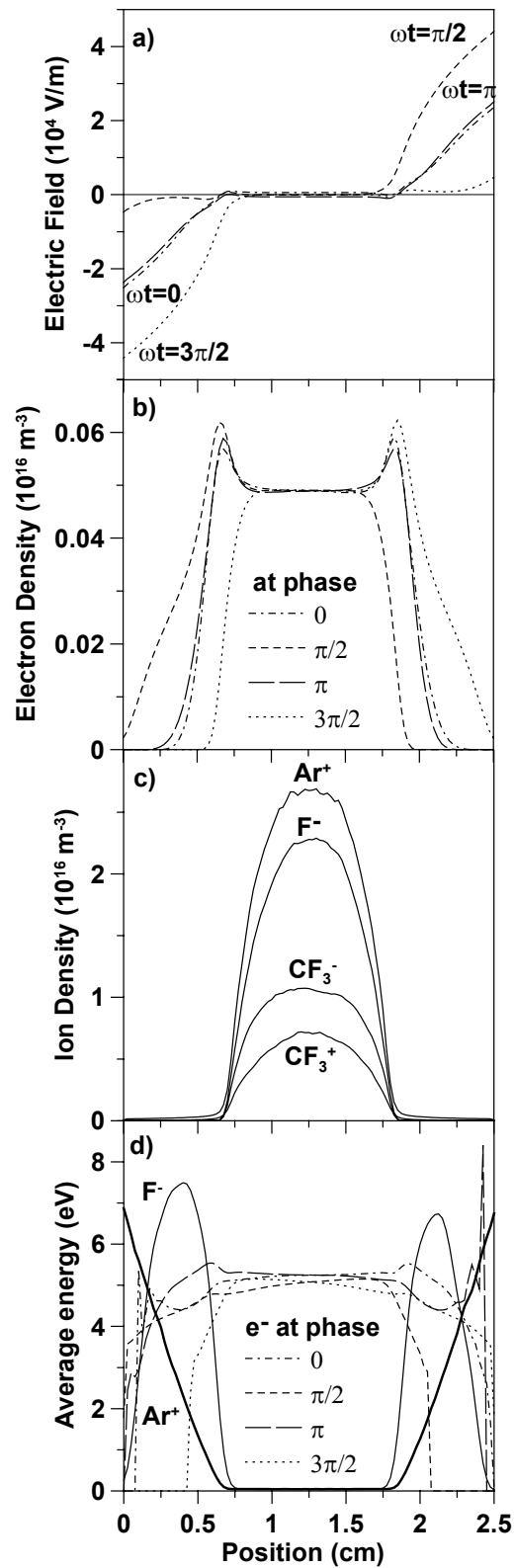


FIGURE 3.5 Electric field (a) and electron density (b) at four times in the RF cycle, ion densities (c), and average electron, Ar<sup>+</sup> and F<sup>-</sup> ion energies (d) in an Ar/CF<sub>4</sub> (0.5/0.5) discharge at  $p = 200$  mTorr and  $\gamma = 0$ .

The average electron energy is around 3 eV in the bulk plasma [Fig. 3.4(d)] and its profile is similar to the one of a pure Ar discharge. The Ar<sup>+</sup> ions have a maximum energy of about 3.5 eV at the electrodes. The F<sup>-</sup> ions reach a maximum energy of 7 eV in the sheath. From the calculated reaction rates (not shown here) it is clear that the ion-CF<sub>4</sub> reactive collisions play no significant role in sustaining the discharge, because of the low concentration of CF<sub>4</sub> molecules.

At equal concentrations of Ar and CF<sub>4</sub> gas (Fig. 3.5) the discharge exhibits more electronegative features. The double layer structure in the electric field and the maxima in the electron density appear [Fig. 3.5(a) and Fig. 3.5(b)], as well as the electric field reversal at phases 0 and  $\pi$ . The electron density is about  $5 \times 10^{14} \text{ m}^{-3}$  in the bulk, i.e., four times lower than for the Ar/CF<sub>4</sub> discharge at a ratio of 0.9/0.1 gas mixture. At the same time, the F<sup>-</sup> ion density increases up to  $2.4 \times 10^{16} \text{ m}^{-3}$  in the bulk. Similarly, the CF<sub>3</sub><sup>-</sup> ion density is higher compared to the 0.9/0.1 gas mixture. The Ar<sup>+</sup> ion is still the major positive ion [Fig. 3.5(c)] because of the larger ionization cross-section of argon compared to that of CF<sub>4</sub>. However, the density of the CF<sub>3</sub><sup>+</sup> ions is now only less than a factor of 4 lower than the Ar<sup>+</sup> ion density. Its value in the center is  $7 \times 10^{15} \text{ m}^{-3}$  [compared to only  $3 \times 10^{14} \text{ m}^{-3}$  at the 0.9/0.1 gas mixture in Fig. 3.4(c)], as is qualitatively expected because of the higher concentration of CF<sub>4</sub> molecules. The average electron energy is almost constant in the bulk plasma at around 5 eV [Fig. 3.5(d)]. The Ar<sup>+</sup> ions have an average energy of 0.04 eV in the bulk plasma, and they reach a maximum average energy of 7 eV at the electrodes, which is two times higher than in the 0.9/0.1 Ar/CF<sub>4</sub> discharge. The average F<sup>-</sup> ion energy is about 0.035 eV in the bulk plasma and it has a maximum value of 7 eV in the sheath.

At high concentration of CF<sub>4</sub> (90%) the discharge structure is definitely electronegative (Fig. 3.6). The double layer and the electron density maxima are well established [Fig. 3.6(a) and Fig. 3.6(b)]. A field reversal is observed at phases 0 and  $\pi$ . The major positive ion is now CF<sub>3</sub><sup>+</sup> [Fig. 3.6(c)]. Indeed, the CF<sub>3</sub><sup>+</sup> density in the bulk plasma has a value of  $3 \times 10^{16} \text{ m}^{-3}$ , whereas the Ar<sup>+</sup> density is only  $7 \times 10^{15} \text{ m}^{-3}$ . A similar dependence of the number densities of the positive ions with the CF<sub>4</sub> content was measured in an inductively coupled Ar/CF<sub>4</sub> discharge [93]. The F<sup>-</sup> have a similar, but somewhat lower density than the CF<sub>3</sub><sup>+</sup> and the CF<sub>3</sub><sup>-</sup> have a similar, but somewhat higher density than the Ar<sup>+</sup>. The electron density is  $3 \times 10^{14} \text{ m}^{-3}$  in the bulk plasma and reaches maxima of  $6 \times 10^{14} \text{ m}^{-3}$  at the bulk-sheath interface. The average electron energy in the bulk is about 6 eV like in a pure CF<sub>4</sub> discharge [cf. Fig. 3.2(c) and Fig. 3.6(d)].

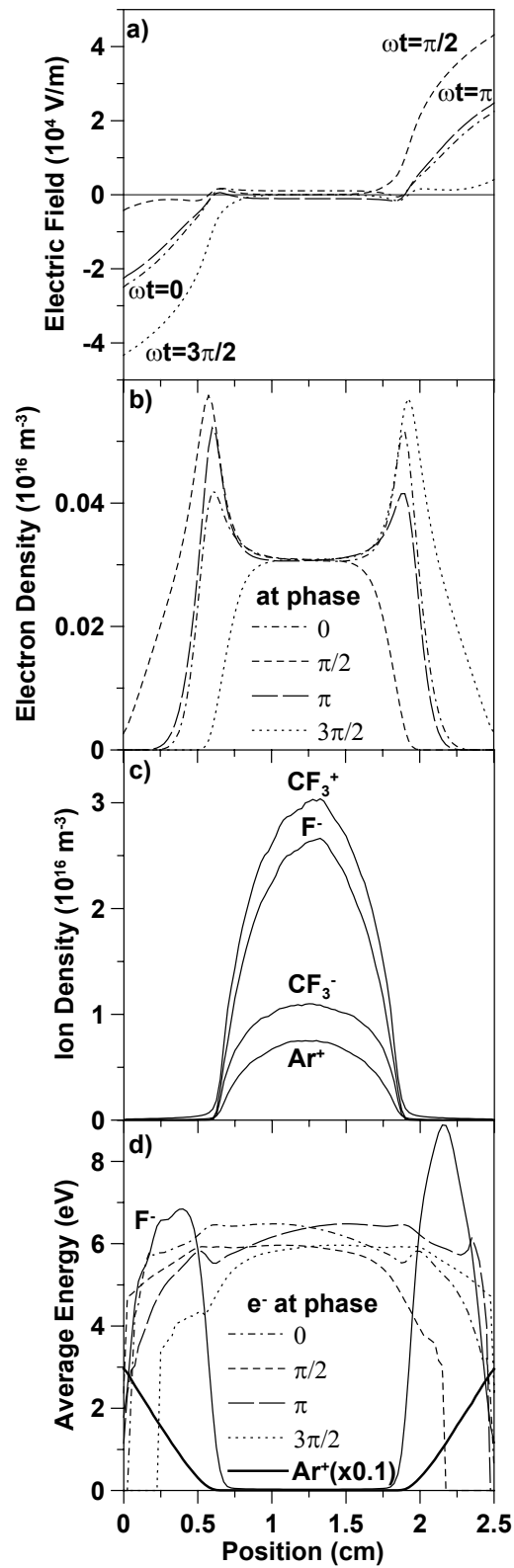


FIGURE 3.6 Electric field (a) and electron density (b) at four times in the RF cycle, ion densities (c), and average electron, Ar<sup>+</sup> and F<sup>-</sup> ion energies (d) in an Ar/CF<sub>4</sub> (0.1/0.9) discharge at  $p = 200$  mTorr and  $\gamma = 0$ .

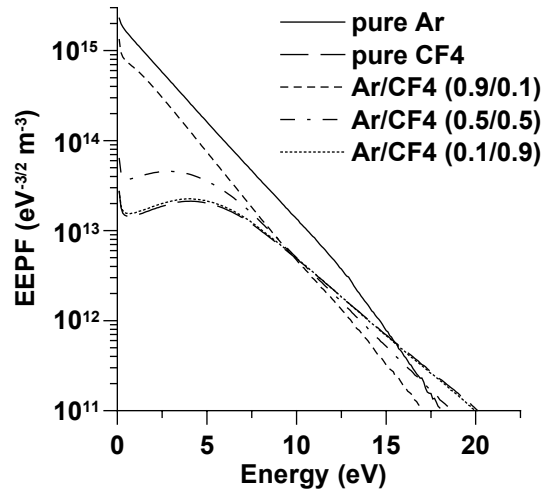


FIGURE 3.7 The EPPF for 5 simulated gas mixtures at  $p = 200$  mTorr and  $\gamma = 0$ .

The maximum value of the average Ar<sup>+</sup> ion energy is 32 eV. The increase of the Ar<sup>+</sup> ion energy in the sheath with decreasing Ar concentration shows that the Ar<sup>+</sup> - Ar collisions are the main energy loss term for the Ar<sup>+</sup> ions. The average F<sup>-</sup> ion energy reaches again its maximum in the sheath with a value of around 8 eV.

The electron energy probability function (EPPF)  $f_e(\varepsilon)$  ( $= F_e(\varepsilon)\varepsilon^{-1/2}$ ) at the center of the discharge is shown in Fig. 3.7 for all simulated gas mixtures. The calculated EPPF in a pure Ar discharge confirms the previous simulated and measured results [56, 96]. The EPPF in a mixture of Ar and CF<sub>4</sub> changes its profile from Maxwellian-like to Druyvesteyn-like with the transition from electropositive to electronegative behavior of the discharge. The high-energy tail in the latter case is due to the strong electric field in the bulk (up to 1000 V/m) (see Fig. 3.3) in comparison with the weak electric field (up to 10 V/m) in electropositive discharges. Detailed discussion over EEDF  $F_e(\varepsilon)$  in electropositive and electronegative discharges can be found in Ref. 56. The calculated EPPF in a pure CF<sub>4</sub> discharge is in good agreement with that presented by Denpoh and Nanbu in Ref. 58 at the same operating conditions.

Finally, to compare the simulation results with the experimental data the developed model is carried out at operating conditions close to those presented in Ref. 16, i.e. for a distance between the electrodes of 6 cm, a pressure ranging from 30 to 100 mTorr and at CF<sub>4</sub> contents from 2% to 10%. The applied voltage amplitude is 240 V. The calculated and measured results for the electronegativity  $\alpha = n_n/n_e$ , where  $n_n$  and  $n_e$  denote the negative ion and electron densities,

respectively, are presented in Fig. 3.8. Both measured and calculated electronegativities increase with the CF<sub>4</sub> content. This behavior is as expected since the attachment probability becomes higher with the CF<sub>4</sub> content. However, the simulations cannot yet predict the increase of the measured electronegativity with pressure. Indeed, the probabilities of all kinds of electron-neutral collisions are proportional to the neutral gas density and consequently to the pressure. As a result the densities of all charged particles rise. Therefore, the probabilities of all production and loss processes in the model increase with pressure but the ratios of negative ions to electrons stay more or less constant at least in the investigated pressure range.

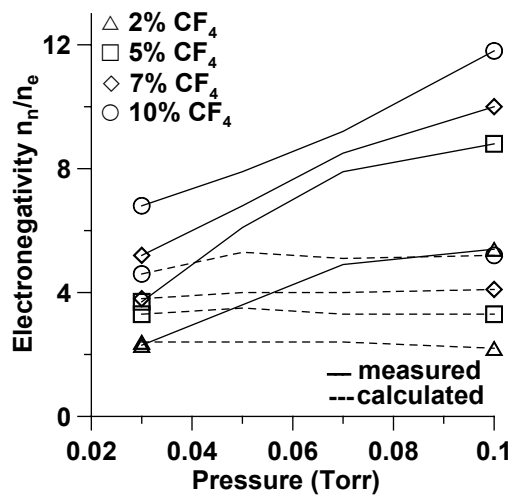


FIGURE 3.8 The measured (solid lines) and calculated (broken lines) electronegativities  $\alpha = n_n / n_e$  in an Ar/CF<sub>4</sub> discharge at a concentration of CF<sub>4</sub> up to 10% over the pressure range from 30 to 100 mTorr.

### 3.4 Summary

A one-dimensional PIC/MC model has been developed to describe the structure of a cc RF discharge in a gas mixture of Ar and CF<sub>4</sub>. The model follows five charged species: electrons, Ar<sup>+</sup>, CF<sub>3</sub><sup>+</sup>, F<sup>-</sup> and CF<sub>3</sub><sup>-</sup>. The collisions treated by the MCC model include electron - Ar collisions, electron - CF<sub>4</sub> collisions, various kinds of collisions of CF<sub>3</sub><sup>+</sup>, F<sup>-</sup>, CF<sub>3</sub><sup>-</sup> or Ar<sup>+</sup> with Ar or CF<sub>4</sub>, and positive-negative ion recombination.

The simulations are performed for 0.9/0.1, 0.5/0.5 and 0.1/0.9 ratios of the Ar/CF<sub>4</sub> mixture, and for pure Ar and pure CF<sub>4</sub> discharges. All calculations are

carried out at the following operating conditions: a distance between the electrodes of 2.5 cm,  $V = 200$  V,  $f = 13.56$  MHz,  $p = 200$  mTorr, and  $\gamma = 0$ .

First of all, the structures of the pure electropositive Ar discharge and of the pure electronegative CF<sub>4</sub> discharge are clarified. Then the calculated electric field, charged particle density distributions and their average energies for Ar/CF<sub>4</sub> mixtures at different molar ratios are presented and discussed, and the transition from an electropositive to an electronegative discharge is illustrated. It is observed that at high concentration of Ar (90%) the structure of the discharge is similar to that of the electropositive discharge, although some features of electronegative discharges, such as the abundance of negative ions, begin to appear. The Ar<sup>+</sup> density exceeds the CF<sub>3</sub><sup>+</sup> density by about two orders of magnitude. At equal concentration of Ar and CF<sub>4</sub> the discharge shows more electronegative features. The double layer structure and the electron density maxima in the sheath, which are representative for an electronegative discharge, appear. Electric field reversal is observed as well. However, the major positive ion is still Ar<sup>+</sup>. At high CF<sub>4</sub> concentration (90%) the discharge behaves as a typical electronegative discharge and CF<sub>3</sub><sup>+</sup> is the major positive ion. The results show that the F<sup>-</sup> ions are the dominant negatively charged species at all Ar/CF<sub>4</sub> ratios investigated.

Finally, the calculated electronegativities in an Ar/CF<sub>4</sub> discharge at a concentration of CF<sub>4</sub> up to 10% over the pressure range from 30 to 100 mTorr are compared with measured data and reasonable agreement is reached.

## **Chapter 4**

# **STUDY OF AR/CF<sub>4</sub>/N<sub>2</sub> DISCHARGES IN SINGLE- AND DUAL-FREQUENCY ETCHING REACTORS**

### **4.1 Introduction**

Conventional capacitively coupled (cc) reactors powered by 13.56 MHz RF sources meet many plasma-processing requirements. However, the scaling evolution of semiconductor devices needs more and more accurate transfer patterns with minimum damage on the substrate, which can be achieved by precise control of both the ion bombardment energy and the ion flux. Single-frequency systems face difficulties providing an independent control of ion energy. For that purpose dual-frequency systems have been introduced and studied [e.g. Refs. 14, 15, 17-19, 34, 42, 43, and 63]. The dual RF excitation set-up allows the plasma density to be determined by one high-frequency (HF), e.g., 13.56 or 27 MHz or very high-frequency (VHF) source, e.g., 100 MHz, while the substrate self-bias voltage is controlled by the secondary low-frequency (LF), e.g. in the order of 1 MHz [Refs. 17-19, 34, 42, 43, and 63]. In addition, the LF - (V)HF scheme provides a significantly wider ion bombardment energy range in comparison with a single-HF configuration. Therefore, the study of this plasma-processing device is of great importance for further improvement of its performance.

In the early 90s Goto *et al.* [14, 15] introduced the cc HF - VHF (13.56–100 MHz) set-up and demonstrated its advantages in low ion energy etching. The discharge was maintained between two electrodes, one of them was driven by a VHF power supply and the other biased by HF. The wafer was placed on the biased electrode. Later on, other dual-frequency schemes, like LF - (V)HF and commensurate frequencies, have been applied [Refs. 17-19, 34, 42, and 63]. Tsai *et al.* [17] experimentally investigated etching of SiO<sub>2</sub> structures in a dual-frequency (27/2 MHz) Ar/CO/CF<sub>x</sub> discharge. The dependence of plasma parameters on the substrate frequency and power has also been numerically studied by PIC [63] and

fluid [34] models. It was shown that the plasma density is predominantly determined by the primary power source while self-bias and ion bombardment energy are determined by the substrate power source. The experimental study of Ar and Ar/CF<sub>4</sub> plasma structures in LF - (V)HF reactors demonstrated that LF biasing and HF plasma production could be functionally separated by increasing the sustaining frequency from 13.56 MHz (HF) to 100 MHz (VHF) [18, 19]. However, if the source frequencies are close to each other (e.g. 6.78 and 13.56 MHz) the nonlinear interaction effects can be strong and the resulting plasma characteristics cannot be independently controlled [42]. Recently, an Ar/CF<sub>4</sub> discharge has been numerically investigated in a pulsed LF - VHF reactor [43]. Reduction of the local charging by allowing negative ions to reach the electrodes during the off phase has been discussed. The simulation results of the present work show that the same effect can be achieved by applying a different dual-frequency configuration. In the present etching reactor the two power supplies are both applied to one of the electrodes and the other electrode is grounded. The wafer is placed on the driven electrode. The purpose of the present chapter is to study numerically the discharge structure and properties, and to compare the simulation results of the plasma parameters in a conventional cc single-frequency (13.56 MHz) and dual-frequency (27 + 2 MHz) reactor by means of a one-dimensional PIC/MCC method. The influence of the second LF on the discharge parameters, such as charged particle densities and energy distributions is discussed.

In the previous chapter the plasma structure and parameters in electropositive Ar, in electronegative CF<sub>4</sub>, and in Ar/CF<sub>4</sub> discharges at different molar ratios are clarified [59]. A rapid decrease in electron density is observed with the addition of even a small amount of CF<sub>4</sub> to Ar, i.e. the dominant negative charge carriers are the negative ions, and this profoundly influences the sheath dynamics. In the present chapter the model is extended to examine the discharge structure in a mixture of Ar, CF<sub>4</sub> and N<sub>2</sub>, which is a feedstock gas for etching in an industrial cc dual-frequency reactor.

In Sec. 4.2 the input parameters are given. In Sec. 4.3 the results of the simulation, i.e. the electric field and potential distributions, charged particle densities, and energy distributions, are presented and discussed. Finally, a summary is given in Sec. 4.4.

## 4.2 Input data

The numerical model used in this investigation is described in detail in Chapter 2. The charged species taken into account in the model are: electrons, Ar<sup>+</sup>, N<sub>2</sub><sup>+</sup>, CF<sub>3</sub><sup>+</sup>, F<sup>-</sup>, and CF<sub>3</sub><sup>-</sup>. The collisions treated by the MCC method include electron - neutral (Ar, CF<sub>4</sub>, and N<sub>2</sub>) collisions, various kinds of collisions of Ar<sup>+</sup>, CF<sub>3</sub><sup>+</sup>, F<sup>-</sup>, CF<sub>3</sub><sup>-</sup>,

or N<sub>2</sub><sup>+</sup> with neutrals, positive - negative ion recombination, and electron - ion recombination.

A schematic diagram of the symmetric dual-frequency cc reactor considered in this study is shown in Fig. 4.1. The plasma is sustained between two parallel plates, each 20 cm in diameter and separated from each other by 2 cm. One of the electrodes is driven by a single- (13.56 MHz) or dual-frequency (27 + 2 MHz) power source. The applied voltage in the dual-frequency reactor is given by Eq. (1.1), presented in Chapter 1. The amplitude of the applied voltage is 700 V for both frequencies. The other electrode is grounded. The simulation is carried out at a pressure of 30 mTorr.

The calculations are performed for an Ar/CF<sub>4</sub>/N<sub>2</sub> mixture at a ratio of 0.8/0.1/0.1. In Figs. 4.2 – 4.5 the RF powered electrode is at position 0 and the grounded electrode is at position 2 cm. The gas temperature is set to 300 K. The simulation grid is uniform and it consists of 100 cells. The electron time step is  $3.7 \times 10^{-11}$  s. To speed up the calculation, the ion time step is set to be 25 times longer than the electron time step. The choice of the grid spacing and the time steps is defined by the accuracy criteria for PIC/MCC codes with explicit mover (see Sec.2.9).

Secondary electron emission is included here because the RF discharge is assumed to be in the  $\gamma$ -regime at the conditions under study [38, 50].

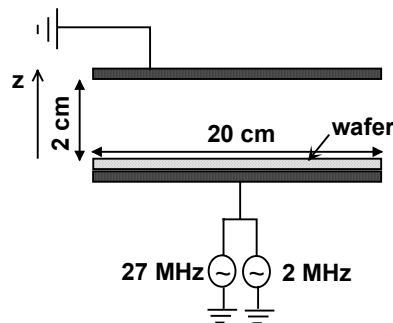


FIGURE 4.1. Schematic diagram of the symmetric dual-frequency etching reactor.

### 4.3 Results and discussion

Typical results of this model are electron and ion densities, fluxes and energy distributions, collision rates and electric field and potential distributions. The calculated discharge quantities in the dual-frequency regime are saved at different

phases in 2 LF and 27 HF cycles since one LF cycle does not contain an integer number of HF cycles. The discharge quantities in the single-frequency regime are saved at different phases in one RF cycle.

### 4.3.1 Potential and electric field distributions

Figs. 4.2 and 4.3 present the simulation results of the potential and electric field distribution in the single- and dual-frequency regime, respectively. The results are given as a function of distance from the driven electrode and as a function of time in one HF (13.56 MHz) cycle in the conventional cc RF reactor, and in two LF (2 MHz) cycles in the dual-frequency (27 + 2 MHz) reactor. The behavior as a function of time and position looks the same for both frequency regimes, but the difference is found in the absolute values. Indeed, the maximum and minimum values of the potential at the driven electrode in the dual-frequency regime are almost twice as large as in the one frequency regime, for the same applied voltage amplitude (700 V), and consequently the electric field in the sheaths is also much stronger [cf. Figs. 4.2(a), (b) and 4.3(a), (b)].

The discharge structure is electronegative in both investigated schemes. A close look at the electric field in the bulk plasma [Figs. 4.2(c) and 4.3(c)] shows the appearance of double-layer structures (i.e. the local maxima or minima of the electric field) and field reversal near the bulk – sheath interface. (cf. with the results for a pure CF<sub>4</sub> discharge, presented in Chapter 3).

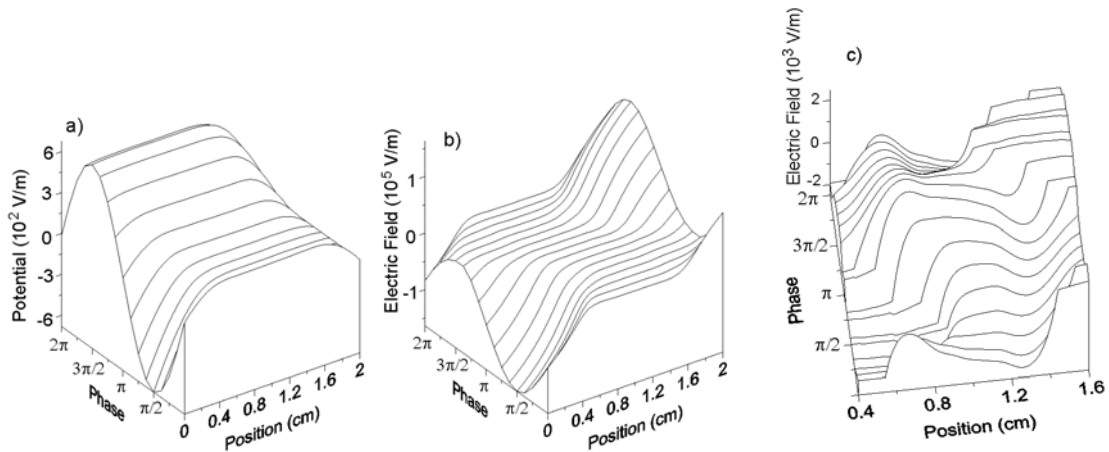


FIGURE 4.2. Potential distribution (a) and electric field distributions in the entire discharge (b), and in the bulk region (c), as a function of time in the HF (13.56 MHz) cycle in an Ar/CF<sub>4</sub>/N<sub>2</sub> discharge at  $p = 30$  mTorr and applied voltage amplitude  $V = 700$  V in the conventional cc RF reactor.

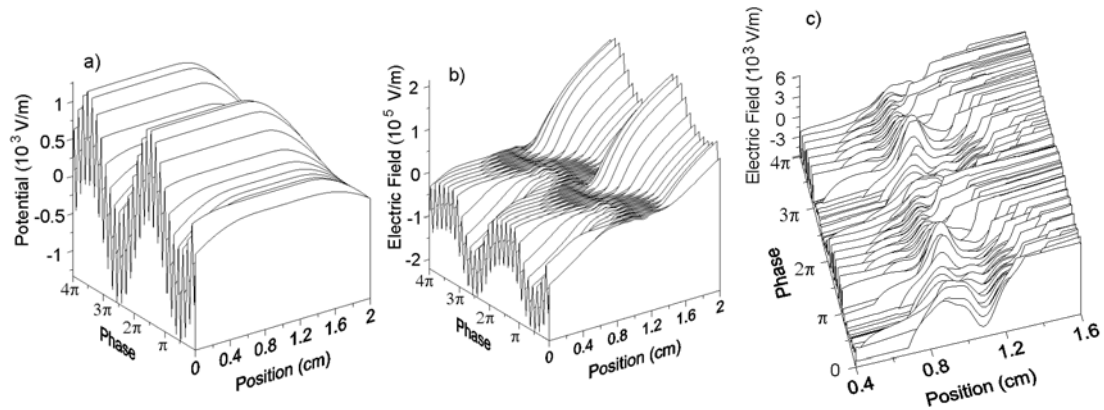


FIGURE 4.3. Potential distribution (a) and electric field distributions in the entire discharge (b), and in the bulk region (c), as a function of time in two LF (2 MHz) cycles in an Ar/CF<sub>4</sub>/N<sub>2</sub> discharge at  $p = 30$  mTorr and applied voltage amplitude  $V = 700$  V in the dual-frequency (27 + 2 MHz) cc RF reactor.

The electric field in the bulk plasma is substantial [up to 2000 V/m and 6000 V/m, Figs. 4.2(c) and 4.3(c), respectively] since the potential in the bulk is not constant in space. The sheaths are wide due to the narrow gap and the strong electric fields. The electric field distribution is related to the charged particle density distributions.

### 4.3.2 Electron density distribution

The electron density distribution in both frequency regimes is shown in Fig. 4.4. In the single-frequency reactor [Fig. 4.4(a)] the electrons move toward one of the electrodes depending on the phase of the applied voltage, i.e., toward the grounded electrode at phase  $\pi/2$ , and toward the powered electrode at phase  $3\pi/2$ . The electron density profile in the bulk is significantly different from the flat profile observed in computational and experimental investigations of an Ar/CF<sub>4</sub> discharge at 10% concentration of CF<sub>4</sub>, applied voltage amplitude 200 or 240 V and at a pressure range from 30 to 200 mTorr [16, 59]. Indeed, peaks although not very prominent, appear at each bulk-sheath interface and in the bulk [Fig. 4.4(a)]. A low energy group of electrons is formed, which pile up in the bulk plasma, because of the strong electric field and low pressure (i.e. low collision frequency) [5]. This group can be detected in the electron energy probability function (EEPF) (see below). Its average energy is about 1.5 eV. Indeed, it is low, compared to the calculated averaged energy in the bulk, which has a value of about 6.5 eV. The peaks at each

bulk-sheath interface are explained by the electron movement back and forth in the presence of negative ions (see Chapter 3).

In the dual-frequency regime the electron density and consequently the sheath width respond to the applied double frequency [Fig. 4.4(b)]. The electrons oscillate in one of the sheaths for a half LF (2 MHz) period with the applied HF (27 MHz). Two outstanding peaks at the sheath-bulk interface are formed, which are related to the double layer structures of the electric field [cf. Figs. 4.4(b) and 4.3(c)]. The electron density in the bulk plasma is calculated for both frequency regimes to be about  $1.5 \times 10^{15} \text{ m}^{-3}$ . This is lower than the density of the major negative ions by one order of magnitude (see below), i.e. the discharge structure is electronegative, both in the single- and dual-frequency regimes.

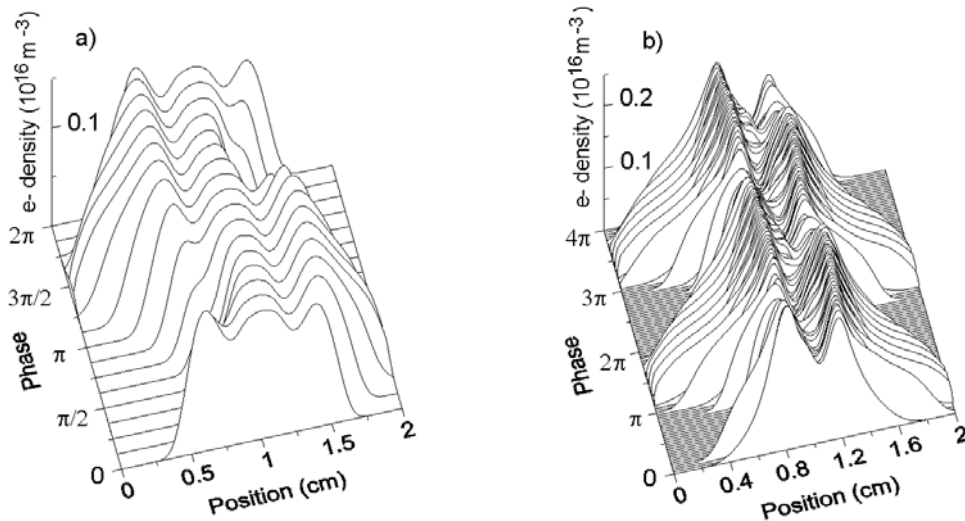


FIGURE 4.4. Electron density distributions as a function of time in the RF cycle in the single-frequency reactor (a) and as a function of time in two LF cycles in the dual-frequency reactor (b). Applied voltage and pressure are the same as in Figs. 4.2 and 4.3, respectively.

### 4.3.3 Ion density distribution

Figure 4.5 presents the ion density distributions for the single- and dual-frequency reactors. In the single-frequency reactor the ion density profiles are constant in time throughout the HF cycle [Fig. 4.5(a)]. The dominant negatively charged species are negative ions, mainly F<sup>-</sup> ( $9 \times 10^{15} \text{ m}^{-3}$ ) and to a lesser extent CF<sub>3</sub><sup>-</sup> ions ( $4.5 \times 10^{15} \text{ m}^{-3}$ ). These results are clearly higher than the electron density [see Fig. 4.4(a)]. Since the diffusive flux of the negative ions is very low and the electric field is always directed outwards, the negative ions are confined in the bulk plasma

and are almost absent in the sheath [Fig. 4.5(a)]. In the sheath mainly positive ions and electrons are found [Figs. 4.5(a) and 4.4(a)]. The main positive ion is Ar<sup>+</sup> and its density in the bulk is  $1.4 \times 10^{16} \text{ m}^{-3}$ . CF<sub>3</sub><sup>+</sup> and N<sub>2</sub><sup>+</sup> ions have densities, which are in the order of  $8 \times 10^{14}$  and  $6 \times 10^{14} \text{ m}^{-3}$ , respectively, hence more than an order of magnitude lower than the density of the Ar<sup>+</sup> ions.

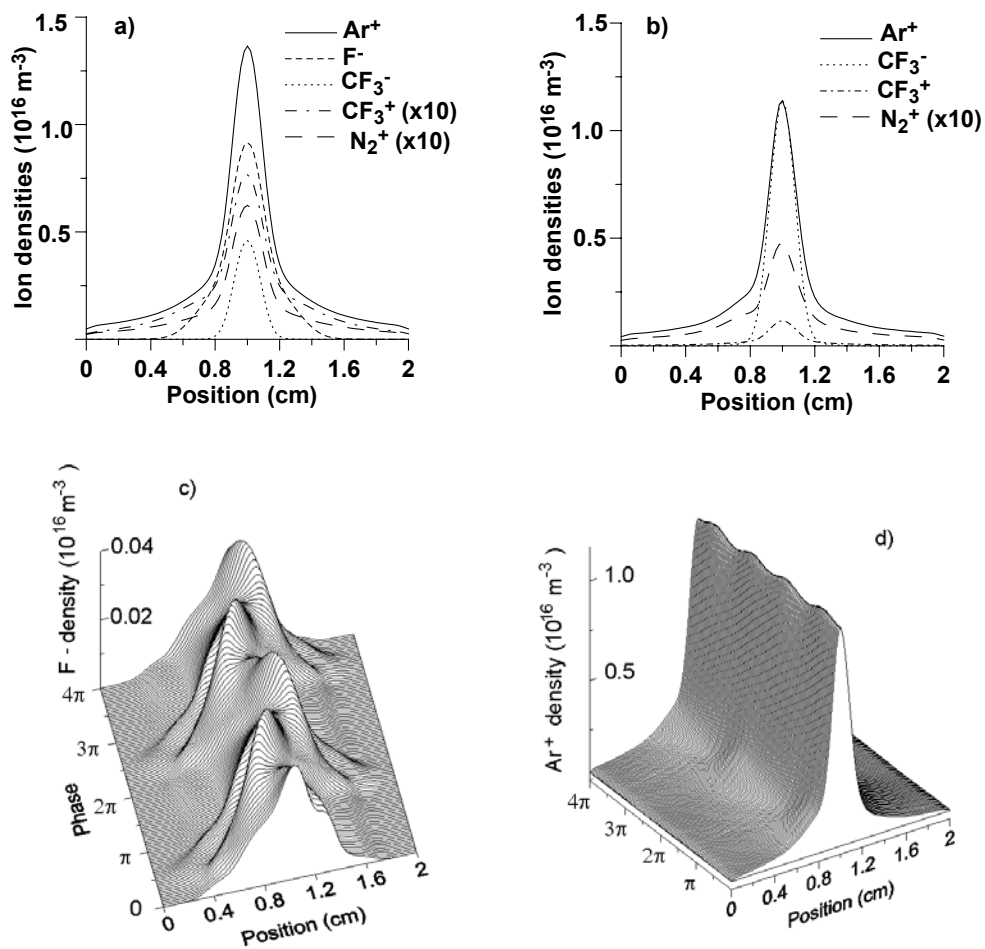


FIGURE 4.5. Ion density distributions in the single-frequency reactor (constant in time) (a) and at  $\omega t = 0$  of the LF cycle in the dual-frequency reactor (b). The F<sup>-</sup> ions and positive ions can respond to some extent to the LF. The F<sup>-</sup> and Ar<sup>+</sup> density distributions as a function of time in two LF cycles in the dual-frequency reactor are shown in (c) and (d). Applied voltage and pressure are the same as in Figs. 4.2 and 4.3, respectively.

For the dual-frequency reactor CF<sub>3</sub><sup>-</sup> ions are the dominant negatively charged species with a density of  $1.1 \times 10^{16} \text{ m}^{-3}$  [Fig. 4.5(b)], whereas the density of the F<sup>-</sup> ions is rather small, i.e. only  $4 \times 10^{14} \text{ m}^{-3}$  [Fig. 4.5(c)]. This is in contrast to investigations for cc single-HF pure CF<sub>4</sub>, Ar/CF<sub>4</sub> and Ar/CF<sub>4</sub>/N<sub>2</sub> discharges (see above and Refs. 11, 12, 35, 37, and 57-59). In the presence of LF (2 MHz) and the high electric field acceleration, the light F<sup>-</sup> ions are not confined in the bulk plasma as in HF discharges. They have enough time to move towards the electrodes. The much heavier CF<sub>3</sub><sup>-</sup> ions cannot respond to the LF and they remain in the bulk plasma [see Fig. 4.5(b)], where the main loss mechanism is the positive-negative ion recombination with extremely low reaction probability. This explains the higher CF<sub>3</sub><sup>-</sup> density compared to the F<sup>-</sup> density. The F<sup>-</sup> density profile is greatly modulated by the LF and F<sup>-</sup> ions are detected at the powered electrode at phase  $\pi/2$  of the LF cycle [Fig. 4.5(c) and see also below for the F<sup>-</sup> ion energy distribution function (IEDF) at the powered electrode]. From the electric field distribution one could expect that F<sup>-</sup> ions are able to reach the powered electrode at phase  $3\pi/2$ , when the electric field is almost 0, like the electrons [Figs. 4.3 and 4.4(b)]. However, at that time F<sup>-</sup> ions are detected at the grounded electrode [Fig. 4.5(c)]. Indeed, the F<sup>-</sup> ions are inert in comparison with the electrons and 2 MHz is not low enough for F<sup>-</sup> to respond instantaneously to the electric field. This explains the time delay (phase shift of half of a period,  $\pi$ ). We have also carried out simulations for a dual-frequency (27+1 MHz) reactor, and they show that F<sup>-</sup> ions reach the electrodes at a phase shifted with  $\pi/2$  in comparison with the phase when the electric field is close to 0. Hence, a lower LF (1 MHz compared to 2 MHz) results in a smaller phase shift ( $\pi/2$  vs.  $\pi$ ).

The positive ion density distributions, at phase 0 of the LF cycle in the dual-frequency reactor are presented in Fig. 4.5(b). The positive ions, can respond to the LF to some extent because the ion plasma frequency  $\omega_{pi}$  (calculated to be  $2.5 \times 10^7 \text{ s}^{-1}$ ,  $5.3 \times 10^6 \text{ s}^{-1}$ , and  $5.8 \times 10^6 \text{ s}^{-1}$  for Ar<sup>+</sup>, CF<sub>3</sub><sup>+</sup>, and N<sub>2</sub><sup>+</sup> ions, respectively) and the applied LF  $\omega_{LF} = 1.3 \times 10^7 \text{ s}^{-1}$  have comparable values. The ion plasma frequency  $\omega_{pi}$  is calculated like the electron plasma frequency  $\omega_{pe}$  from Eq. (2.102) replacing the electron density in the bulk  $n_e$  with the ion density in the bulk  $n_i$ , and the electron mass  $m$  with the ion mass  $M_i$ . The main positive ion is again Ar<sup>+</sup> and its density in the bulk is  $1.1 \times 10^{16} \text{ m}^{-3}$ . CF<sub>3</sub><sup>+</sup> and N<sub>2</sub><sup>+</sup> ions have densities of about  $1.1 \times 10^{15}$  and  $4 \times 10^{14} \text{ m}^{-3}$ , respectively [Fig. 4.5(b)]. The Ar<sup>+</sup> density as a function of time in two LF cycles is given in Fig. 4.5(d). The density profile depends on time although the dependence is weak.

#### 4.3.4 Electron energy distribution

The main advantage of the PIC/MCC method is that it does not require any assumption for the electron energy distribution function (EEDF), which is a crucial parameter in the discharge behavior. The EEDF is an output from the calculation. Figure 4.6 shows the EEPF  $f_e(\varepsilon)$  ( $= F_e(\varepsilon)\varepsilon^{-1/2}$ , where  $F_e(\varepsilon)$  is the EEDF and  $\varepsilon$  is the electron energy) at the center of the discharge and averaged for one HF cycle in the single-frequency reactor and for two LF cycles in the dual-frequency reactor. In the conventional HF reactor the profile of the EEPF is complicated and can be approximated by a Maxwellian distribution in its low energy part (i.e., till about 2 eV), and by a Druyvesteyn distribution in the higher energy part (Fig. 4.6, solid line). A low energy electron group is formed with average energy of 1.5 eV. The electron-neutral (mainly Ar because of the highest concentration in the gas mixture) collision frequency of this group ( $\approx 7 \times 10^6 \text{ s}^{-1}$ ) is smaller than the applied frequency ( $\approx 9 \times 10^7 \text{ s}^{-1}$ ) and the low energy electrons oscillate without collisions in the bulk [5].

In the dual-frequency reactor the profile can be approximated by a bi-Maxwellian distribution (Fig. 4.6, dashed line). The two electron energy groups have energies of 3.5 and 7.5 eV. In the presence of the LF ( $\omega_{LF} \approx 10^7 \text{ s}^{-1}$ ) the two groups effectively interact with the neutrals.

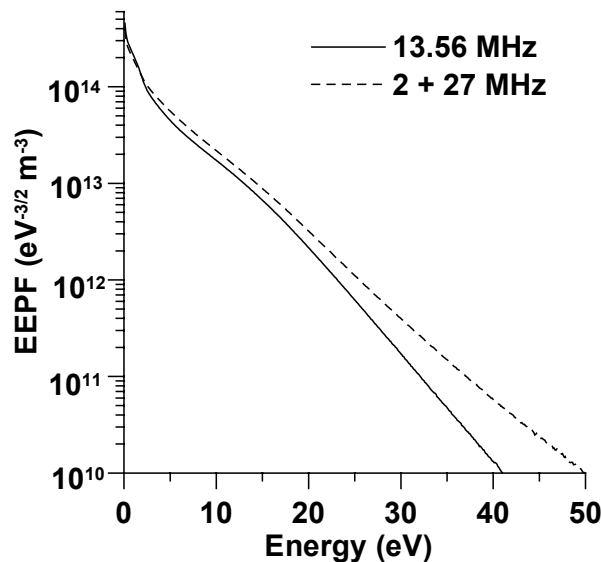


FIGURE 4.6. Electron energy probability function (EEPF) in the center of the discharge averaged over one HF cycle in the single-frequency reactor (solid line) and averaged over two LF cycles in the dual-frequency reactor (dashed line). Applied voltage and pressure are the same as in Figs. 4.2 and 4.3, respectively.

The calculated reaction rates show that all electron–neutral collisions in the dual-frequency regime have reaction rates, which are 2 to 5 times higher than the reaction rates in the single-frequency regime. The high-energy tails in both cases are due to the comparatively strong electric field in the bulk, which is a characteristic feature of electronegative discharges. The averaged electron energy determined by the EEDF is calculated to be 7.5 eV and 7.3 eV in the single- and dual-frequency regime, respectively.

#### 4.3.5 Ion energy distributions

Figure 4.7 presents the normalized F<sup>-</sup> IEDF at the driven electrode, where the wafer is placed in the dual-frequency reactor. Highly energetic F<sup>-</sup> ions (with energy up to 400 eV) are detected at phase  $\pi/2$  of the LF cycle [cf. also Fig. 4.5(c)]. The incident negative ion flux on the wafer reduces the local charging, which is an important issue in improving the performance of the anisotropic etching processes. The negative F<sup>-</sup> ion injection was numerically observed also in an Ar/CF<sub>4</sub> discharge sustained in a pulsed two-frequency reactor during the off phase [43]. In the single-frequency reactor the electron and positive ion fluxes on the wafer have the same magnitude for a short time during the anodic part of the RF cycle. During the cathodic part of the RF cycle only positive ions reach the wafer.

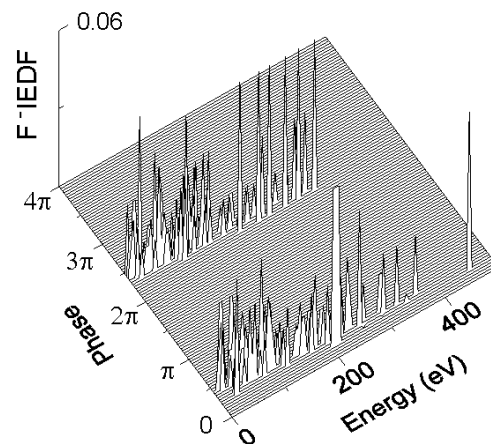


FIGURE 4.7. Normalized F<sup>-</sup> IEDF at the powered electrode as a function of time in two LF cycles in a dual-frequency reactor. Applied voltage and pressure are the same as in Fig. 4.3.

In the dual-frequency reactor the electron flux on the wafer is substantial for a longer time during the anodic part of the LF cycle and it is replaced by the negative F<sup>-</sup> ion flux for a short time of the cathodic part of the LF cycle, reducing the accumulated charge in this way. Detailed study of the negative ion flux is presented in Chapter 8.

The Ar<sup>+</sup>, CF<sub>3</sub><sup>+</sup> and N<sub>2</sub><sup>+</sup> IEDFs at the powered electrode, averaged over one HF cycle in the conventional cc RF reactor are presented in Figs. 8 (a) and (b). The Ar<sup>+</sup>, CF<sub>3</sub><sup>+</sup> and N<sub>2</sub><sup>+</sup> IEDFs at the powered electrode, averaged over 2 LF cycles in the dual-frequency reactor are presented in Figs. 8 (c) and (d). The IEDFs in the single-frequency regime are narrow with one outstanding peak, whereas the IEDFs in the dual-frequency regime are broad and bimodal as is expected in the presence of the LF [97, 98].

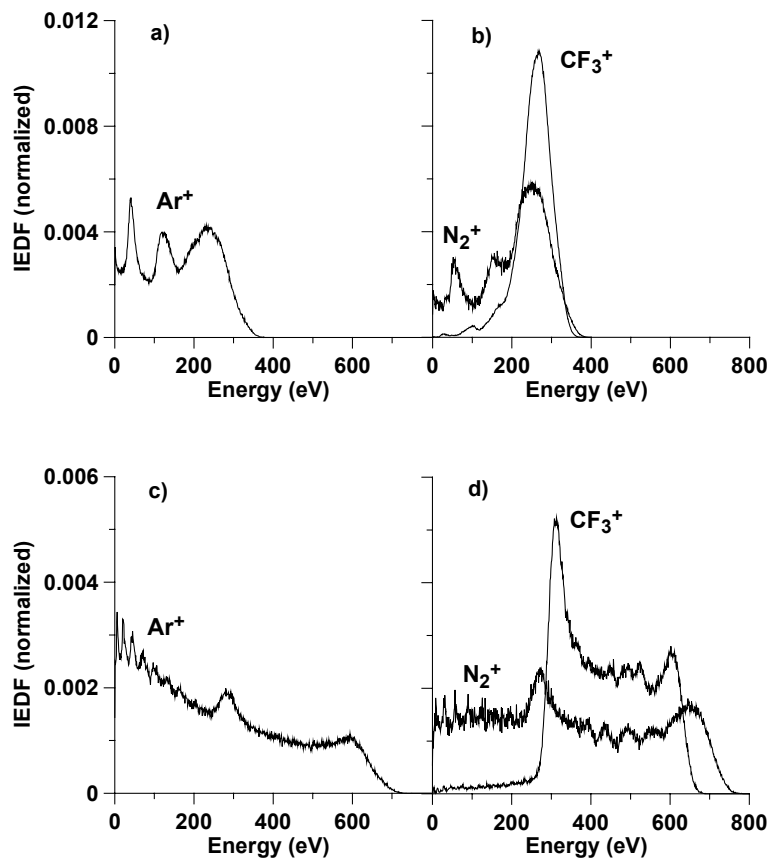


FIGURE 4.8. Ar<sup>+</sup>, CF<sub>3</sub><sup>+</sup>, and N<sub>2</sub><sup>+</sup> IEDFs at the powered electrode, averaged over one HF cycle in the conventional cc RF reactor [(a) and (b)], and averaged over two LF cycles in the dual-frequency reactor [(c) and (d)]. Applied voltage and pressure are the same as in Figs. 4.2 and 4.3, respectively.

The parameter determining the shape of the IEDF is the relation  $\tau_{ion}/\tau_{RF}$ , where  $\tau_{ion}$  is the ion transit time and  $\tau_{RF} = 2\pi/\omega_{RF}$  is the RF period [97]. In the HF regime  $\tau_{ion}/\tau_{RF} \gg 1$ , i.e. the ions take many RF cycles to cross the sheath, and they respond only to the average sheath potential drop. In a collisionless sheath this results in a narrow IEDF with one or two peaks, depending on the value of  $\tau_{ion}/\tau_{RF}$  [96, 97]. The IEDF width  $\Delta E$  is defined as  $\Delta E = E_2 - E_1$ , where  $E_1$  and  $E_2$  are the energies at which the peaks are observed. The width  $\Delta E$  decreases with increasing  $\tau_{ion}/\tau_{RF}$  until, at some point, the two peaks can no longer be resolved. Analytical calculations and experiments in the HF regime show that the energy width  $\Delta E$  is centered at  $e\overline{V}_s$ ,  $\overline{V}_s$  being the mean sheath voltage drop, and it depends on the ion mass as  $\Delta E \sim M_i^{-1/2}$  [97, 98].

However, the sheaths in the etching reactors, at the conditions under study, cannot be considered collisionless. Elastic and charge exchange collisions broaden the IEDF profile and shift it towards lower energies. Charge exchange collisions lead to formation of secondary peaks, which are placed at energies lower than  $E_1$  and  $E_2$  [97, 98].

In the present simulation, for the single-frequency reactor, the two peaks coincide at energies lower than  $e\overline{V}_s$  ( $\overline{V}_s$  is calculated to be 282 V) [Figs. 4.8 (a) and (b)]. The number of secondary peaks in the Ar<sup>+</sup> and N<sub>2</sub><sup>+</sup> IEDFs are due to the frequent resonant and non-resonant charge transfer collisions between Ar<sup>+</sup> or N<sub>2</sub><sup>+</sup> and Ar or N<sub>2</sub> (see the corresponding cross-section data presented in Chapter 2). The charge transfer reaction CF<sub>3</sub><sup>+</sup> - CF<sub>3</sub> is not considered in the model since the density of the CF<sub>3</sub> radicals is much lower in comparison with the CF<sub>4</sub> density, with a value in the order of 10<sup>18</sup> m<sup>-3</sup> [13, 35, 37]. The elastic collisions CF<sub>3</sub><sup>+</sup> - CF<sub>4</sub> shift the position of the primary peak to an energy of 270 eV (cf. with the calculated  $\overline{V}_s$  above). The Ar<sup>+</sup> and N<sub>2</sub><sup>+</sup> peaks are placed at energies of 240 eV and 260 eV, respectively, due to the influence of both types of collisions. The dependence on the ion mass is also observed. Indeed, the heaviest CF<sub>3</sub><sup>+</sup> ion has a narrow IEDF maximum compared to the wider Ar<sup>+</sup> and N<sub>2</sub><sup>+</sup> primary peaks.

In the LF regime the ion transit time  $\tau_{ion}$  is less than the RF period  $\tau_{RF}$ , i.e., the ions cross the sheath in a small fraction of the RF cycle and they reach the electrode with an energy equal to the instantaneous sheath potential drop [97, 98]. In this simulation  $\tau_{ion}/\tau_{LF}$ , where  $\tau_{LF}$  is the LF period ( $f = 2$  MHz), is calculated to be 0.9, 1.2, and 0.7 for Ar<sup>+</sup>, CF<sub>3</sub><sup>+</sup>, and N<sub>2</sub><sup>+</sup> ions, respectively. The two outstanding peaks in the profile correspond to the averaged minimum and maximum sheath

potential drop. In collisionless LF sheaths the distribution is independent of the ion mass [97]. However, in the present dual-frequency regime, the influence of the applied HF (27 MHz) is observed and the IEDF width depends on the ion mass  $M_i$ , i.e. as  $M_i$  is increased,  $\Delta E$  is reduced [cf. the energy width for the 3 positive ions in Figs. 4.8(c) and (d), considering that  $M_{N_2^+} < M_{Ar} < M_{CF_3^+}$ ]. The influence of the collisions is the same as in the single-HF regime (see above). Detailed investigation of the IEDF in both reactors follows in Chapter 5.

#### 4.4 Summary

A one-dimensional PIC/MC model has been developed to describe the structure of a cc RF discharge in a gas mixture of Ar, CF<sub>4</sub> and N<sub>2</sub>. The model follows electrons, Ar<sup>+</sup>, CF<sub>3</sub><sup>+</sup>, F<sup>-</sup>, CF<sub>3</sub><sup>-</sup>, and N<sub>2</sub><sup>+</sup> ions. The collisions treated by the MCC method include electron – neutral (Ar, CF<sub>4</sub>, and N<sub>2</sub>) collisions, various kinds of collisions of Ar<sup>+</sup>, CF<sub>3</sub><sup>+</sup>, F<sup>-</sup>, CF<sub>3</sub><sup>-</sup>, or N<sub>2</sub><sup>+</sup> ions with neutrals, positive - negative ion recombination, and electron – ion recombination.

The simulations are performed for 0.8/0.1/0.1 molar ratios of an Ar/CF<sub>4</sub>/N<sub>2</sub> mixture at a pressure of 30 mTorr in single- (13.56 MHz) and dual-frequency (27 + 2 MHz) cc reactors and a comparison between the two frequency regimes is made. The model yields results for the electron and various ion densities, their energy distributions, the electric field and potential distributions. The results are presented as a function of distance to the driven electrode and as function of time in one HF cycle in the single-frequency reactor, and in two LF cycles in the dual-frequency reactor.

The results show that the structure of the discharge is electronegative in both investigated regimes, i.e. a double layer structure and electron density maxima at the bulk – sheath interface are observed, and the main negative carriers are the negative ions. The electron densities in the bulk have similar values in the two regimes. In the dual-frequency regime the electrons oscillate in one of the sheaths for a half LF (2 MHz) period with the applied HF (27 MHz). The main negative ion in the single-frequency regime is F<sup>-</sup>, whereas it is CF<sub>3</sub><sup>-</sup> in the dual-frequency regime. Indeed, in the presence of LF and the strong electric field acceleration, the light F<sup>-</sup> ions are not confined in the bulk plasma as in single-HF discharges and they have enough time to move towards the electrodes. Highly energetic F<sup>-</sup> ions (with energy up to 400 eV) are detected at phase  $\pi/2$  of the LF cycle at the driven electrode and at phase  $3\pi/2$  of the LF cycle at the grounded electrode. The much heavier CF<sub>3</sub><sup>-</sup> ions cannot respond to the LF and they remain in the bulk plasma. The positive ion densities do not depend on the phase in the single-frequency reactor. However, in the dual-frequency reactor the positive ions respond slightly to the LF. The main

positive ion is Ar<sup>+</sup>. The densities of each of the positive ions have similar values in the two regimes.

The calculated EEPF profiles can be approximated to a Druyvesteyn and bi-Maxwellian distribution with high-energy tails in the single- and dual-frequency regime, respectively. The IEDF in the single-frequency regime is narrow with one outstanding peak, whereas the IEDF in the dual-frequency regime is broad and bimodal. The energy width depends on the ion mass.

In conclusion, the present simulations show that the dual-frequency regime improves the following plasma parameters, which are very important in the etching processes:

- 1) It provides a significantly wider ion bombardment energy range in comparison with the single-HF configuration.
- 2) It reduces the charge accumulation by F<sup>-</sup> injection to the electrodes.
- 3) It randomizes the electron energy by a higher electron-neutral collision frequency in comparison with the single-HF regime at the same pressure. This results in an EEDF distribution, close to the bi-Maxwellian, which can significantly simplify further calculations of plasma quantities determined by the EEDF.

## Chapter 5

# ION ENERGY DISTRIBUTIONS IN SINGLE- AND DUAL-FREQUENCY ETCHING REACTORS

### 5.1 Introduction

In plasma etching the energies of the ions incident on the wafer is crucial in determining the etch rates and anisotropy. This explains the extensive experimental [3, 4, 7-10, 22, 23, 99, and 100], analytical [97, 98, and 101] and numerical [22, 23, 44, 45, 49, 50, 97, and 102] studies of the ion energy distribution function (IEDF) in capacitively coupled (cc) radio frequency (RF) reactors. A good review and analysis of theoretical and experimental investigations of the IEDF are given by Kawamura *et al.* [97]. The main points can be summarized as follows:

a) In *collisionless sheaths* the crucial parameter determining the shape of the IEDF is the relation  $\tau_{ion} / \tau_{RF}$ , where  $\tau_{ion}$  is the *ion transit time* and  $\tau_{RF} = 2\pi / \omega_{RF}$  is the RF period. The ion transit time is calculated by [97]

$$\tau_{ion} = 3\bar{s} \left( \frac{M}{2e\bar{V}_s} \right)^{1/2}, \quad (5.1)$$

where  $\bar{s}$  is the time-averaged sheath thickness,  $\bar{V}_s$  is the average sheath potential drop,  $M$  is the ion mass, and  $e$  is the electron charge.

If  $\tau_{ion} / \tau_{RF} \gg 1$ , i.e. at high frequency (HF), the ions respond to the average sheath potential drop resulting in a narrow IEDF with one or two maxima depending on the value of  $\tau_{ion} / \tau_{RF}$ . If  $\tau_{ion} / \tau_{RF} \ll 1$ , i.e. at low frequency (LF), the ions respond to the instantaneous sheath potential drop resulting in a broad and bimodal IEDF.

b) In *collisional sheaths* charge exchange collisions lead to the appearance of secondary maxima at energies lower than the primary maxima, and both charge exchange and elastic collisions shift the IEDF to lower energies.

The sheaths in conventional RF etching reactors are typically collisional. Analytical models assume limiting approximations such as constant sheath width, sinusoidal sheath potential drop, etc. and therefore give only the qualitative features of the IEDF. Experimental measurements as well as numerical methods present more reliable results. Particle-in-cell (PIC) simulations of RF discharges are attractive for calculation of the particle energy distributions since these quantities can be obtained self-consistently from first principle [46, 47]. Collisional effects are included by coupling the PIC model with a Monte Carlo collision (MCC) method.

The purpose of the present chapter is a detailed numerical investigation of  $\text{Ar}^+$ ,  $\text{CF}_3^+$ , and  $\text{N}_2^+$  IEDFs in cc Ar/ $\text{CF}_4$ / $\text{N}_2$  discharges at a range of different pressures, applied voltages and frequencies, by means of a one-dimensional PIC/MCC method.

In the previous chapter the discharge structure in a mixture of Ar,  $\text{CF}_4$  and  $\text{N}_2$ , which is a feedstock gas for etching in an industrial cc dual-frequency reactor was examined. Simulations were performed in single- (13.56 MHz) and dual- (27 + 2 MHz) frequency cc reactors and a comparison between the two frequency regimes is made. The calculated IEDFs were presented along with other results of the model, i.e. potential and electric field distributions, particle densities, and electron energy distribution function. The results show that the LF-HF scheme provides a significantly wider ion bombardment energy range in comparison with the single- HF configuration. Although several other works investigated plasma properties in dual-frequency reactors by experimental measurements or numerical simulations [e.g. Refs. 14, 15, 17-19, 34, 42, 43, 45, and 63] detailed studies of the ion bombardment energy are very scarce. For example, only the average ion bombardment energy is given in Refs. 14, 15, 34, and 63. Myers *et al.* predicted ion energies and angular distributions in single- and dual-frequency regimes by combining a single- and dual-frequency plasma sheath model with a Monte Carlo simulation of ion transport [45].

In the present chapter the simulations are carried out over a wide range of pressure, applied voltage and frequency. An analytical model of the IEDF in a collisionless sheath in a dual-frequency reactor is developed and a comparison of the simulation results with the analytical results is discussed. The time evolution of the IEDF during the RF cycle is also presented.

In Sec. 5.2 the analytical model of the IEDF in a dual-frequency reactor is presented. In Sec. 5.3 the input parameters are given. In Sec. 5.4 the results of the simulations for  $\text{Ar}^+$ ,  $\text{CF}_3^+$ , and  $\text{N}_2^+$  IEDFs are presented and discussed. Finally, in Sec. 5.5 a summary is given.

## 5.2 Analytical model of the IEDF in a dual-frequency reactor

The bombardment IEDF is determined by the potential difference across the sheath  $V_s(x, t)$ , the collision frequency (i.e., gas pressure), the sheath width  $s$ , the mass of the ions  $M$ , and the applied frequency  $\omega_{RF}$ . In the literature, a number of simple analytical models have been applied for a collisionless sheath, assuming a sinusoidal sheath voltage and constant sheath width [97, 98, and 101]. In the HF regime the ions cross the sheath in a time corresponding to many RF cycles and they respond to the average sheath potential drop  $\bar{V}_s$ . If the time and space dependence of the sheath voltage is described by [98]

$$V_s(x, t) = \bar{V}_s [1 + \lambda \sin(\omega_{RF} t)] \left( \frac{x}{s} \right)^{4/3}, \quad (5.2)$$

where  $\lambda$  is a parameter and  $\lambda \leq 1$ , and  $x$  is the position of the ion in the sheath, then the IEDF  $f(E)$  of the ions with constant flux  $\Gamma$  is a saddle-shaped distribution [98]

$$f(E) = \frac{2\Gamma}{\omega_{RF} \Delta E} \left[ 1 - \left( \frac{2}{\Delta E} \right)^2 (E - e\bar{V}_s)^2 \right]^{-1/2}, \quad (5.3)$$

with an energy width  $\Delta E$  [98]

$$\Delta E = \frac{8\lambda e\bar{V}_s}{3\omega_{RF}s} \left( \frac{2e\bar{V}_s}{M} \right)^{1/2}. \quad (5.4)$$

It is clear that the result of the analytical model presented above cannot be applied for the dual-frequency regime. To develop a simple analytical model for the dual-frequency regime we make the same assumption as in a single- HF reactor, except for the waveform of the sheath potential, i.e. a collisionless sheath and a constant sheath width are assumed. The applied voltage is  $V = V_{HF} \sin(\omega_{HF} t) + V_{LF} \sin(\omega_{LF} t)$ , where  $V_{HF}$  and  $V_{LF}$  are the amplitude, and  $\omega_{HF}$  and  $\omega_{LF}$  are the applied HF (27 MHz) and LF (1 or 2 MHz), respectively. The numerical simulation result of the potential across the sheath at the driven electrode in 2 LF cycles for the (27+2) MHz case is presented in Fig. 5.1 (a). The calculations give also the values of the mean sheath potential  $\bar{V}_s$  and the average sheath width  $\bar{s}$ , which are used in the analytical model (see below). Figures 5.1 (b) and (c) show that the sheath potential drop at the driven electrode is better described with the product of 2 harmonic functions than with the sum of them:

$$V_s(t) = \bar{V}_s [1 + \lambda_1 \sin(\omega_{HF} t)] [1 + \lambda_2 \sin(\omega_{LF} t)], \quad (5.5)$$

where  $\lambda_1$  and  $\lambda_2$  are parameters and  $\lambda_1, \lambda_2 \leq 1$ . The parameters  $\lambda_1$  and  $\lambda_2$  are determined from the plot [Fig. 5.1(a)] considering two time points at  $\omega_{LF}t = \pi/2$  and  $\omega_{LF}t = 3\pi/2$ . The average sheath potential  $\overline{V}_s$  is calculated in the simulation.

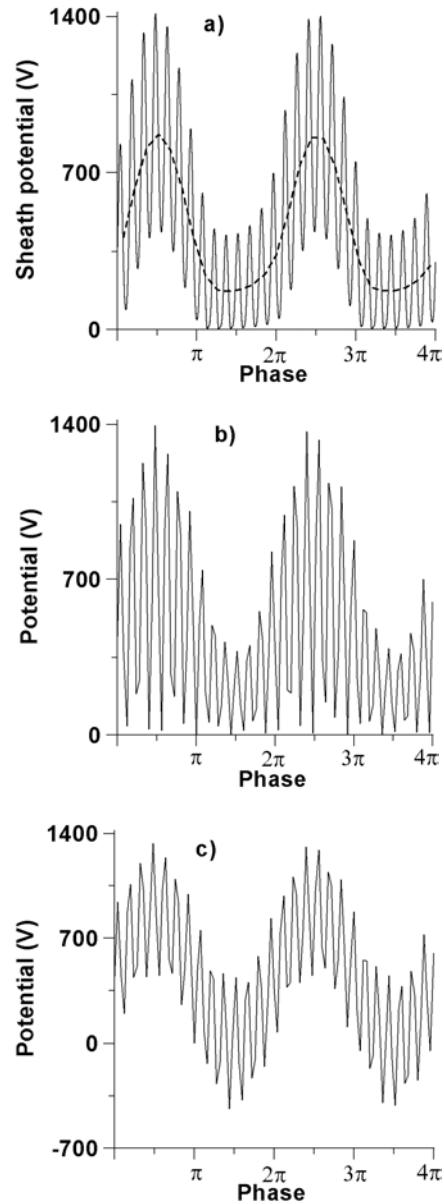


FIGURE. 5.1. Sheath potential at the driven electrode in the (27 + 2) MHz reactor:

a) numerical result, b) analytical function  $V_s(t) = \overline{V}_s(1 + \lambda_1 \sin(\omega_{HF}t))(1 + \lambda_2 \sin(\omega_{LF}t))$ , and c) analytical function  $V_s(t) = \overline{V}_s(1 + \lambda_1 \sin(\omega_{HF}t) + \lambda_2 \sin(\omega_{LF}t))$ . The calculated  $\overline{V}_s$  is 445 V. The dashed line in (a) shows the averaged HF sheath potential as a function of the LF.

It should be mentioned that when the primary frequency is much higher than the secondary frequency, like in the present reactor, the IEDF and energy width equations are the same for the 2 analytical waveforms of  $V_s(t)$ , presented in Figs. 5.1 (b) and (c). However, the calculated  $\lambda_1$  and  $\lambda_2$  differ a lot, which results in a big difference in the energy width  $\Delta E$  [see below Eq. (5.13)].

Next, we assume a spatial dependence of the sheath voltage  $V_s(x,t) = V_s(t)[x(t)/s]^{4/3}$  (see Eq. 5.2), providing that there are no electrons in the sheath, i.e.  $\exp(e\bar{V}_s/kT_e) \ll 1$  [1, 97]. Therefore, the equation of motion is

$$M \frac{d^2x}{dt^2} = \frac{4}{3} \frac{e\bar{V}_s}{s} [1 + \lambda_1 \sin(\omega_{HF}t)] [1 + \lambda_2 \sin(\omega_{LF}t)] \left(\frac{x}{s}\right)^{1/3}. \quad (5.6)$$

To make an analytical integration of (5.6) we assume that the ion path  $x(t)$  is close to that corresponding to the average acceleration, i.e. [98]

$$\frac{x(t)}{s} = \left[ \frac{1}{3s} \left( \frac{2e\bar{V}_s}{M} \right)^{1/2} \right]^3 (t-t_0)^3, \quad (5.7)$$

where  $t_0$  is the time at which the ion enters the sheath. This approximation is valid as long as the ion transit time  $\tau_{ion}$  is longer than or equal to the RF period. In our case this applies to the LF period  $\tau_{LF}$  because  $\tau_{LF} \gg \tau_{HF}$  and hence, when  $\tau_{ion}/\tau_{LF} \geq 1$ , this means that  $\tau_{ion}/\tau_{HF} \geq 1$  is also true. This implies

$$\omega_{LF}(t-t_0) = 2\pi\tau_{ion}/\tau_{LF} \gg 1. \quad (5.8)$$

In the simulation in the (27+2) MHz case  $\tau_{ion}/\tau_{LF}$  is calculated to be 0.9, 1.2, and 0.7 for  $\text{Ar}^+$ ,  $\text{CF}_3^+$ , and  $\text{N}_2^+$  ions, respectively. Therefore, the assumption presented above can be made. In the (27+1)MHz case these values are 0.5, 0.6 and 0.4, respectively, which means that the ion path cannot be assumed close to the average, in particular for  $\text{N}_2^+$ . As will be seen in Sec. 5.4 in this case the deviation of the analytical from the numerical results is larger.

Substituting (5.7) in the equation of motion (5.6) leads to

$$\frac{d^2x}{dt^2} = \frac{2}{9s^2} \left( \frac{2e\bar{V}_s}{M} \right)^{3/2} [1 + \lambda_1 \sin(\omega_{HF}t)] [1 + \lambda_2 \sin(\omega_{LF}t)] (t-t_0). \quad (5.9)$$

Taking into account that  $\omega_{HF} \gg \omega_{LF}$  and (5.8) is true, the time integration of equation (5.9) yields the velocity

$$\frac{dx}{dt} = \frac{2}{9s^2\omega_{LF}^2} \left( \frac{2e\bar{V}_s}{M} \right)^{3/2} \left[ \frac{1}{2}\omega_{LF}^2(t-t_0)^2 - \lambda_2\omega_{LF}(t-t_0)\cos(\omega_{LF}t) \right]. \quad (5.10)$$

The time of arrival at the electrode  $t_1$  [ $x(t_1) = s$ ] is obtained from the average ion path (5.7):

$$(t_1 - t_0) = 3s \left( \frac{M}{2e\bar{V}_s} \right)^{1/2}. \quad (5.11)$$

Thus, the energy of the ions arriving at the electrode is

$$\begin{aligned} E &= e\bar{V}_s \left[ 1 - \frac{2\lambda_2}{3s\omega_{LF}} \left( \frac{2e\bar{V}_s}{M} \right)^{1/2} \cos(\omega_{LF}t_1) \right]^2 \\ &\approx e\bar{V}_s \left[ 1 - \frac{4\lambda_2}{3s\omega_{LF}} \left( \frac{2e\bar{V}_s}{M} \right)^{1/2} \cos(\omega_{LF}t_1) \right], \end{aligned} \quad (5.12)$$

and it is spread over the energy width  $\Delta E$ , centered at  $e\bar{V}_s$

$$\Delta E = \frac{8\lambda_2 e\bar{V}_s}{3s\omega_{LF}} \left( \frac{2e\bar{V}_s}{M} \right)^{1/2}. \quad (5.13)$$

Finally, we obtain the IEDF  $f(E)$  of the ions with constant flux  $\Gamma = dN/dt_1$

$$f(E) = \frac{dN}{dE} = \frac{dN}{dt_1} \left( \frac{dE}{dt_1} \right)^{-1} = \frac{2\Gamma}{\omega_{LF}\Delta E} \left[ 1 - \left( \frac{2}{\Delta E} \right)^2 (E - e\bar{V}_s)^2 \right]^{-1/2}. \quad (5.14)$$

Eq. (5.13) shows that the energy width in the dual-frequency regime depends only on the applied LF. This result is reasonable because the ion transit time is much longer than the HF period. Indeed, the ratio  $\tau_{ion}/\tau_{HF}$  is calculated to be 12, 16, and 10 for  $\text{Ar}^+$ ,  $\text{CF}_3^+$ , and  $\text{N}_2^+$  ions, respectively. Consequently, the ions respond to the average HF potential, which is a function of the LF [see the dashed line in Fig. 5.1 (a)].

### 5.3 Input data

The numerical model used in this investigation is described in detail in Chapter 2. The charged species taken into account in the model are: electrons,  $\text{Ar}^+$ ,  $\text{N}_2^+$ ,  $\text{CF}_3^+$ ,  $\text{F}^-$ , and  $\text{CF}_3^-$ . The collisions treated by the MCC method include electron – neutral ( $\text{Ar}$ ,  $\text{CF}_4$ , and  $\text{N}_2$ ) collisions, various kinds of collisions of  $\text{Ar}^+$ ,  $\text{CF}_3^+$ ,  $\text{F}^-$ ,  $\text{CF}_3^-$ , or  $\text{N}_2^+$  with neutrals, positive – negative ion recombination, and electron – ion recombination.

A schematic diagram of the dual-frequency cc reactor considered in this study is shown in Fig. 4.1. The plasma is sustained between two parallel plates, each 20 cm in diameter and separated from the other by 2 cm. One of the electrodes is driven by a single- (13.56 MHz) or dual-frequency (27 + 2 MHz) power source. The

applied voltage in the dual-frequency reactor is given by Eq. (1.1), presented in Chapter 1.

The calculations are performed for an Ar/CF<sub>4</sub>/N<sub>2</sub> mixture at a ratio of 0.8/0.1/0.1. One group of calculations is performed for an applied voltage amplitude of 300V at a pressure of 20, 30, 50, 70, 100 and 200 mTorr. Another group of simulations is carried out for an applied voltage amplitude of 200, 300, 500 and 700V at a pressure of 30 mTorr. Both groups consider a conventional cc RF (13.56 MHz) reactor. The dependence on the frequency regime is investigated by simulations of the Ar/CF<sub>4</sub>/N<sub>2</sub> mixture at a pressure of 30 mTorr in single- (13.56 MHz) and dual-frequency (27 + 2 MHz or 27 + 1 MHz) cc reactors. The applied HF and LF voltage amplitudes are set to 700V.

The gas temperature is set to 300 K. The simulation grid is uniform and it consists of 100 cells. The electron time step is  $3.7 \times 10^{-11}$  s. To speed up the calculation, the ion time step is set to be 25 times longer than the electron time step. The choice of the grid spacing and the time steps is defined by the accuracy criteria for PIC/MCC codes with explicit mover (see Sec. 2.9).

## 5.4 Results and discussion

### 5.4.1 Effect of pressure

Figure 5.2 presents the simulation results of the Ar<sup>+</sup> (a), CF<sub>3</sub><sup>+</sup> (b), and N<sub>2</sub><sup>+</sup> (c) IEDFs at the powered electrode, averaged over one HF (13.56 MHz) cycle in the conventional cc RF reactor at a pressure of 20, 30, 50, 70, 100 and 200 mTorr. The applied voltage amplitude is 300V. At the applied HF the ions traverse the sheath in a time corresponding to many RF cycles and hence the IEDFs reflect the time averaged sheath potential. Therefore, following the analytical models it is expected that in a collisionless sheath the IEDFs will be narrow with one or two peaks and centered at  $e\bar{V}_s$  [see Eqs. (5.3) and (5.4), and Refs. 97, 98, and 101]. The collisionless approximation in the present simulation can be made only at a very low pressure. It is clearly seen in Fig. 5.2 that at a pressure of 20 mTorr the collisional effects in the sheath are not very prominent, especially for the CF<sub>3</sub><sup>+</sup> IEDF. In all presented simulations CF<sub>3</sub><sup>+</sup> - neutral elastic collisions are considered; the charge transfer reaction CF<sub>3</sub><sup>+</sup> - CF<sub>3</sub> is not taken into account since the density of the CF<sub>3</sub> radicals is much lower in comparison with the CF<sub>4</sub> density, with a value in the order of  $10^{18}$  m<sup>-3</sup> in a pure CF<sub>4</sub> discharge [13, 35, and 37]. Although the CF<sub>3</sub><sup>+</sup> ions lose kinetic energy in the reactive collisions (see Chapter 2), their energy distribution is influenced by the reactive collisions only at high pressure (200 mTorr).

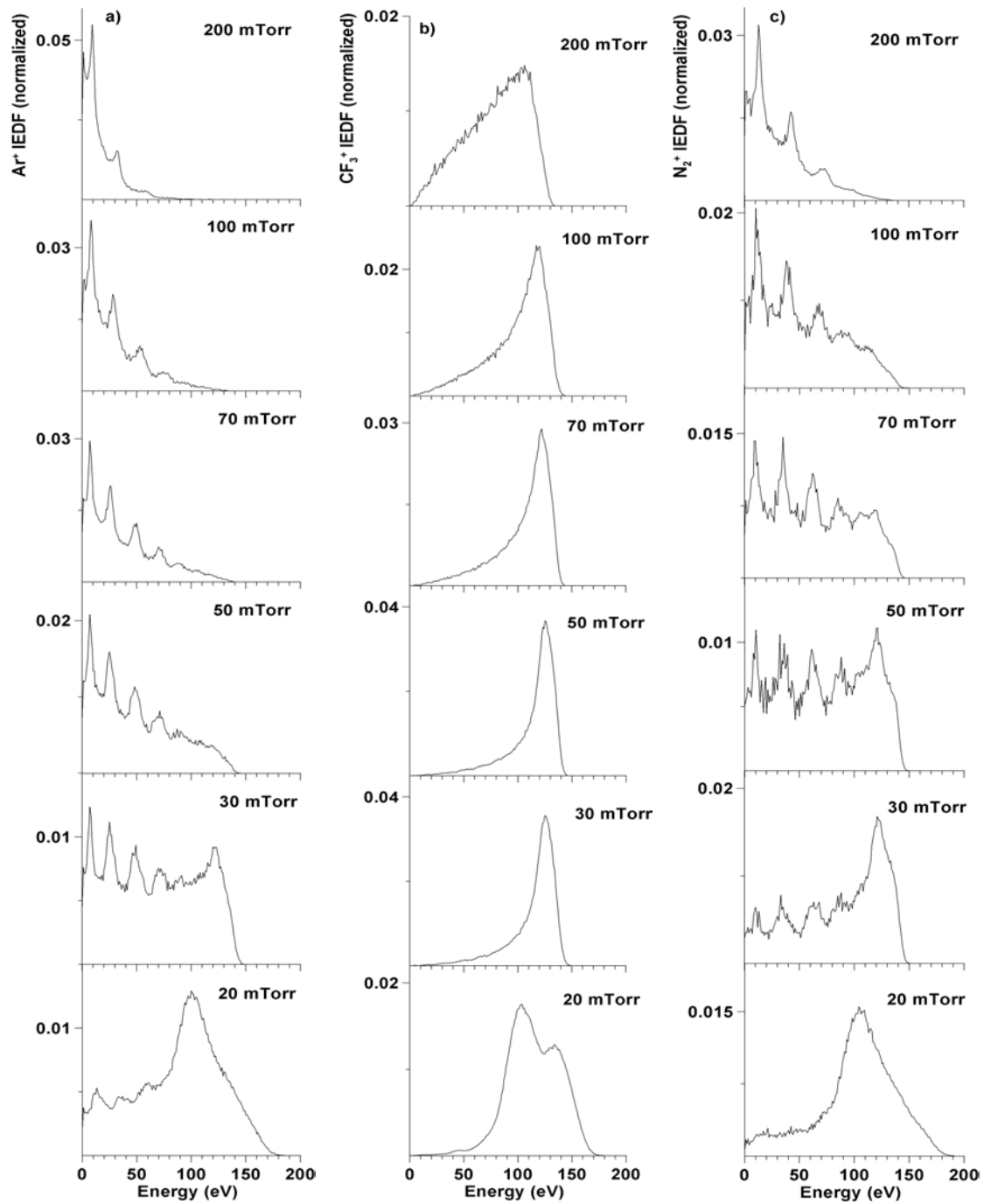


FIGURE 5.2.  $\text{Ar}^+$  (a),  $\text{CF}_3^+$  (b), and  $\text{N}_2^+$  (c) IEDFs at the powered electrode, averaged over one HF cycle in the conventional cc RF reactor at pressure 20, 30, 50, 70, 100 and 200 mTorr. The applied voltage amplitude is 300 V.

Consequently, the  $\text{CF}_3^+$  IEDF shows the influence of the elastic collisions. With increasing the pressure the 2 peaks coincide and move towards lower energy (from 125 eV at 20 mTorr to 110 eV at 200 mTorr) [Fig. 5.2 (b)]. The calculated averaged sheath potential is 125 V.

The simulations take into account both elastic and charge transfer (resonant and non-resonant) collisions between  $\text{Ar}^+$  or  $\text{N}_2^+$  and Ar or  $\text{N}_2$ . Secondary peaks are observed in the  $\text{Ar}^+$  and  $\text{N}_2^+$  IEDFs, and they are due to the charge exchange collisions [cf. Figs. 5.2 (a) and (c) with the  $\text{CF}_3^+$  IEDF in Fig. 5.2 (b)]. Obviously, for  $\text{Ar}^+$  and  $\text{N}_2^+$  ions the charge exchange collision frequency is much higher than the elastic collision frequency [see the corresponding cross-sections presented in Chapter 2]. Hence, the  $\text{Ar}^+$  and  $\text{N}_2^+$  IEDFs present mainly the contribution of the charge transfer collisions. Figures 5.2 (a) and (c) show that increasing the pressure leads to increasing the intensity of the secondary peaks. Moreover, the distance between them rises and the number of the peaks decreases. At the same time the primary peaks become less intense and at some pressure, they even disappear. This is caused by the increasing collision frequency in the sheath, which in turn is due to the shorter mean free path. As a result more and more ions take part in at least one collision on their way towards the electrode and their energy is shifted to lower values. These observations are in consistency with a number of works investigating the influence of pressure on the IEDF (mainly of  $\text{Ar}^+$  ions) considering both elastic and charge transfer collisions (e.g. Refs. 4, 7-9, 22, 23, 44, 45, 49, 50, 98- 100, and 102).

#### **5.4.2 Effect of the applied voltage amplitude**

Figure 5.3 presents the simulation results of the  $\text{Ar}^+$  (a),  $\text{CF}_3^+$  (b), and  $\text{N}_2^+$  (c) IEDFs at the powered electrode, averaged over one HF (13.56 MHz) cycle in the conventional cc RF reactor at a pressure of 30 mTorr and applied voltage amplitude  $V_{RF}$  of 200, 300, 500, and 700 V. It can be seen that the amplitude of the applied voltage has a significant effect on the width of the IEDF and the magnitude of the peaks. Indeed, the average sheath potential increases with increasing  $V_{RF}$ , which results in broader IEDFs and in a shift of the primary peaks to higher energies. The influence of the charge transfer and elastic collisions can be observed in the  $\text{Ar}^+$  and  $\text{N}_2^+$  IEDFs, and in the  $\text{CF}_3^+$  IEDF, respectively, (see Fig. 5.3). The number of secondary peaks and their intensity decreases, and the gap between them increases with increasing the applied voltage amplitude. This is related to a drop in the sheath width and a rise in the plasma density, which in turn results in increasing the ion plasma frequency [22, 23]. These simulation results are in consistency with a number of experimental and theoretical works investigating the influence of the applied voltage on the IEDF (e.g. Refs. 4, 7-10, 22, 23, 50, 99, and 100).

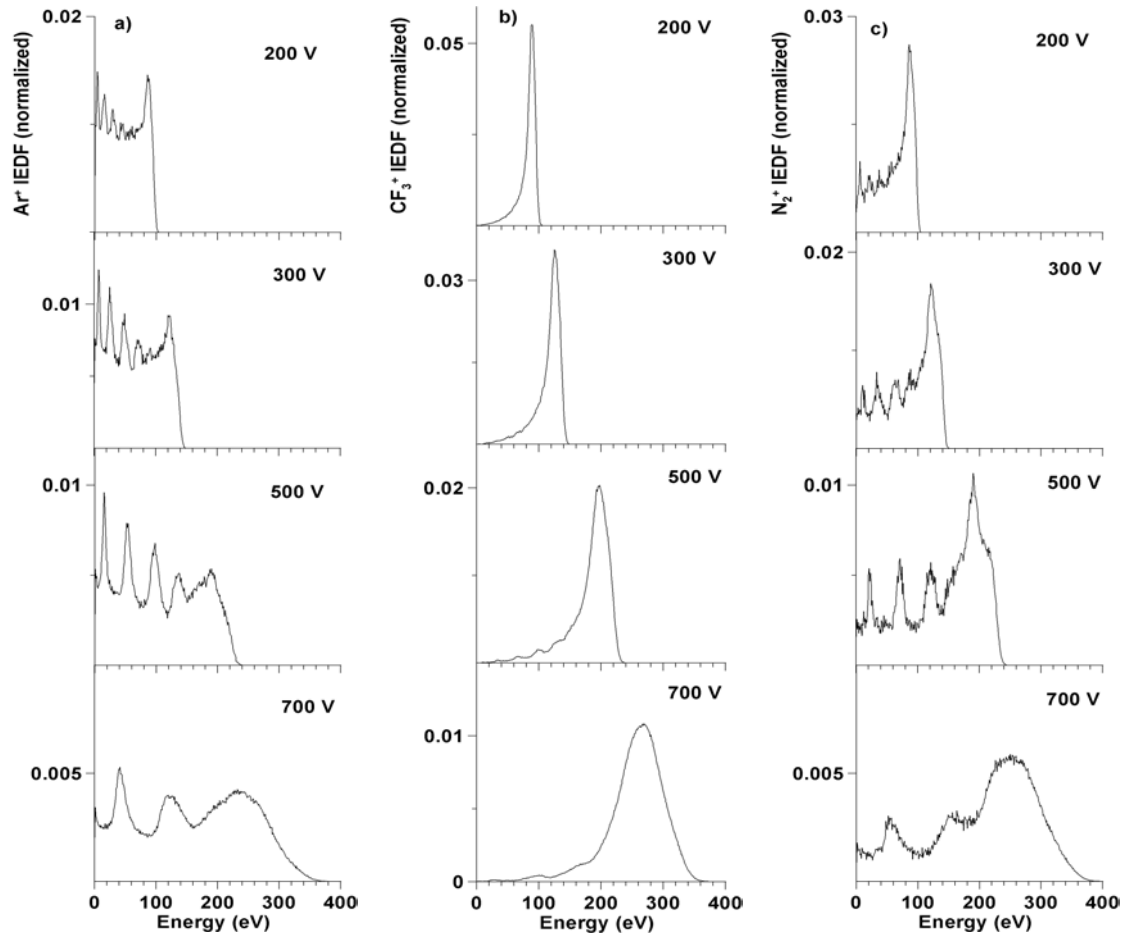


FIGURE 5.3.  $\text{Ar}^+$  (a),  $\text{CF}_3^+$  (b), and  $\text{N}_2^+$  (c) IEDFs at the powered electrode, averaged over one HF cycle in the conventional cc RF reactor at pressure 30 mTorr and applied voltage amplitude 200, 300, 500 and 700 V.

The present detailed investigation of the 3 different ions ( $\text{Ar}^+$ ,  $\text{CF}_3^+$ , and  $\text{N}_2^+$ ) demonstrates not only the influence of the pressure and applied voltage on the IEDF but also the influence of the different types of ion-neutral collisions.

#### 5.4.3 Effect of the applied frequency regime

Fig. 5.4 (solid lines) presents the simulation results of the  $\text{Ar}^+$  (a),  $\text{CF}_3^+$  (b), and  $\text{N}_2^+$  (c) IEDFs at the powered electrode, averaged over two LF (2 MHz) cycles or over one LF (1 MHz) cycle in the dual-frequency reactor at a pressure of 30 mTorr and the applied voltage amplitude of 700V. In the  $(27 + 2)$  MHz case the IEDFs are averaged over two LF cycles since one LF cycle does not contain an integer number

of HF cycles. The analytical calculation results based on Eqs. (5.13) and (5.14) are also given in Fig. 5.4, with dashed lines. A comparison with the IEDFs at the same operating conditions in the single-frequency reactor (Fig. 5.3 at applied voltage amplitude 700V, i.e. the lowest plots) shows that the dual-frequency regime provides a significantly wider ion bombardment energy range, which is one of the main advantages of the dual-frequency reactors used in plasma etching [14, 15, 17-19, 34, 42, 43, 60, and 63]. For example, in the HF regime the maximum  $\text{Ar}^+$  ion energy is calculated to be only 350 eV, while in the (27+2) MHz regime it is calculated to be 700 eV. The increase of the maximum ion energy with the addition of low frequency to the plasma system is also predicted by the numerical simulation, presented by Myers *et al.* [45]. In the presence of LF the ion transit time  $\tau_{ion}$  is less than the LF period  $\tau_{LF}$ , i.e., the ions cross the sheath in a fraction of the LF cycle and they reach the electrode with an energy equal to the instantaneous sheath potential drop (see the calculated  $\tau_{ion} / \tau_{LF}$  for the 3 investigated ions, presented in Sec. 5.2).

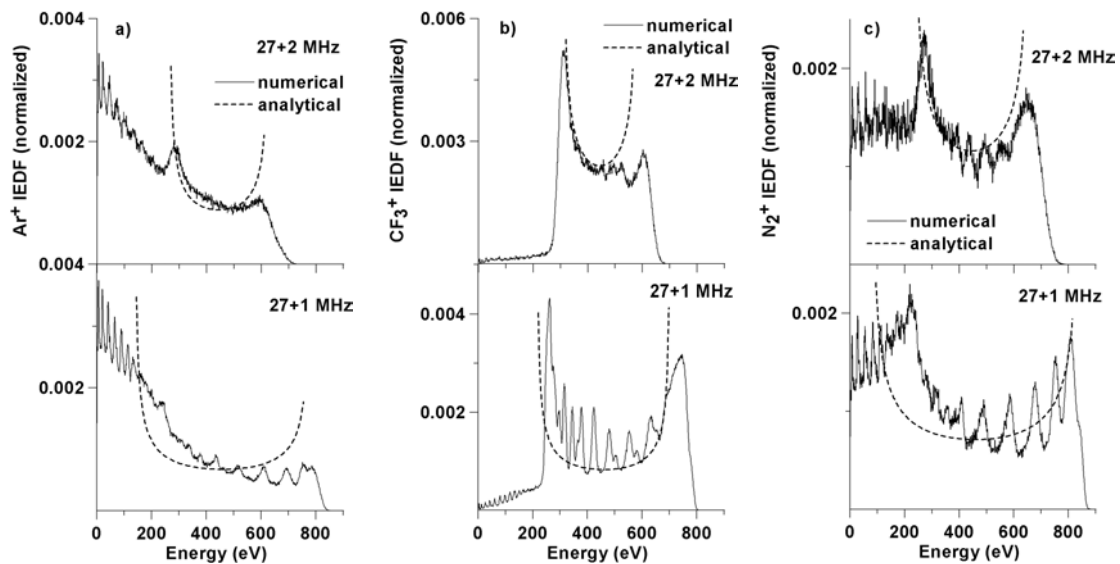


FIGURE 5.4.  $\text{Ar}^+$  (a),  $\text{CF}_3^+$  (b), and  $\text{N}_2^+$  (c) IEDFs at the powered electrode, averaged over two LF (2 MHz) cycles and over one LF (1 MHz) cycle in the dual-frequency reactor at pressure 30 mTorr and applied voltage amplitude 700 V (solid lines). The analytical calculation results are given with the dashed lines.

The two outstanding peaks in the profiles, presented in Fig. 5.4, correspond to the averaged minimum and maximum sheath potentials [cf. with Fig. 5.1 (a), dashed line]. The peak intensity at the lower energy is higher because the sheath potential has an average minimum value for a longer time than an average maximum value.

The influence of the collisions is the same as discussed in the conventional cc RF (13.56 MHz) reactor (see above). However, at the  $(27+1)$  MHz scheme secondary peaks are observed in the  $\text{CF}_3^+$  IEDF although no charge transfer collisions are included. The reason is probably the frequency of 1 MHz (2 times lower compared to 2 MHz) in which the ions respond to the instantaneous HF potential as a function of the LF.

The results of the simple analytical model developed in Sec. 5.2 are in good agreement with the simulation results in the  $(27+2)$  MHz regime (Fig. 5.4, upper part) and to a lesser extent with the simulation results in the  $(27+1)$  MHz regime (Fig. 5.4, lower part). Although the analytical model does not consider collisions we suggest that this consistency is a result of the good sheath potential waveform approximation. The energy width is calculated from Eq. (5.13) with the values of  $\overline{V}_s$  and average sheath width  $s$ , obtained from the simulation. The parameter  $\lambda_2$  is determined from the plot of the sheath potential (see Sec. 5.2). In the  $(27+2)$  MHz regime the calculated  $\overline{V}_s$ ,  $s$  and  $\lambda_2$  are equal to 445 V,  $6.8 \times 10^{-3}$  m, and 0.55, respectively. The plots are fitted in such a way that the analytical value of  $f(E)$  at  $e\overline{V}_s$  is equal to that calculated in the simulation. Hence, we should not focus on the absolute values of the analytical curves, but only on the energy width and the position of the 2 peaks. As it can be seen in the  $(27+1)$  MHz scheme  $2\pi\tau_{ion} / \tau_{LF}$  is larger than but close to one (see Sec. 5.2) and consequently, Eq. (5.8) is not valid, which leads to a discrepancy between the numerical and analytical calculations of the energy width and the position of the peaks (see Fig. 5.4, lower part). In this regime the calculated  $\overline{V}_s$ ,  $s$  and  $\lambda_2$  are equal to 459 V,  $7.4 \times 10^{-3}$  m, and 0.52, respectively.

The present results show that the developed analytical model can be used to predict the positions of the primary peaks in the dual-frequency regime if the condition (5.8) is satisfied.

Finally, the IEDFs at different times of the HF cycle in the single-frequency regime and at different times of the LF cycle in the dual-frequency regime are presented in Figs. 5.5 and 5.6. The  $\text{Ar}^+$  IEDF in single- and dual-frequency reactors is shown in Figs. 5.5 (a) and (b), respectively. The  $\text{CF}_3^+$  IEDF in single- and dual-

frequency reactors is shown in Figs. 5.6 (a) and (b), respectively. The profile of the  $N_2^+$  IEDF is similar to the  $Ar^+$  IEDF, and is therefore not shown. Obviously, in the HF regime the ions respond only to the average sheath drop and their energy distribution is peaked close to  $e\overline{V_s}$  ( $\overline{V_s}$  is calculated to be 285V) [Figs. 5.5(a) and 5.6(a)]. In the dual-frequency regime [Figs. 5.5(b) and 5.6(b)] a considerable modulation of the IEDF is observed during the LF cycle.

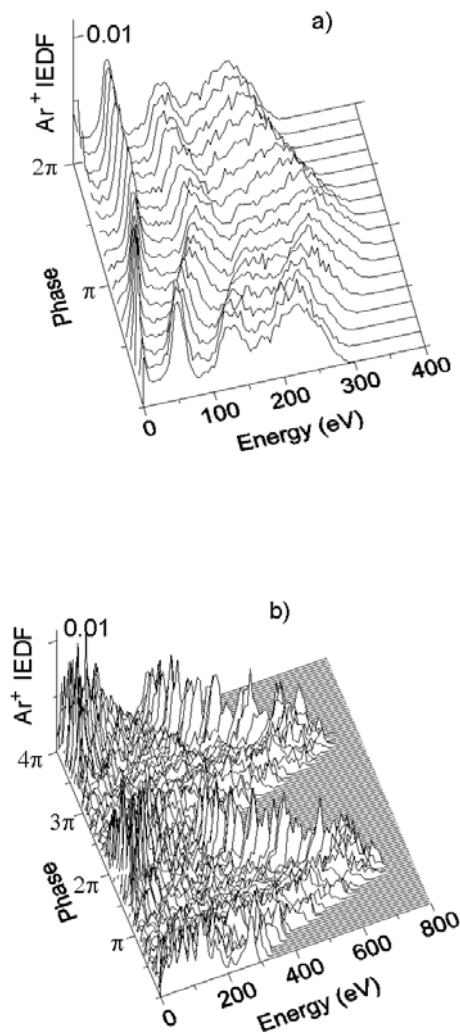


FIGURE 5.5.  $Ar^+$  IEDF at different phases in one HF cycle in the single- (13.56 MHz) frequency reactor (a) and at different phases in two LF cycles in the dual- (27 + 2 MHz) frequency reactor (b) at pressure 30 mTorr and applied voltage amplitude 700 V.

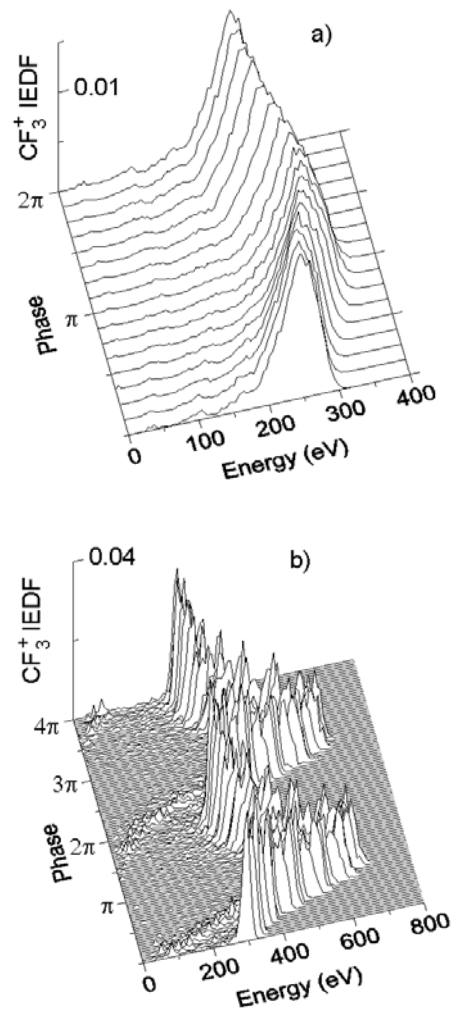


FIGURE 5.6.  $CF_3^+$  IEDF at different phases in one HF cycle in the single- (13.56 MHz) frequency reactor (a) and at different phases in two LF cycles in the dual- (27+2 MHz) frequency reactor (b) at pressure 30 mTorr and applied voltage amplitude 700 V.

The ion transit time is close to the LF period (see the calculated  $\tau_{ion} / \tau_{LF}$  given in Sec. 5.2) and the ions respond to the instantaneous sheath potential. The time dependence in the RF cycle presented in Figs. 5.5 and 5.6 is a demonstration of the main observations summarized in the introduction.

Finally, because of the importance of ion-molecule collisions for the calculation of the IEDFs, cross-section data used in the model are discussed briefly once again. The  $Ar^+$ -Ar,  $N_2$  and  $N_2^+$ -Ar,  $N_2$  elastic and charge transfer cross-section

data are presented in Figs. 2.13 and 2.14, respectively. It can be seen that the cross-sections for the resonant charge transfer for both ions exceed the cross-sections for elastic collisions for energies above 1 eV. Any reactive collision of  $\text{CF}_3^+$  with  $\text{CF}_4$ , after which there is no production of the ion, only its energy is reduced more or less significantly [see Fig. 2.16, curve (5)], cannot be considered as charge transfer. The reason is that the post-collision velocity of the ion is not close to the thermal velocity of the neutrals (see Sec. 2.3.8 for calculation of the post-collision velocities). The presented theoretical cross-section, which is the sum of all reactive  $\text{CF}_3^+ + \text{CF}_4$  collision cross-sections [Fig. 2.16, curve (3)] is about four times less in the range of relative energy 20 – 200 eV than the values experimentally measured by Peko *et al.* [103]. The influence of the two cross-section sets on the results can be investigated in a future work.

## 5.5 Summary

$\text{Ar}^+$ ,  $\text{CF}_3^+$ , and  $\text{N}_2^+$  IEDFs are numerically investigated in  $\text{Ar}/\text{CF}_4/\text{N}_2$  discharges in cc single- and dual-frequency reactors by our one-dimensional PIC/MC model. The influence of pressure, applied voltage amplitude and applied frequency regime on the IEDFs is discussed.

The simulations are carried out over a wide range of pressure and applied voltage amplitude covered in the conventional cc plasma etching reactors. The results show that the IEDFs shift toward low energies with increasing pressure or decreasing applied voltage amplitude. The influence of the different types of ion-neutral collisions is presented for the three investigated ions.

The dependence on the frequency regime is investigated by simulations in single- (13.56 MHz) and dual-frequency (27 + 2 MHz or 27 + 1 MHz) cc reactors. It is observed that the dual-frequency regime provides a significantly wider ion bombardment energy range in comparison with the single-frequency regime. An analytical model for the IEDF in a collisionless sheath for the dual-frequency reactor is developed and a comparison with the numerical calculation is discussed. The analytical model can be used to predict the position of the primary peaks.

Finally, the time dependences of the IEDFs in an RF cycle in single- (HF) and dual- (HF-LF) frequency reactors are presented. It is shown that in the HF regime the IEDF slightly depends on the phase of the RF cycle, whereas in the HF-LF regime the IEDF is greatly modulated during the LF cycle.



## **Chapter 6**

# **INFLUENCE OF THE EXTERNAL PROCESS PARAMETERS ON PLASMA CHARACTERISTICS IN DUAL- FREQUENCY REACTORS**

### **6.1 Introduction**

In Chapters 4 and 5, the influence of a secondary, low, frequency on the plasma characteristics is studied and a detailed investigation of the ion energy distribution function (IEDF) in Ar/CF<sub>4</sub>/N<sub>2</sub> plasmas by means of the particle-in-cell/Monte Carlo (PIC/MC) method is made [60, 61]. The PIC/MC method was employed also to study asymmetric dual-frequency reactors [64-67] and to investigate the optimal reactor parameters for independent control of ion current and ion bombardment energy [67] in Ar plasmas. However, the electronegative gas CF<sub>4</sub> is a basic component in gas mixtures for plasma etching of Si or SiO<sub>2</sub>. Discharges in electronegative gases behave differently from discharges in electropositive gases, like pure Ar (see Chapter 3) [59]. Therefore, investigation of discharges in CF<sub>4</sub> mixtures is important in further optimization of the etching process.

This chapter presents the study of the complex gas mixture Ar/CF<sub>4</sub>/N<sub>2</sub>, used for etching in a dual-frequency reactor at different applied frequencies and voltages of the two power sources by means of a PIC/MC method. Special attention is paid to the conditions when the independent control of the ion flux and energy is possible because this is the main advantage of the two-frequency scheme. To our knowledge there are only computer simulations of the influence of the LF source in Ar discharges (e.g. Refs. 64-67). There are investigations of complex gas mixtures by hybrid or fluid models, however, in magnetically enhanced cc single- and dual-frequency reactors (e.g. Refs. 104 and 105).

In Sec. 6.2 the input parameters and the outline of the model are given. In Sec. 6.3 the results of the simulation, i.e. the plasma and ion current density,

electron and ion average energies and energy distributions, average sheath potential and width, and ionization rates, are presented and discussed. In order to facilitate the reader, who might be more familiar with the applied power than voltage, we present the calculated power of the two sources, corresponding to the applied voltages in Sec. 6.4. Section 6.5 presents comparison with measured results for the electron density in the plasma center and the ion current density at the electrodes. Finally, in Sec. 6.6 a summary is given.

## 6.2 Input Data

The considered dual-frequency reactor and model are the same as presented in Chapter 4 and 5. The applied voltage is given by Eq. (1.1).

The calculations are performed for an Ar/CF<sub>4</sub>/N<sub>2</sub> mixture at a molar ratio of 0.8/0.1/0.1 at a pressure of 30 mTorr. The simulation grid is uniform and it consists of 100 cells. The electron time step varies from 10<sup>-11</sup> till 3.7 × 10<sup>-11</sup> s depending on the electron plasma frequency. To speed up the calculation, the ion time step is set to be 25 to 50 times longer than the electron time step, and different weights for electrons and ions are applied. The choice of the grid spacing and the time steps is defined by the accuracy criteria for PIC/MC codes with explicit mover (see Sec. 2.9).

One set of simulations is carried out at a LF of 2 MHz and a HF of 27, 40, 60 and 100 MHz and keeping HF or LF voltage amplitude constant, while the other voltage amplitude is varying. Another set of simulations is performed for (27 + 2) and (27 + 1) MHz at different values of constant HF voltage amplitude, while the LF voltage amplitude is varying. An additional set of simulations is carried out in a single-frequency reactor at a HF of 60 MHz and varying the driving voltage amplitude in order to make a comparison with the dual-frequency scheme.

The average electron and ion energies  $\langle \varepsilon_{e,i} \rangle$  presented below are obtained from the electron energy distribution function (EEDF) and the IEDF, respectively, denoted as  $F(\varepsilon_{e,i})$ ,

$$\langle \varepsilon_{e,i} \rangle = \frac{\int_0^{\infty} \varepsilon_{e,i} F(\varepsilon_{e,i}) d\varepsilon}{\int_0^{\infty} F(\varepsilon_{e,i}) d\varepsilon}. \quad (6.1)$$

## 6.3 Results and discussion

### 6.3.1 From HF to VHF, keeping the HF voltage amplitude constant and varying the LF voltage amplitude.

Figure 6.1 presents the simulation results, averaged over one or two LF cycles, for the plasma density in the discharge center (a), the ion current density at the powered electrode (PE) (b), the electron energy in the discharge center (c), the sheath potential (d) and width (e), as a function of the LF voltage amplitude  $V_{LF}$ . The calculated characteristics for the (27+2) MHz case are averaged over two LF cycles since one LF cycle does not contain an integer number of HF cycles. The operating conditions are the following: the HF is chosen to be 27, 40, 60 and 100 MHz and the LF is 2 MHz; the HF voltage amplitude  $V_{HF}$  is kept at 200 V and the LF voltage amplitude is 0, 100, 200, 300 or 400 V. It can be seen that for all investigated frequency schemes the introduction of the second LF voltage source decreases the plasma density (i.e. sum of all charged particle densities) in the discharge center [Fig. 6.1(a)]. Further, the drop is not very pronounced for the (60+2) and (100+2) MHz cases, while it decreases more clearly with increasing LF voltage for the other two frequency schemes, i.e. (27+2) and (40+2) MHz. This means that for the latter cases the applied LF has influence on the plasma density as well as on the ion current density and electron energy, as it is observed below [Fig. 6.1(b) and (c)] and decoupling is impossible to be achieved. A drop of the plasma density with increase of the LF voltage was also observed in computer simulations of Ar discharges in a dual-frequency reactor [66, 67]. As it is shown below the sheath width increases with the increase of the LF voltage. The expansion of the sheath width leads to decrease of the sheath capacitance, and therefore the discharge current decreases with increasing the LF voltage. The decrease in the discharge current causes a decrease in the ionization rate and consequently in the plasma density.

The ion current density exhibits a similar behavior as the plasma density, with an exception for the case of (27+2) MHz [Fig. 6.1(b)]. For this case the ion current density shows a minimum at LF voltage of 100 V and because of that, we made an additional simulation at 50 V. It is observed that the ion current decreases with varying the LF voltage from 0 till 100 V and it increases with further increase of the LF voltage, i.e. the ion loss increases.

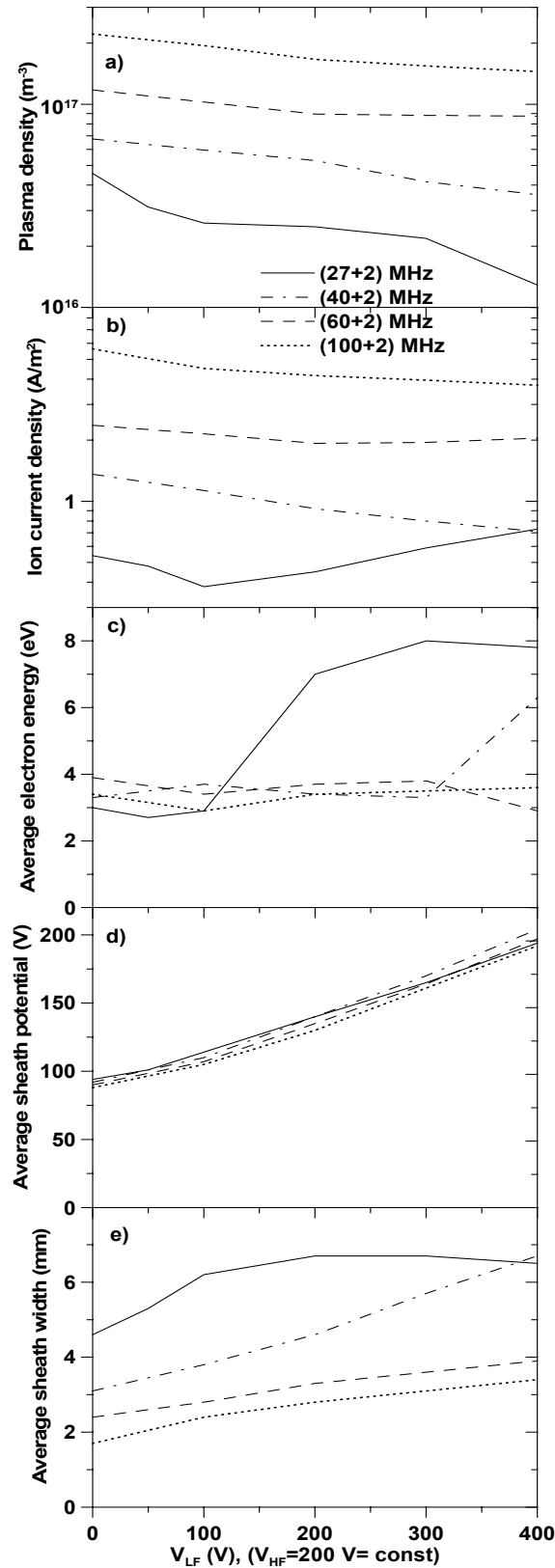


FIGURE 6.1. Calculated plasma density in the discharge center (a), ion current density at the PE (b), electron energy in the discharge center (c), sheath potential (d) and width (e), averaged over the LF cycle, as a function of the LF voltage amplitude, at a HF voltage amplitude of 200 V for the (27+2), (40+2), (60+2) and (100+2) MHz regimes.

On the other hand, the electron energy also increases abruptly after 100 V [Fig. 6.1(c)] and consequently the ionization rate, i.e. the ion production increases. The net effect of these processes is, however, a drop in the plasma density. The average electron energy and the ion current show little dependence on the LF voltage for the (60+2) and (100+2) MHz cases. Hence, in first instance, we would conclude that the frequency ratio should be high enough to achieve decoupling of the ion flux and energy. However, further simulations at HF of 27 MHz and at different LF and applied voltages show that the frequency ratio is not the parameter defining the decoupling. These simulations are presented below in a separate section, where the abrupt change in the plasma behavior at a ratio  $V_{LF}/V_{HF}$  of 1 and above, when the applied HF is 27 MHz, is discussed.

A rise in the LF voltage leads to an increase of the sheath potential and to expansion of the sheath [Fig. 6.1(d) and (e)]. A similar behavior of the sheath width was observed experimentally [18, 19] and numerically [66, 67]. On the other hand an increase of the applied HF contracts the sheath, as it is also found in single-frequency reactors [51, 52, 106] so that in the (60+2) and (100+2) MHz cases the sheath width increases more slowly than in the (27+2) and (40+2) MHz regimes. The sheath edge position is defined at the grid point where the quasi-neutrality of the plasma is broken.

Figure 6.2 presents the average bombardment energy of the  $\text{Ar}^+$  (a),  $\text{CF}_3^+$  (b), and  $\text{N}_2^+$  (c) ions. The operating conditions are the same as in Fig. 6.1. The ion energy increases with LF voltage because the sheath potential increases [Fig. 6.1(d)].

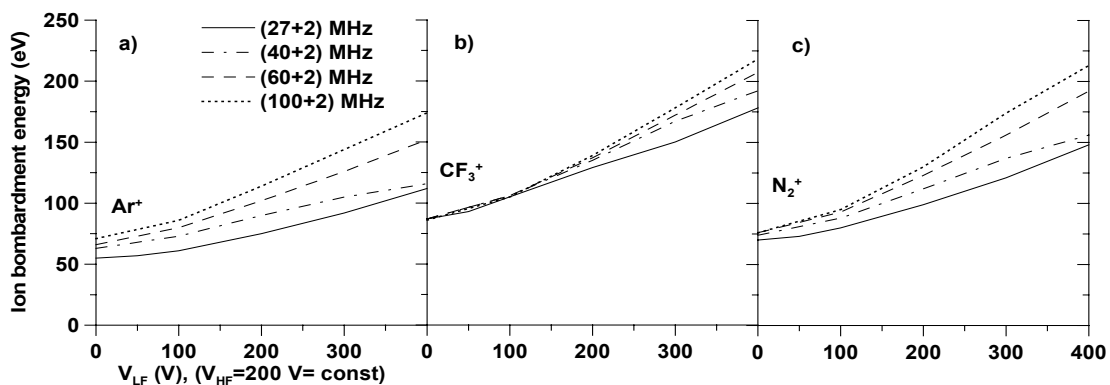


FIGURE 6.2. Calculated  $\text{Ar}^+$  (a),  $\text{CF}_3^+$  (b), and  $\text{N}_2^+$  (c) average bombardment energy as a function of the LF voltage amplitude. The operating conditions are the same as in Fig. 6.1.

Since the  $\text{CF}_3^+$  ions do not experience charge exchange (see Chapter 2 for details about ion-neutral collisions), and therefore retain their energy, their average energy at the electrodes is higher, in comparison with the other two ions for the same operating conditions.

Concerning the influence of the HF, it appears from Fig. 6.1 that the plasma density and ion current increase, and the sheath width decreases with HF, for the same LF voltage. The electron energy is between 3 and 4 eV for all frequency conditions for LF voltages up to 100 V, but only for the (60+2) and (100+2) MHz cases, it remains at similar values for higher LF voltages, i.e. it is almost not affected by the HF above 60 MHz for any investigated LF voltages. If we exclude the (27+2) MHz case, the average sheath potential decreases very slightly with the primary frequency for the same applied LF voltage [Fig. 6.1(d)]. The average ion energy (Fig. 6.2) increases with HF because the sheath width decreases, and consequently the ions experience fewer charge exchange and elastic collisions with neutrals on their way to the electrodes, and therefore they retain their energy. A similar dependence of the plasma characteristics on the driving frequency was found in single-frequency reactors [51, 52, 106].

It is not necessary to present the IEDF for all simulated operating conditions, because they exhibit similar behavior but we have chosen to present them at HF and LF voltages of 200 V for the four frequency schemes (see Fig. 6.3). The average sheath potential is calculated to be between 130 and 140 V and consequently, the IEDF has two peaks and the energy width is centered at this value [see Eq. (5.13) and Chapter 5] for all frequency regimes. The second peak of  $\text{Ar}^+$  and  $\text{N}_2^+$  IEDFs for the (27+2) MHz case is, however, not well developed because of the frequent charge exchange and elastic collisions with neutrals (see Chapters 2 and 5).

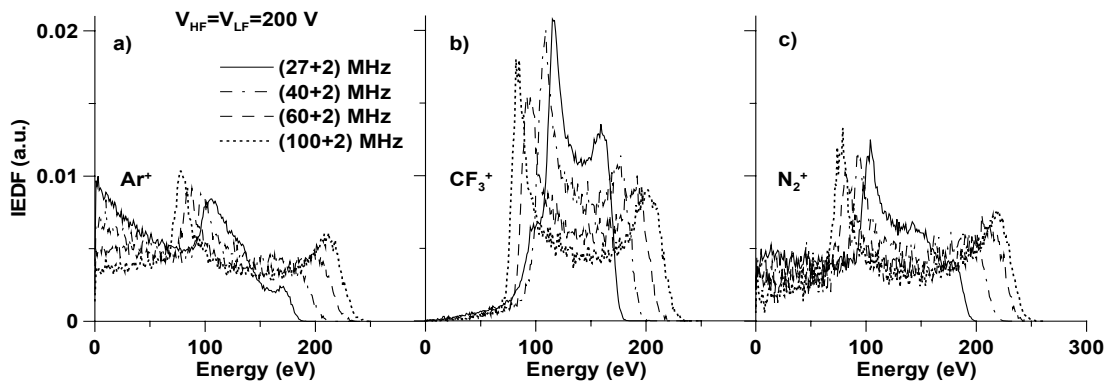


FIGURE 6.3. Calculated  $\text{Ar}^+$  (a),  $\text{CF}_3^+$  (b), and  $\text{N}_2^+$  (c) IEDF, averaged over the LF cycle, at HF and LF voltage amplitudes of 200 V for the (27+2), (40+2), (60+2) and (100+2) MHz regimes.

Indeed, the sheath width is largest at the  $(27 + 2)$  MHz regime, which leads to more collisions in comparison with the other frequency regimes.

The bi-modal structure of the IEDF in the dual-frequency reactors was discussed in detail in Chapter 5 [61]. Figure 6.3 shows that the energy width,  $\Delta E$ , increases with the HF when all the other operating parameters are the same. According to Eq. (5.13) the energy width does not depend on the HF explicitly. However, it depends on the average sheath width, which decreases with increase of the primary frequency [Fig. 6.1(e)]. The average sheath potential and the parameter  $\lambda_2$  are calculated to be almost the same for all considered frequency schemes. Consequently, the energy width increases with the HF. The same behavior was observed for the other applied LF voltage amplitudes.

In the study presented in Chapter 4 it is found that highly energetic  $F^-$  ions reach the electrodes for a short time of the cathodic part of the LF cycle [60]. In the presence of low frequency and strong electric field, the light  $F^-$  ions are no longer confined in the bulk plasma and they partially respond to the instantaneous electric field. In the present investigation it is observed that the maximum value of the  $F^-$  flux, which is calculated to be about  $10^{16} \text{ m}^{-2}\text{s}^{-1}$  for all the frequency regimes, does not increase considerably with increasing the LF voltage. Indeed, since the electric field in the sheath becomes stronger more  $F^-$  ions acquire high energy so that more ions can reach the electrodes. On the other hand, the plasma density decreases considerably for the  $(27 + 2)$  MHz regime and stays more or less the same for the other frequency regimes when the LF voltage increases. Therefore, the maximum value of the  $F^-$  flux does not change with increase of the LF voltage amplitude. However, the  $F^-$  ions reach the electrodes for a longer time of the LF cycle when the LF voltage increases, and consequently the time-averaged flux increases. The incident negative ion flux on the wafer reduces the local charging, and hence, it would be more useful to present the ratio of the  $F^-$  flux to the positive ion flux at the electrodes than to present only the negative ion flux. Figure 6.4 shows the ratio of the  $F^-$  flux to the positive ion flux, both averaged over the LF cycle, as a function of the LF voltage for the different frequency regimes. The operating conditions are the same as in Fig. 6.1. The ratio increases with LF voltage, except for the  $(27 + 2)$  MHz regime when the LF voltage increases from 300 to 400 V. This is because the positive ion flux also increases with the LF voltage [cf. Fig. 6.1(b)]. The ratio decreases with increasing the HF because the time-averaged positive flux increases while the time-averaged  $F^-$  flux decreases slightly with the HF. It is found that the negative ion flux is 0 when the LF voltage is 0, i.e. in single-frequency reactors, for all investigated HFs. For the  $(60 + 2)$  and  $(100 + 2)$  MHz cases, the  $F^-$  flux is close to 0 even when a LF voltage of 100 V is applied [Fig. 6.4].

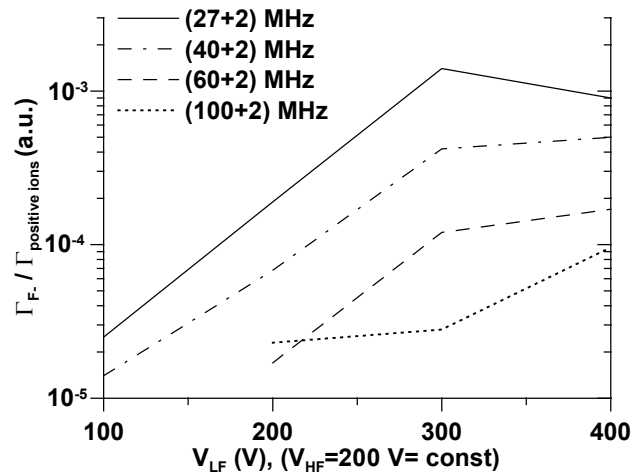


FIGURE 6.4. Calculated ratio of F<sup>-</sup> flux to positive ion flux at the electrodes, averaged over the LF cycle, as a function of the LF voltage amplitude. The operating conditions are the same as in Fig. 6.1.

### 6.3.2 From HF to VHF, varying the HF voltage amplitude and keeping the LF voltage amplitude constant.

Figure 6.5 presents the simulation results, averaged over one or two LF cycles, for the plasma density in the discharge center (a), the ion current density at the powered electrode (b), the electron energy in the discharge center (c), the sheath potential (d) and width (e), as a function of the HF voltage amplitude. The operating conditions are the following: the HF is chosen to be 27, 40, 60 or 100 MHz and the LF is 2 MHz; the HF voltage amplitude is 100, 200, 250, 300 or 400 V and the LF voltage amplitude is kept at 200 V. Simulations for (100 + 2) MHz with a HF voltage above 250 V could not be performed, because the plasma density increases so much that the bulk plasma expands in the reactor volume.

The plasma density increases with HF voltage for all investigated HF frequencies, with an exception for (27 + 2) MHz. In the latter case, it varies slightly from  $2.4 \times 10^{16}$  to  $2.8 \times 10^{16} \text{ m}^{-3}$  when the HF voltage increases from 100 to 300 V and then it goes up to  $4 \times 10^{16} \text{ m}^{-3}$  at a HF voltage of 400 V. The ion current shows a similar behavior as the plasma density for the (27 + 2) MHz case [Fig. 6.5(b)]. At the same time the average electron energy decreases from 8 to 3 eV with increasing HF voltage [Fig. 6.5(c)] and it should therefore be expected that the ionization rate would drop, which means that the plasma density would decrease because the ion loss also increases to some extent.

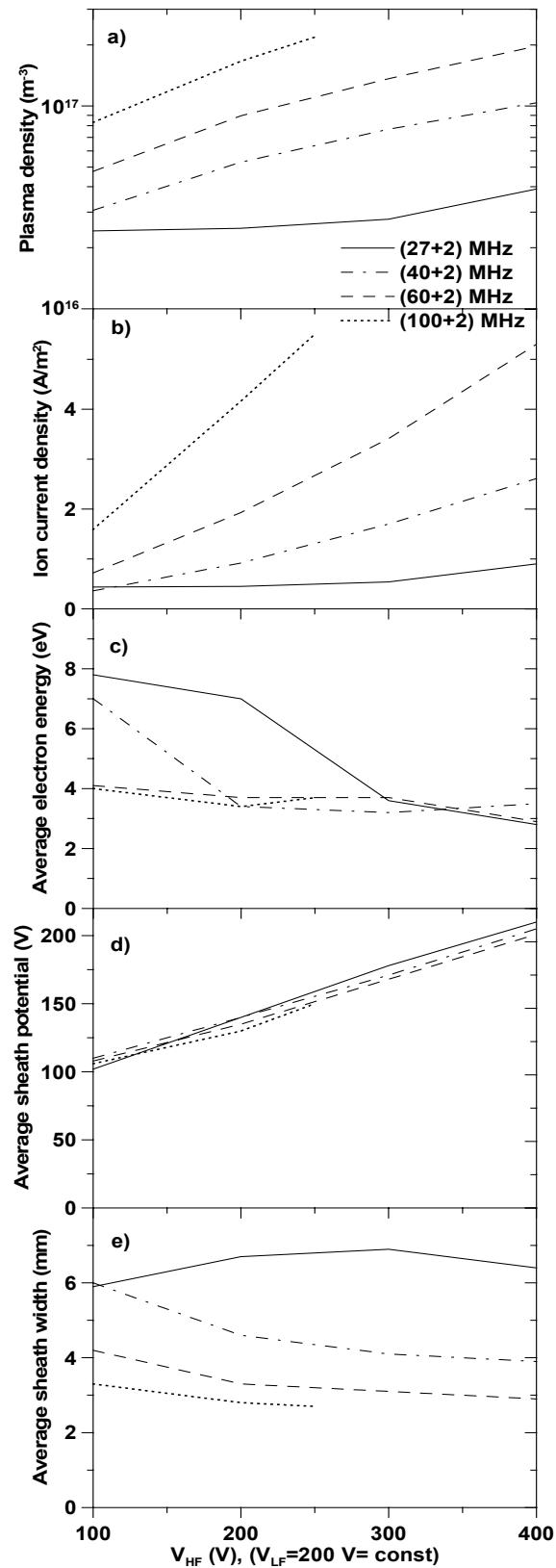


FIGURE 6.5. Calculated plasma density in the discharge center (a), ion current density at the PE (b), electron energy in the discharge center (c), sheath potential (d) and width (e), averaged over the LF cycle, as a function of the HF voltage amplitude at a LF voltage of 200 V for the (27+2), (40+2), (60+2) and (100+2) MHz regimes.

However, the average electron energy is not always a good characteristic of the electron energy because the EEDF  $F_e(\varepsilon)$  is usually non-Maxwellian. Therefore, we present the electron energy probability function (EEDF)  $f_e(\varepsilon) = F_e(\varepsilon)\varepsilon^{-1/2}$  and the ionization rate (sum of all ionization rates of electrons with Ar, CF<sub>4</sub> and N<sub>2</sub>) for the (27+2) MHz case at different HF voltages, in Fig. 6.6(a) and (b), respectively. The number of low energy electrons increases hundred times with HF voltage while the number of high energy electrons responsible for ionization increases about ten times. This explains the drop of the average electron energy [Fig. 6.5(c)] and the simultaneous increase of the ionization rate [Fig. 6.6(b)]. The peaks in the ionization rate shift with the HF voltage because of the electron density profile. A more detailed discussion follows in Sec. 6.3.4, which is focused on the influence of the LF source at a HF of 27 MHz.

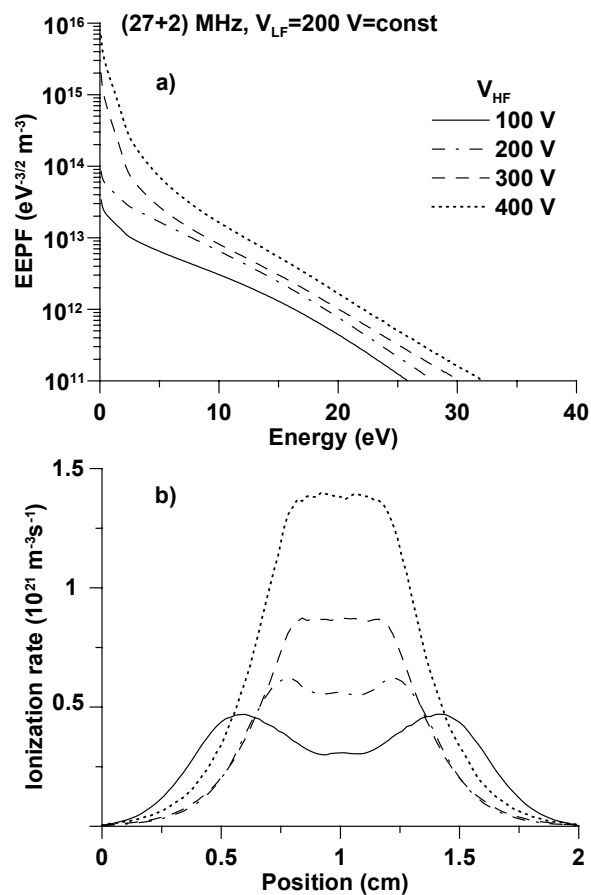


FIGURE 6.6. Calculated EEPF (a) and electron impact ionization rates (b), averaged over the LF cycle, at a LF voltage of 200 V and different HF voltages for the (27+2) MHz regime.

For the other frequency regimes, the plasma density increases more clearly and it scales linearly with the HF voltage amplitude, which is the same voltage scale law as in single-frequency reactors [1, 50]. The ion current density also increases with HF voltage, and as it will be shown below, it scales as  $j \sim V_{HF}^{3/2}$  (see Sec. 6.3.3). Further, the electron energy is almost not affected by the HF voltage for the (60+2) and (100+2) MHz regimes [Fig. 6.5(c)]. For (40+2) MHz it decreases from 7 to 3.5 eV when the HF voltage increases from 100 to 200 V and then it stays more or less the same with further rise of the HF voltage. The electron energy in conventional cc reactors was found to be essentially independent of the applied voltage [50]. Consequently, the secondary voltage source has no influence on the plasma density, ion flux and electron energy, except for the (27+2) MHz case and to some extent for (40+2) MHz. In the next section we consider in detail the (60+2) MHz regime, to show that the plasma density and ion flux can be controlled independently by the HF voltage source.

The sheath potential increases linearly with the applied HF voltage amplitude [Fig. 6.5(d)]. The sheath width increases slightly for (27+2) MHz and it decreases somewhat for the other regimes [Fig. 6.5(e)].

Figure 6.7 presents the average bombardment energy of the  $Ar^+$  (a),  $CF_3^+$  (b), and  $N_2^+$  (c) ions, as a function of the HF voltage amplitude. The operation conditions are the same as in Fig. 6.5. The ion energy increases with HF voltage because the sheath potential increases [Fig. 6.5(d)].

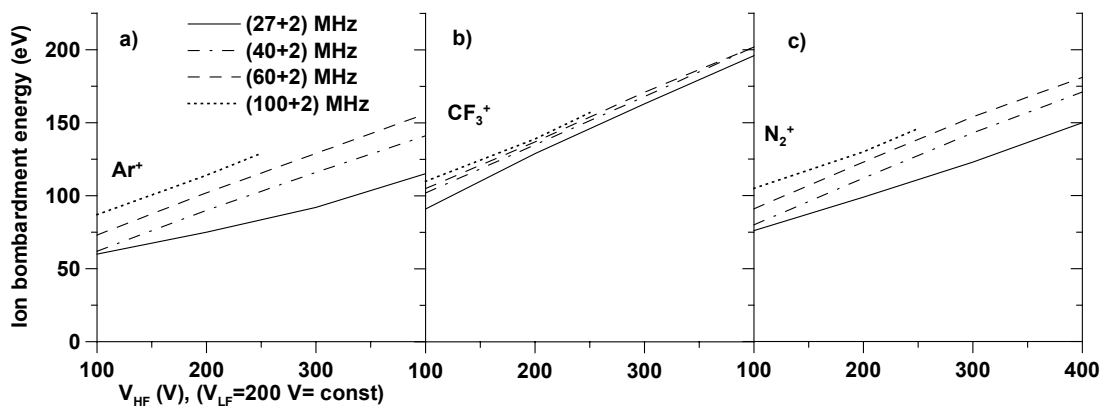


FIGURE 6.7. Calculated  $Ar^+$  (a),  $CF_3^+$  (b), and  $N_2^+$  (c) average bombardment energy as a function of the LF voltage amplitude. The operating conditions are the same as in Fig. 6.5.

The influence of the applied HF on the plasma characteristics is the same as in the previous section, where the HF voltage is kept constant and the LF voltage is varying (see above).

### **6.3.3 Independence of the plasma density, ion current density and electron energy from the LF voltage source at (60+2) MHz.**

As it can be seen from the simulation results discussed above, the LF voltage has significant effect on the plasma characteristics when the HF is 27 MHz. For (40+2) MHz the dependence on the LF voltage is strong only when the LF voltage amplitude is twice as high as the HF voltage amplitude, i.e. when  $V_{LF}$  is 400 or 200 V and  $V_{HF}$  is 200 or 100 V (see Fig. 6.1 and 6.5, respectively). For the (60+2) and (100+2) MHz regimes, the plasma density, ion current density and electron energy are nearly independent from the LF voltage when the HF voltage is kept constant, and when the LF voltage is kept constant they scale with the HF voltage similar to that in single-frequency reactors. In this section, we consider the simulations performed for the (60+2) MHz regime and present additional simulation results in a single-frequency reactor at a driving frequency of 60 MHz and applied voltage amplitude of 100, 200, 300 or 400 V. Figure 6.8 shows the simulation results, averaged over one LF cycle, for the plasma density in the discharge center (a), the ion current density at the powered electrode (b), and the electron energy in the discharge center (c). The solid lines denote the results as a function of the LF voltage when the HF voltage is kept constant at 200 V. The dashed lines represent the calculations as a function of the HF voltage keeping the LF voltage constant at 200 V. Finally the dash-dotted lines illustrate the results for a single-frequency reactor of 60 MHz, as a function of the driving voltage, which is noted as  $V_{HF}$ .

The plasma density slightly decreases from  $10^{17}$  to  $9 \times 10^{16}$  m<sup>-3</sup> when the LF voltage increases from 100 to 400 V and the HF voltage is kept at 200 V (solid line). The ion current density is also nearly independent from the LF voltage and its value is about 2 A/m<sup>2</sup>. The average electron energy in the bulk varies between 3 and 4 eV. It can be seen that the LF voltage does not affect the EEPF and ionization rate [Fig. 6.9 (a) and (b), respectively].

For the opposite operating condition, i.e. when the HF voltage is varying and the LF voltage is kept constant at 200 V (dashed line) it is found that the plasma density scales linearly with the HF voltage  $V_{HF}$  [Fig. 6.8 (a), dashed line]. It increases from  $5 \times 10^{16}$  to  $2 \times 10^{17}$  m<sup>-3</sup>. The dotted line presents the voltage scaling law: plasma density ( $n$ )  $\sim V_{HF}$ .

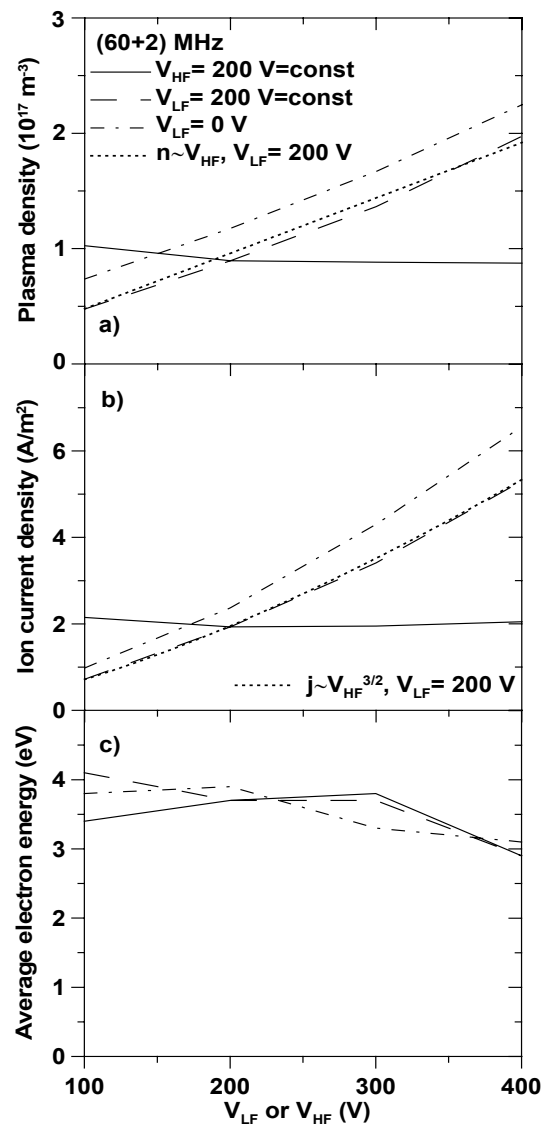


FIGURE 6.8. Calculated plasma density in the discharge center (a), ion current density at the PE (b), and electron energy in the discharge center (c), averaged over the LF cycle, as a function of the LF voltage amplitude (solid lines) or HF voltage amplitude (dashed lines) for the (60+2) MHz regime. The results for a single-frequency reactor at 60 MHz are shown as a function of the driving voltage (dash-dotted lines). Finally, the dotted lines present the scaling law of the plasma density  $n \sim V_{HF}^3$  (a) and of the ion current density  $j \sim V_{HF}^{3/2}$  (b) with the applied HF voltage amplitude at a LF voltage of 200 V.

The same scaling law was observed in single-frequency reactors [1, 50]. Consequently, the plasma density shows the same dependence on the driving

frequency, as if the second voltage source was not connected. However, the values of the plasma density are lower in comparison with the single-frequency regime at the same driving voltage amplitudes [compare the dashed and dash-dotted lines in Fig. 6.8(a)]. It was already observed that introducing the second voltage source decreases the plasma density for any of the investigated frequency schemes [Fig. 6.1(a)].

The ion current density  $j$  increases with HF voltage from 0.7 to 5.3 A/m<sup>2</sup> [Fig. 6.8(b), dashed line]. It is found to scale as  $j \sim V_{HF}^{3/2}$  [see the dotted line in Fig. 6.8(b)]. Simulation results in single-frequency regime show that the ion current density scales as  $j \sim V_{HF}^{1.45}$  [Fig. 6.8(b), dash-dotted line]. Therefore, like the plasma density, the ion current density shows the same dependence on the driving frequency as if the second voltage source was not connected, but its values are somewhat lower than that in the single-frequency reactor for the same HF voltage amplitude.

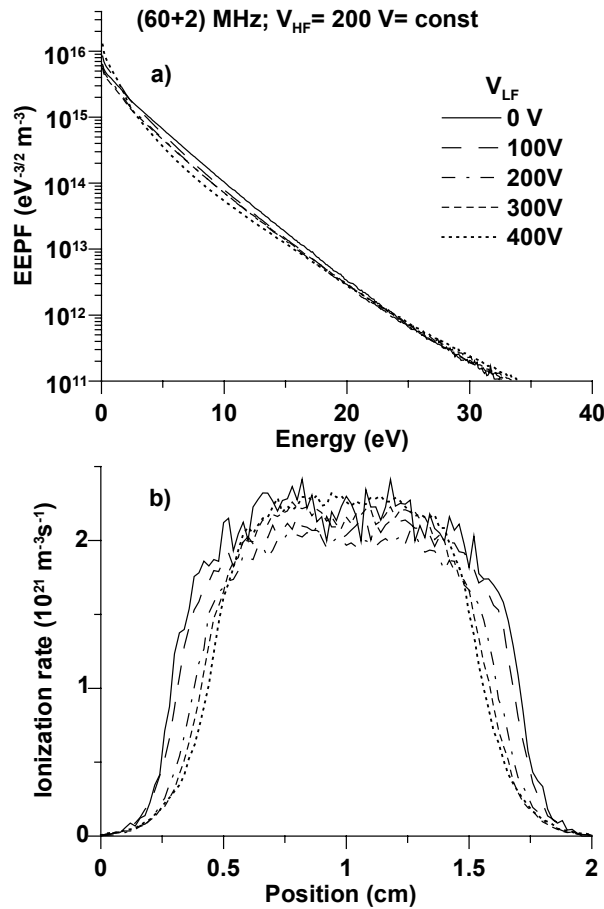


FIGURE 6.9. Calculated EEPF (a) and electron impact ionization rates (b), averaged over the LF cycle, at a HF voltage of 200 V and different LF voltages for the (60+2) MHz regime.

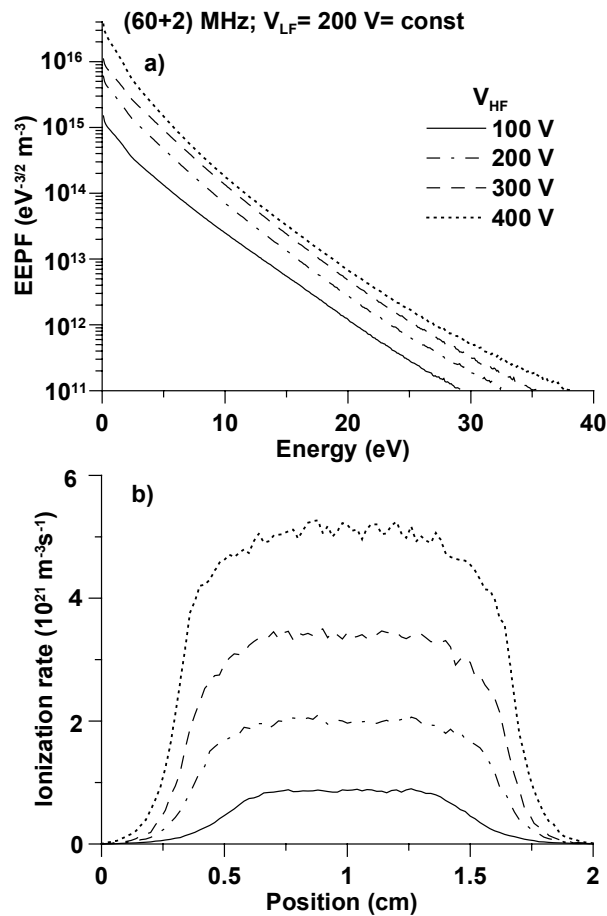


FIGURE 6.10. Calculated EEPF (a) and electron impact ionization rates (b), averaged over the LF cycle, at a LF voltage of 200 V and different HF voltages for the (60+2) MHz regime.

The electron energy in the bulk varies between 3 and 4 eV. It can be seen that the slope of the EEPF is almost the same for all investigated HF voltage amplitudes [Fig. 6.10(a)], and the distribution is more or less Maxwellian so that the average electron energy does not change considerably. However, the number of high-energy electrons increases with HF voltage and consequently the ionization rate also increases [Fig. 6.10(b)]. When only one frequency is applied, the behavior of the average electron energy [Fig. 6.8(c) dash-dotted line], as well as the EEPF and ionization rate are very similar. For that reason we do not present the calculated EEPF and the ionization rates in single-frequency regime here.

### 6.3.4 Dependence of the sheath potential and width, and the ion energy on the HF and LF voltage sources.

Below we discuss the simulation results of the sheath potential and width, and the ion energy for the (60+2) MHz case. However, it should be noted that these characteristics exhibit a similar behavior in the other investigated frequency regimes.

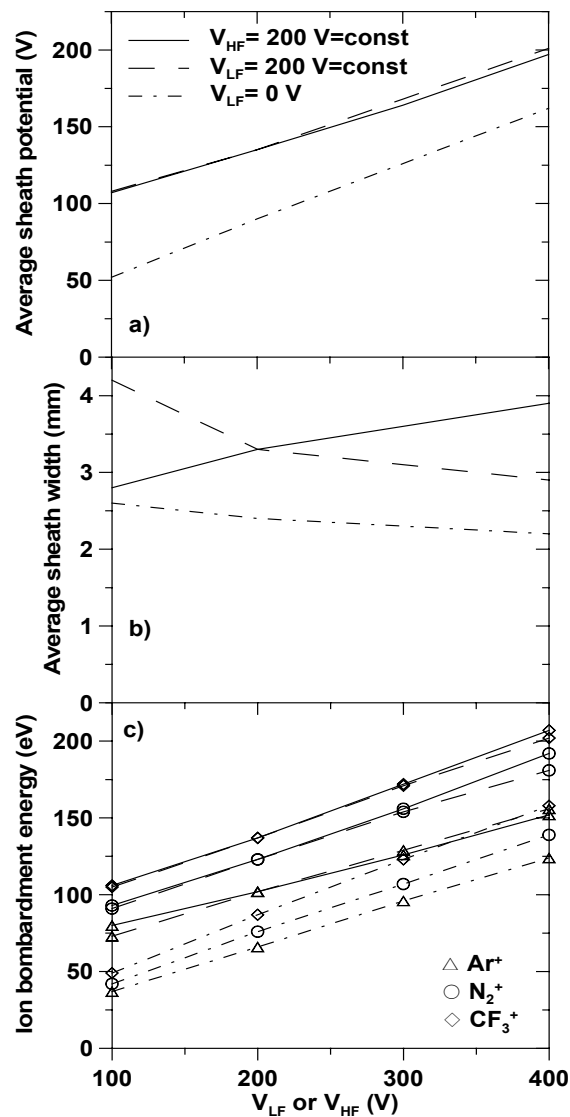


FIGURE 6.11. Calculated sheath potential (a) and width (b), and ion bombardment energy (c), averaged over the LF cycle, as a function of the LF voltage amplitude (solid lines) or HF voltage amplitude (dashed lines) for the (60+2) MHz regime. The results for a single-frequency reactor at 60 MHz are shown as a function of the driving voltage (dash-dotted lines).

The sheath potential increases linearly with the applied voltage and consequently with the LF or HF voltage amplitude [Fig. 6.11(a), solid and dashed lines, respectively, and see Eq. (1.1)].

The sheath expands from 2.8 to 3.9 mm [Fig. 6.11(b), solid line] with increasing the LF voltage, and it contracts from 4.4 to 2.9 mm when increasing the HF voltage in the dual-frequency regime [Fig. 6.11(b), dashed line], but it is wider in comparison with the single-frequency case for the same HF voltage (compare with dash-dotted line). The sheath width is essentially independent from the applied voltage in the single-frequency case [Fig. 6.11(b), dash-dotted line]. Other authors also observed that the applied voltage did not influence the sheath width in a single-frequency reactor [49, 50]. The average ion bombardment energy [Fig. 6.11 (c)] increases with both the LF or HF voltage amplitude, because the sheath potential increases with the applied voltage [see Fig. 6.11(a)].

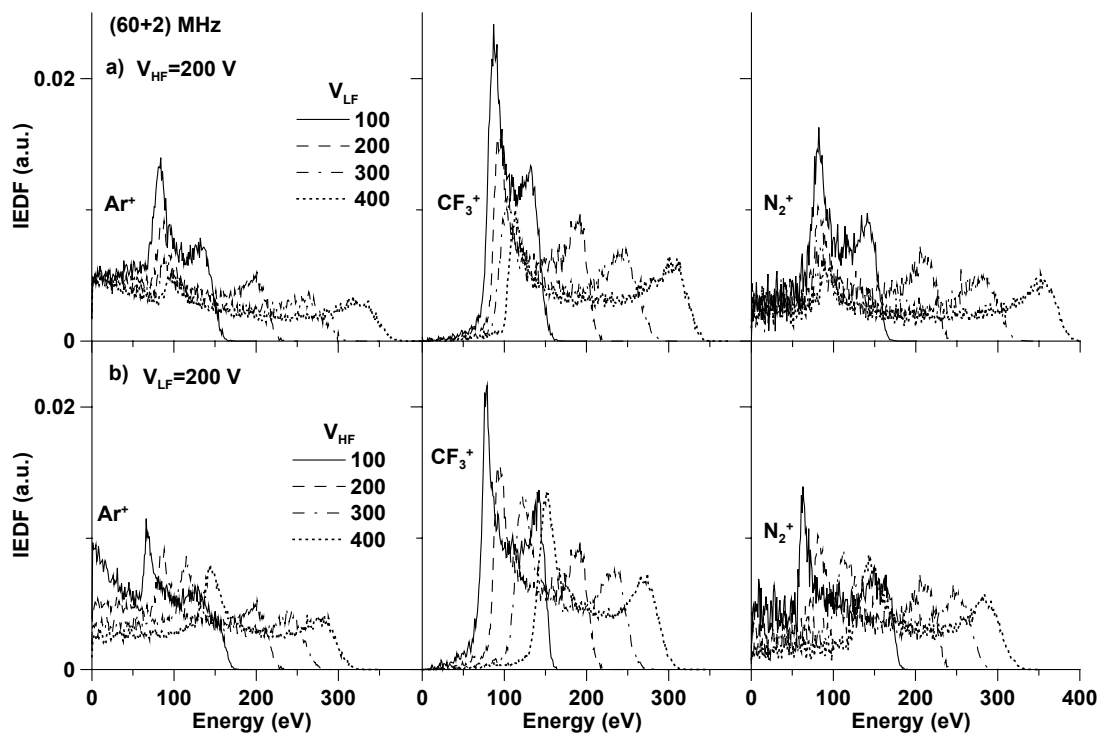


FIGURE 6.12. Calculated  $\text{Ar}^+$ ,  $\text{CF}_3^+$ , and  $\text{N}_2^+$  IEDF, averaged over the LF cycle, for the (60+2) MHz regime at a HF voltage amplitude of 200 V and different LF voltage amplitudes (a), and at a LF voltage amplitude of 200 V and different HF voltage amplitudes (b).

Figure 6.12 presents the IEDFs of the three considered positive ions in the  $(60+2)$  MHz regime at a LF voltage of 100, 200, 300 or 400 V and a HF voltage of 200 V (a); and at a HF voltage of 100, 200, 300 or 400 V and a LF voltage of 200 V (b). The IEDF is broader when the LF or HF voltage increases, while keeping the other voltage constant. It should be noted that the IEDF depends on the voltages in the same way for all frequency regimes. Hence, we present only the results here for  $(60+2)$  MHz.

The average ion energy is calculated to have similar values when the sum of the LF and HF voltages is the same [cf. solid and dashed lines in Fig. 6.11(c)] because the average ion energy follows the average sheath potential  $\overline{V}_s$ , in spite of the fact that the IEDF appears to be broader when the LF voltage amplitude is larger [for example, cf. the dotted lines in Fig. 6.12(a) and (b)]. The energy width is centered at  $e\overline{V}_s$  (see Chapter 5) and when the IEDF is wider the first maximum appears at lower energy if the  $\overline{V}_s$  is the same. Consequently, although the maximum energy is higher when the LF voltage is higher, the average ion energy has similar values in case of equal sum of HF and LF voltage amplitudes like the average sheath potential has similar values (see Fig. 6.11(a), solid and dashed lines).

Let us compare the  $\text{Ar}^+$  IEDF for HF and LF voltage amplitudes of 200 and 400 V, and 400 and 200 V, respectively, so that their sum is 600 V in both cases (Fig. 6.12, dotted lines). The energy width is about 230 eV at LF voltage of 400 V and HF voltage of 200 V and only 135 eV at LF voltage of 200 V and HF voltage of 400 V. The sheath width is calculated to be 3.9 mm and 2.9 mm, respectively, for the two considered cases [Fig. 6.11(b)]. Because the average sheath potential and the LF are the same, from Eq. (5.13) one would expect that the IEDF is broader at LF voltage of 200 V and HF voltage of 400 V since the sheath width is smaller. In fact, the opposite is observed. The reason can be found in the different sheath potential form as a function of the phase in the LF cycle. Numerically, this information is contained in the parameter  $\lambda_2$  (see Chapter 5 for details about the calculation of  $\lambda_2$ ), which is calculated to be 0.72 and 0.3 at LF voltage amplitude of 400 and 200 V, respectively. Figure 6.13 presents the sheath potential in different phases of the LF cycle, when the HF and LF voltage amplitudes are 200 and 400 V (a), and 400 and 200 V (b), respectively.

The ion transit time is calculated to be much longer than the HF period and comparable to the LF period, and therefore the ions respond to the average HF sheath potential, which is a function of the LF (see the dashed lines in Fig. 6.13) [61]. The averaged minimum and maximum of the sheath potential are 55 and 430 V [Fig. 6.13(a)], and 130 and 310 V [Fig. 6.13(b)], respectively. The two

outstanding peaks in the IEDF profiles (Fig. 6.12) correspond to the averaged minimum and maximum sheath potential [61]. This explains the broader energy distribution when the LF voltage amplitude is larger than the HF voltage, in comparison to the opposite case. This observation is valid for all investigated frequency regimes. Consequently, the ion energy depends on both voltage sources and cannot be controlled independently by the LF source. However, the IEDF is broader with increasing the LF voltage and keeping the sum of the LF and HF voltages constant.

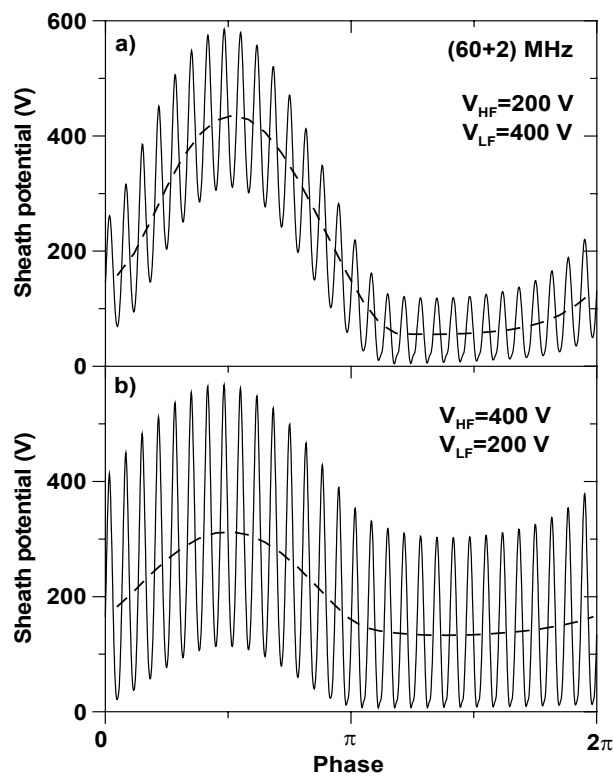


FIGURE 6.13. Calculated sheath potential as a function of the phase in the LF cycle, for the (60+2) MHz regime at HF and LF voltage amplitudes of 200 and 400 V (a), and 400 and 200 V, respectively (b). The dashed lines present the average HF sheath potential as a function of the phase in the LF cycle.

### 6.3.5 Dependence of the plasma characteristics on the LF voltage source in the (27+2) and (27+1) MHz regimes.

As it is discussed above, the LF source has critical influence on the plasma density, ion flux and electron energy at (27+2) MHz [Fig. 6.1(a), (b) and (c)]. Further simulations were performed at (27+2) and (27+1) MHz regimes in order to explain the nonlinear dependence of the plasma behavior on the LF voltage source. Figure 6.14 presents the simulation results averaged over one or two LF cycles, for the plasma density in the discharge center (a), the ion current density at the powered electrode (b), the electron energy in the discharge center (c), the sheath potential (d) and width (e), and the ion energy at the driven electrode (f). The solid and dashed lines represent the calculation results for the (27+2) and (27+1) MHz regimes, respectively, at a HF voltage of 200 V and a LF voltage of 0, 50, 100, 200, 300 or 400 V (bottom x-axis). In the same figure, results are also shown for the (27+2) MHz case at a HF voltage of 700 V and a LF voltage of 0, 100, 300, 500, 700, 900 or 1100 V (dotted line and top x-axis). The simulations for (27+1) MHz, when the LF voltage is higher than 200 V, could not be performed because the two sheaths expand and become comparable with the electrode gap, so that the plasma cannot be sustained.

The same trend is observed in the effect of the LF voltage on the plasma behavior in the three investigated cases. The plasma density considerably decreases with LF voltage [Fig. 6.14(a)]. The ion current density has a minimum at LF to HF voltage ratio  $V_{LF}/V_{HF}$  of about 0.5, i.e. when the LF voltage is 100 or 300 V and the HF voltage is 200 or 700 V, respectively. Further, the ion current density increases with the LF voltage amplitude [Fig. 6.14(b)]. The electron energy has more or less the same values for  $V_{LF}/V_{HF}$  up to 0.5 and then it increases abruptly [Fig. 6.14(c)].

We suppose that the reason for the observed nonlinear plasma characteristics is the transition from electropositive to electronegative plasma behavior when the ratio  $V_{LF}/V_{HF}$  is 1 and higher (e.g. at a HF voltage of 200 V and LF voltages of 200, 300 and 400 V in Figs. 6.1 and 6.14, and at HF voltages of 100 and 200 V, and a LF voltage of 200 V, for the (27+2) regime, presented in Fig. 6.5). This transition is observed in the Ar/CF<sub>4</sub> discharge (see Chapter 3) when the CF<sub>4</sub> concentration is increased [59]. At low concentration of CF<sub>4</sub> (10%) the discharge exhibits more electropositive features, such as the electric field in the center is close to 0, and consequently the electron energy is about 3 eV. The electron density has a flat profile. However, the main negative species are the F<sup>-</sup> and CF<sub>3</sub><sup>-</sup> ions [59]. The same features are observed in the presented dual-frequency reactor at a ratio  $V_{LF}/V_{HF}$  below 1.

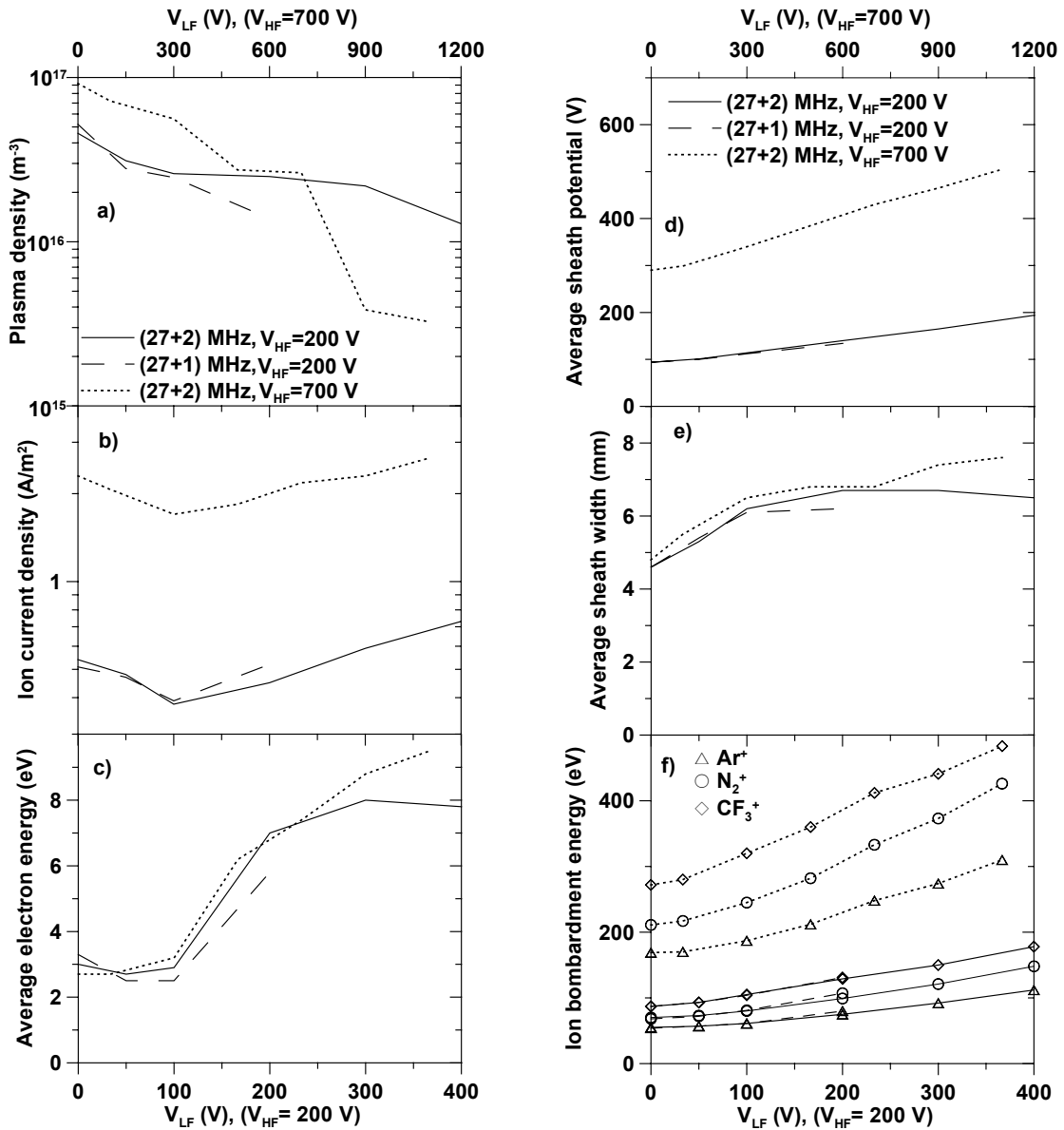


FIGURE 6.14. Calculated plasma density in the discharge center (a), ion current density at the powered electrode (b), electron energy in the discharge center (c), sheath potential (d) and width (e), and ion bombardment energy (f), averaged over the LF cycle, as a function of the LF voltage amplitude, at a HF voltage of 200 V, for (27+2) (solid lines, bottom x-axis) and (27+1) MHz (dashed lines, bottom x-axis), as well as at a HF voltage of 700 V for (27+2) MHz (dotted lines, top x-axis).

On the other hand at high concentration (90%) of  $\text{CF}_4$  the discharge is definitely electronegative and the double layer of the electric field and the electron density maxima at the bulk-sheath interface are well established. The substantial bulk electric field leads to an average electron energy in the bulk of 6 eV and higher. The electronegativity ( $= n_n / n_e$ , where  $n_n$  and  $n_e$  denote the negative ion and electron densities, respectively) increases with the concentration of  $\text{CF}_4$  [59]. This behavior is also observed in the dual-frequency reactor at a ratio  $V_{LF} / V_{HF}$  of 1 and higher, although the  $\text{CF}_4$  concentration is only 10%. For example, for the (27+2) MHz regime the electronegativity is calculated to increase from 6 to 35 when the LF voltage increases from 100 to 400 V at a HF voltage of 200 V, and it decreases from 60 to 3 when the HF voltage increases from 100 to 400 V at a LF voltage of 200 V.

At a ratio  $V_{LF} / V_{HF}$  of 1 and higher the electric field distribution has a profile similar to that presented in Chapter 4 for the dual-frequency reactor and in Chapter 3 at 90% concentration of  $\text{CF}_4$ , i.e. the double layer structure appears and the electric field in the bulk is substantial (up to several thousands V/m). The strong electric field in the bulk explains the abrupt increase in the electron energy from 3 to 7 eV and higher in Figs. 6.1 (c) and 6.14 (c), as well as the abrupt decrease in the electron energy at a HF of 300 V for the (27+2) MHz regime in Fig. 6.5 (c). When the ratio  $V_{LF} / V_{HF}$  is below 1 the electric field in the center is close to 0 and the profile is similar to that in electropositive discharges (see Chapter 3). In Fig. 6.15 we present the electron density distribution, averaged over the LF cycle, at a HF voltage of 200 V and a LF voltage of 100, 200, 300 or 400 V (a), and at a LF voltage of 200 V and a HF voltage of 100, 200, and 300 (b). In order to make the plots clear we do not present the electron density distributions at LF voltages of 0 and 50 V and HF voltage of 200 V, and at a HF voltage of 400 V and a LF voltage of 200 V. For these cases the profile is flat and the electron density in the bulk is  $3.1 \times 10^{15}$ ,  $3 \times 10^{15}$  and  $4.5 \times 10^{15}$ , respectively.

The transition from electropositive to electronegative behavior is observed with increase of the  $V_{LF} / V_{HF}$  ratio. The profile of the average electron density [Fig. 6.15(b)] and the electron energy distribution [see Fig. 6.6(a)] explains the dependence of the ionization rate profile presented in Fig. 6.6(b) on the HF voltage. Consequently, at a HF of 27 MHz, the plasma production depends not only on the HF source but also on the LF source when the voltage ratio  $V_{LF} / V_{HF}$  is close to 1 or higher, which corresponds to close values of the calculated power of the two sources or when the LF power exceeds the HF power (see Sec. 6.4).

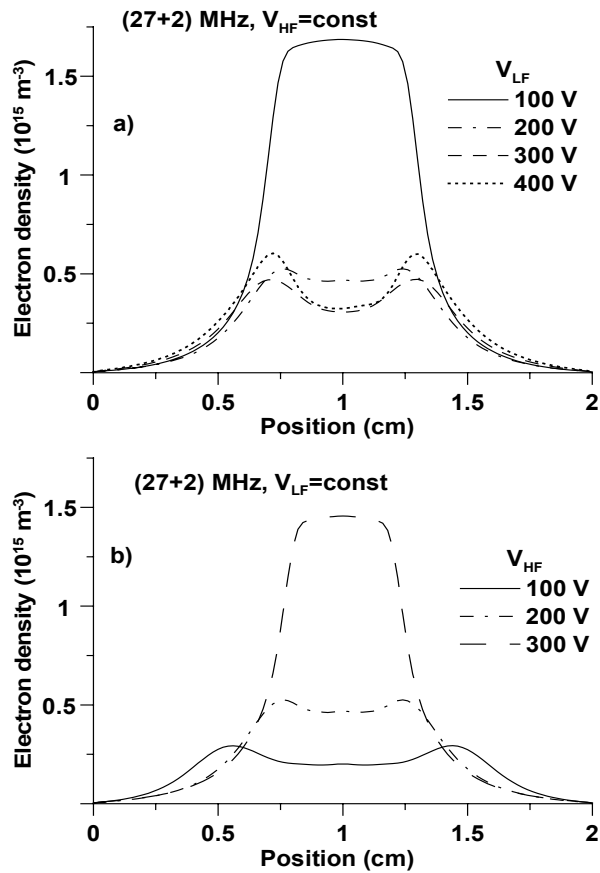


FIGURE 6.15. Calculated electron density distribution, averaged over the LF cycle, at a HF voltage of 200 V and a LF voltage of 100, 200, 300 and 400 V (a), and at a LF voltage of 200 V and a HF voltage of 100, 200, and 300, (b) for the  $(27+2)$  MHz regime.

Although the  $(27+1)$  and  $(60+2)$  regimes have a similar HF/LF ratio, it is observed that the LF voltage source has substantial influence on the ion current density and plasma density at a HF of 27 MHz and the decoupling is possible only at higher primary frequencies. Therefore, independent control of plasma density and ion current is determined by the primary frequency and not by the frequency ratio, which was also experimentally observed [18, 19].

The sheath voltage and width increase with the LF voltage because the applied voltage increases [Figs. 6.14(d) and (e)]. The ion bombardment energy also increases with the LF voltage amplitude. It has very similar values for the  $(27+1)$  and  $(27+2)$  MHz cases when the HF voltage is kept constant at 200 V [Fig. 6.14(f),

solid and dashed lines]. However, the IEDF is broader at the LF of 1 MHz when all the other operating conditions are the same (Fig. 6.16). As it can be deduced from Eq. (5.13) the energy width is indeed inversely proportional to the LF. A more detailed discussion about the dependence of the energy width on the LF in a dual-frequency reactor can be found in Chapter 5.

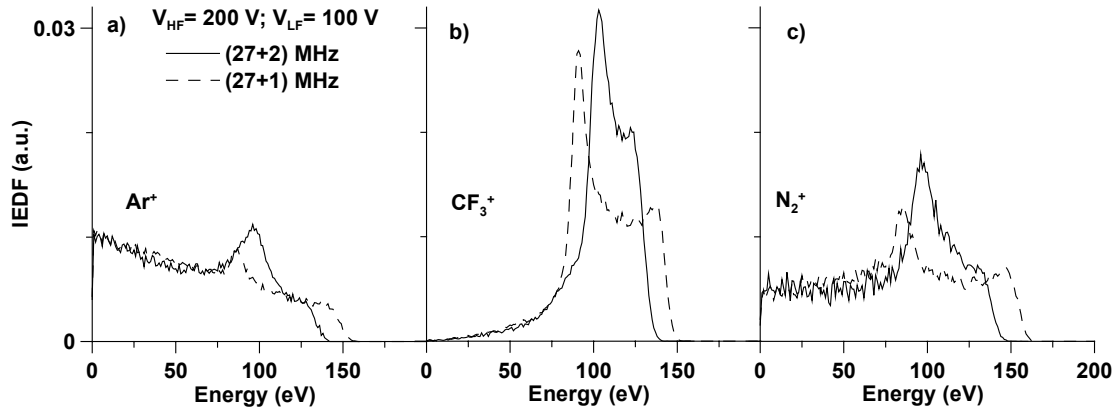


FIGURE 6.16. Calculated  $\text{Ar}^+$  (a),  $\text{CF}_3^+$  (b), and  $\text{N}_2^+$  (c) IEDF, averaged over the LF cycle, at HF and LF voltage amplitudes of 200 and 100 V, respectively, for (27+2) (solid lines) and (27+1) MHz (dashed lines).

## 6.4 Calculated power

In our model, the applied voltage is the determining parameter. However, because the experimentalists might be more familiar with the applied power, the calculated power of the two sources, corresponding to the different applied voltages, is presented for all investigated frequency regimes.

The time-averaged power  $p_{abs}$  per unit volume absorbed by the discharge is calculated from [1]

$$p_{abs} = \frac{1}{\tau_{RF}} \int_0^{\tau_{RF}} j_{Tz}(t) E_z(t) dt, \quad (6.2)$$

where  $j_{Tz}$  and  $E_z$  are the calculated total electric current density and electric field, respectively, and  $\tau_{RF}$  is the RF period. The total current density is the sum of the

displacement and conduction  $j_{cond}$  (due to the motion of the free charges) current densities, i.e.

$$j_{Tz} = \varepsilon_0 \frac{\partial E_z}{\partial t} + j_{cond}. \quad (6.3)$$

In the dual-frequency regime the calculated power is represented by Fourier series in order to obtain the power introduced in the discharge by the two sources, i.e

$$f(t) = \frac{a_0}{2} + \sum_{n=1}^{\infty} [a_n \cos(nt) + b_n \sin(nt)], \quad (6.4)$$

where the Fourier coefficients  $a_n$  ( $n = 0, 1, \dots$ ) and  $b_n$  ( $n = 1, 2, \dots$ ) in case of periodic function  $f(x)$ ,  $x$  defined in  $[-\pi, \pi]$  are found from

$$a_n = \frac{1}{\pi} \int_{-\pi}^{\pi} f(t) \cos(nt) dt$$

$$b_n = \frac{1}{\pi} \int_{-\pi}^{\pi} f(t) \sin(nt) dt. \quad (6.5)$$

As expected all coefficients are close to 0 except for the coefficients corresponding to LF and HF.

Table 6.1 shows the calculated HF and LF power in W, for the (27+2), (40+2), (60+2), (100+2), and (27+1) MHz regimes when the HF voltage is kept constant at 200 V and the LF voltage is varying. The LF power increases and the HF power decreases with the LF voltage. For a HF of 27 MHz the HF power decreases until it reaches comparable values with the LF power and then increases or does not change (see also Table 6.2). Table 6.2 presents the calculated HF and LF power in W, for the (27+2) MHz regime when the HF voltage is kept constant at 700 V and the LF voltage is varying.

Table 6.3 shows the calculated HF and LF power in W, for the (27+2), (40+2), (60+2), and (100+2) MHz regimes when the LF voltage is kept constant at 200 V and the HF voltage is varying, and in the single-frequency reactor at 60 MHz. The HF and LF power increase when the HF voltage increases.

TABLE 6.1. The calculated HF and LF power in W for the (27+2), (40+2), (60+2), (100+2), and (27+1) MHz regimes when the HF voltage is kept constant at 200 V and the LF voltage is varying.

HF+LF	(27+2)		(40+2)		(60+2)		(100+2)		(27+1)	
V <sub>LF</sub> (V)	P <sub>HF</sub> (W)	P <sub>LF</sub> (W)	P <sub>HF</sub>	P <sub>LF</sub>						
0	5	0	13	0	25	0	61	0	5	0
50	4	1	12	1	-	-	-	-	4	1
100	3	1	10	3	20	5	48	10	4	1
200	3	2	8	5	17	10	41	20	4	3
300	4	5	6	6	16	16	37	32	-	-
400	5	8	5	8	15	23	34	43	-	-

TABLE 6.2. The calculated HF and LF power in W for the (27+2) MHz regime when the HF voltage is kept constant at 700 V and the LF voltage is varying.

V <sub>LF</sub> (V)	0	100	300	500	700	900	1100
P <sub>HF</sub> (W)	51	45	34	31	33	31	32
P <sub>LF</sub> (W)	0	4	12	23	40	52	72

TABLE 6.3. The calculated HF and LF power in W for the (27+2), (40+2), (60+2), and (100+2) MHz regimes, when the HF voltage is kept constant at 200 V and the LF voltage is varying. The calculated power in single-frequency of 60 MHz is also given.

HF+LF	(27+2)		(40+2)		(60+2)		60 MHz	(100+2)	
V <sub>HF</sub> (V)	P <sub>HF</sub> (W)	P <sub>LF</sub> (W)	P <sub>HF</sub>	P <sub>LF</sub>	P <sub>HF</sub>	P <sub>LF</sub>	P	P <sub>HF</sub>	P <sub>LF</sub>
100	2	2	2	2	4	4	8	11	9
200	3	2	8	5	17	10	25	41	20
250	-	-	-	-	-	-	-	63	26
300	6	3	19	8	39	16	55	-	-
400	11	4	34	12	73	24	71	-	-

## 6.5 Comparison with experiment

Recently, the electron density in the bulk plasma and the positive ion current density at the electrodes have been measured in Ar/CF<sub>4</sub> discharges sustained in a symmetric dual-frequency reactor [107]. Simulations have been carried out at similar operating conditions in order to make a comparison between measured and calculated characteristics. The experimental operating conditions are the following: Ar/CF<sub>4</sub> gas mixture at a ratio of 0.83/0.17, pressure at 54 mTorr, gas temperature of 500 K, (27 + 2) MHz and single-27 MHz regimes, applied HF power of 250 W and applied LF power of 250 W. The actual HF or LF power dissipated in the discharge is in the range 180 – 200 W. The simulation operating conditions are the same except for the power values. As it is discussed, the applied voltages are the input of the model and the power absorbed by the discharge is calculated (see Sec. 6.4). The applied HF and LF voltage amplitudes are 1500 and 1200 V, respectively, for the dual-frequency regime. The calculated HF and LF power are 175 and 187 W, respectively. In the single-frequency the applied voltage amplitude and calculated power are 1200 V and 180 W, respectively.

Table 6.4 presents the measured [107] and calculated results. A reasonable agreement is found, especially for the dual-frequency regime. The calculated higher electron density in both regimes is probably due to one of the approximations made in the model, i.e. the model does not consider electron-radical collisions, of which the collision frequency increases with increase of the pressure and applied power.

TABLE 6.4. Comparison between measured and calculated electron density  $n_e$  in the bulk center and positive ion current density  $j$  at the electrodes.

(27+2) MHz		
	$n_e$ (m <sup>-3</sup> )	$j$ (A/m <sup>2</sup> )
measured	$1.8 \times 10^{16}$	7.4
calculated	$3.5 \times 10^{16}$	5.8
27 MHz		
	$n_e$ (m <sup>-3</sup> )	$j$ (A/m <sup>2</sup> )
measured	$2 \times 10^{16}$	4.0
calculated	$4.4 \times 10^{16}$	5.2

## 6.6 Summary

A detailed numerical investigation by means of the PIC/MC method was made to study the influence of the reactor parameters on the plasma characteristics in Ar/CF<sub>4</sub>/N<sub>2</sub> plasmas in a dual-frequency reactor. The calculated plasma density and electron energy in the discharge center, ion flux and energy onto the electrodes, the sheath potential and width, the EEPF and IEDF, and ionization rates were presented as a function of the LF or HF voltage amplitude and applied LF or HF.

It is observed that the decoupling of the two sources is possible with increase of the applied HF to values of 60 MHz and higher, and it is not defined by the frequency ratio. Both voltage sources have influence on the plasma characteristics at HF of 27 MHz and to some extent at 40 MHz. At HF of 60 and 100 MHz, the plasma density and ion current density show the same dependence on the driving frequency as if the second voltage source was not connected, but their values are somewhat lower than that in the single-frequency reactor for the same HF voltage amplitude. The electron energy, EEPF and ionization rates are almost unaffected by the LF source. The sheath potential increases with HF or LF voltage amplitude because the applied voltage increases. The sheath width slightly increases with LF voltage and slightly decreases with HF voltage, while it is not influenced by the driving voltage in the single-frequency reactor.

The plasma density and ion current increase, and the sheath width decreases with HF when the other operating conditions are the same. The average sheath potential decreases very slightly with the primary frequency. The average ion energy increases with the HF because the sheath width decreases. A similar dependence of the plasma characteristics on the driving frequency was found in single-frequency reactors.

The average ion bombardment energy increases with HF or LF voltage amplitude when the other voltage amplitude is kept constant, because the sheath potential increases with the sum of the applied HF and LF voltages. However, the IEDF becomes broader when increasing the LF voltage and keeping the sum of the LF and HF voltages constant, i.e. the average sheath potential is the same. The reason is that the ions respond to the averaged HF sheath potential as a function of the LF. Finally, the ion energy distribution function is broader when increasing the applied HF or decreasing the applied LF.

In conclusion, independent control of the ion flux and energy in a voltage driven dual-frequency reactor is possible when increasing the HF and varying the LF voltage while keeping the HF voltage constant. The present study covers a wide range of different applied voltages and frequencies of the dual-frequency reactor so that they can be adjusted to obtain desirable plasma characteristics and therefore this study can be useful in improving control over the etching process.

## **Chapter 7**

# **PLASMA BEHAVIOR IN ASYMMETRIC DUAL-FREQUENCY REACTORS**

### **7.1 Introduction**

In Chapters 4 and 6, the influence of the two frequency sources on the plasma characteristics in symmetric Ar/CF<sub>4</sub>/N<sub>2</sub> discharges by means of the PIC/MCC method is studied numerically, and the parameters at which the independent control of the ion flux and energy is possible are discussed. Also a detailed investigation of the ion energy distribution function (IEDF) in single- and dual-frequency reactors is presented in Chapter 5.

The discharges are, however, generally asymmetric, i.e., the area of the powered electrode (PE) is typically smaller than the area of the grounded electrode (GE). This asymmetry determines the formation of a self-bias voltage at the PE, which in turn influences the ion-bombarding energy.

In the literature, the PIC/MCC method was employed to study asymmetric dual-frequency reactors and to investigate the optimal reactor parameters for independent control of ion current and energy, but these studies have been carried out only in Ar discharges [64-67].

The purpose of the present Chapter is to study the plasma behavior in a gas mixture of Ar, CF<sub>4</sub>, and N<sub>2</sub> in an asymmetric dual-frequency reactor by means of a 1-dimensional (1d) spherical coordinate space and 3d velocity space PIC/MCC algorithm. The PIC/MCC model is attractive because the fields and energy distributions are obtained self-consistently. A 2d cylindrical PIC/MCC model, which would account for the discharge asymmetry (e.g. Ref. 64), would require a very long computational time to reach convergence for a complex electronegative gas mixture, as investigated in the present work. Therefore, the geometry of the present model has been changed to a spherical one since the spherical system is the simplest model, which accounts for the unequal area of the PE and GE [1, 21]. It should be

noted that the effects of the 2d cylindrical geometry could not be fully presented by the 1d spherical geometry. However, it has already been shown that the 1d spherical geometry is a reasonable approximation and gives reliable results (e.g. Refs. 1, 21 and 64).

Dependence of the plasma characteristics on the electrode area ratio is investigated in the (60+2) MHz regime. A comparison with the results in the symmetric reactor is presented. It has been shown in Chapter 6 that the decoupling of the power sources in symmetric dual-frequency reactors is possible at a HF of 60 MHz and above [62]. It is observed that this is valid in asymmetric reactors as well. In order not to repeat the discussion in Chapter 6, we present in this work only the influence of the applied HF and LF sources on the plasma characteristics for the (60+2) MHz regime in the asymmetric reactor. The results for the other frequency regimes, i.e. at a HF of 27, 40, or 100 MHz and a LF of 1 or 2 MHz are similar to those obtained in the symmetric reactor [62], taking into account the nonzero dc bias voltage and its influence on the sheath potential and width, and therefore on the ion energy at the PE.

The model used in this study is presented in Sec. 7.2. In Sec. 7.3 the results of the simulation, such as potential, electric field and electron density distributions, sheath potential and width, ion current density, and electron and ion energy distributions, are presented and discussed. Finally, in Sec. 7.4 a summary is given.

## 7.2 1d spherical model

A schematic diagram of the cc RF reactor considered in this study is shown in Fig. 7.1. A 1d spherical model is used to simulate the asymmetric discharge [21]. The inner electrode, which is a sphere with a radius  $r_a = 5$  cm and an area  $S_a$ , is driven by a dual-frequency voltage source, i.e. the applied voltage is a sum of the HF and LF voltages

$$V = V_{HF} \sin(\omega_{HF}t) + V_{LF} \sin(\omega_{LF}t), \quad (7.1)$$

where  $V_{HF}$  and  $V_{LF}$  are the HF and LF voltage amplitudes, and  $\omega_{HF}$  and  $\omega_{LF}$  are the applied HF and LF. The outer electrode with radius  $r_b = 7$  cm and an area  $S_b$  is grounded and the electrode area ratio  $S_b/S_a$  is 1.96, correspondingly. The inner and outer radii have been chosen in order to have the same PE area and electrode gap as in the parallel plate symmetric reactor considered in our previous studies [see Chapters 4-6]. In order to study the dependence of the plasma characteristics on the electrode area ratio, simulations are carried out also for  $r_a = 3$  and 4 cm, and  $r_b = 5$  and 6 cm, respectively, so that the distance between the electrodes is kept constant at 2 cm and the electrode area ratio is 2.78 and 2.25, respectively.

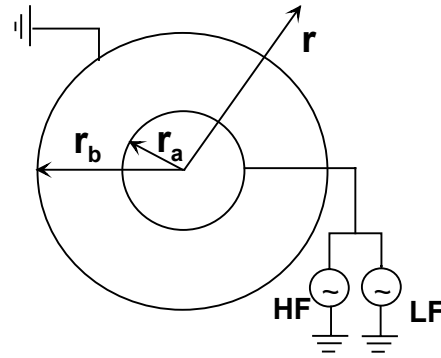


FIGURE 7.1. Spherical model of the asymmetric dual-frequency reactor.

The computation is based on a 1d spherical coordinate space and 3d velocity space PIC/MCC algorithm [46, 47]. The model presented in Chapter 2 has been developed for Cartesian coordinates. In order to simulate the asymmetric reactor presented in Fig. 7.1 the model has been transformed to spherical coordinates, i.e.  $r$ -axis instead of  $z$ -axis is considered, and the three velocity components are  $V_r$ ,  $V_\theta$ , and  $V_\varphi$ . The potential equations (2.13) and matrix elements (2.18) and (2.22) in spherical coordinates are given in the Appendix A.

### 7.3 Input data

The calculations are performed for an Ar/CF<sub>4</sub>/N<sub>2</sub> mixture at a molar ratio of 0.8/0.1/0.1. All simulations are carried out at a pressure of 30 mTorr. The gas temperature is set to 300 K. The simulation grid is uniform and it consists of 100 cells. The electron time step varies from  $10^{-11}$  till  $3.7 \times 10^{-11}$  s depending on the electron plasma frequency. To speed up the calculation, the ion time step is set to be 25 to 50 times longer than the electron time step, and different weights for electrons and ions are applied. The choice of the grid spacing and the time steps is defined by the accuracy criteria for PIC/MC codes with explicit mover [69].

### 7.4 Results and discussion

In the presented figures the position of the PE is at 0 cm, which for the symmetric reactor corresponds to  $z = 0$  cm, and for the asymmetric reactor corresponds to  $r_a = 3, 4, \text{ or } 5$  cm. The position of the GE is at 2 cm, which for the symmetric reactor corresponds to  $z = 2$  cm, and for the asymmetric reactor corresponds to  $r_b = 5, 6, \text{ or } 7$  cm, respectively.

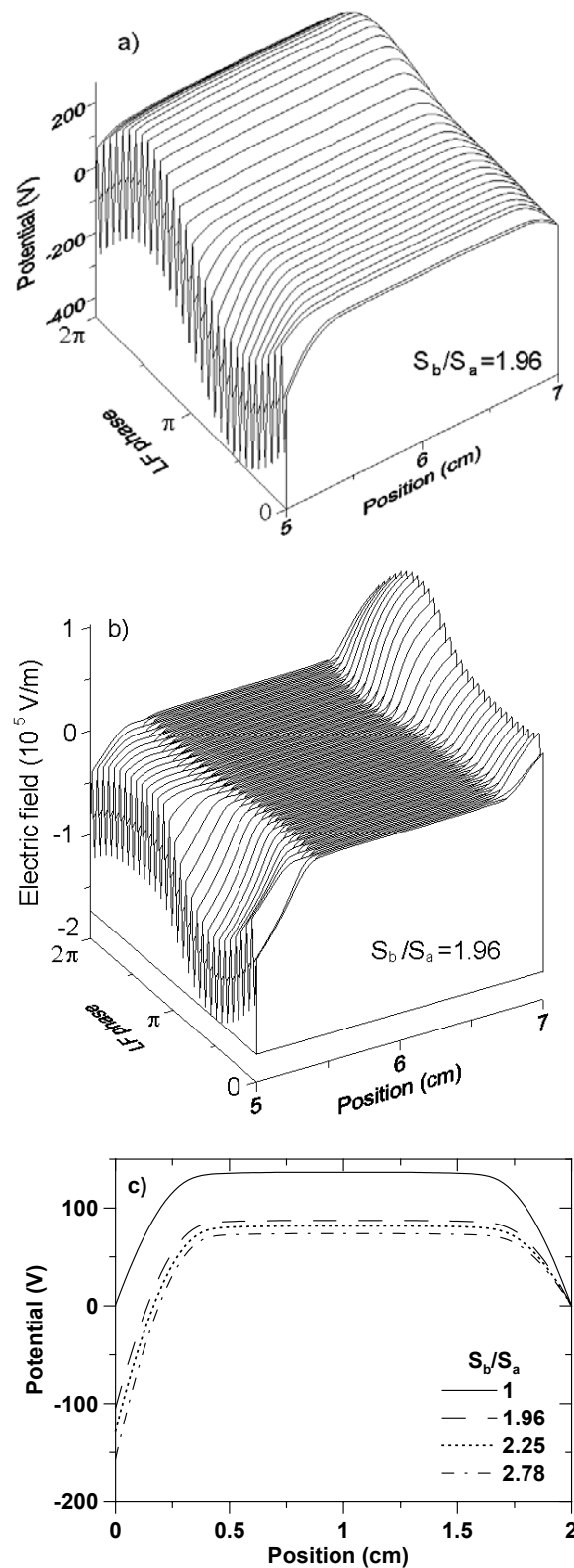


FIGURE 7.2. Calculated potential (a) and electric field (b) distributions as a function of the phase in the LF cycle for  $S_b/S_a = 1.96$ , and time-averaged potential distribution for different electrode area ratios (c) for the (60+2) MHz regime. The HF and LF voltage amplitudes are set to 200 V.

### 7.4.1 Influence of the electrode area ratio on the plasma characteristics

The time dependence of the potential and electric field distributions in the asymmetric reactor is shown in Figs. 7.2(a) and (b), respectively, for the electrode area ratio of 1.96 in the (60+2) MHz regime. The HF and LF voltage amplitudes are set to 200 V. The profiles are similar for the other investigated electrode area ratios. Figure 7.2(c) presents the potential distribution, averaged over the LF cycle, for different electrode area ratios. It is observed that the dc self-bias voltage at the PE is different from zero in case of unequal area of the two electrodes. The plasma potential decreases and the absolute value of the dc bias voltage increases with the increase of the electrode area ratio, as expected. The electric field is much stronger in the sheath at the PE because of the larger potential difference.

The sheath potential and width are essential for understanding the sheath dynamics as well as for determining the ion-bombarding energy. Figure 7.3 shows the instantaneous sheath thickness in front of the PE and GE,  $s_a(t)$  and  $s_b(t)$ , respectively, in the symmetric (solid lines) and asymmetric (dotted lines) reactors. The sheath oscillates with the applied two frequencies. Unlike in the symmetric reactor the two sheaths in the asymmetric reactor have different width. The sheath width, averaged over the LF cycle, as a function of the electrode area ratio, is presented in Fig. 7.4 (dashed lines, right y-axis). The dc bias voltage leads to a broader sheath at the PE (around 3.8 mm) in comparison with that at the GE (around 3 mm) and at the PE in the symmetric reactor (3.3 mm).

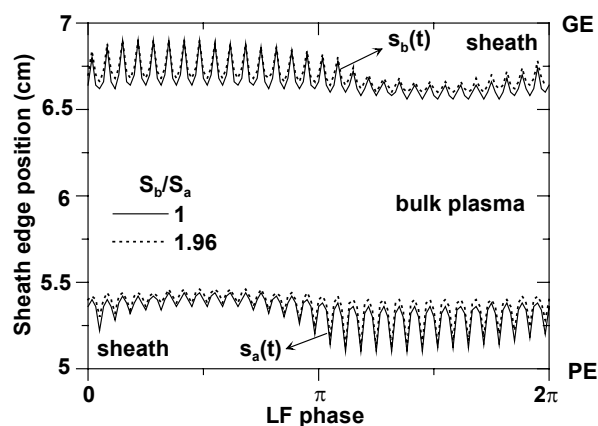


FIGURE 7.3. Calculated instantaneous sheath thickness in front of the PE [ $s_a(t)$ ] and GE [ $s_b(t)$ ] as a function of the phase in the LF cycle in the symmetric reactor, i.e.  $S_b/S_a = 1$ , (solid lines), and in the asymmetric reactor  $S_b/S_a = 1.96$  (dotted lines).

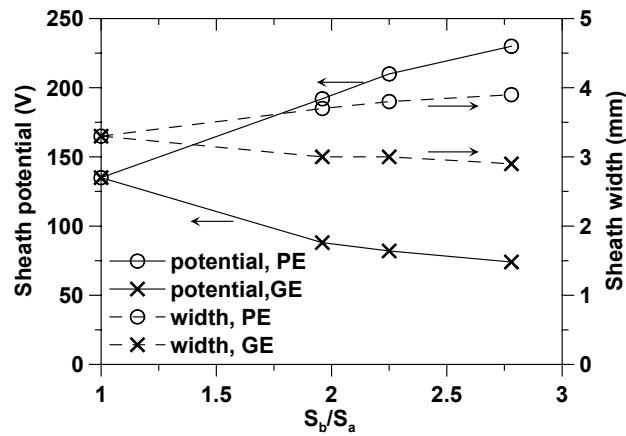


FIGURE 7.4. Calculated sheath potential (solid lines, left y-axis) and width (dashed lines, right y-axis) at the PE and GE, averaged over the LF cycle, as a function of the electrode area ratio  $S_b/S_a$ .

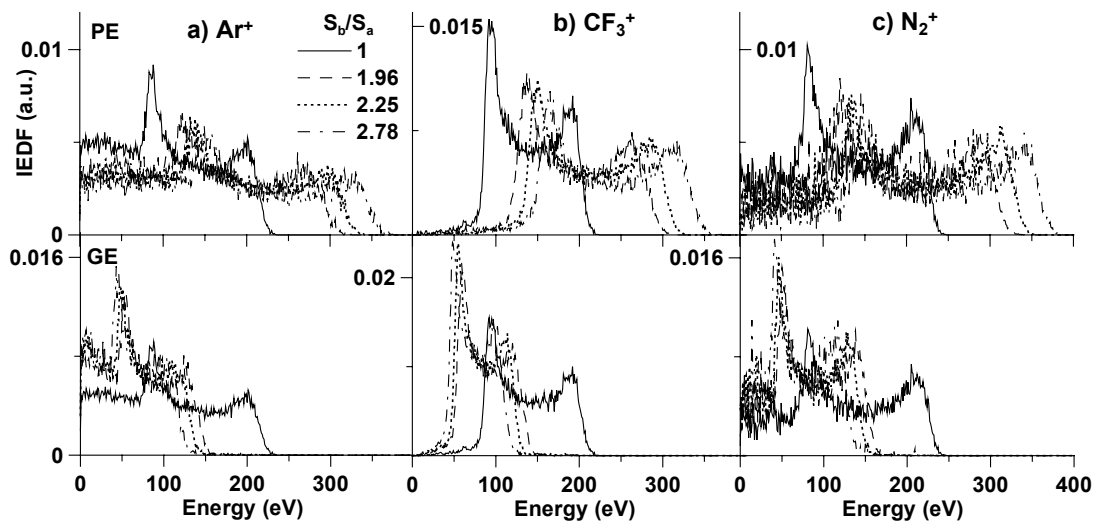


FIGURE 7.5. Calculated  $\text{Ar}^+$  (a),  $\text{CF}_3^+$  (b), and  $\text{N}_2^+$  (c) IEDF at the PE and the GE for different electrode area ratios.

It is observed that the sheath width is almost independent from the electrode area ratio in the asymmetric reactor, i.e. it varies only from 3.7 to 3.9 mm at the PE and from 3 to 2.9 mm at the GE when the electrode area ratio varies from 1.96 to 2.78.

Figure 7.4 presents also the sheath potential at the PE and GE, defined as the drop from the potential in the bulk plasma to the electrode potential, averaged over the LF cycle, as a function of the electrode area ratio (solid lines, left y-axis). The increase of the dc bias voltage leads to an increase of the sheath potential at the PE, while the decrease in the plasma potential determines the drop in the sheath potential at the GE.

The calculated  $\text{Ar}^+$  (a),  $\text{CF}_3^+$  (b), and  $\text{N}_2^+$  (c) IEDFs at the PE and GE are presented in Fig. 7.5 for different electrode area ratios. The IEDF has two peaks and the energy width is centred at the averaged sheath potential [see Eq. (5.13) and Chapter 5 for details]. The abundance of low energy ions in the  $\text{Ar}^+$  and  $\text{N}_2^+$  IEDFs is a result of the high charge exchange collision frequency [9, 61]. The ion energy at the PE reaches higher maximum values and the ion energy at the GE shifts to lower values when the electrode area ratio increases because of the increase at the PE and decrease at the GE of the average sheath potential, respectively.

The average  $\text{Ar}^+$ ,  $\text{CF}_3^+$ , and  $\text{N}_2^+$  ion-bombarding energies at the PE (solid lines) and GE (dashed lines), calculated from the IEDFs [see Eq. (6.1)] are presented in Fig. 7.6. They increase at the PE and decrease at the GE following the sheath potential behavior.

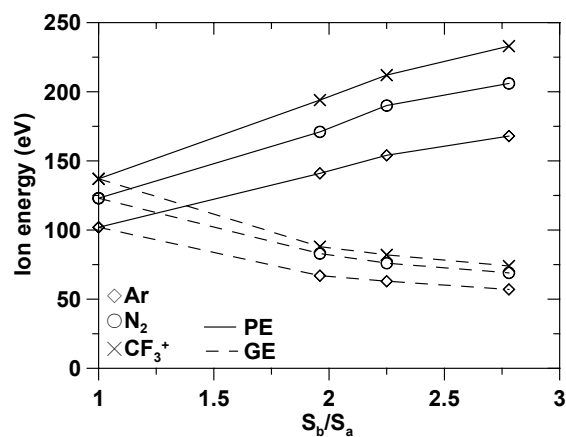


FIGURE 7.6. Calculated average  $\text{Ar}^+$ ,  $\text{CF}_3^+$ , and  $\text{N}_2^+$  ion-bombarding energy at the PE (solid lines) and GE (dashed lines).

The time dependence of the electron density is shown in Fig. 7.7(a). The electrons oscillate with the applied HF in one of the sheaths for a half LF cycle, but the profile in the bulk does not depend on the phase in the LF cycle. In the symmetric reactor the electron density has a flat profile in the bulk plasma (see Chapter 7). In the asymmetric reactor a maximum is observed at the bulk-sheath interface to the PE. Figure 7.7(b) shows the time-averaged electron density distribution for different electrode area ratios. It is observed that the electron density profile is almost independent of the electrode area ratio in the asymmetric reactor, and it is not too much different from the electron density profile in the symmetric reactor, except for the asymmetric profile.

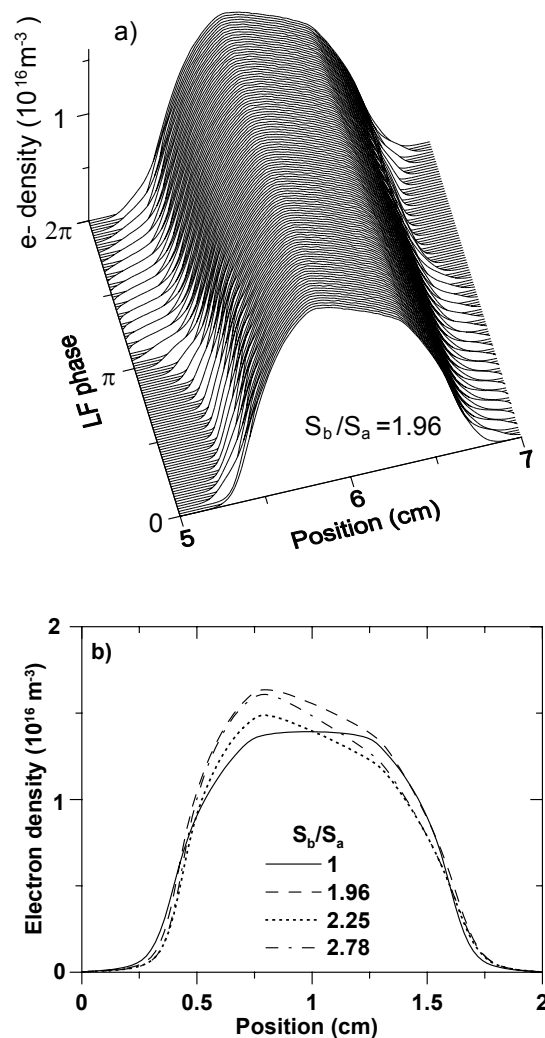


FIGURE 7.7. Calculated electron density distribution (a) as a function of the phase in the LF cycle for  $S_b/S_a = 1.96$ , and electron density distribution, averaged over the LF cycle, for different electrode area ratios (b).

The average electron energy in the bulk appears to be also independent from the electrode area ratio. It is calculated to be about 3.5 eV for any of the investigated electrode area ratios. The electron energy probability function (EPPF) in the plasma center has a similar profile for all investigated electrode area ratios, and therefore, we have chosen to present it only for the electrode area ratios of 1 and 1.96 (see Fig. 7.8). The EPPF is close to a Maxwellian profile.

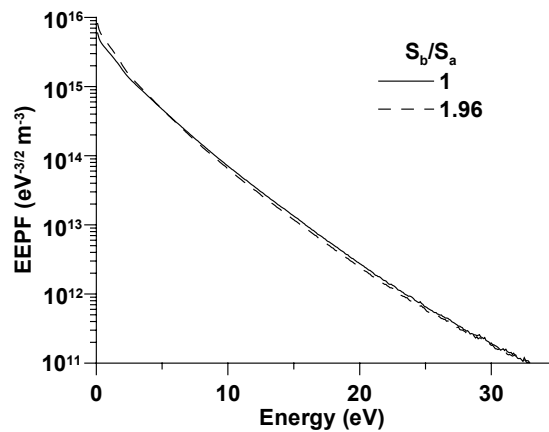


FIGURE 7.8. Calculated electron energy distribution function in the bulk plasma for  $S_b/S_a = 1$  and 1.96.

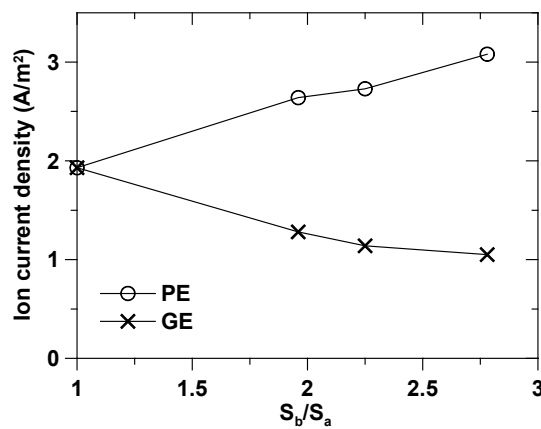


FIGURE 7.9. Calculated ion current density at the PE and GE as a function of the electrode area ratio.

Figure 7.9 presents the ion current density as a function of the electrode area ratio. The ion current density increases at the PE and decreases at the GE when the electrode area ratio increases because the PE area decreases and the GE area increases, respectively. The total current on both electrodes is calculated to be the same because of the requirement for current continuity.

In conclusion, the electron density and energy, and the sheath width are almost independent of the electrode area ratio in the asymmetric reactor, and they are similar to the results in the symmetric reactor. The dc bias voltage, and consequently the sheath voltage and ion energy increase at the PE with the electrode area ratio. The sheath voltage ratio is given by [21]

$$\frac{V_a}{V_b} = \left( \frac{S_b}{S_a} \right)^q \quad (7.2)$$

where  $q$  is a scaling exponent factor. Measurements and theoretical and simulation results revealed that  $q$  is close to 1 [107, 108]. Figure 7.10 presents the calculated sheath voltage ratio  $V_a/V_b$  as a function of the electrode area ratio for different investigated frequency regimes. The fits to the calculated data are also presented (dashed lines). It is found that the scaling exponent factor is between 0.72 and 1.18, hence in good agreement with data in the literature.

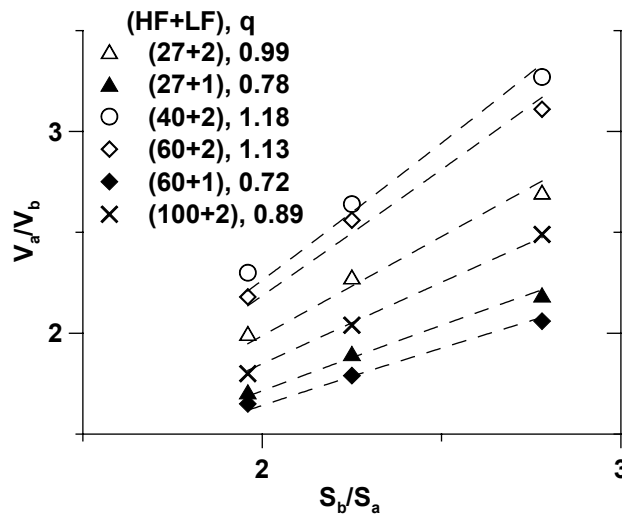


FIGURE 7.10. Calculated sheath voltage ratio  $V_a/V_b$  as a function of the electrode area ratio  $S_b/S_a$  for different frequency regimes. The HF and LF voltage amplitudes are set to 200 V in all frequency schemes.

### 7.4.2 Influence of the power source parameters on the plasma characteristics

In Chapter 6 we showed that the decoupling of the power sources in symmetric dual-frequency reactors is possible at a HF of 60 MHz and above [62]. We observed that this is valid in asymmetric reactors as well. In order not to repeat the discussion in Chapter 6, in this work we present only the influence of the applied HF and LF voltage amplitudes on the plasma characteristics for the (60+2) MHz regime in the asymmetric reactor for an electrode area ratio of 1.96. As mentioned in the introduction, the results for the other frequency regimes, i.e. at a HF of 27, 40, or 100 MHz and a LF of 1 or 2 MHz are similar to those in the symmetric reactor taking into account the effect of the nonzero dc bias voltage.

The time-averaged potential distribution when the HF or LF voltage amplitude is kept constant is shown in Figs. 7.11(a) and (b), respectively, for the (60+2) MHz regime. The operating conditions are the following: the HF voltage is kept constant at 200 V while the LF voltage is set to 0, 100, 200, 300, or 400 V [Fig. 7.11(a)], and the LF voltage is kept constant at 200 V while the HF voltage is set to 100, 200, 300, or 400 V [Fig. 7.11(b)].

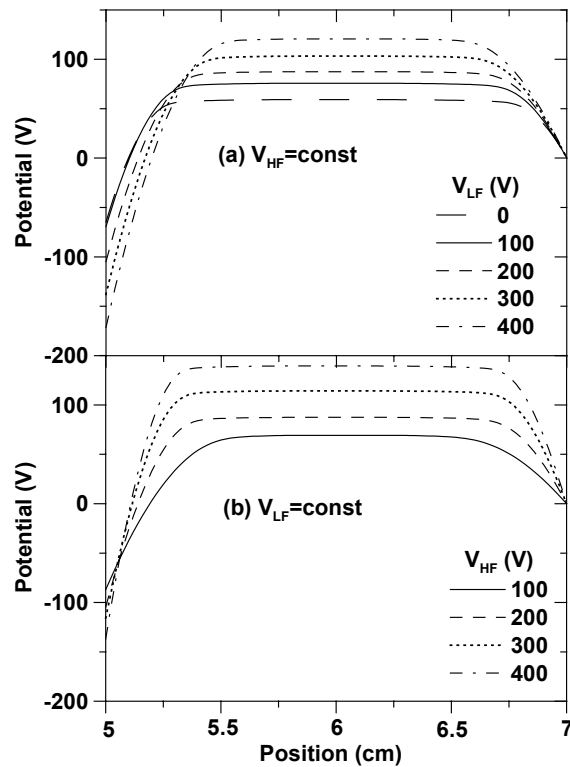


FIGURE 7.11. Calculated potential distribution, averaged over the LF cycle, when the HF (a) or LF (b) voltage amplitude is kept constant at 200 V for the (60+2) MHz regime.

As expected, both plasma potential and dc bias voltage at the PE increase with the increase of the applied voltage, which is the sum of the HF and LF voltages [see Eq. (7.1)]. Consequently, the sheath voltage at the PE and GE also increases with the applied HF or LF voltage amplitude (see below).

Figures 7.12(a) and (b) present the electron density distribution when the HF or LF voltage amplitude is kept constant, respectively. The operating conditions are the same as in Fig. 7.11. The application of a second (low) frequency decreases the electron density [Fig. 7.12(a)], as was also found in the symmetric reactor (see Chapter 6). Further, it is observed that the electron density in the bulk has similar values when the LF voltage amplitude increases from 100 to 400 V. Hence, the LF voltage has no significant influence on the electron density, except compared to the simulation where no LF is applied. The electron density, and consequently the plasma density, scale linearly with the HF voltage [Fig. 7.12(b)]. The same behavior was observed in the symmetric reactor (see Chapter 6). The average electron energy is between 3 and 4 eV for all investigated cases.

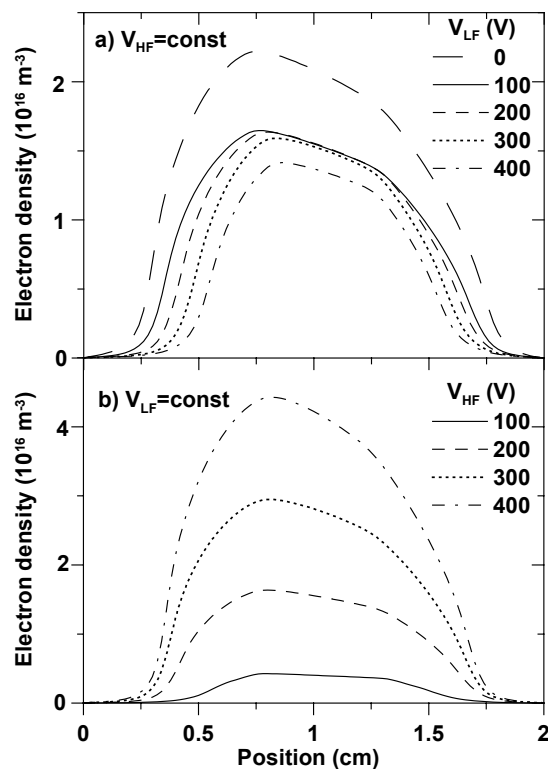


FIGURE 7.12. Calculated electron density distribution, averaged over the LF cycle, when the HF (a) or LF (b) voltage amplitude is kept constant at 200 V for the (60+2) MHz regime.

Figure 7.13 shows the ion current density at the PE and GE as a function of the LF (a) or HF (b) voltage amplitude while the other voltage amplitude is kept constant at 200 V. For a comparison we present the results in the single-frequency asymmetric reactor with the same driving voltage as the HF voltage in the dual-frequency reactor [Fig. 7.13(b), dotted lines]. It can be seen that the ion current density is independent of the LF voltage and depends only on the HF voltage. It is found to scale as  $j \sim V_{HF}^{1.4}$ . We carried out the same simulation set for the (60+1) MHz regime and found that the plasma and ion current density have very similar values as in the (60+2) MHz regime. Indeed, at a HF of 60 MHz the plasma density and ion flux can be controlled independently by the HF source. The application of the LF source only lowers the ion current density [cf. dotted and dashed lines in Fig. 7.13(b)], as it was also found in the symmetric reactor (see Chapter 6).

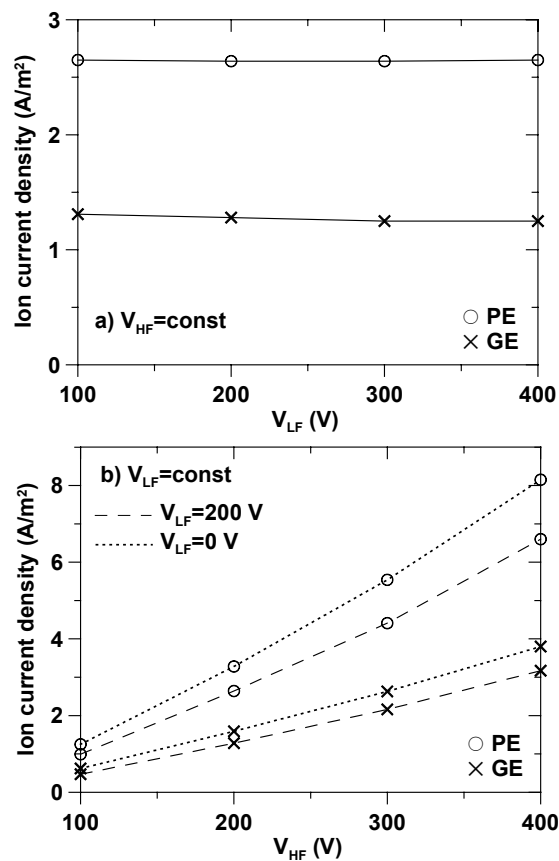


FIGURE 7.13. Calculated ion current density at the PE and GE as a function of the LF (a) or HF (b) (dashed lines) voltage amplitude, while the other voltage amplitude is kept constant at 200 V for the (60+2) MHz regime, and as a function of the driving voltage in the single-frequency reactor at 60 MHz (b) (dotted lines).

Both HF and LF sources have influence on the sheath potential and width, and consequently on the ion-bombarding energy. Figure 7.14 presents the sheath potential (a), the sheath width (b), and the average  $\text{Ar}^+$ ,  $\text{CF}_3^+$ , and  $\text{N}_2^+$  ion-bombarding energies (c) at the PE and GE, as a function of the LF voltage. All presented characteristics increase linearly with the LF voltage. The sheath potential is higher and the sheath is wider at the PE than at the GE, as it was observed above. The same is true for the ion energy.

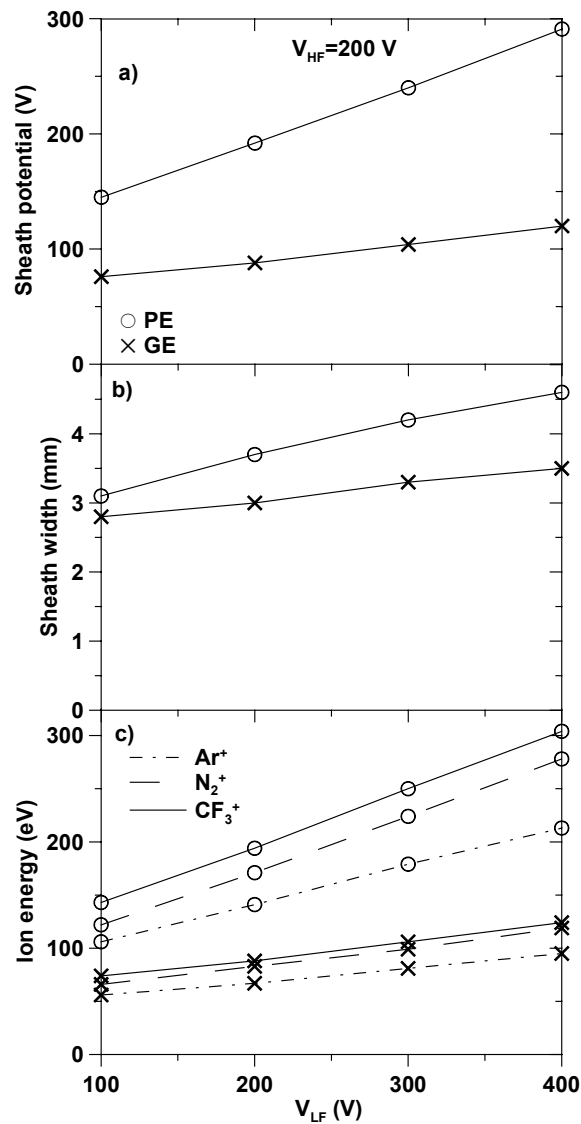


FIGURE 7.14. Calculated sheath potential (a) and width (b), and  $\text{Ar}^+$ ,  $\text{CF}_3^+$ , and  $\text{N}_2^+$  ion-bombarding energies (c) at the PE and GE, as a function of the LF voltage amplitude, while the HF voltage amplitude is kept constant at 200 V for the (60+2) MHz regime.

The sheath potential at the PE and GE (dashed lines) and the sheath potential in the single-frequency reactor (dotted line), as a function of the HF voltage are presented in Fig. 7.15(a). It increases with the applied HF voltage amplitude. The sheath width in the dual-frequency reactor decreases with the HF voltage [Fig. 7.15(b), dashed lines], as it was also found in the symmetric reactor (see Chapter 6). The sheath width in the single-frequency reactor does not change in front of the PE, and it decreases slightly in front of the GE [Fig. 7.15(b), dotted lines]. The sheath width in the single-frequency reactor does not change in front of the PE, and it decreases slightly in front of the GE [Fig. 7.15(b), dotted lines].

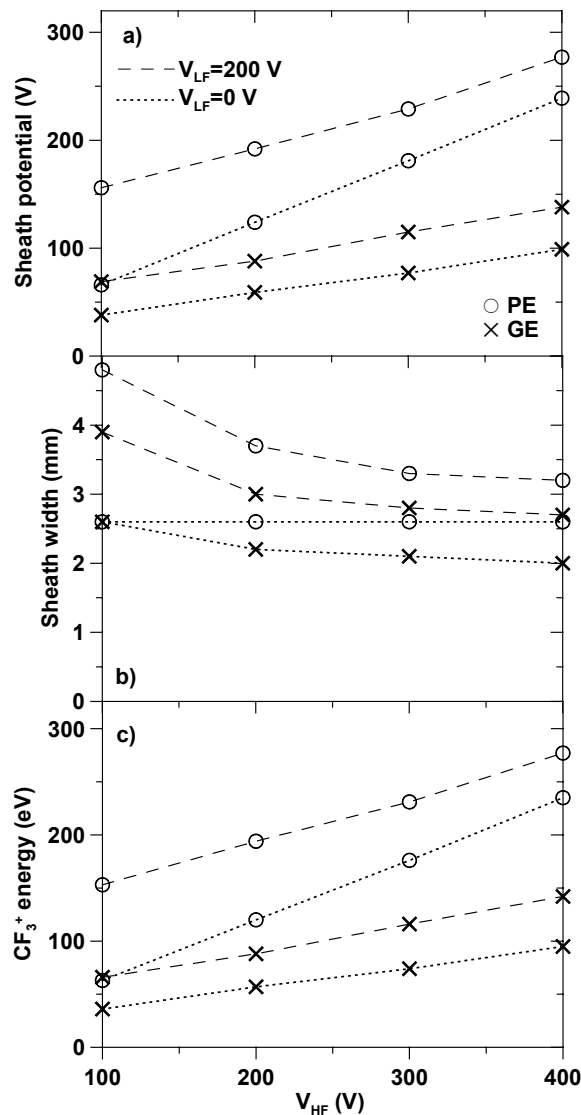


FIGURE 7.15. Calculated sheath potential (a) and width (b), and  $CF_3^+$  ion-bombarding energy (c) at the PE and GE, as a function of the HF voltage amplitude, while the LF voltage amplitude is kept constant at 200 V for the (60+2) MHz regime (dashed lines), and as a function of the driving voltage in the single-frequency reactor at 60 MHz (dotted lines).

The average  $\text{CF}_3^+$  ion energy at the PE and GE is presented in Fig. 7.15(c) as a function of the HF voltage (dashed lines), and as a function of the driving voltage in the single-frequency reactor (dotted lines). The  $\text{Ar}^+$  and  $\text{N}_2^+$  energies have the same behavior but the values are lower in comparison with that of  $\text{CF}_3^+$  because of the frequent charge exchange collisions [see Chapter 5]. The ion energy increases with the applied HF voltage. It is higher when the LF power source is applied. Again the presented characteristics are more pronounced at the PE than at the GE.

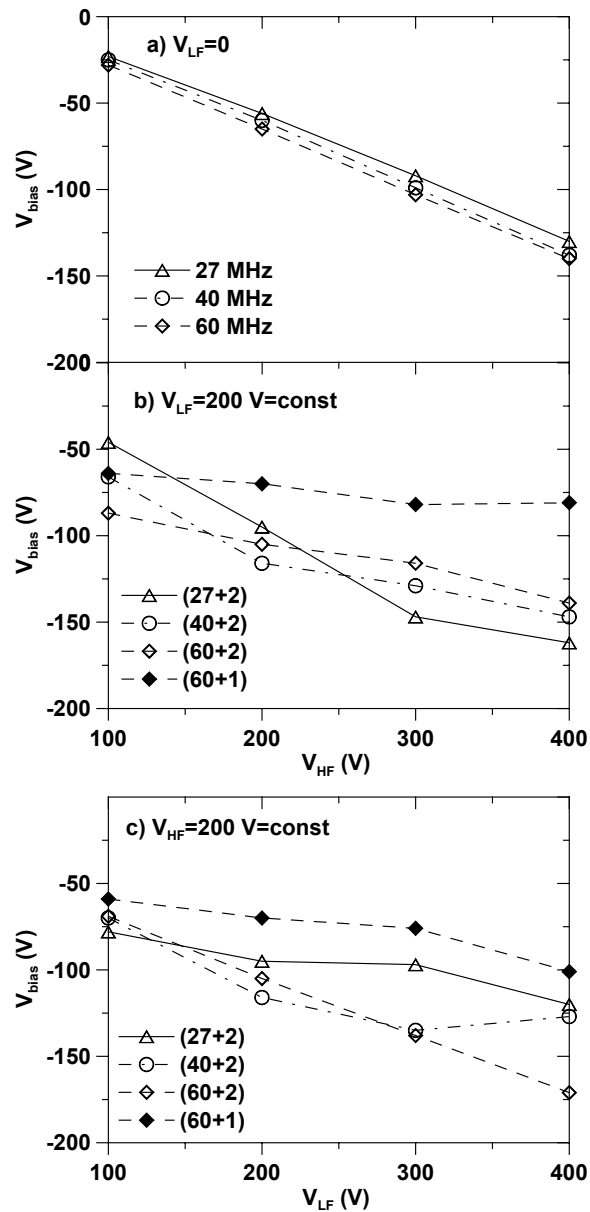


FIGURE 7.16. Calculated dc self-bias voltage as a function of the driving voltage in the single-frequency reactor for the applied frequencies of 27, 40, and 60 MHz (a), as a function of the HF voltage, while the LF voltage is kept constant at 200 V (b), and as a function of the LF voltage, while the HF voltage is kept constant at 200 V (c) for the (27+2), (40+2), (60+2) and (60+1) MHz regimes.

Finally, the dc bias voltage in the single-frequency reactor, i.e. at LF voltage of 0 V, as a function of the driving voltage for the applied frequencies of 27, 40 and 60 MHz (a), and in the dual-frequency reactor as a function of the HF voltage (b) and LF voltage (c), for the (27+2), (40+2), (60+2) and (60+1) MHz regimes are presented in Fig. 7.16. In the single-frequency reactor the dc bias voltage scales linearly with the driving voltage and increases very slightly with the applied frequency. Generally, in the dual-frequency reactor the bias voltage increases also with the applied LF or HF voltage but the dependence is not linear at all. A clear dependence on the HF cannot be established. If we compare the (60+1) MHz and (60+2) MHz regimes, it appears that the dc bias voltage decreases when the LF increases.

## 7.5 Summary

A detailed numerical investigation by means of the PIC/MC method was made to study the influence of the reactor parameters such as the electrode area ratio and HF and LF power source parameters on the plasma characteristics in Ar/CF<sub>4</sub>/N<sub>2</sub> discharges in an asymmetric dual-frequency reactor. A comparison with the symmetric dual-frequency reactor, as well as with the asymmetric single-frequency reactor is discussed.

It is observed that the electron density and temperature and sheath width are nearly independent from the electrode area ratio in the asymmetric reactor, and are more or less similar to the results in the symmetric reactor. The electron density has a maximum at the bulk-sheath interface to the PE. The sheath width is larger in front of the powered (smaller) electrode. The plasma potential decreases and the absolute value of the dc bias voltage increases with the electrode area ratio. The ratio of the sheath voltage at the PE to the sheath voltage at the GE is more or less linearly proportional to the ratio of the GE area to the PE area. Because of the formation of the dc bias voltage the IEDF at the PE is much broader than that at the GE and at the PE in the symmetric reactor. Moreover, the ion energy at the PE reaches higher maximum values when the electrode area ratio increases.

As in the symmetric reactor, it is observed that the decoupling of the two sources is possible with increase of the applied HF to values of 60 MHz and above, and it is not defined by the frequency ratio. The plasma density and ion current density are determined only by the HF source. The dc bias voltage and plasma potential, and therefore the sheath potential and ion energy increase with HF or LF voltage amplitude. The sheath width increases with the LF voltage and decreases with the HF voltage.

The dc bias voltage scales linearly with the driving voltage and increases very slightly with the applied frequency in the asymmetric single-frequency reactor. In the dual-frequency reactor the dc bias voltage also increases with the HF or LF

voltages, but the dependence is not linear. A dependence on the HF cannot be established, while the LF appears to decrease the dc bias voltage.

## Chapter 8

# NEGATIVE ION BEHAVIOR IN SINGLE- AND DUAL-FREQUENCY REACTORS

### 8.1 Introduction

In single-frequency capacitively coupled radio-frequency (RF) discharges the ion density profile is typically constant throughout the RF cycle since the ions cannot respond to the rapidly oscillating electric field. For example, if the applied RF is 13.56 MHz, i.e. in the order of  $10^7$  Hz the calculated electron plasma frequency  $f_{pe} = \omega_{pe} / 2\pi$ ,  $\omega_{pe}$  defined by Eq. (2.102), is in the order of  $10^8$  Hz, while the ion plasma frequency defined by [1]

$$f_{pi} = \frac{\omega_{pi}}{2\pi} = \frac{1}{2\pi} \left( \frac{e^2 n_i}{\epsilon_0 M} \right)^{1/2} \quad (8.1)$$

for a singly charged ion, is only in the order of  $10^6$  Hz. In Eq. (8.1)  $n_i$  is the ion density in the bulk plasma and  $M$  is the ion mass. The electric fields within the sheaths established at steady state point from plasma to the electrodes. Consequently, the electrostatic force acting on the negative ions is directed into the plasma and it confines them there, while the positive ions enter the sheaths and are accelerated to the walls. This is confirmed by the simulation results of the charged particle density and energy distributions presented in Chapter 4.

In dual-frequency reactors, however, under certain conditions the ions can respond to the electric field because the applied second, LF, for example 2 MHz, i.e.  $2 \times 10^6$  Hz, is in the order of the ion plasma frequency. As it is observed in the simulation results presented in Chapter 5, the positive ion density profile depends slightly on time in the LF cycle. The  $F^-$  ion density distribution, on the other hand, is found to be considerably modulated throughout the LF cycle. Highly energetic ions are detected at the electrodes. Indeed, the light  $F^-$  ions respond more or less to the

applied electric field and move across from one sheath to the other, and they can be lost at the electrodes, which is unexpected appearance. For example, a negative ion flux at the electrodes is numerically predicted [43] and experimentally observed [110] in a pulsed dual-frequency capacitively coupled discharge during the off-phase, which could be logically anticipated. However, in the present dual-frequency reactor the negative ions are detected at the electrodes when the power source is active. In this case the much heavier  $\text{CF}_3^-$  ions are still confined in the bulk and represent the major negative charge. The  $\text{F}^-$  flux at the electrodes can vary significantly depending on the reactor parameters, i.e. applied frequencies and voltage amplitudes (see Chapter 6).

The negative charge injection can reduce the local charging, which is essential for establishing of charge-free plasma processes for etching. Consequently, a systematic study of the negative ion behavior in electronegative discharges, such as in  $\text{CF}_4$  mixture, is important for further improvement of the etching process. The purpose of the present chapter is to clarify the movement of the negative ions in the sheaths and plasma and the energy they gain or lose in these regions. The trajectories and energies of randomly sampled  $\text{F}^-$  and  $\text{CF}_3^-$  ions are presented in both single- and dual-frequency regimes. The influence of operating conditions on the negative ion flux is also presented. The simulations have been carried out for both symmetric and asymmetric discharges.

In Sec. 8.2 the input parameters are given. In Sec. 8.3 the results of the simulations, i.e. the electric field distribution as a function of time in the LF or RF cycle, instantaneous sheath thickness, and trajectories and energies of the negative ions are shown and discussed. Finally, a summary is given in Sec. 8.4.

## 8.2 Input Data

The developed 1d model is described in Chapter 2. The simulations have been carried out for a pure  $\text{CF}_4$  discharge in a single-frequency reactor (see Chapter 3) and for an  $\text{Ar}/\text{CF}_4/\text{N}_2$  discharge in symmetric and asymmetric dual-frequency reactors (see Chapter 4 and 7, respectively, for the reactor geometry).

Randomly sampled negative ions are followed, i.e. their new position, velocity and consequently energy are calculated by Eqs. (2.8) and (2.9), and are saved in every ion time-step. If the sampled ion participates in a collision the post-collision velocity is calculated. The ion is followed until it is lost. As it is found in previous simulations in single-frequency reactors, the main loss mechanism is recombination with positive ions in the plasma. Electron detachment, which mainly takes place in the sheaths, has significantly lower reaction rates in comparison with recombination (see Chapter 3). All reaction processes of  $\text{CF}_3^-$  and  $\text{F}^-$  ions including electron detachment are presented in the Appendix B, Tables B.2 and B.3, respectively, along

with their threshold energies. The corresponding analytical cross-sections calculated from the ion-molecule collision model for endothermic reactions are presented in Figs. 2.17 and 2.18. It is helpful to mention here that the lowest threshold energy for an electron detachment process of  $F^-$  is 3.521 eV, and of  $CF_3^-$  is 1.871 eV. In the dual-frequency regime a third loss mechanism appears to be possible, which is absorption of the negative ions at the electrodes. A sufficient number of ions have been traced at different simulation times so that the trajectories and energies of the negative ions presented below can be considered representative.

The operating conditions in the single- 13.56 MHz regime are the same as in Chapter 3 for a pure  $CF_4$  discharge: a gas pressure of 200 mTorr, an electrode distance of 2.5 cm, and an applied voltage amplitude of 200 V. The operating conditions for the symmetric and asymmetric (27+2) MHz regime are the following: the applied HF and LF voltages are 200 and 400 V, respectively, for a gas mixture  $Ar/CF_4/N_2$  at a ratio of 0.8/0.1/0.1, a gas pressure of 30 mTorr, and an electrode distance of 2 cm. In order to show the dependence of the flux on the reactor parameters, negative ions have been traced also in (40+2)-, (60+2)- and (100+2) MHz regimes at HF and LF voltage amplitudes of 200 and 400 V. Neutral gas temperature is set to 300 K (0.026 eV).

### 8.3 Results and discussion

The figures presented below show the calculated position, particle energy and the velocity component in z- or r- direction, depending on the coordinate system, which is considered, i.e. Cartesian for the symmetric reactor and spherical for the asymmetric reactor, at every ion time-step as a function of time represented by a LF or RF cycle.

#### 8.3.1 Single-frequency reactors

A pure  $CF_4$  discharge sustained in a single-frequency reactor is considered at the operating conditions described above. Figures 8.1(a) and (b) present the calculated electric field distribution in the entire discharge and in the bulk region, respectively. The electric field in the sheaths is considerably stronger (the maximum is in the order of  $4.5 \times 10^4$  V/m) in comparison with the electric field in the bulk plasma, presented in Fig. 8.1(b) (up to  $2 \times 10^3$  V/m). The electric field is directed from plasma to the electrodes. Consequently, if a negative ion is created in the sheath, for example, after an electron attachment collision, it will be accelerated towards the plasma and gain energy from the electric field. This explains the comparatively high averaged  $F^-$  and  $CF_3^-$  ion energies up to 8 eV, calculated in the sheaths [see Fig 3.2(c)].

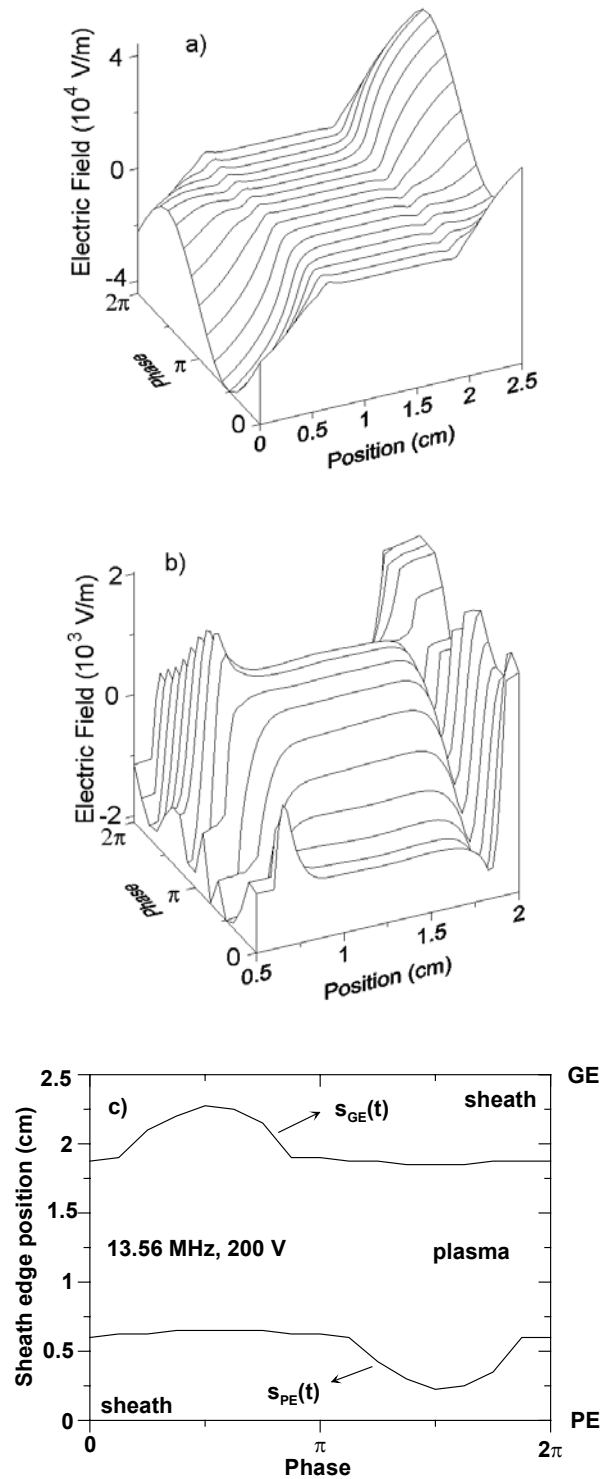


FIGURE 8.1. Calculated electric field distribution in the entire discharge (a) and in the plasma region (b) as well as the calculated sheath edge position in front of the PE and GE (c), as a function of time in one RF cycle. A pure  $\text{CF}_4$  discharge is sustained in a 13.56 MHz reactor, at an applied voltage of 200 V, a pressure of 200 mTorr, and an electrode distance of 2.5 cm.

Figure 8.1(c) presents the calculated sheath edge position in front of the PE and GE,  $s_{PE}(t)$  and  $s_{GE}(t)$ , respectively, as a function of the phase in the RF cycle. This figure is included in order to give an idea about the plasma and sheath regions for the considered operating conditions.

Figure 8.2(a) presents the calculated position, energy, and velocity in the z-direction of randomly sampled  $F^-$  ions created by electron attachment collisions in the sheaths and lost in electron detachment collisions, as a function of time, represented by RF cycles. The positions of the PE and GE are noted at 0 and 2.5cm, respectively. The ions are sampled at different times during the simulation. While traveling from the sheath to the plasma the ions gain sufficiently high energy and they can participate in reactive collisions with corresponding threshold energies or in elastic collisions [see the abrupt changes in the energy and velocity of the ions presented in Fig. 8.2(a)]. If the reactive collision is an electron detachment, the ion disappears. The life-time of  $F^-$  ions created in the sheaths is typically less than 10 RF cycles, i.e.,  $7 \times 10^{-7}$  s for a RF of 13.56 MHz.

Figure 8.2(b) shows the trajectory, energy, and velocity in the z-direction of randomly sampled  $F^-$  ions created by attachment collisions in the bulk plasma and lost in recombination. The energy and z-velocity is only presented for one of the ions, noted with (1), since the corresponding values of the other two ions are in the same range. The electric field in the bulk plasma is weak and the ions move slowly, participating only in elastic collisions with neutrals. Consequently, their energy does not change considerably. The calculated averaged  $F^-$  ion energy in the bulk plasma is around 0.04eV, i.e. close to the neutral gas temperature (see Chapter 3). It can be seen that the life-time of the  $F^-$  ions is more than 1000 RF cycles, i.e. above  $7 \times 10^{-5}$  s for a RF of 13.56MHz, which explains the long computational time needed to reach convergence in PIC/MCC simulations of electronegative discharges. Although the recombination frequency is low, this charge neutralization process is the main loss mechanism of the negative ions. Only around 1.5% of all  $F^-$  ions, lost for the time of simulation, disappeared in electron detachment collisions. Indeed, negative ions are almost absent in the sheaths. The few ions presented there are created by electron attachment collisions and they gain sufficient energy while moving to the bulk plasma, therefore, they participate in reactive collisions. Often these ions are lost in electron detachment collisions.

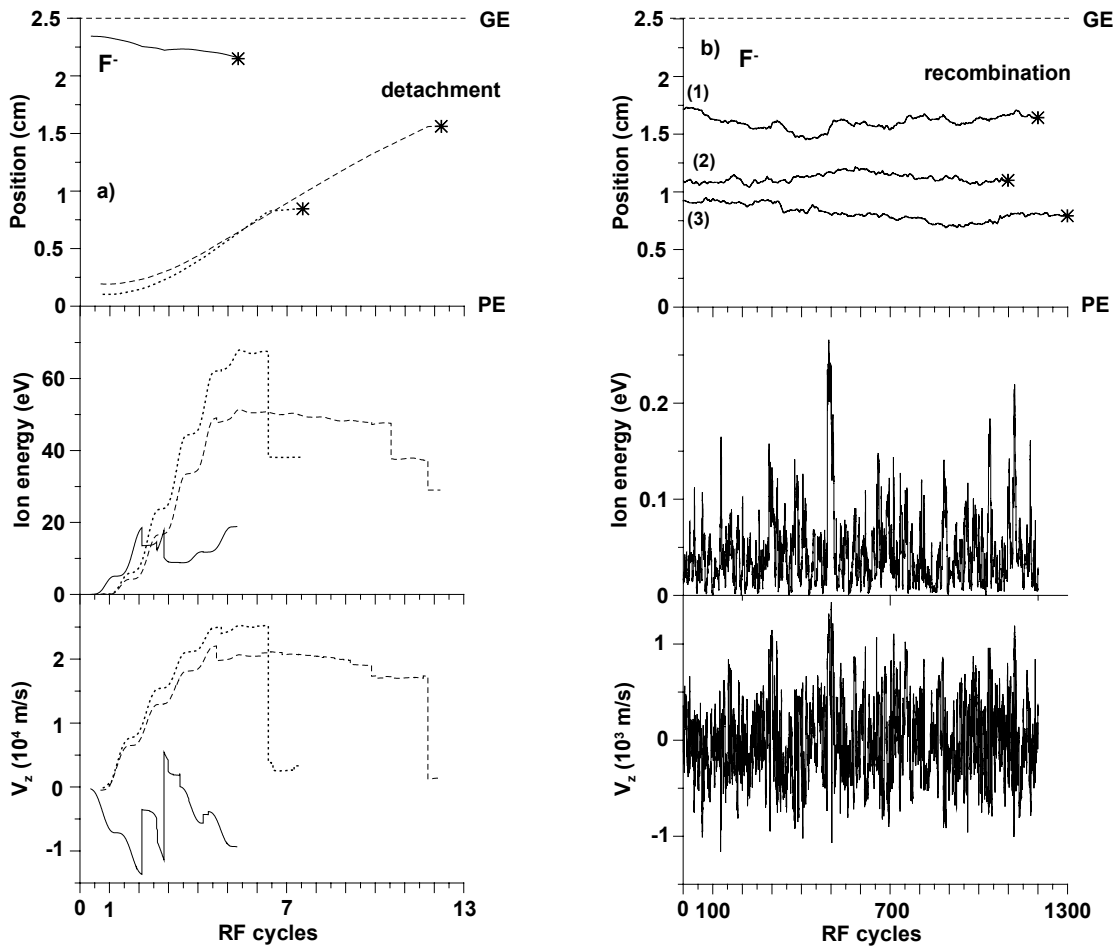


FIGURE 8.2. Calculated position, energy and  $z$ -velocity of randomly sampled  $F^-$  ions, created in electron attachment processes, as a function of time represented by RF cycles ( $\tau_{RF} = 7.4 \times 10^{-8}$  s). The ions are lost in electron detachment (a) or in recombination (b) collisions. The position of the PE and GE is also shown. The operating conditions are the same as in Fig. 8.1.

The same conclusions can be made for the  $CF_3^-$  behavior, only its life-time is longer. Figure 8.3 presents the position, energy, and  $z$ -velocity component of randomly sampled  $CF_3^-$  ions, as a function of time, represented by RF cycles. The energy and  $z$ -velocity of only one of the ions, noted with (1), are shown since the corresponding values of the other two ions are in the same range. The ions are created by electron attachment collisions and at the beginning their energy is close to the neutral gas energy. If an ion is created in the sheath or at the sheath-plasma interface, like ions (1) and (3), it moves slowly toward the center. Such ion initially gains some energy from the electric field at the beginning from a few eV to a few 10 eV, depending on the position in the sheath where it is created. This energy is

dissipated in a short time by the collisions with neutrals. If an ion is created in the plasma center, like the ion (2), its maximum energy does not exceed a few 0.1eV. The calculated averaged  $\text{CF}_3^-$  ion energy in the bulk plasma is around 0.04eV (see Chapter 3). Again, like for  $\text{F}^-$  ions, recombination with positive ions in the plasma is the main loss mechanism of  $\text{CF}_3^-$  ions, and its rate is low. As it can be seen the ions (1) and (2) stay in the plasma for more than 3000 RF cycles and recombination has not taken place yet. Ion (3) becomes lost by recombination after 2200 RF cycles. Electron detachment of  $\text{CF}_3^-$  ions takes place mainly in the sheaths, where the  $\text{CF}_3^-$  ions gain sufficiently high energy to participate in reactive collisions, but the probability is low. Less than 1% of the  $\text{CF}_3^-$  ions are lost in electron detachment collisions.

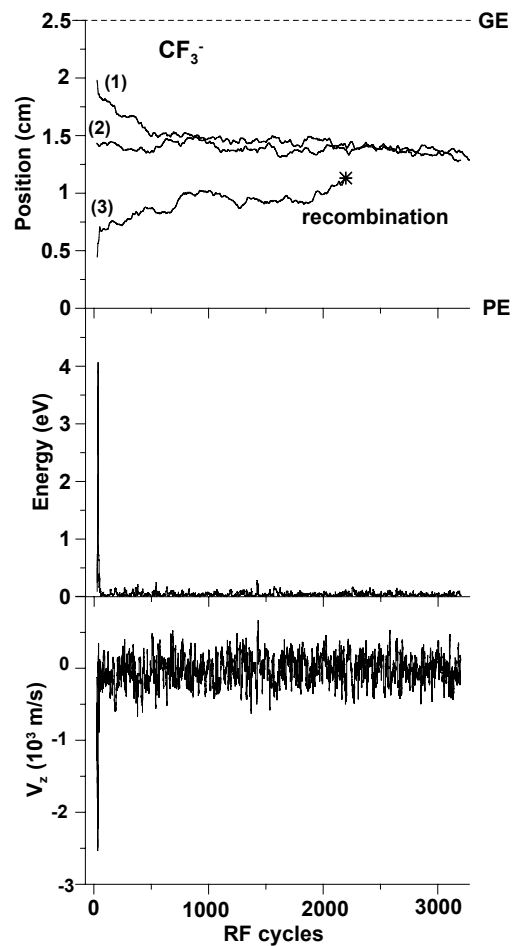


FIGURE 8.3. Calculated position, energy and  $z$ -velocity of randomly sampled  $\text{CF}_3^-$  ion, created in electron attachment collisions, as a function of time represented by RF cycles ( $\tau_{RF} = 7.4 \times 10^{-8}$  s). The  $\text{CF}_3^-$  ions (1) and (2) have not been lost for the time of observation, the ion (3) is lost in a recombination process. The operating conditions are the same as in Fig. 8.1.

The  $F^-$  and  $CF_3^-$  ions have the same behavior in the asymmetric discharge sustained in a single-frequency reactor, i.e. they are confined in the plasma.

### 8.3.2 Dual-frequency reactors

As it is observed in Chapters 4 and 6, in the dual-frequency regime the  $F^-$  ions can reach the electrodes and, consequently reduce the local charging. Figures 8.4(a) and (b) present the calculated electric field distribution in the entire discharge and in the bulk region, respectively, in a symmetric  $Ar/CF_4/N_2$  discharge sustained in a dual- (27+2) MHz reactor. The applied HF and LF voltages are 200 and 400V, respectively, and the gas pressure is 30mTorr. The maximum of the electric field in the sheaths is now in the order of  $10^5$  V/m and in the bulk plasma it is in the order of  $10^4$  V/m). Indeed, at a HF of 27 MHz and when the applied LF voltage amplitude is comparable or higher than the HF voltage amplitude, the behavior of the discharge is strongly electronegative. The electric field in the plasma is then strong and double layers appear at the bulk-sheath interfaces. In the presence of the LF the  $F^-$  ions respond more or less to the time-variation of the electric field and are not confined in the bulk plasma. The sheaths oscillate with the applied frequencies [see Fig. 8.4(c)] and the sheath width is large enough, therefore  $F^-$  ions gain considerable energy when they move towards the plasma for some time in the LF cycle so that they can traverse the narrow bulk plasma and continue to the other sheath. The electric field retards the ions until they change their direction again to the center. As a result, the  $F^-$  ions can oscillate from one sheath to the other and after several LF cycles some of them can reach the electrodes.

Figure 8.5 (a) presents the position, energy, and z-velocity component of randomly sampled  $F^-$  ions, which are lost at the electrodes, as a function of time, represented by LF cycles. Other ions can be lost in electron detachment collisions [see Fig. 8.5(b)]. The time corresponding to 1 LF (2 MHz) cycle is  $5 \times 10^{-7}$  s, hence the life-time of  $F^-$  in these cases is in the order of  $5 \times 10^{-6}$  s. In the dual-frequency reactor electron detachment can take place both in the bulk plasma and in the sheaths because the  $F^-$  ions have high enough energy to participate in a reactive collision in the entire discharge. The calculated average energy is above 15 eV in the bulk plasma and above 100 eV in the sheaths. In this case the main loss mechanisms are the absorption at the electrodes and electron detachment collisions (see below). The  $F^-$  density distribution is considerably modulated in the LF cycle (see Chapter 4) and negative ions are present in the sheaths not only because they are created in electron attachment collisions but also because they respond to the oscillating electric field.

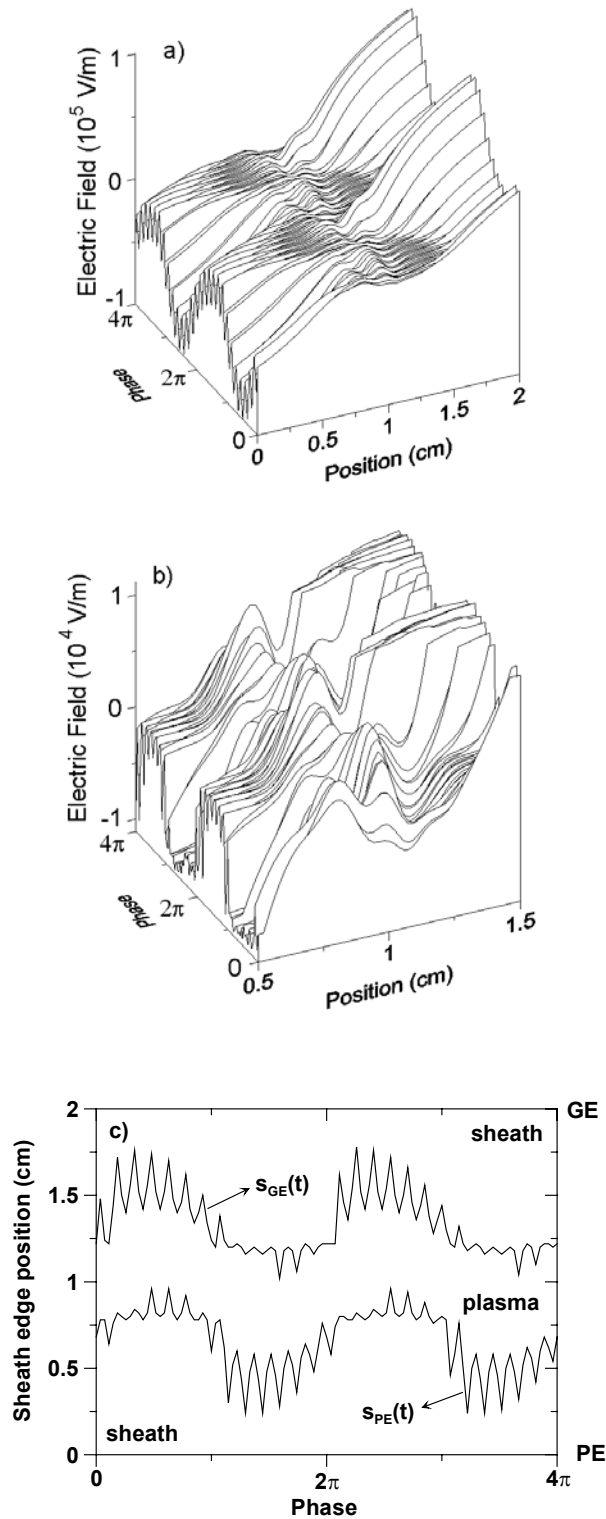


FIGURE 8.4. Calculated electric field distribution in the entire discharge (a) and in the plasma region (b), as well as the calculated sheath edge position in front of the PE and GE (c), as a function of time in two LF cycles. A symmetric Ar/CF<sub>4</sub>/N<sub>2</sub> discharge is sustained in the (27+2) MHz reactor, at applied HF and LF voltages of 200 and 400V, respectively, a pressure of 30mTorr, and an electrode distance of 2 cm.

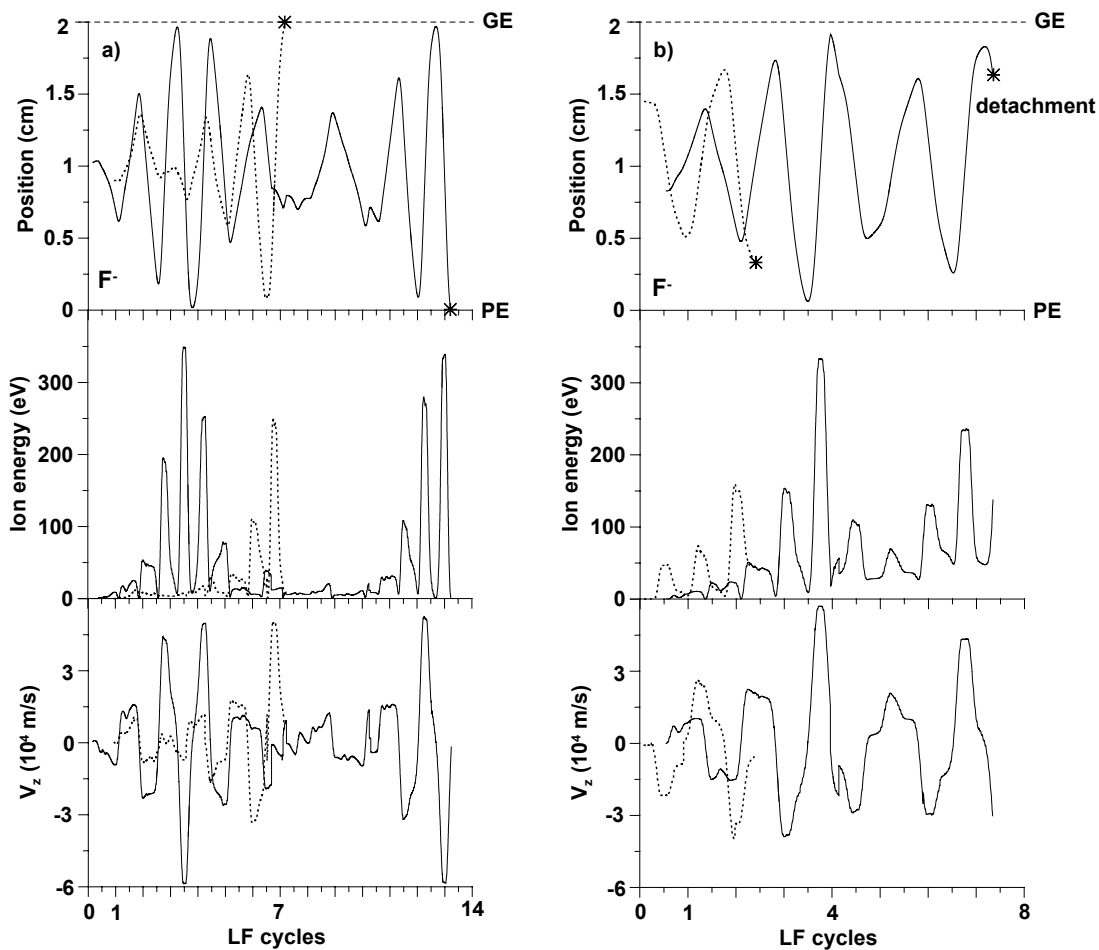


FIGURE 8.5. Calculated position, energy and  $z$ -velocity of randomly sampled  $F^-$  ions, created in electron attachment collisions, as a function of time represented by LF cycles ( $\tau_{LF} = 2 \times 10^{-7}$  s). The ions are lost at the electrodes (a) or in electron detachment collisions (b). The operating conditions are the same as in Fig. 8.4.

The much heavier  $CF_3^-$  ions, however, are still confined in the plasma and recombination with positive ions is their major loss mechanism. The tracing of randomly sampled  $CF_3^-$  ions is presented in Fig. 8.6. The ions are not yet lost after more than 200 LF cycles, hence their life-time is longer than  $10^{-4}$  s. The energy and  $z$ -velocity component are shown of the ion, noted with (1). The energy of the other ion at the beginning rises up to 30 eV but it is quickly dissipated in the collisions with neutrals and then it has values close to the energy of the ion (1). The  $CF_3^-$  averaged energy in the bulk plasma is above 0.2 eV, i.e. higher than the calculated

value of 0.04eV in the single-frequency regime, due to the stronger electric field in the bulk plasma in the dual-frequency regime (see above).

As it is found in Chapter 6 the sheath width decreases [see Fig. 6.1(e)], and consequently, the bulk plasma increases with the HF so that most F- ions gather less energy and cannot traverse the bulk plasma. In addition, a transition to an electropositive behavior is observed, which means that the electric field in the bulk plasma is close to 0. Consequently, few ions can reach the electrodes when the applied HF increases from 27 to 100 MHz.

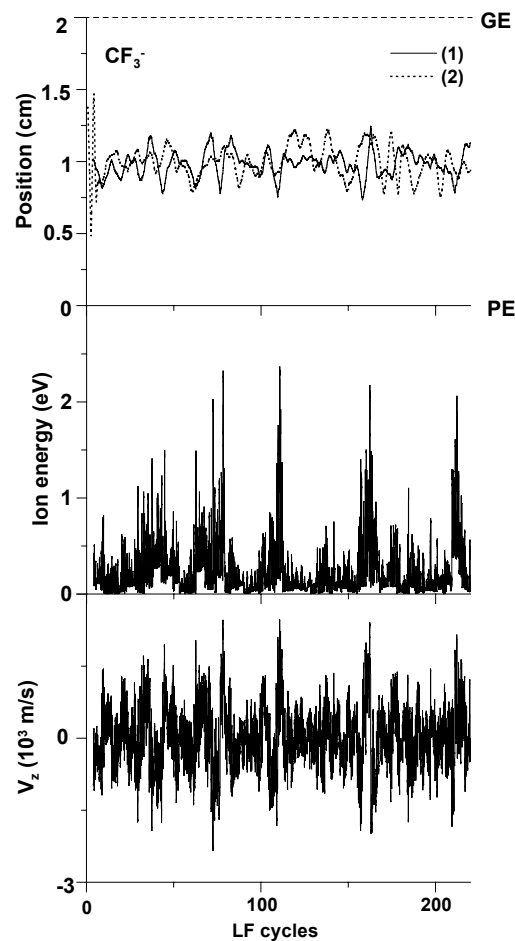


FIGURE 8.6. Calculated position, energy and  $z$ -velocity of a randomly sampled  $\text{CF}_3^-$  ions, created in electron attachment collisions, as a function of time represented by LF cycles ( $\tau_{LF} = 5 \times 10^{-7}$  s). The two ions have not been lost for the time of observation. The operating conditions are the same as in Fig. 8.4.

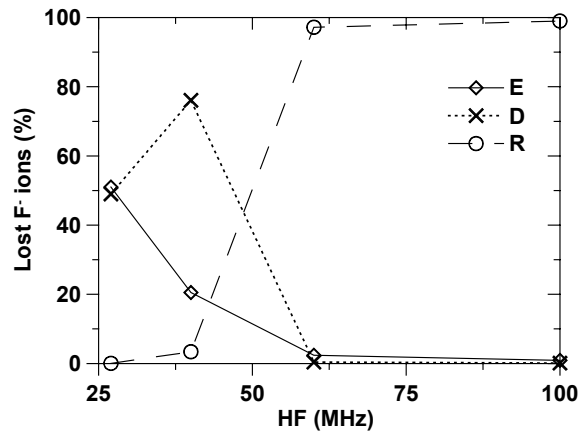


FIGURE 8.7. Calculated percentage of the  $F^-$  ions lost at the electrodes (solid line), or by electron detachment (dotted line) or recombination (dashed line) in symmetric  $Ar/CF_4/N_2$  discharges sustained in the (27+2)-, (40+2)-, (60+2)- and (100+2) MHz regimes, at applied HF and LF voltage amplitudes of 200 and 400 V, respectively, a pressure of 30 mTorr, and an electrode distance of 2 cm.

Figure 8.7 presents the percentage of the  $F^-$  ions lost at the electrodes, or by electron detachment or recombination collisions in the (27+2)-, (40+2)-, (60+2)- and (100+2) MHz regimes, at applied HF and LF voltage amplitudes of 200 and 400 V, respectively. The absorption at the electrodes and electron detachment collisions are the main loss mechanisms for the (27+2)- and (40+2) MHz regimes. With increase of the HF recombination becomes the main loss mechanism. Hence, the  $F^-$  ion flux at the electrodes is strongest for the operating conditions, which give rise to a strongly electronegative discharge behavior and when the sheaths are comparatively wide.

The presented results explain the differences in negative ion density distributions and calculated energies observed in single- and dual-frequency reactors (see Chapters 3, 4 and 6). In the single-frequency reactor  $F^-$  and  $CF_3^-$  ions are confined in the bulk plasma and  $F^-$  ions represent the major negative charge because of the larger electron attachment cross-section in comparison with the corresponding cross-section for  $CF_3^-$  [see Fig. 3.2(b)]. Their density distributions are constant throughout the RF cycle. In the dual-frequency reactor under certain operating conditions (see above), the  $F^-$  density distribution depends on the time in the LF cycle. Figure 8.8 presents the  $F^-$  density distribution as a function of time in 2 LF cycles (a) and averaged over 2 LF cycles (b, dashed line), the  $CF_3^-$  density distribution (b, solid line), which profile is constant in time, and the energy distribution of the  $F^-$  ions lost at the electrodes (c).

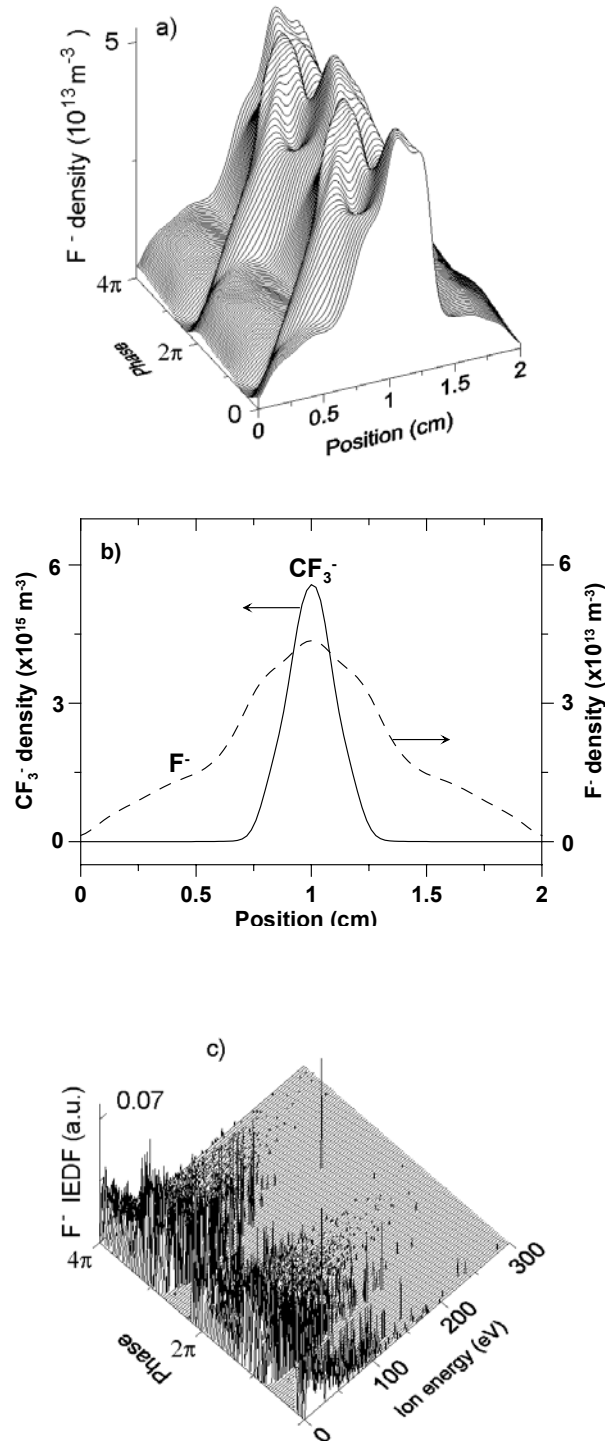


FIGURE 8.8. Calculated F<sup>-</sup> density distribution as a function of time in 2 LF cycles (a) and averaged over 2 LF cycles (b, dashed line), CF<sub>3</sub><sup>-</sup> density distribution, which profile is constant throughout the LF cycle (b, solid line), and the energy distribution of the F<sup>-</sup> ions lost at the electrodes (c). The operating conditions are the same as in Fig. 8.4.

The presented characteristics are calculated for the Ar/CF<sub>4</sub>/N<sub>2</sub> discharge sustained in the (27+2) MHz reactor, at HF and LF voltage amplitudes of 200 and 400 V, respectively. The F<sup>-</sup> ions are lost mainly by fast electron detachment or absorption at the electrodes, i.e. compare the life-time in the order of  $5 \times 10^{-6}$  s in these cases to the life-time above  $7 \times 10^{-5}$  s in case of recombination. Hence, the F<sup>-</sup> density in the bulk plasma decreases to  $5 \times 10^{13}$  m<sup>-3</sup> for the considered operating conditions [Fig. 8.8(a)]. The CF<sub>3</sub><sup>-</sup> ions are still confined in the bulk plasma, their density distribution is constant throughout the LF cycle and they represent the main negative charge with a density of  $6 \times 10^{15}$  m<sup>-3</sup> in the center [Fig. 8.8(b)]. The energy of the F<sup>-</sup> ions absorbed at the electrodes can reach values of 200 eV [Fig. 8.8(c)].

Finally, an asymmetric Ar/CF<sub>4</sub>/N<sub>2</sub> discharge, sustained in a (27+2) MHz reactor, is considered. The applied HF and LF voltage amplitudes are 200 and 400 V, respectively. A 1-d spherical model is used to simulate the asymmetric discharge (see Chapter 7). The inner, PE, is positioned at  $r = 5$  cm, and the GE at  $r = 7$  cm so that the electrode area ratio is 1.96, and the electrode distance is 2 cm.

As it is found in Chapter 7, the sheath voltage ratio is almost inversely proportional to the electrode area ratio. In the asymmetric discharge the dc bias voltage increases the sheath voltage in front of the smaller (powered) electrode, consequently the electric field is much stronger than that in front of the GE. Figure 8.8 presents the calculated electric field distribution in the entire discharge (a) and in the bulk plasma (b), as well as the sheath edge position (c), as a function of time in two LF cycles. It can be seen that the maximum of the electric field at the PE is almost twice as high as the maximum at the GE. In addition the sheath in front of the PE is broader than the sheath in front of the GE [see also Figs. 7.3 and 7.4]. Therefore, the F<sup>-</sup> ions reach mainly the GE because their energy is not high enough to reach the PE when they move from the bulk plasma to the PE and are retarded by the electric field.

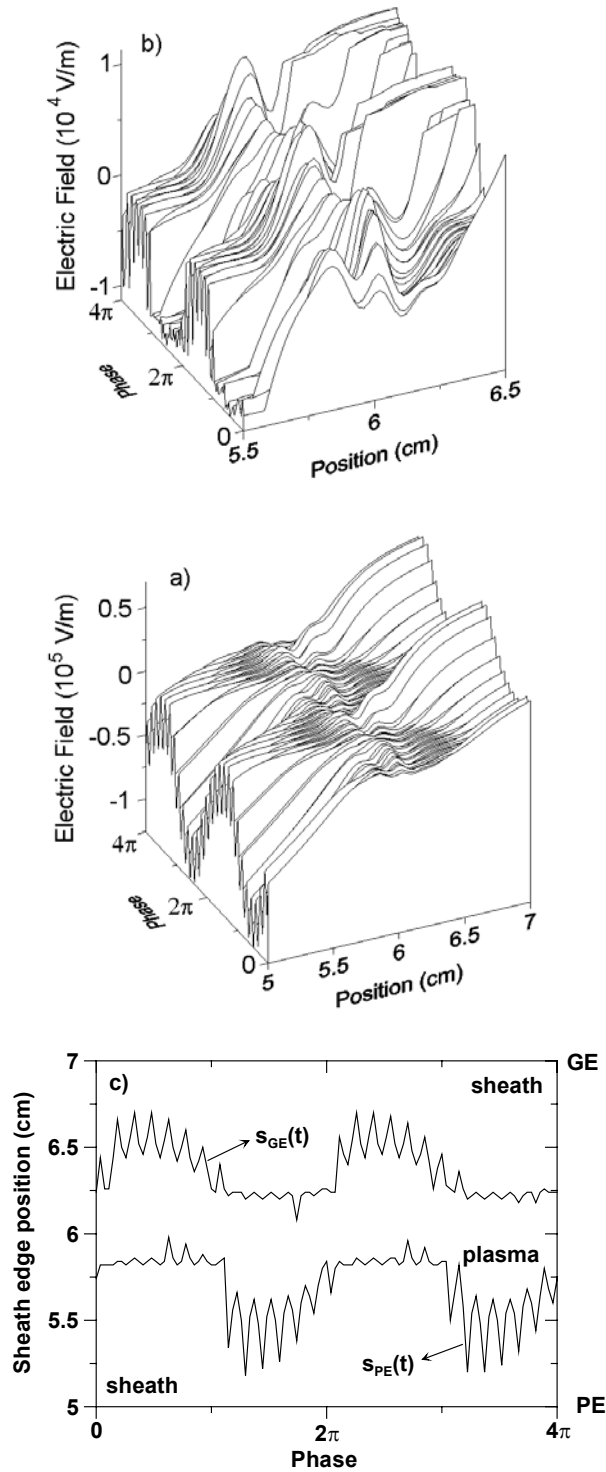


FIGURE 8.9 Calculated electric field distributions in the entire discharge (a) and in the plasma region (b), as well as the calculated sheath edge position in front of the PE and GE (c), as a function of time in two LF cycles. An asymmetric Ar/CF<sub>4</sub>/N<sub>2</sub> discharge is sustained in a dual- (27+2) MHz reactor, at applied HF and LF voltages of 200 and 400V, respectively, a pressure of 30mTorr, and an electrode distance of 2 cm. The PE is positioned at  $r = 5$  cm, and the GE at  $r = 7$  cm, and the electrode area ratio is 1.96.

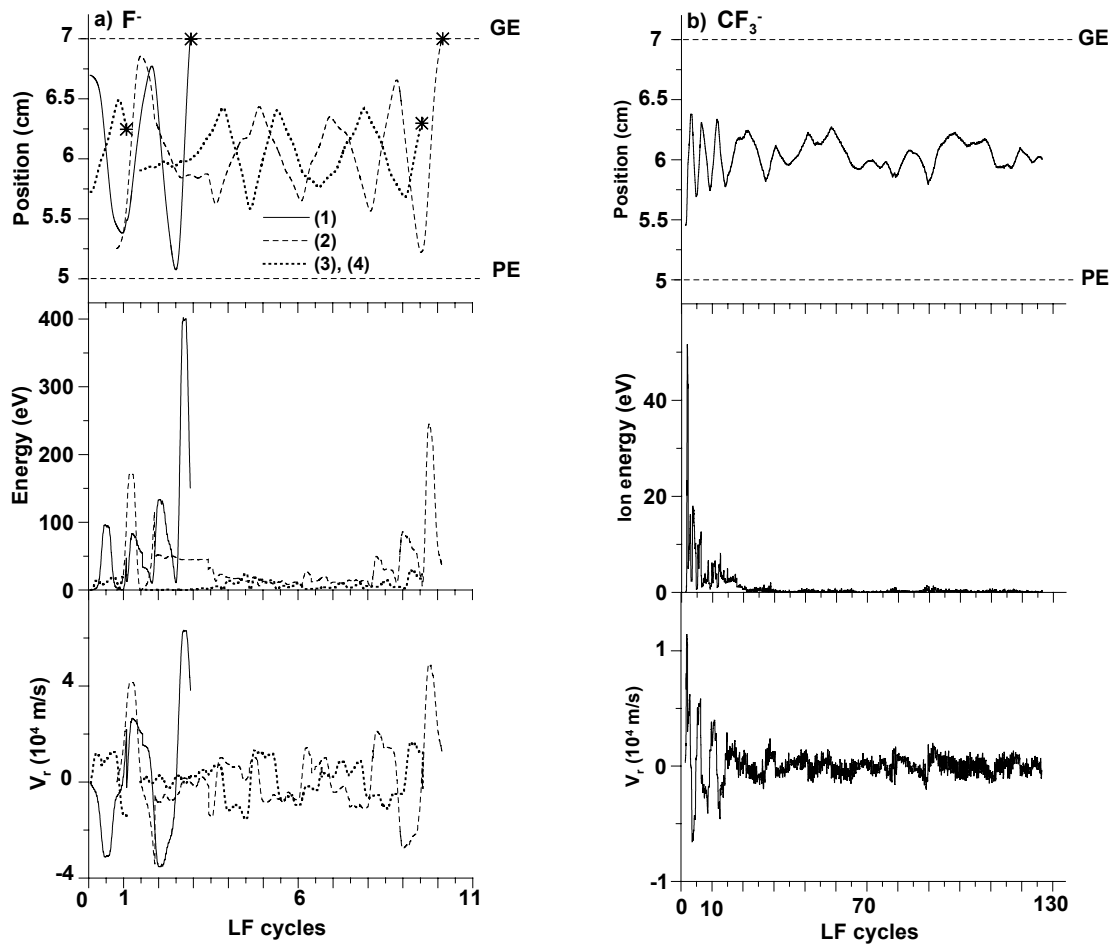


FIGURE 8.10. Calculated position, energy and  $z$ -velocity of randomly sampled  $F^-$  (a) and  $CF_3^-$  (b) ions, created in electron attachment processes, as a function of time represented by LF cycles ( $\tau_{LF} = 2 \times 10^{-7}$  s). The  $F^-$  ions (1) and (2) are lost at the electrodes, and (3) and (4) are lost in electron detachment collisions. The  $CF_3^-$  ion has not been lost for the time of observation. The operating conditions are the same as in Fig. 8.9.

The calculated position, energy and  $r$ -velocity component of randomly sampled  $F^-$  and  $CF_3^-$  ions, as a function of time, represented by LF cycles, are presented in Fig. 8.10 (a) and (b), respectively. All the ions are created in electron attachment collisions. The  $F^-$  ions (1) and (2) are lost at the GE, (3) and (4) are lost in electron detachment processes [Fig. 8.10(a)]. The  $CF_3^-$  ions behave in the same way as in the symmetric discharge sustained in a dual-frequency reactor, i.e. they are confined in the plasma [Fig. 8.10(b)].

#### 8.4. Summary

Randomly sampled  $F^-$  and  $CF_3^-$  ions have been traced in single- and dual-frequency reactors, at different operating conditions, both in symmetric and asymmetric discharges.

It is shown that in symmetric or asymmetric single-frequency reactors both types of negative ions are confined in the plasma and the loss mechanisms are recombination in the plasma and electron detachment in the sheaths. Comparatively high energies are calculated in the sheaths because the negative ions created by attachment collisions in the sheaths gain energy from the electric field in their way towards the plasma.

In the dual-frequency reactor, however, in the presence of a LF, the light  $F^-$  ions respond more or less to the applied electric field and can reach the electrodes. The  $F^-$  energy is sufficiently high in the sheaths and plasma; hence electron detachment of  $F^-$  can take place in the entire discharge. The absorption at the electrodes and electron detachment collisions are the main loss mechanism. The negative  $F^-$  ion flux at the electrodes is strongest when the operating conditions give rise to a strongly electronegative discharge behavior, and the sheaths are comparatively wide while the bulk plasma is narrow. The  $F^-$  ion flux decreases when the applied HF increases because the sheath width decreases and the discharge exhibits more electropositive features, i.e. the electric field in the plasma is close to 0. The much heavier  $CF_3^-$  ions are still confined in the bulk but their average energy is calculated to be higher than the calculated average energy in the single-frequency reactor.

In the asymmetric discharge, sustained in a dual-frequency reactor the  $F^-$  ions reach mainly the GE because the electric field to the smaller electrode, i.e. PE, is much stronger than the electric field to the GE.



## **Chapter 9**

### **CONCLUSIONS**

#### **9.1 Summary**

Significant advances have been made in numerical simulation of RF discharges used for material processing in the last decade. A variety of models has been developed in order to study the discharge physics and chemistry. This work has been focused on developing a 1d3v PIC/MCC model with minimum approximations and on its application to study symmetric fluorocarbon-based discharges sustained in single- and dual-frequency etching reactors. The developed model has also been extended to study asymmetric discharges.

The PIC model has become more or less a standard technique for any gas mixture. The model consists of charged particles moving about due to the forces they generate and the applied fields. It uses classical mechanics for the equations of motion and Maxwell's equations for the electric and magnetic fields generated by the particle densities. The PIC is based on the theory of charge assignment and field interpolation. A MC procedure is used to treat the collisions. This MC simulation of collisions between particles requires knowledge of a number of cross-section data, reaction rates or any characteristics, which represent the collision frequency. Such experimental data for a given gas mixture are not always available in the literature and a theoretical approach has been used in order to simulate the collisions properly. The present model uses several techniques in order to include collisions in the model, i.e. the null-collision method, an ion-molecule model for endothermic reactions, and the MCC method to simulate positive-negative ion recombination and electron-positive ion recombination from a given rate constant.

The typical output of the model is the time- and space dependence of charged particle density and energy distributions, fluxes, potential and electric field distributions, collision rates, and sheath characteristics such as sheath voltage and width.

The discharge characteristics in a gas-mixture of Ar and CF<sub>4</sub> have been studied and the transition from electropositive to electronegative behavior has been clarified. Results of the simulation are in agreement with results for similar simulations performed by others, especially for pure Ar and pure CF<sub>4</sub> discharges. The calculated electronegativities in an Ar/CF<sub>4</sub> discharge are in good agreement with the experimental data.

Dual-frequency reactors have become the industry standard for etching of silicon-based substrates. The novelty of the present work is the development of a numerical model for a complex gas mixture of Ar, CF<sub>4</sub>, and N<sub>2</sub> used for etching in an industrial dual-frequency reactor. The plasma behavior has been investigated and compared in the conventional single-frequency and dual-frequency reactors. In contrast with the single-HF reactor, where the negative ions are confined in the plasma, in the dual-frequency regime the negative ions can respond to the applied LF electric field and it is found that energetic negative F<sup>-</sup> ions reach the electrodes, consequently they can influence the etching process. The negative ion flux at the electrodes is strongest when the operating conditions give rise to a strong electronegative discharge behavior. It has been observed that the ion-energy distribution is significantly wider in the dual-frequency in comparison with the conventional reactors. Finally, the electron-neutral collision frequency increases several times in the dual-frequency reactor, which randomizes the electron energy.

The ion-bombarding energy is important in determining the etch rates and anisotropy as it is discussed in Chapter 1. Consequently, a systematic study of this characteristic could help the improvement of the etching process. The simulations have been carried out over a wide range of pressure and applied voltage amplitude covered in both single- and dual-frequency reactors. An analytical model for the energy width of the IEDF in a dual-frequency reactor has been developed. Good quantitative agreement is obtained between the theoretical and simulation results.

The two-frequency scheme allows independent control of the ion flux and ion bombardment energy, which is important for surface etching applications, and this cannot be achieved by the conventional cc reactor. A detailed numerical investigation has been made to study the influence of the reactor parameters on the plasma characteristics in Ar/CF<sub>4</sub>/N<sub>2</sub> plasmas in a dual-frequency reactor. It is observed that the decoupling of the two sources is possible with increase of the applied HF to values of 60 MHz and higher, and it is not defined by the frequency ratio. The charged particle and ion current densities can be controlled only by the HF source. The ion-bombarding energy, on the other hand, depends on both power sources. Therefore, an independent control of the ion flux and energy in a voltage driven dual-frequency reactor is possible, for example, when increasing the HF and varying the LF voltage keeping the HF voltage constant. The calculated electron

density in the bulk plasma and the positive ion current density at the electrodes have been compared with experimental data at the same operating conditions, and reasonable quantitative agreement has been found.

Etching discharges are generally asymmetric, i.e., the area of the PE is typically smaller than the area of the GE. The developed 1d3v PIC/MCC model in Cartesian coordinates has been extended to consider also spherical coordinates so that the study of asymmetric discharges is possible in one dimension. A detailed numerical investigation has been made to study the influence of the reactor parameters such as the electrode area ratio and both power source parameters on the plasma characteristics in an asymmetric dual-frequency reactor. A comparison with the symmetric dual-frequency reactor, as well as with the asymmetric single-frequency reactor has been carried out. The asymmetry determines the formation of a self-bias voltage at the PE, which in turn influences the ion-bombarding energy. The IEDF at the PE is much broader than that at the GE and at the PE in the symmetric reactor. Moreover, the ion energy at the PE reaches higher maximum values when the electrode area ratio increases. The influence of the power source parameters is more or less the same as in symmetric reactors.

In conclusion, the present investigation has covered the influence of a wide range of different reactor parameters of single- and dual-frequency reactors on the plasma behavior so that they can be adjusted to obtain desirable plasma characteristics. Therefore, this study can be useful in improving control over the etching process.

## 9.2 Future opportunities

The PIC/MCC simulation does not consider radical densities and this approximation has been discussed in Sec. 2.11. However, simulation of both charged and neutral species is necessary to examine the discharge structure and behavior. Generally, a fluid or hybrid model is more suitable to follow the radicals and excited states, since the PIC/MC method assumes that the background gas neutrals are distributed uniformly in the discharge, which is not applicable to the other neutral species. Consequently, it would be interesting to develop a fluid or hybrid model for the same gas mixture using the same collision data as in the present PIC/MCC model in order to calculate the radical densities. The comparison of the charged particle densities calculated by both models can give information about the effect of disregarding the radical species in PIC/MCC modeling.

As it has been discussed in Chapter 1,  $N_2$  is added to Ar/ $CF_4$  gas mixtures in order to control radical temperature. The other gas, which is often used in etching of silicon and silicon dioxide, is  $O_2$ . The developed model can be readily modified in order to simulate Ar/ $CF_4$ / $O_2$  discharges by replacing  $N_2$  with  $O_2$  once the necessary

cross-section data or reaction rates are available. Then the calculated plasma characteristics in a dual-frequency reactor can be compared with experimental data, for example, presented in Ref. 107.

## **Samenvatting**

In de voorbije tien jaar zijn er belangrijke vorderingen gemaakt op het gebied van numerische simulaties van RF ontladingen voor materiaalbehandeling. Een grote verscheidenheid aan modellen is ontwikkeld om de ontladingsfysica en -chemie te bestuderen. Dit doctoraatswerk beschrijft de ontwikkeling van een 1d3v PIC/MCC model met een minimum aan benaderingen, en de toepassing van dit model op de studie van symmetrische CF<sub>4</sub>-bevattende ontladingen in “enkele en dubbele frequentie” etsreactoren. Het ontwikkelde model is ook verder uitgebreid ter bestudering van asymmetrische ontladingen.

Het PIC model is min of meer een standaardtechniek geworden voor de bestudering van plasma's. Het model bestaat erin geladen deeltjes te laten bewegen onder invloed van de krachten die ze genereren en de aangelegde velden. Het maakt gebruik van de klassieke mechanica voor de bewegingsvergelijkingen en de wetten van Maxwell voor de beschrijving van de elektrische en magnetische velden gegenereerd door de deeltjesdichtheden. Het PIC model is gebaseerd op de theorie van de toewijzing van ladingen en veld interpolatie. Een MC procedure wordt gebruikt om botsingen te beschrijven. Deze MC simulatie van botsingen tussen deeltjes veronderstelt kennis van een aantal werkzame doorsneden, reactiesnelheden, of andere karakteristieken die nodig zijn om de botsingsfrequentie te berekenen. In de literatuur echter is een dergelijke experimentele dataset niet altijd beschikbaar, en daarom moet vaak een theoretische benadering gebruikt worden om de botsingen correct te beschrijven. Het huidige model gebruikt verscheidene technieken om botsingen in het model op te nemen, nl. de zgn. 'null-collision' methode, een ion-molecule model voor endotherme reacties, en de MCC methode om vanuit een gegeven snelheidsconstante de recombinatie tussen een positief en een negatief ion, en tussen een elektron en een positief ion, te simuleren.

De gegevens die typisch verkregen worden uit het model, omvatten de ruimtelijke en tijdsgeresolveerde dichtheid van de geladen deeltjes en energieverdelingen, fluxen, verdeling van de potentiaal en het elektrisch veld, botsingssnelheden, en sheath-karakteristieken zoals de sheath-spanning en de sheath-dikte.

In dit werk zijn de ontladingskarakteristieken van een Ar/CF<sub>4</sub> gasmengsel bestudeerd en de overgang van elektropositief naar elektronegatief gedrag is opgehelderd. De resultaten zijn in overeenstemming met resultaten voor gelijkaardige simulaties uitgevoerd door anderen, in het bijzonder de resultaten voor zuivere Ar en zuivere CF<sub>4</sub> ontladingen. De berekende elektronegativiteiten in een Ar/CF<sub>4</sub> ontlading zijn in goede overeenstemming met experimentele gegevens.

“Dubbele frequentie” reactoren zijn de industriële standaard geworden voor het etsen van silicium-gebaseerde substraten. Het innovatieve concept van dit werk is de ontwikkeling van een numerisch model voor een complex gasmengsel van Ar, CF<sub>4</sub>, en N<sub>2</sub> dat als etsgas gebruikt wordt in een industriële etsreactor. Het plasmagedrag is onderzocht en de vergelijking is gemaakt tussen een conventionele enkele frequentie reactor en de dubbele frequentie reactor. In tegenstelling tot de enkele frequentie reactor, waarin de negatieve ionen gevangen zitten in het plasma, kunnen de negatieve ionen in het dubbele frequentie regime reageren op het aangelegde laagfrequente (LF) elektrische veld. De bevinding is dat energetische negatieve F<sup>-</sup> ionen de elektroden kunnen bereiken, en zo het etsproces kunnen beïnvloeden. De flux aan negatieve ionen naar de elektroden is het sterkst wanneer de ontladingsvoorwaarden aanleiding geven tot een sterk elektronegatief ontladingsgedrag. Er is vastgesteld dat de ionen energie distributiefunctie (IEDF) in belangrijke mate breder is in de dubbele frequentie reactor in vergelijking met de conventionele reactoren. Tenslotte verhoogt de elektron-neutraal botsingsfrequentie sterk in de dubbele frequentie reactor, waardoor de elektronenenergie randomiseert.

De energie van de bombarderende ionen is een bepalende factor voor de etssnelheid en de ets-anisotropie. Daarom kan een systematische studie van deze karakteristiek een vooruitgang betekenen in de verbetering van het etsproces. De simulaties zijn uitgevoerd over het brede gebied in druk en aangelegde spanning waarin zowel de enkele als de dubbele frequentie reactoren operationeel zijn. Een analytisch model voor de energiebreedte van de IEDF in een dubbele frequentie reactor werd ontwikkeld. Er werd een goede kwantitatieve overeenstemming tussen theoretische resultaten en simulatie resultaten bekomen.

De dubbele frequentie implementatie laat een onderling onafhankelijke controle van de ionenflux en ionen-bombarderende energie toe, hetgeen belangrijk is voor ets-toepassingen van oppervlakken, en hetgeen niet mogelijk is in een conventionele reactor. Een gedetailleerde numerische studie is uitgevoerd om de invloed van de reactor parameters op de plasma karakteristieken in Ar/CF<sub>4</sub>/N<sub>2</sub> plasma's in een dubbele frequentie reactor te onderzoeken. Er is vastgesteld dat de ont koppeling van beide bronnen mogelijk is door een verhoging van de aangelegde hoge-frequentie (HF) tot waarden van 60 MHz en hoger, en dat dit niet bepaald wordt door de verhouding van de frequenties. De dichtheden van de geladen deeltjes

en de ionenstroom kunnen gecontroleerd worden door middel van enkel de HF bron. De ionen-bombarderende energie daarentegen, is afhankelijk van beide bronnen. Daardoor is een onafhankelijke controle van de ionenflux en -energie in een spanning-aangedreven dubbele frequentie reactor mogelijk, bv. door toename van de HF en variatie van de LF spanning, terwijl de HF spanning constant wordt gehouden. De berekende elektronendichtheid in de bulk van het plasma en de stroomdichtheid van de positieve ionen aan de elektroden zijn vergeleken met experimentele gegevens bij dezelfde werkingsvoorwaarden, en een redelijke kwantitatieve overeenstemming is bereikt.

Ontladingen die gebruikt worden voor etstoepassingen zijn in het algemeen asymmetrisch, d.i., de oppervlakte van de aangedreven elektrode ("powered electrode"; PE) is typisch kleiner dan de oppervlakte van de geaarde elektrode ("grounded electrode"; GE). Het ontwikkelde 1d3v PIC/MCC model in Carthesische coördinaten werd daarom uitgebreid naar sferische coördinaten, zodat de studie van asymmetrische ontladingen mogelijk wordt in één dimensie. Een gedetailleerde numerische studie is uitgevoerd om de invloed van de reactor parameters, zoals de verhouding van de oppervlakten van de elektroden en de parameters van beide bronnen, op de plasma karakteristieken in een asymmetrische dubbele frequentie reactor te onderzoeken. Een vergelijking is gemaakt met de symmetrische dubbele frequentie reactor, alsook met de asymmetrische enkele frequentie reactor. De asymmetrie bepaalt de vorming van een "bias" spanning aan de PE, hetgeen op zijn beurt de ionen-bombarderende energie beïnvloedt. De IEDF aan de PE is veel breder dan aan de GE en dan aan de PE in de symmetrische reactor. Bovendien bereikt de ionenenergie aan de PE hogere maximumwaarden bij toenemende verhouding van de elektroden oppervlakten. De invloed van de parameters van de bronnen is min of meer gelijk aan die in symmetrische reactoren.

De conclusie luidt dat het voorliggende onderzoek de invloed van een breed gebied in verschillende reactor parameters van enkele en dubbele frequentie reactoren op het plasma gedrag omvat, zodanig dat deze aangepast kunnen worden om de gewenste plasma karakteristieken te bereiken. Daarom kan deze studie nuttig zijn voor het verbeteren van de controle over het etsproces.



## Appendix A

### SOLVING OF THE POTENTIAL EQUATIONS IN SPHERICAL COORDINATES

In order to simulate an asymmetric discharge in one dimension, the developed model in Cartesian coordinates has been transformed to spherical coordinates, i.e. r-axis instead of z- axis is considered, and the 3 velocity components are  $V_r$ ,  $V_\theta$ , and  $V_\phi$ . The spherical model of the asymmetric dual-frequency reactor is presented in Fig. 7.1. Now the powered (PE) and grounded (GE) electrodes have different area  $A_0$  and  $A_N$ , respectively. The potential equations (2.13) in spherical coordinates are [74]

$$r_{j+1/2}^2 \Phi_{j+1} - (r_{j+1/2}^2 + r_{j-1/2}^2) \Phi_j + r_{j-1/2}^2 \Phi_{j-1} = - \frac{(r_{j+1/2}^3 - r_{j-1/2}^3) \Delta r}{3\epsilon_0} \rho_j, \quad (\text{A.1})$$

where  $r_{j\pm 1/2} = r_j \pm \Delta r$ , and  $j = 1, 2, \dots, N-1$ ,  $N$  being the number of grid cells. In the present simulation a uniform grid has been chosen, i.e.  $\Delta r$  is equal between every two neighbor points but the volume of the cell  $V_c$  is different, which is taken into account in the MCC simulation of charge neutralization (see Sections 2.7 and 2.8). The boundary conditions are [74]

$$\Phi_N = 0 \quad (\text{A.2})$$

and

$$E_{1/2} = \frac{\Phi_0 - \Phi_1}{\Delta r} = \frac{1}{\epsilon_0} \left( \sigma_0 + \frac{r_0^2}{r_{1/2}^2} + \frac{\rho_0}{3} \left( r_{1/2} - \frac{r_0^3}{r_{1/2}^2} \right) \right). \quad (\text{A.3})$$

The potential equations and boundary conditions combined with the circuit equation are written in the following matrix form

$$\begin{pmatrix} b_0 & c_0 & 0 & \cdot & \cdot & \cdot & \cdot \\ a_1 & b_1 & c_1 & 0 & \cdot & \cdot & \cdot \\ 0 & a_2 & b_2 & c_2 & 0 & \cdot & \cdot \\ \cdot & \cdot & \cdot & \cdot & \cdot & \cdot & \cdot \\ \cdot & \cdot & \cdot & \cdot & \cdot & \cdot & \cdot \\ \cdot & \cdot & \cdot & 0 & a_{N-2} & b_{N-2} & c_{N-2} \\ \cdot & \cdot & \cdot & \cdot & 0 & a_{N-1} & b_{N-1} \end{pmatrix}^t \times \begin{pmatrix} \Phi_0 \\ \Phi_1 \\ \Phi_2 \\ \cdot \\ \cdot \\ \Phi_{N-2} \\ \Phi_{N-1} \end{pmatrix}^t = -\frac{\Delta r}{3\epsilon_0} \begin{pmatrix} d_0 \\ d_1 \\ d_2 \\ \cdot \\ \cdot \\ d_{N-2} \\ d_{N-1} \end{pmatrix}^t. \quad (\text{A.4})$$

The matrix elements in spherical coordinates are [74]

$$\begin{aligned} a_j &= r_{j-1/2}^2, & j &= 1, 2, \dots, N-1; \\ b_0 &= -r_{1/2} - \frac{\Delta r}{4\pi\epsilon_0\alpha_0}, & b_j &= -(r_{j-1/2}^2 + r_{j+1/2}^2), & j &= 1, 2, \dots, N-1; \\ c_j &= r_{j+1/2}^2, & j &= 0, 1, \dots, N-2; \\ d_0 &= (r_{1/2}^3 - r_0^3) \frac{\rho_0^t}{2} + 3r_0^2 \sigma_0^{t-\Delta t} + \frac{3}{4\pi} \left( Q_{conv}^t - Q^{t-\Delta t} + \frac{V(t)}{\alpha_0} \right), \\ d_j &= (r_{j+1/2}^3 - r_{j-1/2}^3) \rho_j^t, & j &= 1, 2, \dots, N-1, \end{aligned} \quad (\text{A.5})$$

where  $\alpha_0 = 1/C$ ,  $C$  being the capacitance of the external capacitor,  $Q$  is the charge on one plate of the external capacitor, and  $Q_{conv}$  is the charge deposited by the convection (particle) current (see also Sec. 2.2.2).

**Appendix B** **$CF_x^{+/-} + CF_4$  AND  $F + CF_4$  REACTIVE COLLISION DATA**TABLE B.1.  $CF_3^+$  -  $CF_4$  reactions considered in the model and the corresponding thermodynamic threshold energies  $\Delta E$ , adopted from Ref. 77.

$CF_3^+ + CF_4 \rightarrow$	$\Delta E$ (eV)	$CF_3^+ + CF_4 \rightarrow$	$\Delta E$ (eV)
1. $CF_3^+ + CF_3 + F$	5.621	21. $CF_2^+ + CF + F_2 + 2F$	19.024
2. $CF_2^+ + CF_4 + F$	5.843	22. $CF_3^+ + C + 4F$	20.392
3. $CF^+ + CF_4 + F_2$	7.546	23. $CF_2^+ + CF + 4F$	20.624
4. $CF_3^+ + CF_2 + F_2$	7.598	24. $CF^+ + CF + 2F_2 + F$	20.727
5. $CF^+ + CF_4 + 2F$	9.146	25. $CF^+ + CF + F_2 + 3F$	22.327
6. $CF_3^+ + CF_2 + 2F$	9.198	26. $CF_2^+ + C + 2F_2 + F$	23.035
7. $CF_2^+ + CF_3 + F_2$	9.864	27. $CF^+ + CF + 5F$	23.927
8. $CF_2^+ + CF_3 + 2F$	11.464	28. $CF_2^+ + C + F_2 + 3F$	24.635
9. $CF^+ + CF_3 + F_2 + F$	13.167	29. $CF^+ + C + 3F_2$	24.738
10. $CF_3^+ + CF + F_2 + F$	13.181	30. $CF_2^+ + C + 5F$	26.235
11. $CF_2^+ + CF_2 + F_2 + F$	13.441	31. $CF^+ + C + 2F_2 + 2F$	26.338
12. $CF^+ + CF_3 + 3F$	14.767	32. $CF^+ + C + F_2 + 4F$	27.938
13. $CF_3^+ + CF + 3F$	14.781	33. $CF^+ + C + 6F$	29.538
14. $CF_2^+ + CF_2 + 3F$	15.041	34. $C^+ + C + 3F_2 + F$	32.555
15. $CF^+ + CF_2 + 2F_2$	15.144	35. $C^+ + C + 2F_2 + 3F$	34.155
16. $CF^+ + CF_2 + F_2 + 2F$	16.744	36. $C^+ + C + F_2 + 5F$	35.755
17. $CF_3^+ + C + 2F_2$	17.192	37. $C^+ + C + 7F$	37.355
18. $CF_2^+ + CF + 2F_2$	17.424	38. $F^+ + 2C + 3F_2$	38.717
19. $CF^+ + CF_2 + 4F$	18.344	39. $F^+ + 2C + 2F_2 + 2F$	40.317
20. $CF_3^+ + C + F_2 + 2F$	18.792	40. $F^+ + 2C + F_2 + 4F$	41.917
		41. $F^+ + 2C + 6F$	43.517

TABLE B.2.  $CF_3^- - CF_4$  reactions considered in the model and the corresponding thermodynamic threshold energies  $\Delta E$ , adopted from Ref. 77.

$CF_3^- + CF_4 \rightarrow$	$\Delta E$ (eV)	$CF_3^- + CF_4 \rightarrow$	$\Delta E$ (eV)
1. $CF_3 + CF_4 + e$	1.871	35. $CF_3^- + C + F_2 + 2F$	18.792
2. $F + CF_2 + CF_4$	1.927	36. $CF_3 + C + 2F_2 + e$	19.063
3. $CF_2 + CF_4 + F + e$	5.448	37. $F + 2CF + 2F_2$	19.091
4. $CF_3^- + CF_3 + F$	5.621	38. $F + CF_2 + C + 2F_2$	19.119
5. $2CF_3 + F + e$	7.492	39. $CF_2 + CF + 4F + e$	20.229
6. $F + CF + CF_4 + F$	7.510	40. $CF_3^- + C + 4F$	20.392
7. $F + CF_2 + CF_3 + F$	7.548	41. $CF_3 + C + F_2 + 2F + e$	20.663
8. $CF_3^- + CF_2 + F_2$	7.598	42. $F + 2CF + F_2 + 2F$	20.691
9. $CF_3^- + CF_2 + 2F$	9.198	43. $F + CF_2 + C + F_2 + 2F$	20.719
10. $CF + CF_4 + F_2 + e$	9.431	44. $CF_3 + C + 4F + e$	22.263
11. $CF_3 + CF_2 + F_2 + e$	9.469	45. $F + 2CF + 4F$	22.291
12. $F + 2CF_2 + F_2$	9.525	46. $F + CF_2 + C + 4F$	22.319
13. $CF + CF_4 + 2F + e$	11.031	47. $2CF + 2F_2 + F + e$	22.612
14. $CF_3 + CF_2 + 2F + e$	11.069	48. $CF_2 + C + 2F_2 + F + e$	22.640
15. $F + 2CF_2 + 2F$	11.125	49. $2CF + F_2 + 3F + e$	24.212
16. $F + CF + CF_3 + F_2$	11.531	50. $CF_2 + C + F_2 + 3F + e$	24.240
17. $2CF_2 + F_2 + F + e$	13.046	51. $F + CF + C + 2F_2 + F$	24.702
18. $F + CF + CF_3 + 2F$	13.131	52. $2CF + 5F + e$	25.812
19. $CF_3^- + CF + F_2 + F$	13.181	53. $CF_2 + C + 5F + e$	25.840
20. $F + C + CF_4 + F_2$	14.219	54. $F + CF + C + F_2 + 3F$	26.302
21. $2CF_2 + 3F + e$	14.646	55. $CF + C + 3F_2 + e$	26.623
22. $CF_3^- + CF + 3F$	14.781	56. $F + CF + C + 5F$	27.902
23. $C + CF_4 + F_2 + F + e$	15.042	57. $CF + C + 2F_2 + 2F + e$	28.223
24. $CF_3 + CF + F_2 + F + e$	15.052	58. $F + 2C + 3F_2$	28.713
25. $F + CF_2 + CF + F_2 + F$	15.108	59. $CF + C + F_2 + 4F + e$	29.823
26. $F + C + CF_4 + 2F$	15.819	60. $F + 2C + 2F_2 + 2F$	30.313
27. $C + CF_4 + 3F + e$	16.642	61. $CF + C + 6F + e$	31.423
28. $CF_3 + CF + 3F + e$	16.652	62. $F + 2C + F_2 + 4F$	31.913
29. $F + CF_2 + CF + 3F$	16.708	63. $2C + 3F_2 + F + e$	32.234
30. $CF_2 + CF + 2F_2 + e$	17.029	64. $F + 2C + 6F$	33.513
31. $F + C + CF_3 + F_2 + F$	17.142	65. $2C + 2F_2 + 3F + e$	33.834
32. $CF_3^- + C + 2F_2$	17.192	66. $2C + F_2 + 5F + e$	35.434
33. $CF_2 + CF + F_2 + 2F + e$	18.629	67. $2C + 7F + e$	37.034
34. $F + C + CF_3 + 3F$	18.742		

TABLE B.3.  $F^- - CF_4$  reactions considered in the model and the corresponding thermodynamic threshold energies  $\Delta E$ , adopted from Ref. 77.

$F^- + CF_4 \rightarrow$	$\Delta E$ (eV)	$F^- + CF_4 \rightarrow$	$\Delta E$ (eV)
1. $CF_4 + F + e$	3.521	11. $CF + 2F_2 + e$	15.102
2. $F^- + CF_3 + F$	5.621	12. $CF + F_2 + 2F + e$	16.702
3. $CF_3 + F_2 + e$	7.542	13. $F^- + C + 2F_2$	17.192
4. $F^- + CF_2 + F_2$	7.598	14. $CF + 4F + e$	18.302
5. $CF_3 + 2F + e$	9.142	15. $F^- + C + F_2 + 2F$	18.792
6. $F^- + CF_2 + 2F$	9.198	16. $F^- + C + 4F$	20.392
7. $CF_2 + F_2 + F + e$	11.119	17. $C + 2F_2 + F + e$	20.713
8. $CF_2 + 3F + e$	12.719	18. $C + F_2 + 3F + e$	22.313
9. $F^- + CF + F_2 + F$	13.181	19. $C + 5F + e$	23.913
10. $F^- + CF + 3F$	14.781		

TABLE B.4.  $CF_2^+ - CF_4$  reactions considered in the model and the corresponding thermodynamic threshold energies  $\Delta E$ , adopted from Ref. 77.

$CF_2^+ + CF_4 \rightarrow$	$\Delta E$ (eV)	$CF_2^+ + CF_4 \rightarrow$	$\Delta E$ (eV)
1. $CF^+ + CF_4 + F$	3.303	14. $CF^+ + CF + 4F$	18.084
2. $CF_2^+ + CF_3 + F$	5.621	15. $CF_2^+ + C + F_2 + 2F$	18.792
3. $CF^+ + CF_3 + F_2$	7.324	16. $CF_2^+ + C + 4F$	20.392
4. $CF_2^+ + CF_2 + F_2$	7.598	17. $CF^+ + C + 2F_2 + F$	20.495
5. $CF^+ + CF_3 + 2F$	8.924	18. $CF^+ + C + F_2 + 3F$	22.095
6. $CF_2^+ + CF_2 + 2F$	9.198	19. $CF^+ + C + 5F$	23.695
7. $CF^+ + CF_2 + F_2 + F$	10.901	20. $C^+ + C + 3F_2$	26.712
8. $CF^+ + CF_2 + 3F$	12.501	21. $C^+ + C + 2F_2 + 2F$	28.312
9. $CF_2^+ + CF + F_2 + F$	13.181	22. $C^+ + C + F_2 + 4F$	29.912
10. $CF_2^+ + CF + 3F$	14.781	23. $C^+ + C + 6F$	31.512
11. $CF^+ + CF + 2F_2$	14.884	24. $F^+ + 2C + 2F_2 + F$	34.474
12. $CF^+ + CF + F_2 + 2F$	16.484	25. $F^+ + 2C + F_2 + 3F$	36.074
13. $CF_2^+ + C + 2F_2$	17.192	26. $F^+ + 2C + 5F$	37.674

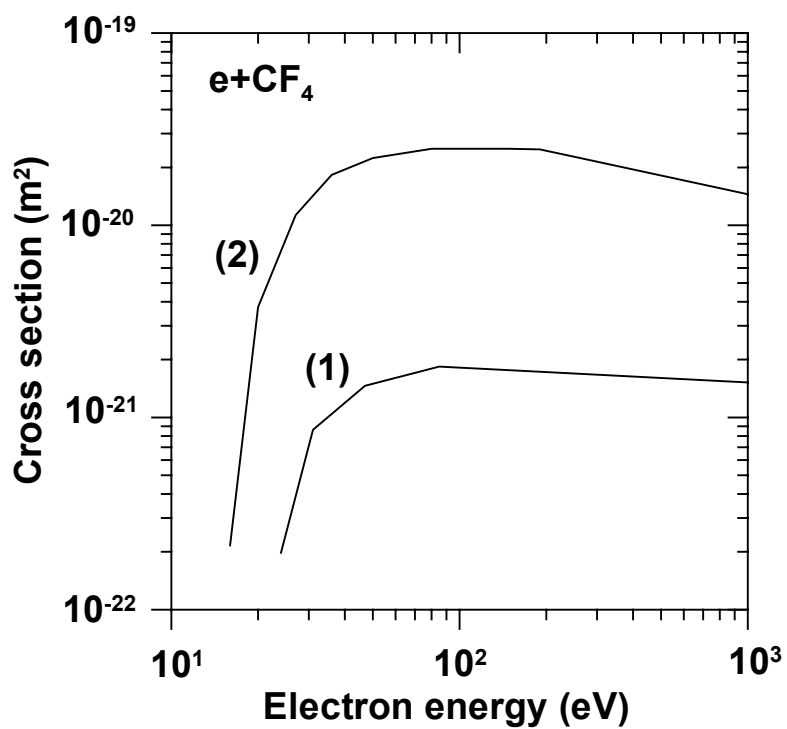


FIGURE B.1. Cross-section data for  $CF_2^+$  ionization (1) and  $CF_3^+$  ionization (2), presented by Eqs. (3.1) and (3.2), respectively, in Chapter 3. The data are taken from Ref. 80. The threshold energy of (1) is higher and its cross-section is one order of magnitude less than the corresponding characteristics of (2).

## Appendix C

### Published Articles

1. Particle-in-cell/Monte Carlo simulation of a capacitively coupled radio frequency Ar/CF<sub>4</sub> discharge: Effect of gas composition.

V. Georgieva, A. Bogaerts, and R. Gijbels

*J. Appl. Phys.* **93**, 2369 (2003).

2. Numerical study of Ar/CF<sub>4</sub>/N<sub>2</sub> discharges in single- and dual-frequency capacitively coupled plasma reactors.

V. Georgieva, A. Bogaerts and R. Gijbels

*J. Appl. Phys.* **94**, 3748 (2003).

3. Numerical investigation of ion-energy-distribution functions in single- and dual-frequency capacitively coupled plasma reactors.

V. Georgieva, A. Bogaerts and R. Gijbels

*Phys. Rev. E* **69**, 026406 (2004).

4. Numerical simulation of dual-frequency etching reactors: Influence of the external process parameters on the plasma characteristics.

V. Georgieva and A. Bogaerts

*J. Appl. Phys.* **98**, 023308 (2005).

5. Plasma characteristics of an Ar/CF<sub>4</sub>/N<sub>2</sub> discharge in an asymmetric dual frequency reactor: Numerical investigation by a PIC/MC model.

V. Georgieva and A. Bogaerts

Submitted for publication to *Plasma Sources Sci. Technol.*

6. Negative ion behavior in single- and dual-frequency etching reactors: a computer simulation study by a PIC/MCC

V. Georgieva and A. Bogaerts

Submitted for publication to *Phys. Rev. E*.

### **Contributions to International Conferences**

1. Particle in Cell/ Monte Carlo Simulation of a CC RF Discharge in a Mixture of Ar and CF<sub>4</sub>.

V. Georgieva, A. Bogaerts and R. Gijbels

Poster at the *Workshop on the Exploration of Low Temperature Plasma Physics*, 22-23 November 2001, Kerkrade, the Netherlands.

2. Particle-in-cell/Monte Carlo simulation of a cc RF Ar/CF<sub>4</sub> discharge: effect of gas mixture.

V. Georgieva, A. Bogaerts and R. Gijbels

Poster at the *ESCAMPIG 16 and ICPR 5 – Joint Conference*, 14-18 July 2002, Grenoble, France.

3. Particle-in-cell/Monte Carlo simulation of a cc RF Ar/CF<sub>4</sub> discharge: effect of gas mixture.

V. Georgieva, A. Bogaerts and R. Gijbels

Poster at the *International WE-Hereaus Summerschool, Course on Low Temperature Plasma Physics and Applications and Master Class on Modeling of Reactive Plasmas* 8-17 September 2002, Bad Honnef, Germany.

4. Particle-in-cell/Monte Carlo simulation of cc RF Ar/CF<sub>4</sub>/N<sub>2</sub> discharges.

V. Georgieva, A. Bogaerts and R. Gijbels

Poster and full paper published in the conference proceedings, *ISPC 16*, 22-27 June 2003, Taormina, Italy

5. Numerical study of a cc RF Ar/CF<sub>4</sub>/N<sub>2</sub> discharge.

V. Georgieva, A. Bogaerts, R. Gijbels and I. Kolev

Poster at the *XXVIth ICPIG*, 15-20 July 2003, Greifswald, Germany.

6. Numerical study of an Ar/CF<sub>4</sub>/N<sub>2</sub> discharge in an asymmetric dual-frequency reactor.

V. Georgieva and A. Bogaerts

Poster at the *XXVIIth ICPIG*, 18-22 July 2005, Eindhoven, the Netherlands.

7. Influence of the applied frequencies on plasma characteristics in dual-frequency reactors: a numerical study.

V. Georgieva and A. Bogaerts

Poster at the *ISPC 17*, 08-12 August 2005, Toronto, Canada.

### **Invited Seminars**

1. Influence of the external process parameters on the plasma characteristics in dual-frequency etching reactors.

V. Georgieva and A. Bogaerts

Seminar at the *Ecole Polytechnique, Laboratoire de Physique et Technologie des Plasmas*, September 30, 2005, Palaiseau, France.



## **Bibliography**

- [1] M. A. Lieberman and A. J. Lichtenberg, *Principles of Plasma Discharges and Materials Processing* (John Wiley & Sons, New York, 1994).
- [2] B. Chapman, *Glow Discharge Processes* (John Wiley & Sons, New York, 1980).
- [3] W. M. Greene, M. A. Hartney, W. G. Oldham, and D. W. Hess, *J. Appl. Phys.* **63**, 1367 (1988).
- [4] A. Manenschijn, G. C. A. M. Janssen, E. van der Drift, and S. Radelaar, *J. Appl. Phys.* **69**, 1253 (1991).
- [5] V. A. Godyak and R. B. Piejak, *Phys. Rev. Lett.* **65**, 996 (1990).
- [6] V. A. Godyak, R. B. Piejak, and B. M. Alexandrovich, *Plasma Sources Sci. Technol.* **1**, 36 (1992).
- [7] J. K. Olthoff, R. J. Van Brunt, and S. B. Radovanov, *J. Appl. Phys.* **72**, 4566 (1992).
- [8] J. K. Olthoff, R. J. Van Brunt, S. B. Radovanov, J. A. Rees and R. Surowiec, *J. Appl. Phys.* **75**, 115 (1994).
- [9] R. J. M. M. Snijkers, M. J. M. van Sambeek, G. M. W. Kroesen, and F. J. de Hoog, *Appl. Phys. Lett.* **63**, 308 (1993).
- [10] D. Barton, D. J. Heason, R. D. Short and J. W. Bradley, *Meas. Sci. Technol.* **11**, 1726 (2000).
- [11] J. L. Jauberteau, G. J. Meeusen, M. Haverlag, G. M.W. Kroesen and F. J. de Hoog, *J. Phys. D* **24**, 261 (1990).
- [12] M. Haverlag, A. Kono, D. Passchier, G. M.W. Kroesen, W. J. Goedheer and F. J. de Hoog, *J. Appl. Phys.* **70**, 3472 (1991).

- [13] J. P. Booth, G. Cunge, P. Chabert, and N. Sadeghi, *J. Appl. Phys.* **85**, 3097 (1999).
- [14] H. H. Goto, H.-D. Löwe, and T. Ohmi, *J. Vac. Sci. Technol. A* **10**, 3048 (1992).
- [15] H. H. Goto, H.-D. Löwe, and T. Ohmi, *IEEE Trans. Semicond. Manuf.* **6**, 58 (1993).
- [16] K. Kaga, T. Kimura, T. Imaeda and K. Ohe, *Jpn. J. Appl. Phys., Part1* **40**, 6115 (2001).
- [17] W. Tsai, G. Mueller, R. Lindquist, B. Frazier, and V. Vahedi, *J. Vac. Sci. Technol. B* **14**, 3276 (1996).
- [18] T. Kitajima, Y. Takeo, and T. Makabe, *J. Vac. Sci. Technol. A* **17**, 2510 (1999).
- [19] T. Kitajima, Y. Takeo, Z. Lj. Petrović, and T. Makabe, *Appl. Phys. Lett.* **77**, 489 (2000).
- [20] M. A. Lieberman, *IEEE Trans. Plasma Sci.* **16**, 638 (1988).
- [21] M. A. Lieberman, *J. Appl. Phys* **65**, 4186 (1989).
- [22] C. Wild and P. Koidl, *Appl. Phys. Lett.* **54**, 505 (1989).
- [23] C. Wild and P. Koidl, *J. Appl. Phys.* **69**, 2909 (1991).
- [24] K. Nanbu, *Phys. Rev. E* **55**, 4642 (1997).
- [25] R. N. Franklin, *J. Phys. D* **35**, 536 (2002).
- [26] K. Nanbu and G. Wakayama, *Vacuum* **65**, 11 (2002).
- [27] J. Robiche, P.C. Boyle, M. M. Turner, and A. R. Ellingboe, *J. Phys. D* **36**, 1810 (2003).
- [28] V. A. Godyak and N. Sternberg, *Phys. Rev. A* **42**, 2299 (1990).
- [29] M. A. Lieberman and S. Ashida, *Plasma Sources Sci. Technol.* **5** 145 (1996).
- [30] Y. T. Lee, M. A. Lieberman, A. J. Lichtenberg, F. Bose, H. Baltes, and R. Patrick, *J. Vac. Sci. Technol. A* **15**, 113 (1997).
- [31] J.-P. Boeuf, *Phys. Rev A* **36**, 2782 (1987).
- [32] J. D. P. Passchier and W. J. Goedheer, *J. Appl. Phys* **73**, 1073 (1993).

- [33] M. A. Sobolewski, Phys. Rev E **56**, 1001 (1997).
- [34] H. C. Kim and V. I. Manousiouthakis, J. Vac. Sci. Technol. A **16**, 2162 (1998).
- [35] N. V. Mantzaris, A. Boudouvis and E. Gogolides, J. Appl. Phys. **77**, 6169 (1995).
- [36] E. Gogolides and H. H. Sawin, J. Appl. Phys. **72**, 3971 (1992).
- [37] E. Gogolides, M. Stathakopoulos and A. Boudouvis, J. Phys. D **27**, 1878 (1994).
- [38] Ph. Belenguer and J.-P. Boeuf, Phys. Rev A **41**, 4447 (1990).
- [39] M. Surendra, D. B. Graves, and G. M. Jellum, Phys. Rev A **41**, 1112 (1990).
- [40] A. Bogaerts, R. Gijbels and W. Goedheer, J. Appl. Phys. **78**, 2233 (1995).
- [41] A. Bogaerts, R. Gijbels and W. Goedheer, Jpn. J. Appl. Phys., **38**, 4404 (1999).
- [42] S. Rauf and M. J. Kushner, IEEE Trans. Plasma Sci. **27**, 1329 (1999).
- [43] K. Maeshige, G. Washio, T. Yagisawa and T. Makabe, J. Appl. Phys. **91**, 9494 (2002).
- [44] M. J. Kushner, J. Appl. Phys. **58**, 4024 (1985).
- [45] F. R. Myers, M. Ramaswami, and T. S. Cale, J. Electrochem. Soc. **141**, 1313 (1994).
- [46] C. K. Birdsall and A. B. Langdon, *Plasma Physics via Computer Simulation* (McGraw-Hill, New York, 1985).
- [47] C. K. Birdsall, IEEE Trans. Plasma Sci. **19**, 65 (1991).
- [48] R. W. Hockney and J. W. Eastwood, *Computer Simulation Using Particles*, (Inst. of Phys. Publishing, Bristol, U.K., 1988).
- [49] D. Vender and R. W. Boswell, IEEE Trans. Plasma Sci. **18**, 725 (1990).
- [50] M. Surendra and D. B. Graves, IEEE Trans. Plasma Sci. **19**, 144 (1991).
- [51] M. Surendra and D.B. Graves, Appl. Phys. Lett. **59**, 2091 (1991).
- [52] V. Vahedi, C. K. Birdsall, M. A. Lieberman, G. DiPeso, and T. D. Rognlien, Phys. Fluid B **5**, 2719 (1993).
- [53] V. Vahedi and M. Surendra, Comput. Phys. Commun. **87**, 179 (1995).

- [54] K. Nanbu and Y. Kitatani, *Vacuum* **47**, 1023 (1996).
- [55] M. Yan and W. J. Goedheer, *Plasma Sources Sci. Technol.* **8**, 349 (1999).
- [56] M. Yan, A. Bogaerts, W. J. Goedheer and R. Gijbels, *Plasma Sources Sci. Technol.* **9**, 583 (2000).
- [57] K. Denpoh and K. Nanbu, *J. Vac. Sci. Technol. A* **16**, 1201 (1998)
- [58] K. Denpoh and K. Nanbu, *Jpn. J. Appl. Phys., Part1* **39**, 2804 (2000).
- [59] V. Georgieva, A. Bogaerts, and R. Gijbels, *J. Appl. Phys.* **93**, 2369 (2003).
- [60] V. Georgieva, A. Bogaerts and R. Gijbels, *J. Appl. Phys.* **94**, 3748 (2003).
- [61] V. Georgieva, A. Bogaerts and R. Gijbels, *Phys. Rev. E* **69**, 026406 (2004).
- [62] V. Georgieva and A. Bogaerts, *J. Appl. Phys.* **98**, 023308 (2005).
- [63] V. Vahedi and G. DiPeso, *J. Comput. Phys.* **131**, 149 (1997).
- [64] G. Wakayama and K. Nanbu, *IEEE Trans. Plasma Sci.* **31**, 638 (2003).
- [65] J. K. Lee, N. Yu. Babaeva, H. C. Kim, O. V. Manuilenko, and J. W. Shon, *IEEE Trans. Plasma Sci.* **32**, 47 (2004).
- [66] P.C. Boyle, A. R. Ellingboe, and M. M. Turner, *Plasma Sources Sci. Technol.* **13**, 493 (2004).
- [67] P.C. Boyle, A. R. Ellingboe, and M. M. Turner, *J. Phys. D* **37**, 697 (2004).
- [68] M. A. Lieberman, ICPIG XXVII, Eindhoven, the Netherlands, 18-22 July, 2005.  
To be found at <http://www.eecs.berkeley.edu/~lieber/plasmaproc21cent.pdf>
- [69] E. Kawamura, C. K. Birdsall and V. Vahedi, *Plasma Sources Sci. Technol.* **9**, 413 (2000).
- [70] M. Nagai, M. Hori, and T. Goto, Oral presentation at *ISPC 17*, 08-12 August 2005, Toronto, Canada.
- [71] K. Nanbu, *IEEE Trans. Plasma Sci.* **28**, 971 (2000).
- [72] G. A. Bird, *Molecular Gas Dynamics*, (Clarendon Press, Oxford, U.K., 1976).
- [73] G. A. Bird, *Molecular Gas Dynamics and Direct Simulation of Gas Flows*, (Clarendon Press, Oxford, U.K., 1994).

- [74] J. P. Verboncoeur, M. V. Alves, V. Vahedi and C. K. Birdsall, *J. Comp. Phys.* **104**, 321 (1993).
- [75] W. H. Press, S. A. Teukolsky, W. T. Vetterling, B. P. Flannery, *Numerical recipes in Fortran 77, Vol. 1 of Fortran Numerical Recipes*, (Cambridge University Press, U.K., 1986, 1992), available at <http://library.lanl.gov/numerical/>
- [76] H. R. Skullerud, *Brit. J. Appl. Phys.*, ser. 2, 1567 (1968).
- [77] K. Denpoh, PhD Thesis, Tohoku University, Sendai, Japan.
- [78] K. Nanbu and K. Denpoh, *J. Phys. Soc. Jpn.* **67**, 1288 (1998)
- [79] A.V. Phelps and Z. Lj. Petrovic, *Plasma Sources Sci. Technol.* **8**, R21 (1999).
- [80] M. Kurihara, Z. Lj. Petrovic and T. Makabe, *J. Phys. D* **33**, 2146 (2000).
- [81] R. A. Bonham, *Jpn. J. Appl. Phys.*, Part1 **33**, 4157 (1994).
- [82] A.V. Phelps and L. C. Pitchford, *Phys. Rev. A* **31**, 2932 (1985); A.V. Phelps et al., Joint Institute for Laboratory Astrophysics (JILA) Information Center Report No.26 (1985), (to be found on [ftp://jila.colorado.edu/collision\\_data/](ftp://jila.colorado.edu/collision_data/)).
- [83] W. G. Vincenti and C. H. Kruger Jr., *Introduction to Physical Gas Dynamics*, (New York, NY: Wiley, 1967).
- [84] A. Okhrimovskyy, A. Bogaerts, R. Gijbels, *Phys. Rev. E* **65**, 037402 (2002).
- [85] A. V. Phelps, *J. Phys. Chem. Ref. Data* **20**, 557 (1991); A. V. Phelps, *J. Appl. Phys.* **76**, 747 (1994); [ftp://jila.colorado.edu/collision\\_data/](ftp://jila.colorado.edu/collision_data/).
- [86] M. R. Spalburg and E. A. Gislason, *Chem. Phys.* **94**, 339 (1985).
- [87] S. Rauf and M. J. Kushner, *J. Appl. Phys.* **82**, 2805 (1997).
- [88] J. Henriques, E. Tatarova, V. Guerra and C. M. Ferreira, *J. Appl. Phys.* **91**, 5622 (2002).
- [89] T. Kimura and K. Ohe, *J. Appl. Phys.* **92**, 1780 (2002).
- [90] H. Singh, J. W. Coburn and D. B. Graves, *J. Vac. Sci. Technol. A* **19**, 718 (2001).
- [91] F. Debal, J. Bretagne, M. Jumet, M. Wautelet, J. P. Dauchot and M. Hecq, *Plasma Sources Sci. Technol.* **7**, 219 (1998).

- [92] T. Kimura and K. Ohe, J. Appl. Phys **92**, 1780 (2002).
- [93] H. Singh and D. B. Graves, J. Appl. Phys **87**, 4098 (2000).
- [94] K. Hioki, H. Hirata, S. Matsumura, Z. Lj. Petrovic and T. Makabe, J. Vac. Sci. Technol. A **18**, 864 (2000).
- [95] M. D. Bowden, R. Tabata, P. Suanpoot, K. Uchino, K. Muraoka and M. Noguchi, J. Appl. Phys. **90**, 2158 (2001).
- [96] T. Kimura, K. Kaga and K. Ohe, Jpn. J. Appl. Phys., Part1 **39**, 1351 (2000).
- [97] E. Kawamura, V. Vahedi, M. A. Lieberman and C. K. Birdsall, Plasma Sources Sci. Technol. **8**, R45 (1999).
- [98] W. J. Goedheer, Plasma Sources Sci. Technol. **9**, 507 (2000).
- [99] J. Liu, G. L. Huppert, and H. H. Sawin, J. Appl. Phys. **68**, 3916 (1990).
- [100] F. Becker, I. W. Rangelow, K. Maßeli, and R. Kassing, Surf. Coat. Technol., **74-75**, 485 (1995).
- [101] P. Benoit-Cattin and L. C. Bernard, J. Appl. Phys. **39**, 5723 (1968).
- [102] A. Metze, D. W. Ernie, and H. Oskam, J. Appl. Phys. **60**, 3081 (1986).
- [103] B. L. Peko, I.V. Dyakov, R. L. Champion, M. V. V. S. Rao, and J. K. Olthoff, Phys. Rev E **60**, 7449 (1999).
- [104] A. Vasenkov and M. Kushner, , J. Appl. Phys. **95**, 834 (2004).
- [105] S. Rauf, IEEE Trans. Plasma Sci. **31**, 471 (2003).
- [106] T. Kitamura, N. Nakano, T. Makabe and Y. Yamaguchi, Plasma Sources Sci. Technol. **2**, 40 (1993).
- [107] G. Curley, J.P. Booth, and J. Guillon, Poster presentation at the *XXVIIth ICPIG*, 18-22 July 2005, Eindhoven, the Netherlands.
- [108] Y. Raizer, M. Shneider, and N. Yatsenko, *Radio-Frequency Capacitive Discharges* (CRC Press, Boca Raton, London, Tokyo, 1995)
- [109] M. V. Alves, M. A. Lieberman, V. Vahedi, and C. K. Birdsall J. Appl. Phys. **69**, 3823 (1991).

- [110] T. Ohmori, T. K. Goto, T. Kitajima, and T. Makabe, *Appl. Phys. Lett.* **83**, 4637 (2003).